# MICROPATTERNED DIAMOND VACUUM FIELD EMISSION DEVICES

By

Anurat Wisitsorat-at

Dissertation

Submitted to the Faculty of the

Graduate School of Vanderbilt University

in partial fulfillment of the requirements

for the degree of

DOCTOR OF PHILOSOPHY

in

Electrical Engineering

May, 2002

Nashville, Tennessee

Approved by

Prof. Weng Poo Kang (Chair)

Prof. Jimmy L. Davidson

Prof. Francis M. Wells

Prof. Arthur J. Brodersen

Prof. David V. Kerns

ACKNOWLEDGMENTS

I would like to express my deepest gratitude, appreciation, and thanks to my dissertation advisor, Dr. W.P. Kang for his invaluable assistance, encouragement, and thoughtful guidance throughout my graduate work at Vanderbilt University. I would like to express my appreciation to Dr. Davidson, the director of Vanderbilt Diamond Microelectronic Laboratory, for his invaluable assistance, criticism, and suggestion. I would like to thank Mr. Mick Howell, the research engineer of Vanderbilt Diamond Microelectronic Laboratory for his invaluable technical support, encouragement, and friendship. I would also like to thanks Drs. T. Fisher, D. V. Kerns, F. Wells, and A. Brodersen for serving in my Ph.D committee. I would like to acknowledge Dr. Hofmiester for the help in diamond brazing, Mr. Charles Ellis for the use of Microelectronics laboratory at Auburn University, and Dr. M. George for the use of Raman spectroscopy at Fisk University. I also wish to acknowledge my colleagues at Vanderbilt, upon whose help I drew from on many occasions.

I am grateful for a fellowship award from Thai government for my graduate study. I greatly appreciate Research Assistantship Awards from National Reconnaissance Office (NRO), Tennessee Valley Authority (TVA), and Department of Defense (DOD).

And most importantly, I give heartful thanks to my parents, my sister and brother, and my friends for their continuous support and love, which inspired me during hard times.

TABLE OF CONTENTS

LIST OF TABLES

LIST OF FIGURES

# CHAPTER I

# INTRODUCTION

## Overview of vacuum microelectronics and vacuum field emission devices

The development of planar technology for solid-state microelectronic devices and integrated circuits has wilted the role of conventional thermionic vacuum tubes in electronics. Despite the major drawback in the ease of fabrication, thermionic vacuum tubes have other disadvantages. These include large size, high operating temperature, high operating voltage, and high power consumption. Although advanced solid-state microelectronic devices have been very successful for modern microelectronic applications, they have some disadvantages. These solid-state devices are vulnerable to radiation and high temperature. In addition, the lifetime of solid-state devices are not very long and the operating speed is limited by the carrier saturation velocity in the solid. On the other hand, the “junctionless” vacuum tube devices are temperature and radiation tolerant, high speed, and long life. These superior performances of vacuum tube devices over the solid-state devices can be realized if miniature vacuum tubes in micron-size can be produced and batch fabricated.

The research of vacuum microelectronics has been focused on the development of vacuum microelectronic devices (VMDs) utilizing micron-size electron field emitters, which can be used in microelectronic switching, amplification and control completely analogous to the conventional thermionic vacuum tube devices. Since electron field emission instead of thermionic emission is used to generate the charge carrier, VMDs can operate at room temperature. Thus, the high operating temperature requirement, as in vacuum tube, has been removed. In addition, electron field emission can provide higher current density than thermionic emission. By keeping vacuum as the active volume of the devices, VMDs should hold high temperature and radiation tolerant, high reliability and long life properties as thermionic vacuum tubes do. In addition, because of their small size, VMDs can operate much faster than the traditional vacuum tubes. Moreover, VMDs can operate faster than solid-state microelectronic devices because electrons can move much faster in vacuum than in solid-state material.

**Table 1.1.** Summary of device properties of electron field emission devices, standard thermionic vacuum tubes, and solid-state devices for potential applications.

| Property | Electron field emission devices | Standard thermionic vacuum tubes | Solid-state devices | Advantages and disadvantages of field emission devices |
|---|---|---|---|---|
| Size | Micron range | Centimeter range | Micron to sub micron range | Much smaller size than standard vacuum tubes |
| Operating Temperature | Room temperature | 1000-2000°C | Room temperature | General applications |
| Operating voltage (V) | 50-10kV | 100-100k V | 2.5-15 V | Medium to high operating voltage |
| Current stability | Fair | Fair | Excellent | Acceptable current stability |
| Current density | 0.1-100k $A/cm^2$ | 0.01-10k $A/cm^2$ | 1m-0.1 $A/cm^2$ | Very high current density applications |
| Operating power | Subwatts to tens of watt range | Fews to hundreds of watt range | Milliwatts to subwatts range | High power applications |
| Power consumption | Subwatts to tens of watt range | Tens to thousands of watt range | Milliwatts to subwatts range | More efficient than standard vacuum tubes |
| Speed | Very fast | Medium | Fast | Very high speed applications |
| High temperature and radiation tolerant | Excellent | Excellent | Poor | High temperature and radiation hardened applications |
| Reliability | Good | Excellent | Fair | Better reliability than solid state devices |
| Life time | Long | Very Long | Medium | Longer life time than solid state devices |
| Technology development | Recent developing technology | Well established technology | Very Well established technology | Technology improvement need to be done |

The development of electron field emitters would eliminate the need of the thermionic vacuum tube devices in some potential applications such as cathode ray tube (CRT) for display

devices and electron guns. The replacement of the thermionic vacuum tubes with miniature electron field emitters will substantially improve performance and reduce size and weight of these systems. However, there are several problems challenging the development of VMDs. Generally, electron field emission requires strong electric field to extract electrons into vacuum. The resulted high operating voltage requirement is the main barrier for practical applications. Furthermore, field emission has high current density. Thus, emission current stability and reliability are also potential problems of the field emission devices. If the operating voltage of field emission devices can be made comparable to that of solid-state devices and stability problem can be solved, VMDs will be a potential replacement for semiconductor devices in many applications. **Table 1.1** summarizes device properties of micro field emitter devices, standard thermionic vacuum tubes, and solid-state devices for potential applications and comments on the efficacy of field emission devices.

The core research of vacuum microelectronics is the search for electron field emission devices with low operating voltage, high and stable emission current for potential applications. Recent works on field emission have been focused on new cathode structure for vacuum microelectronic applications. These include the use of electric field enhancement on sharp microtips and low work function emitter materials.

Metal field emission diode and triode are the first developed field emission devices [1-12]. However, metal field emission diode and triode have limited potential applications because of their high work functions and high turn-on electric fields. In addition, the problem of impurity adsorption on metal surfaces leads to current instability and thereby very high vacuum condition is required for stable operation. Furthermore, current technology for making sharp metal emitter with low turn-on voltage is limited. Therefore, several approaches such as field forming process [6,8] and co-adsorption of silicon (Si) and titanium (Ti) on tungsten (W) emitter [13] have been proposed to improve the emission characteristics and stability of the metal emitter. However, these approaches complicate the fabrication process and do not yield significant improvement.

Silicon field emission diode and triode are the next well-developed electron field emission devices and have been widely studied because of the well-established silicon microprocessing technology [14-31]. The field emission of these devices is relatively poor due to its high work function, poor thermal, mechanical, and chemical properties. For example, silicon field emitter is very sensitive to impurity adsorption, which could cause significant performance

deterioration and device failure. To obtain a stable operation, they require extremely high vacuum condition. In addition, low thermal conductivity and low breakdown electric field prohibit the use of silicon tips for high power or high emission current applications. Poor thermal conductivity of silicon results in thermal instability of silicon emitters operated at high emission current. Emission current was found to degrade with time and eventually silicon tips were destroyed due to heat accumulation and atomic migration [33-34]. Therefore, a number of techniques have been proposed to improve the emission characteristics and stability of the silicon emitters. These include silicidation by metal adsorption [35-36], surface coating with different materials such as TiN [37], and advanced emitter structures such as $p^{+}$-$n^{++}$ junction [38], MOSFET [39], MIS cathode [40-41], MOS cathode [42-43], and porous silicon diodes [44]. These techniques result in complicated fabrication processes with little improvement in device performances.

Electron emission from several other materials such as GaN [45-47], BN [48], ZrN [49], GaAs [50], and resist polymers [51] have been reported. These are wide band gap materials with small electron affinity or work function and thus should be suitable for electron field emission devices. However, electron field emitters made of these materials have not shown promising performance for potential applications.

Recently, electron field emission from diamond or diamond-coated surfaces have been shown experimentally to yield large currents at low electric fields relative to that of metals or narrow band-gap semiconductors. Many believe the observed low field emission from diamond arises from its low or negative electron affinity (NEA) property [52-62]. The NEA property of diamond, unlike other materials, is stable in gas ambient. Additionally, diamond has excellent mechanical and chemical properties suitable for vacuum microelectronic applications. Diamond is relatively inert to chemical adsorption because it is a stable and chemically inert material. Thus, diamond field emission devices would not require high vacuum condition for operation. In addition, diamond has strong crystal structure, and hence field emission devices made of diamond should be able to operate with long life. Furthermore, diamond can operate at high temperature or at high power because of its high electrical breakdown field and high thermal conductivity. Thus, diamond emitters possess promising performance for potential applications such as flat panel displays, intense electron sources for microwave generation, high power

devices, and vacuum microelectronic devices. **Table 1.2** summarizes material properties of diamond, silicon and metal for field emission application [63].

**Table 1.2.** Summary of material properties of diamond, silicon and metal for field emission applications

| Property | Diamond | Silicon | Metal | Advantages of diamond |
|---|---|---|---|---|
| Electron affinity (eV) | Low EA and NEA on some facets | 4.05 | 4-6 | Low operating voltage |
| Electrical breakdown field (V/cm) | $1x10^7$ | $2.5x10^5$ | N/A | High power application |
| Thermal conductivity (W/cm·°C) | 20 | 1.5 | 5-0.5 | High emission current |
| Electrical mobility ($cm^2/V·s$) | $1.5x10^3$ | $2.0x10^3$ | $10^2$-$10^3$ | High carrier saturation velocity |
| Surface chemical stability | Relatively inert to adsorption | Very sensitive to adsorption | Quite sensitive to adsorption | High stability, larger emitting area |
| Vacuum requirement (Torr.) | Relatively low vacuum ($10^{-5}$-$10^{-6}$) | Very high vacuum ($10^{-10}$-$10^{-11}$) | Very high vacuum ($10^{-9}$-$10^{-11}$) | Practical vacuum environment |
| Technology development | Recent developing technology | Well established technology | Well established technology but with slow advancement | Technology improvement need to be done |

However, there are several problems associated with present diamond or other forms of carbon emitters. First, many reports to date involve nonuniformly diamond or diamond-like carbon (DLC) or other forms of carbon coated silicon and metal tips [63-83], planar diamond or DLC or other forms of carbon films [84-125], or irregular ion etched conical structures [126-127]. These fabrication methods, while seemingly relatively simple, produce non-uniform emitter microstructures, which result in inconsistent emission behavior and no long-term stability. Control of the uniformity and microstructure of diamond film for field emission device applications is needed. Second, since diamond-processing technology has been recently

developed, there is no reported development of complete diamond emitter structures for device applications, such as diodes with built-in anode and triodes with built-in gate and anode. Third, enhancement of the diamond field emission characteristics is required for lower operating voltage for IC-compatible applications. Last, the stability of diamond field emission should be improved.

A useful and practical technique for fabrication of diamond field emitters is the molding process, which is a practical technique to produce well-controlled and uniform micro-emitter structures suitable for a number of applications. We have designed and developed precisely micro-patterned pyramidal polycrystalline diamond microtips on diamond film by molding technique [128-129] and demonstrated high emission current at low electric field.

Objective of the research

The purpose of this research is to develop, for the first time, the micro-patterned polycrystalline diamond field emitters, which can operate at low voltage for IC-compatible applications in vacuum microelectronics. This study focuses on:

- Diamond microtip structural design that includes the design of ultra sharpened pyramidal diamond microtip.
- Develop practical techniques for optimizing field emission performances of diamond tips that includes incorporation of $sp^2$ content in diamond film, utilizing vacuum-thermal-electric (VTE) treatment, and boron doping.
- Characterization of diamond field emission parameters that includes geometrical factor of diamond tips, the field emission enhancement factors contributed by $sp^2$ content, VTE treatment, and boron doping.
- Fabrication and characterization of monolithic micro-patterned diamond field emitter diodes and triodes.
- Analysis and modeling of diamond based field emission vacuum diodes and triodes.

Organization of the dissertation

There are eight chapters in this dissertation and they are organized in the following topics:

- *Chapter I* provides an overview of vacuum microelectronics and electron field emission devices. Motivation for the development of electron field emission devices and the advantages and suitability of diamond to be used as field emission vacuum diodes and triodes are described. Finally, the goal of the research is mentioned.
- *Chapter II* contains a theoretical background of basic electron emission in vacuum, electron field emission from metal, silicon, and diamond. This chapter also provides an extensive survey of recent theoretical and experimental work on diamond field emission.
- *Chapter III* provides a theoretical background for field emission vacuum diodes and triodes, which includes basic principle of operations, device characteristics and modeling.
- *Chapter IV* explains the proposed research and the methodological approaches to be used to achieve the objectives.
- *Chapter V* describes the details of experimental, consisting of device fabrication and characterization techniques.
- *Chapter VI* presents experimental results, discussion, analysis, and modeling of the experimental results.
- *Chapter VII* concludes the results of proposed research.
- *Chapter VIII* suggests the research topics related to this research that should be further explored in the future.

CHAPTER II

# A LITERATURE REVIEW ON ELECTRON EMISSION

## Basic of electron emission in vacuum

Electron emission is the process of emitting electrons from a solid surface into vacuum. Electrons in solid are bounded to the core atoms via electrostatic force. The potential barrier as a result of the electrostatic force is called work function (Φ). In order to remove electrons from a solid surface, energy via various means must be applied to the solid so that electrons can overcome the potential barrier and emit into vacuum. The most common processes of electron emission are thermionic emission, thermionic-field emission, and field emission. In these processes, energies in form of heat or electric field are exerted to induce electron emission. The mechanisms for these processes can be explained by considering the energy band diagram of a metal-vacuum system as shown in **Figure 2.1**.

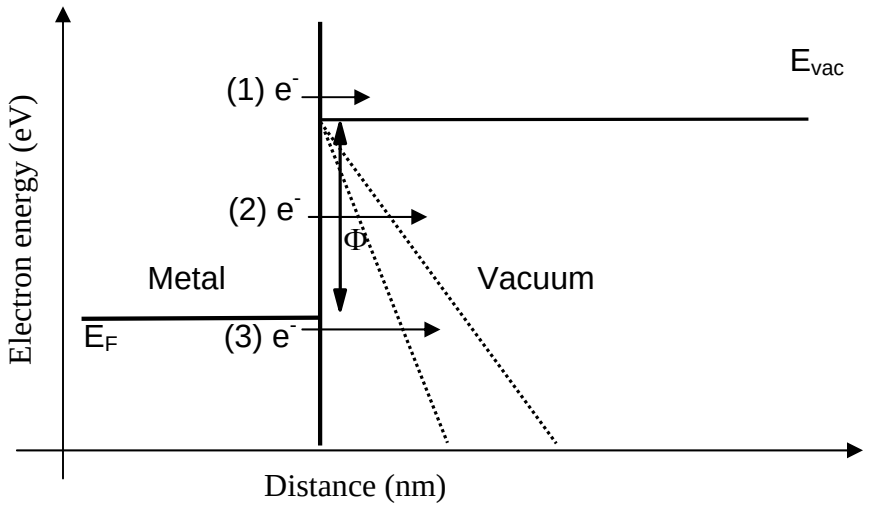


**Figure 2.1.** Mechanisms for thermionic, thermionic-field, and field emission.

For thermionic emission, electrons emit into vacuum mainly due to heat application. At temperature of 0 K, all electrons in metal have energy below the Fermi level ($E_F$). As temperature increases, some electrons gain kinetic energy and have total energy above Fermi level. If temperature is sufficiently high, some electrons can have total energy higher than

vacuum level ($E_{vac}$). These electrons [(1) $e^-$ in **Figure 2.1**] are readily to emit into vacuum with no applied potential. Thermionic emission from metal is normally obtained at very high temperature of 1500-2500 °C depending on the metal work function.

At moderate temperature, some electrons have total energy above Fermi level but below vacuum level. These electrons [(2) $e^-$ in **Figure 2.1**] are not readily to emit into vacuum. In order for these electrons to emit into vacuum, a moderate electric field must be applied to thin down the potential barrier as illustrated in **Figure 2.1**. This thermal-field activated emission process, via quantum-mechanical tunneling, is called thermionic-field emission. Depending on the metal work function, thermionic-field emission from metal can be observed at moderate temperature of 700-1500 °C.

At low temperature, most of electrons have total energy below Fermi level. A strong electric field must be applied to thin down the potential barrier thereby allowing electrons [(3) $e^-$ in **Figure 2.1**] quantum-mechanically tunnel into vacuum. This is called field emission because electric field is the main energy source that induces electron emission.

Electron emission can also occurs by other methods such as light exciation (photoelectric electron emission), external electron energy (secondary electron emission), and internal polarization switching (ferroelectric electron emission). These interesting electron emission phenomena are beyond the scope of this research. Electron field emission as the main topic of this research is further described in following sections.

Electron field emission from metal and silicon

A complete electron field emission mechanism from a metal cathode can be illustrated using energy band diagrams of the emitting systems with a planar cathode and a sharp cone cathode as shown in **Figure 2.2** and **Figure 2.3**, respectively.

First, let's consider the planar metal cathode (**Figure 2.2 (a)**). Applying a voltage (V) between anode and cathode creates a uniform electric field E=V/d across the vacuum gap (d) as shown in **Figure 2.2 (c)**. If the applied electric field is sufficiently strong, electrons (mostly with energy below the Fermi level) can quantum-mechanically tunnel through the triangle barrier into the vacuum and are accelerated by electric field until they reach the anode. At the vacuum-metal (anode) interface, electrons collide with the metal and lose their energy as heat.

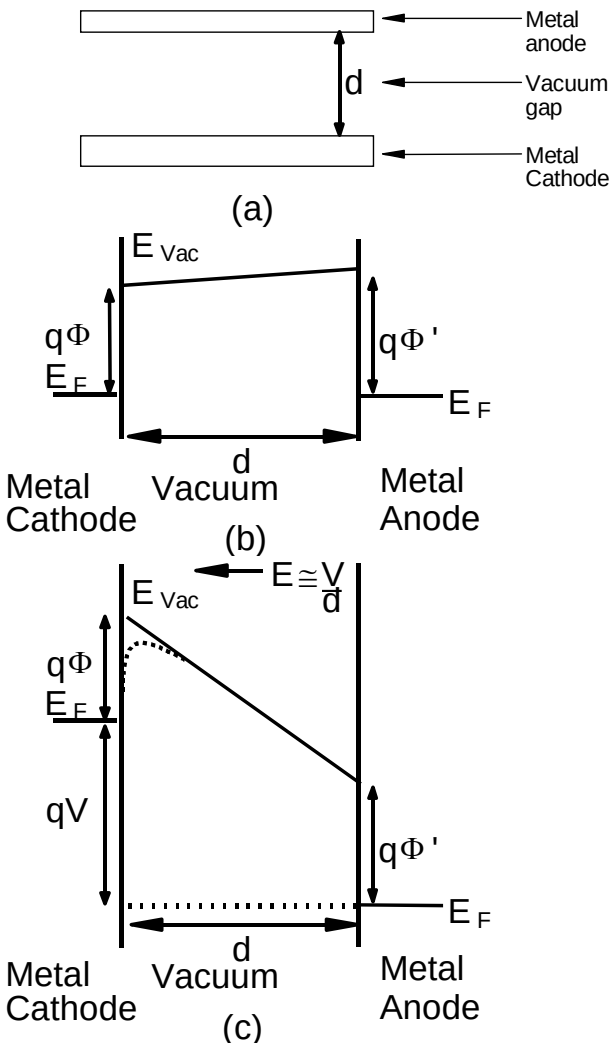


**Figure 2.2.** Metal cathode structure and energy band diagrams. (a) Planar metal cathode structure. (b) Energy band diagram at thermal equilibrium. (c) Energy band diagram under forward bias.

The electron field emission from metal has been verified theoretically and experimentally to follow the Fowler-Nordheim equation [134]:

$$J= K_1(E^2/\Phi)\exp(-K_2\,\Phi^{3/2}/E) \qquad (2.1)$$

where $K_1$ and $K_2$ are constants: $K_1 = 1.54\text{x}10^{-6}$ A·eV/V$^2$, $K_2 = 6.83\text{x}10^7$ V/(cm·(eV)$^{3/2}$), J is the emission current density (A/cm$^2$), $\Phi$ is the work function of the emitting surface (eV) and E (V/cm) is the electric field across the parallel plates, which is given by

$$E=V/d \qquad (2.2)$$

where V is the anode-cathode voltage and d is the anode-cathode spacing. In this equation, the image effect has been ignored, since it was considered to have minor effects on emission current at low electric field.

From the equation, the emission characteristic strongly depends on the work function of the cathode. Material with lower work function gives a higher emission current at a given applied electric field. Considering the absolute value in the exponent of the equation, $\Phi$ is usually around 4-6 eV for metals, thus $\Phi^{3/2}$ and the exponential factor are approximately 10 and $10^{-3\times10^8/E}$ respectively. Therefore, an applied field greater than $3\times10^6$ V/cm is needed to make any sensible emission measurement from a planar metal cathode [135].

The dash curve shown in **Figure 2.2 (c)** represents the image effect due to the interaction of electron in vacuum and the metal cathode. The interaction modifies the triangle potential barrier to be

$$V = \begin{cases} 0 & x < x_0 \\ \Phi - Ex - \dfrac{q^2}{16\pi x} & x > x_0 \end{cases}$$

where $x_0$ satisfies

$$\Phi = Ex_0 + \frac{q^2}{16\pi x_0}$$

The Fowler-Nordhiem equation that accounts for the image effect is given by [136]:

$$J = K_1 E^2/(\Phi t^2(y))\exp(-K_2 v(y)\Phi^{3/2}/E) \quad (2.3)$$

where y, v(y), and t(y) are non-dimensional functions of E and $\Phi$ which are defined as

$$y = K_3E^{1/2}/\Phi \quad (2.4)$$

$$v(y) = \{[1+(1-y^2)^{1/2}]/2\}^{1/2}\{E(k^2)-y^2K(k^2)/[1+(1-y^2)^{1/2}]\} \quad (2.5)$$

$$t(y) = v(y) - \frac{2}{3}y\frac{dv(y)}{dy} \quad (2.6)$$

$K(k^2)$ and $E(k^2)$ are the complete elliptic integrals of the first and second kind, which are given by

$$K(k^2) = \int_0^{\pi/2} (1 - k^2 \sin^2\phi)^{-1/2}\, d\phi$$
$$E(k^2) = \int_0^{\pi/2} (1 - k^2 \sin^2\phi)^{1/2}\, d\phi \qquad (2.7)$$

$k^2$ is defined by

$$k^2 = 2(1-y^2)^{1/2}/[1+(1-y^2)^{1/2}] \qquad (2.8)$$

$K_3 = 3.62 \times 10^{-4}$ eV.$(cm/V)^{1/2}$ and all other variables were defined previously. The value of v(y) is typically 0.7-0.9 in normal operating field and it goes to zero as y goes to one (E goes to $(y\Phi/K_3)^2$). It was found empirically that v(y) can be approximated with good accuracy by the simple function:

$$v(y) = \cos(\pi y/2) \qquad (2.9)$$

According to the image-corrected F-N equation, the F-N plot of $Ln(I/E^2)$ vs. 1/E will not give exactly a straight line. It can be shown that the F-N slope in this case is modified to be [137-138]:

$$d[Ln(I/E^2)]/d(1/E) = -K_2 s(y)\Phi^{3/2} \qquad (2.10)$$

where s(y) is defined as:

$$s(y) = v(y) - (1/2)y(dv/dy) \qquad (2.11)$$

The values of s(y) are typically 1-0.83, thus the deviation of F-N slope is quite small over a wide range of applied electric field and usually can not be observed in most of the experimental results.

Next, let's consider the sharp cone structure as illustrated in **Figure 2.3**. The sharp cone structure is generally referred as the "Spindt cathode", which has been developed by using various types of metal materials. The sharp cone structure results in *non-uniform* electric field as illustrated in **Figure 2.3 (c)**. The electric field is highest at the tip apex and rapidly decreases outward to the anode. Thus, the F-N equation, Eq. (2.1), which is derived for planar cathode with an assumption that there is uniform electric field in the vacuum gap, cannot be precisely applied. The precise calculation of potential distribution, electric field, and emission current for a sharp microstructure involves numerical calculation of 3-dimensional Poisson equation and Schrodinger equation for electron emission [139-141]. However, the emission current for a sharp microstructure can be obtained with a simple modification of Fowler-Nordheim equation for a

planar metal cathode by replacing the parallel electric field in Eq. (2.2) with electric field at the apex of the sharp microstructure that is

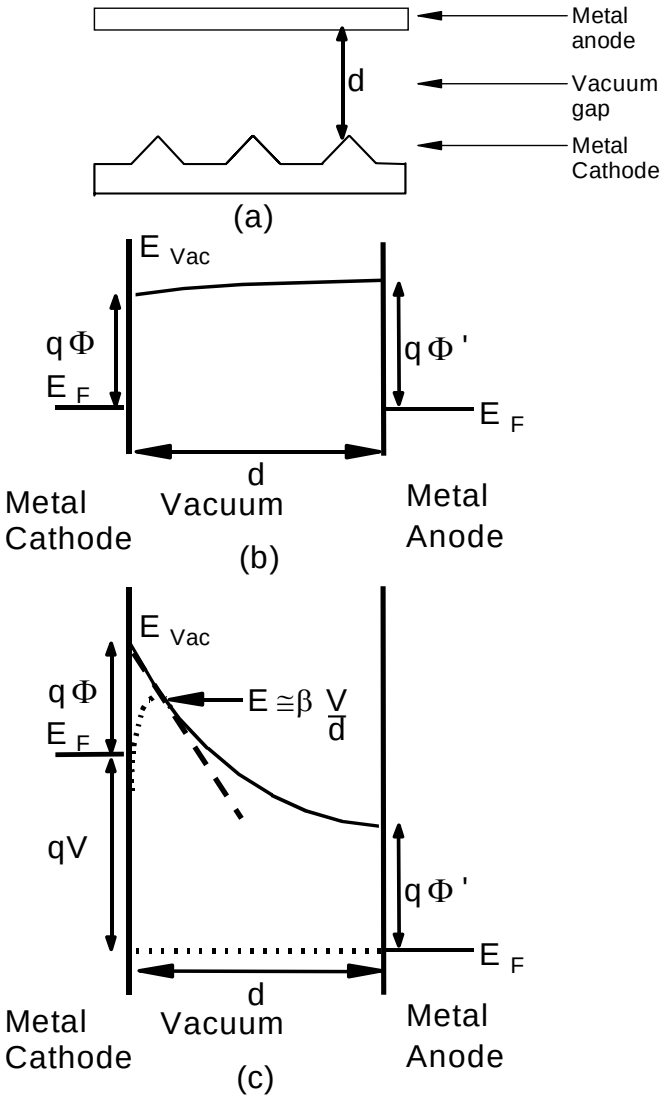


**Figure 2.3.** Metal cathode structure and energy band diagrams. (a) Sharp cone metal cathode structure. (b) Energy band diagram at thermal equilibrium. (c) Energy band diagram under forward bias.

$$E=\beta V/d \tag{2.12}$$

where β is defined as the geometrical field enhancement factor, which is the factor of which electric field is increased due the sharp microstructure relative to the planar structure. It is well known that the geometrical field enhancement factor increases with sharpness of the tip and

the field at the apex of the tip is inversely proportional to the tip radius. This simple approximation implies that the emission current for a sharp microstructure is equivalent to the emission current of a planar cathode of the same vacuum gap but the effective electric field is increased by the factor of β. This approximation agrees very well with experimental results because the electric field of a sharp tip is strongest at the apex and reduced rapidly for the region away from the apex and thus it can be assumed that most of emission current arises from electron tunneling within the vicinity of this highest electric field region. Even with the sharp cone structure, the operating voltage of the cathode is still high, since the field enhancement factor is limited to 100-500 by the technology of making the sharp metal tips.

The sharp cone concept was later extended to silicon cathode structure. **Figure 2.4** illustrates the electron emission mechanism of a silicon field emitter. The silicon cathode is usually heavily doped ($n^+$) to achieve low work function for silicon ($\Phi \approx \chi = 4.12$ eV) and good ohmic contact with metal. The potential drop across the depletion region in the $n^+$ silicon (V') is generally very small compare to the potential drop across the vacuum gap because only small voltage is required for electrons to quantum-mechanically tunnel through the thin depletion potential barrier into the conduction band of $n^+$ silicon. Thus, it is practical to assume that most of the potential drop across the vacuum gap and the enhanced electric field $E=\beta V/d$ is established at the apex of the tip. The enhanced electric field at the apex allows electrons in conduction band of silicon to quantum-mechanically tunnel through the silicon-vacuum potential barrier into the vacuum. Finally, electrons are accelerated by the electric field and collected at the anode.

Silicon emitters have shown some improvements over the metal cathodes. Since the work function of silicon is in the same order of magnitude as metal work function, the improvement obtained from silicon emitter is the increasing in the geometrical field enhancement factor due to the availability of advanced silicon technology for making sharper tips. In addition, the well-established IC technology allows the fabrication of more complex triode device structures and makes mass production of the emitters possible. However, silicon emitters have limited applications, because the operating voltage of silicon cathode is still high compared to that of solid-state device. In addition, silicon emitter has a serious surface adsorption problem, which leads to instability and reproducibility problem. The life of the emitter is short because of tip destruction under high electric field.

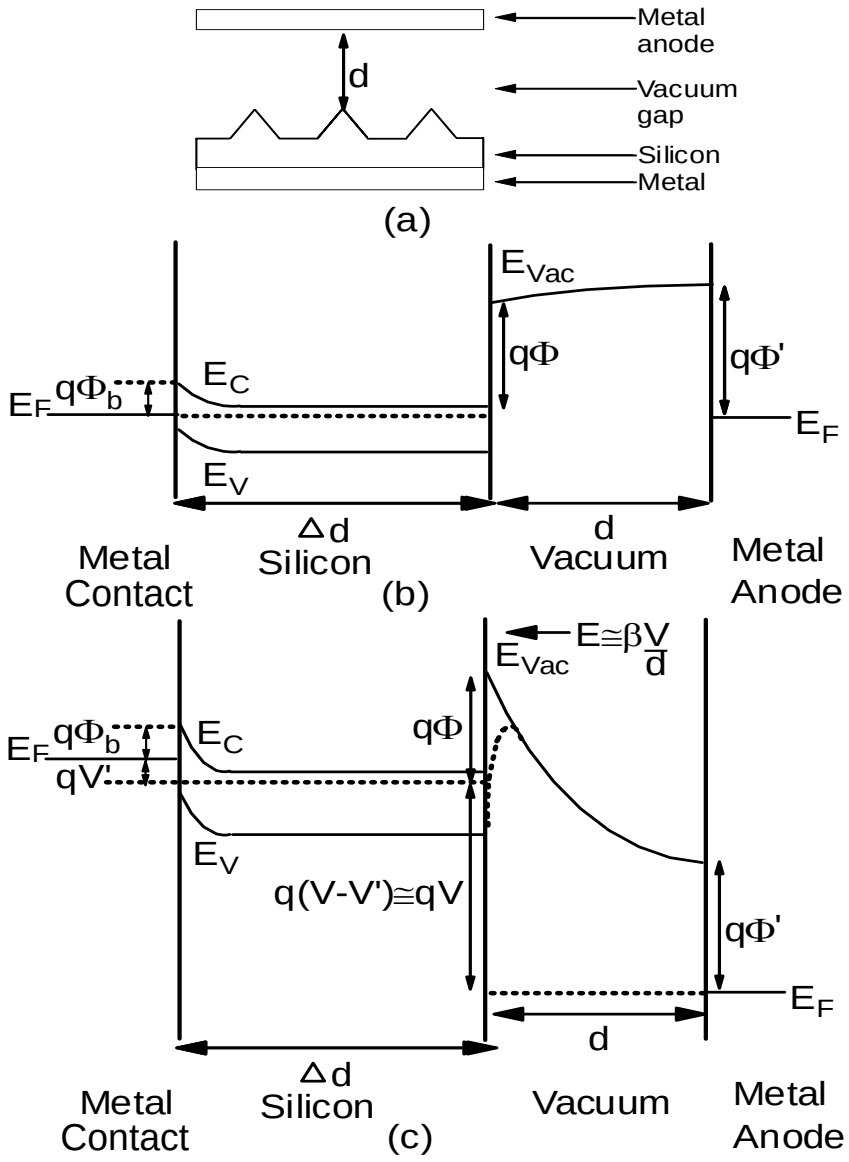


**Figure 2.4.** Silicon cathode structure and energy band diagrams. (a) Sharp cone silicon cathode structure. (b) Energy band diagram at thermal equilibrium. (c) Energy band diagram under forward bias.

Electron field emission from diamond

Structural types and fabrication techniques of diamond field emitters

Diamond field emitters can be classified into three main groups. The first is the planar diamond emitter without a well-defined tip structure. Planar diamond films can be achieved by

diamond deposition on a planar metal or silicon substrate. The second is the diamond coated silicon or metal field emitter. The last is the monolithic diamond emitter with well-patterned diamond microtip structure on diamond film.

Diamond coated field emitter can be divided into two types based on morphology of the diamond coatings. The first type is the isolated-single-particle coating. For this type, a nearly spherical single diamond particle with size ranging from 0.1 to 1 μm is grown on the silicon tip. The second type is the continuous thin film coating. For this type, a continuous film is grown over the silicon or metal tip. Several fabrication techniques have been developed for diamond, DLC or other form of carbon coating on metal or silicon tips and other planar substrates.

The common process for diamond coating on metal or silicon tips and planar substrates is via chemical vapor deposition (CVD) [64-73,84-108]. CVD diamond growth involves chemical reaction of hydrogen ($H_2$) and methane ($CH_4$) gases to form solid diamond and carbon phases. Hot filament CVD (HFCVD) or plasma enhance CVD (PECVD) technique utilizes heat or plasma energy to induce methane decomposition and enhance the growth process. The mechanism for CVD diamond growth onto the sharp silicon tip structure is different from that on planar substrate [67]. There are two possible mechanisms giving rise to preferential formation of diamond particles on the tips. The first one is the stereometric effect at the top of the tip due to enhanced feeding. The second one is the effect of hydrogen atmosphere. When hydrogen atoms reach the tip, they undergo recombination and form molecular hydrogen, which results in a large energy release. Thus, the top of the tip appears to be heated to a much higher temperature than the main part of the tip. As a result, the tip serves as the area of preferential deposition of the diamond for the endothermic reaction of methane decomposition [67].

Conventional PECVD technique can be modified for diamond or carbon deposition. Diamond-like carbon deposition has been developed by modified PECVD process using the mixture of $H_2$/He/$CH_4$ or $H_2$/$C_6H_6$ or $CH_4$/$N_2$ gases [80-82,115 -118]. Disordered tetrahedral carbon can be formed by the mixture of $N_2$/$O_2$/$CH_4$ in PECVD process [119-120].

Ion beam sputtering [121], filtered vacuum arc, and pulsed laser ablation [83,122-124] techniques are also used for diamond-like carbon deposition. In these techniques, carbon ions were evaporated from a solid graphite target and directed onto the substrate via magnetic or electric field. Amorphous diamond can also be formed by these techniques but higher energy is required for amorphous carbon deposition [79,110-114].

A dielectrophoresis coating method has recently been developed for coating of single-crystal diamond and graphite on silicon or metal tips [74-78]. This technique utilized diamond or graphite powder mixing in a non-conducting solution and an applied electric field. Metal or silicon emitters were dipped into the solution and bias positively with respect to an external electrode. The neutral particles were attracted to and deposited on metal or silicon tips due to polarization effects in non-uniform electric field of the tip surface. Another technique using squeegee and diamond paste with filler to deposit diamond onto circular planar silicon grit is an alternative fabrication method for planar diamond structure [109].

It was claimed that successful development of diamond coatings on silicon or metal field emitter would result in economic viability of device production compared with the direct use of natural diamond material. However, electron field emission enhancement obtained by this technique is not optimal because the coated tips do not remain as sharp as the uncoated tips. A tip sharpening process such as ion beam etching is required to obtain the optimum field emission enhancement [125]. In addition, it is difficult to obtain uniform coating of diamond or DLC on metal or silicon tip. The non-uniform coating could result in poor emission stability and reliability.

Diamond microtips on diamond substrate is a preferred diamond field emitter structure. Several fabrication techniques have been proposed. A crude technique is to perform ion milling on a diamond surface [126-127]. Diamond tips with cone structure were formed by this technique. The sharpness of diamond cone depends on the milling incident angle. As the incident angle increases, the sidewalls of the diamond grains are etched more rapidly than the top surface of the diamond grains, which results in sharp cone formation. Significant field emission enhancement has been observed after ion milling process. In addition to the increasing in field enhancement factor, ion milling also results in the change in diamond surface chemistry that may reduce the work function of the emitting surface. Since ion milling results in revealing various crystallographic planes of diamonds, particular sites that have low work function appear at the diamond/vacuum interface. However, this technique is not suitable for many practical purposes because the shape, size and sharpness of cones formed by this method cannot be precisely controlled.

Recently, techniques using mold transfer for the fabrication of monolithic diamond tips have been reported [128-129, 142-146]. Okano [142-145] reported diamond tips fabricated on

silicon mold utilizing HFCVD having large size (100 μm x 100 μm) and blunt tip apex with poor field emission performances. Concurrently, Vanderbilt researchers [128-129] reported diamond pyramidal microtips by mold transfer and MPECVD process, having small size (3 μm x 3 μm) and tip radius curvature of 200 Å with high emission performances. Lately, another group [146] reported uniform wedge-shape diamond emitters by a similar mold transfer technique having small size of 5 μm x 5 mm and comparable tip radius curvature of 300 Å with good emission performances.

Energy band diagram of diamond

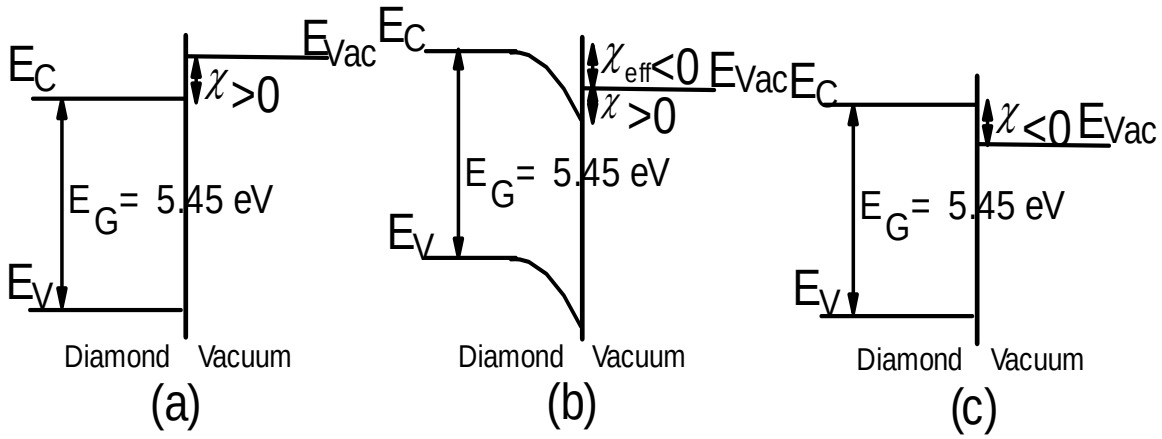


**Figure 2.5.** Energy band diagrams of diamond. (a) Positive electron affinity. (b) Effective negative electron affinity. (c) True negative electron affinity.

Electron field emission from diamond has been experimentally observed to yield high emission current at low applied electric field. However, the mechanisms responsible for low field emission from diamond are not clearly understood. Diamond surfaces have remarkable energy band diagrams, which are different from most of other semiconductors. A complete knowledge on energy band diagram of diamond surfaces is a key information to understand electron field emission from diamond.

Diamond is an indirect wide band-gap material with $E_g$ =5.45 eV. Three distinct types of diamond surfaces have been widely studied [52-63]. For hydrogen-free diamond surfaces, the electron affinity is small and positive as illustrated in **Figure 2.5(a)**. Partially hydrogenated (111) and (100) diamond surfaces have effective negative electron affinity (NEA), as illustrated

in **Figure 2.5(b)**. The hydrogen is deposited as ionic species to form an affinity lowering surface dipole. This reduction in electron affinity, together with a short characteristic band bending at the surface results in the effective negative electron affinity surface. Furthermore, diamond surface coated with a thin layer of metal such as Zirconium (Zr) [147], Cobalt (Co) [147-148], Ni [149], and (111)-(2x1) diamond-TiO surface [150] also exhibit effective negative electron affinity property. Last, the diamond (100)-(2x1):H and completely hydrogenated surface is believed to be a true NEA surface as illustrated in **Figure 2.5(c).** In addition, it is believed that a true NEA surface also exists on the Cesium or Cesium oxide coated diamond (100) surface [151]. The occurrence of the true NEA has not been found for conventional semiconductor materials and is thought by many to never occur.

Assuming a small positive electron affinity for diamond surface, a complete energy band diagram for electron emission from the surface may be drawn analogous to those for silicon as shown in **Figure 2.6**. For electron emission to occur, electrons must quantum-mechanically tunnel through the potential barrier at metal-diamond interface into diamond. Electrons will then drift through diamond bulk and go over a small potential barrier at diamond-vacuum interface into vacuum.

Small or even negative electron affinity of diamond is believed by many to be responsible for observed low field emission from diamond because small electron affinity would allow electrons from the conduction band to emit into vacuum easily with low applied electric field. However, electron in conduction band of diamond is limited because diamond is a wide band gap material and n-type diamond is still not available. Thus, electron must be injected from metal into conduction band of diamond in order for emission to occur. High electric field should be required for electrons to tunnel through metal-diamond interface because the potential barrier at metal-diamond interface would be as high as work function of silicon or metals. Thus, the basic energy band diagram as described is inadequate for the explanation of the observed low field emission from diamond.

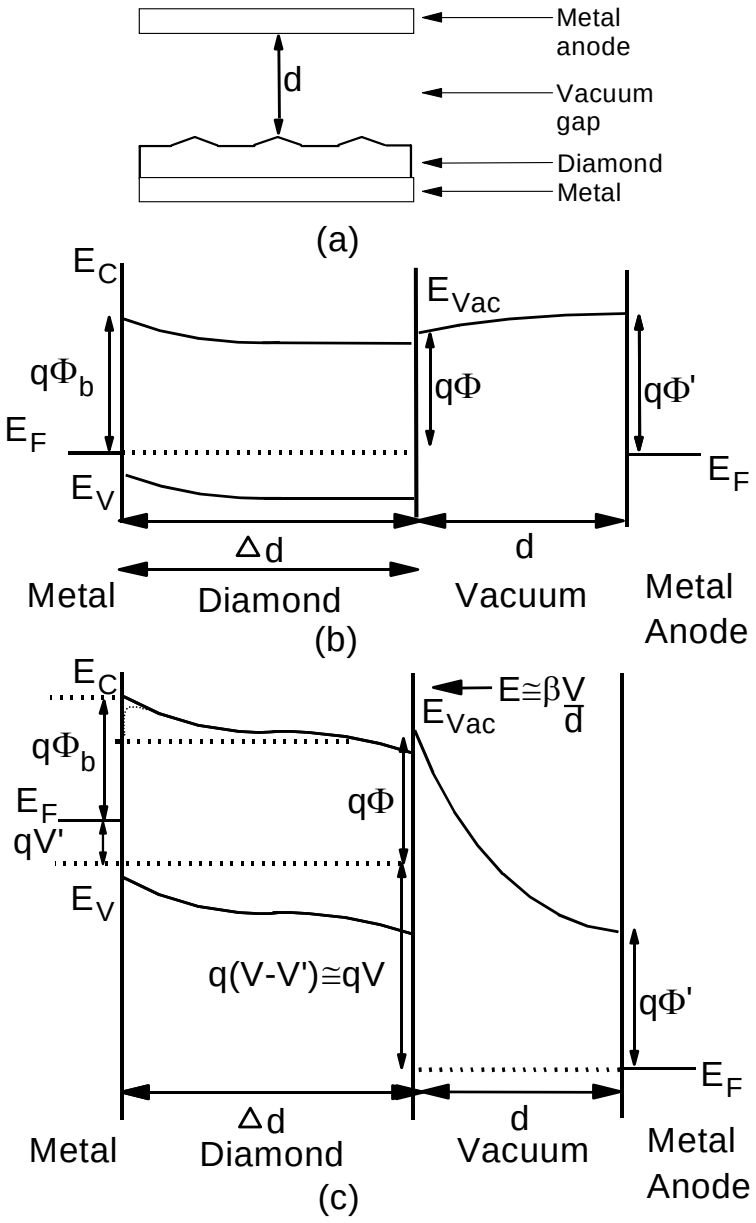


**Figure 2.6.** Diamond cathode structure and energy band diagrams. (a) Diamond cathode structure. (b) Energy band diagram at thermal equilibrium. (c) Energy band diagram under forward bias.

In order to understand the field emission mechanism from diamond, a better knowledge of carrier transport through diamond-metal interface and the diamond film is needed. In addition, a more complete energy band structure, which includes the effect of grain boundary and defects of polycrystalline diamond, also need to be studied. Furthermore, unknown characteristics of diamond surfaces such as sharp facets of as-grown diamond with unknown field enhancement

factor further complicated the emission mechanisms from diamond surfaces. Several field emission mechanisms and field emission enhancement models for various types of diamond emitters have been proposed. The following section summarized some of the proposed theories and models.

Field emission enhancement model

Simple field enhancement model

Sharp microstructures have been used to effectively enhance electron field emission from diamond [128]. The electric field at a given applied potential is enhanced by sharp microstructures and thereby electron tunneling is enhanced. Field emission from the diamond sharp microtips exhibits significant enhancement both in total emission current and stability compared to planar diamond emitter. To apply the simple field enhancement model, the microstructure must have certain geometry with a smooth surface. The geometrical field enhancement factor β depends only on the geometry of the microstructure. The field enhancement factor β for various shapes of microstructure [16] has been estimated based on electrostatic theory and shown in **Figure 2.7**.

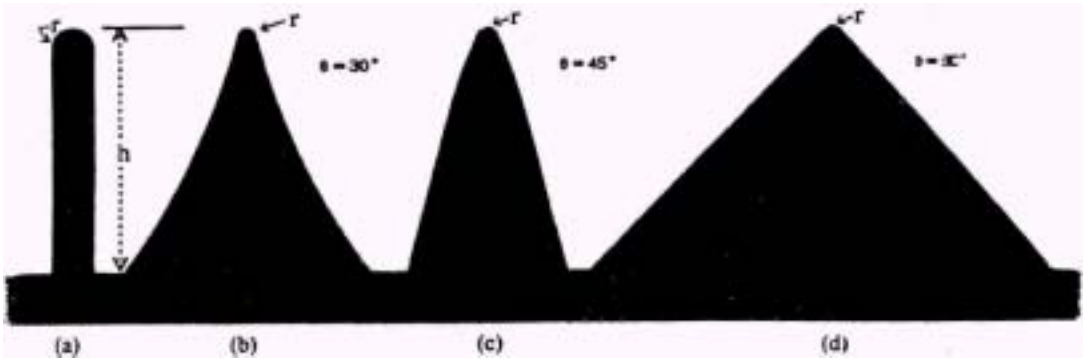


**Figure 2.7.** Various shapes of field emitters. (a) Rounded whisker. (b) Sharpened pyramid. (c) Hemi-spheroidal. (d) Pyramid.

The electric field at the surface of a sphere, **Figure 2.7(a)**, of a rounded whisker can be evaluated using elementary electrostatic theory and expressed in closed form as a function of polar angle θ as [16]

$$E=(V/d)(h/r+3\cos\theta) \quad (2.13)$$

$$\beta= h/r+3\cos\theta \quad (2.14)$$

where h is the height of the sphere from the base, r is the radius of the tip, V and d are defined previously. For h>>r, E ≅ (h/r)(V/d) and β≅ h/r. It has been shown that the field at the apex of a rounded whisker shape is approximately equal to that of a floating sphere and is given by E = (h/r)(V/d). Thus, it has primarily concluded that the round whisker shape is the closest to the "ideal" field emitter. On the contrary, a wide-angle pyramidal shape is not an optimum field emitter even though its thermal and mechanical stability is excellent. In addition, it was primarily found that a wedge molybdenum shape emitter [2] has an effective emitting area about 100 times greater than a conical shape emitter and a correspondingly larger current density. This geometric effect should be applied to diamond emitter. However, recently reported wedge-shape diamond tip arrays fabricated by mold transfer technique did not exhibit significant field emission enhancement compared to the pyramidal shape one [146].

Two step field enhancement (TSFE) model

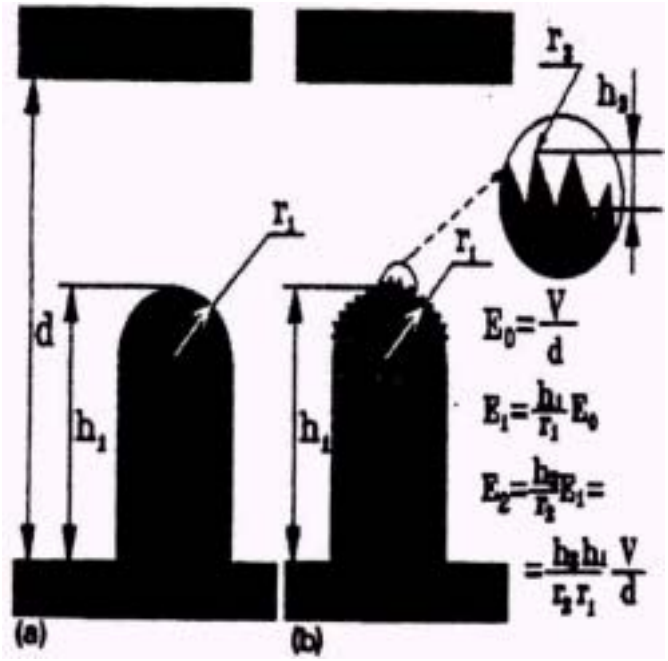


**Figure 2.8.** Geometry of emitters. (a) The simple field enhancement approach. (b) The TSFE approach.

This model is a modified version of the simple field enhancement model developed to account for the complicated morphology of diamond surface. The emitting surface may be thought of as a number of small protrusions act as tiny tips. The emitting tip with height $h_1$ and sharpness of radius $r_1$ is assumed to consist of a number of tiny tips with height $h_2$ and sharpness of radius $r_2$ as shown in **Figure 2.8**. The electric field on the blunt tip is equal to

$$E_1 = (h_1 / r_1)(V/d) \quad (2.15)$$

and the field enhancement at the end of protrusions is equal to

$$E_2 = (h_2 / r_2)\, E_1 = (h_1\, h_2 / r_1\, r_2)(V/d) \quad (2.16)$$

where V and d are defined previously.

The TSFE model was applied to analyze electron emission from diamond coated silicon field emitters [68]. The emission current were calculated using the F-N analysis on diamond coated silicon field emitters based on the TSFE model and found to be in good agreement with experimental data. The calculations of the emission current using this model were made on the assumption that electrons that tunnel from the valence band mainly contribute to the emission current. Therefore, the work function used in FN analysis was the energy gap of diamond (5.45 eV). High field enhancement factor from the structure was assumed in the calculation. However, ultra sharp protrusions have not been physically observed and a clearer explanation for the formation of stable ultra sharp protrusions on diamond coated silicon field emitter is needed. Thus, the results from this model still cannot be justified. Nevertheless, it has been proposed that the ultrasharp protrusions may be formed under the assumption that the diamond particles are relatively large (of micrometer range) and thus they are not truly smooth or spherical but have microstructures with some spikes of deep-submicrometer sizes. The (111) surface on the spike microstructure may be thought of as spikes of deep-submicrometer sizes or ultra sharp protrusions because (111) part of the surface with NEA could be the only actively emitting spot.

Lowering of the surface work function model

In the lowering of the surface work function model, it is assumed that the sharp microtip and the complicated morphology surface result in significant reduction of the surface work function. A significant enhancement in field emission after diamond coating on silicon tip was observed which could also be attributed to the lowering of the surface work function by diamond. The field emission current in μA range was claimed to obtain from diamond coated

silicon field emitters with excellent long-term of current stability. The calculated results from this model agreed well with experimental data [68] but it is unclear how diamond could have sufficient amount of electrons in the conduction band or near the conduction band to produce large emission currents.

In addition, it has been found that the diamond surface work function can be lower by coating with a low work function material such as Cs [152]. It has been found that the diamond surface treated with $O_2$ plasma and Cs deposition substantially enhances the electron emission for Li-doped and N-doped diamond [92]. It has been suggested that oxygen-terminated diamond surface reacts with Cs to form an oxygen-stable diamond-O-Cs surface that lowers the surface work function of diamond. It has been proposed that the lowering of work function on diamond surface by Cs be attributed to dipole formation due to electron rearrangement within the surface region. The dipole formation at diamond surface is significant because the large Cs ion and the small lattice constant of diamond contribute to low electronegativity (encouraging charge transfer and dipole formation), which cause the Cs-O separation larger than it would be for small alkalis and hence leads to the formation of a large dipole. The addition of one-half monolayer of Cs was found by theoretical calculation to produce a shift of the surface dipole by 3.3 eV, resulting in an effective NEA of -0.85 eV on this surface [152]. Assuming that the O-Cs bond has a dipole moment of ~10D, then only 0.1% of the surface carbon atoms need to be bound to an O-Cs group to lower the work function by ~1 eV. Therefore, it was primarily concluded that the reduction of work function by this treatment is responsible for the field emission enhancement. Recently, another Cs treatment experiment by co-deposition of Cs and carbon independently confirmed that the Cs-treated carbon film has a low work function of 1.1-1.6 eV [111]. However, the lowering of work function by Cs treatment for field emission enhancement is not a practical technique because Cs is an expensive and reactive element.

Recently, hydrogen treatment on diamond surfaces was found to improve field emission characteristic significantly [59-60,145,149]. The lowering of work function of diamond surfaces by hydrogen termination was believed to be the most probable explanation for the observed field emission enhancement. The termination of hydrogen on diamond surface is known to form a positive surface dipole that could produce band bending and result in lowering of electron affinity and work function of diamond surfaces. Similar field enhancement effects have been found on diamond coated with Titanium dioxide ($TiO_2$) [151]. On the other hand, oxygen

treatment was found to degrade field emission characteristic of diamond surface [145,149]. The degraded emission property was believed to cause by the increasing of work function of diamond. The termination of oxygen on diamond surface is known to form a negative surface dipole to produce band bending which results in increasing of electron affinity and work function of diamond surfaces.

Hot electron emission and metal-insulator-metal (MIM) model

It has been proposed that the emission mechanisms of diamond with graphitic particles involve the creation of electroformed conducting channel via hot electron emission process in metal-insulator-metal (metal-diamond-graphite) microstructure. This model arises from experimental observation on the field emission characteristics of diamond-coated Mo emitters [85-87]. The emission characteristic of the diamond-coated Mo emitters has a broad electron energy spectral (FWHM~1 eV), which is larger than FWHM of a clean Mo tip of ~0.23 eV with a large spectral shift of ~2-3 eV (the different between center of energy spectral and the Fermi level of the Mo substrate). These emission characteristics are similar to the emission spectra of the metal-insulator-metal (MIM) graphite microstructure, which has been explained by the hot electron emission model [153].

The hot electron emission model for MIM graphite microstructure is illustrated in **Figure 2.9**. In this structure, it is assumed that carbon particles in the form of graphite flakes placed on an oxidized electrode surface play the role of an isolated conducting sheet as illustrated in **Figure 2.9(a)**. Such a flake could therefore enhance the electric field distribution locally across the junction where it forms a contact with the electrode surface. Since the oxide will block the transportation of carriers from the substrate metal, this field enhancement will eventually lead to a significant voltage drop across the oxide layer sandwiched between the flake and the metal substrate. The energy band diagram of the MIM structure is illustrated in **Figure 2.9(b)**. Under an applied field condition, electrons will tunnel from the metal substrate into the conduction band of the insulator by a tunnel-hopping process and then be accelerated toward the top metallic layer. At the top metallic layer, the electrons that are heated internally will undergo a coherent scattering process, which has been explained by electron diffraction model [154-155].

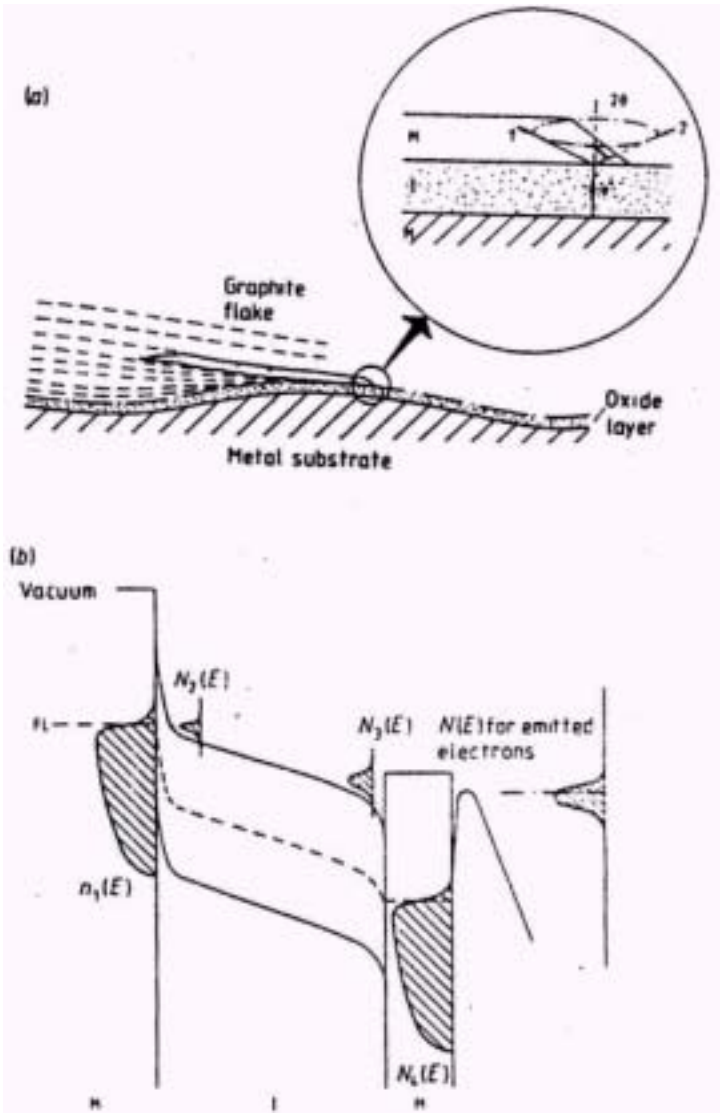


**Figure 2.9.** MIM structure and hot electron emission model. (a) A schematic representation of how a graphite flake could give rise to a bunching of the equipotentials and hence a local field enhancement sufficient to promote the MIM emission process detailed in the inset. (b) A band diagram representation of the emission regime.

The coherent scattering process from a MIM (Al-$SiO_2$-Au) structure based on electron diffraction model is illustrated in **Figure 2.10**. In this model, it is assumed that when a beam of monoenergetic electrons of a few electron volts incident normally on the gold (Au) film, they are diffracted through the various gold plane (hkl) (with spacing $d_{(hkl)}$ between planes) of the film by an amount $2\theta$ where $\theta$ is given by the Brag's relation $\sin\theta=\lambda/2d_{(hkl)}$ where $\lambda=12.27/(V_b+\eta)^{1/2}$ is the electron wavelength, where $V_b$ is the voltage applied between the electrodes, and $\eta$ is the Fermi energy of Au. For Au, the separation of the (111) plane, which is the most intensely

diffracting plane, $d_{(111)}$ is 2.35 °A. Thus $2\theta=81°$ for $V_b$ =10V, which means that the electrons diffracted almost into the plane of electrode, and thus will not normally be able to escape from the electrode. However, if the diffraction occurs near the edge of a pinhole of the gold cathode as shown in **Figure 2.10(b)**, electrons in the portion of the cone of diffraction close to the edge of the pinhole would have sufficient energy to surmount the surface potential (work function) of the Au electrode. The condition that electrons arrive at the edge of the pinhole can emerge from the surface can be derived from the velocity diagram as shown in **Figure 2.11**. In the diagram, the vectors from O to semicircle represent all possible velocity vectors $v_{||}$ of the diffracted electrons, arriving at pinhole edges in the plane of the film, can have and the vectors drawn for O' represent all possible velocity vectors normal to the pin hole edges outside the metal. The electron kinetic energy ($mv_{\perp}^2/2$) required for tunneling normal through surface barrier is $\eta+\Phi$, where $\Phi$ is the surface work function. Thus the electrons that can tunnel through the surface barrier must satisfy the condition of their kinetic energy ($mv_{\perp}^2/2$) > the surface barrier ($\eta+\Phi$) or $v_{\perp}= v_{||} \cos\beta > [2(\eta+\Phi)/m]^{1/2}$, where $v_{\perp}= v_{||} \cos\beta$ is the velocity normal to the plane of the film and $\beta$ is the angle between the vector velocity and the normal vector to the plane of the film. In other word, electrons whose velocity vectors $v_{||}$ lie within an angle $\beta_0$ of the normal to the surface can emerge from the surface. Therefore, this implies that the hot electron with the energy of few electron volts accelerated from the conduction band of the insulator can tunnel through vacuum via a pinhole or an edge of the metal electrode.

According to the electron diffraction model, the metal-insulator-vacuum triple junction, enlarged in the inset of **Figure 2.9(a)** represents a favorable configuration similar to a pinhole of the gold film for allowing electrons to be emitted into the vacuum under relatively low field condition. Therefore, it is likely that a conduction channel will be formed preferentially in this region via diffraction of hot electrons through insulator-graphite structure when electric field is applied to the gap.

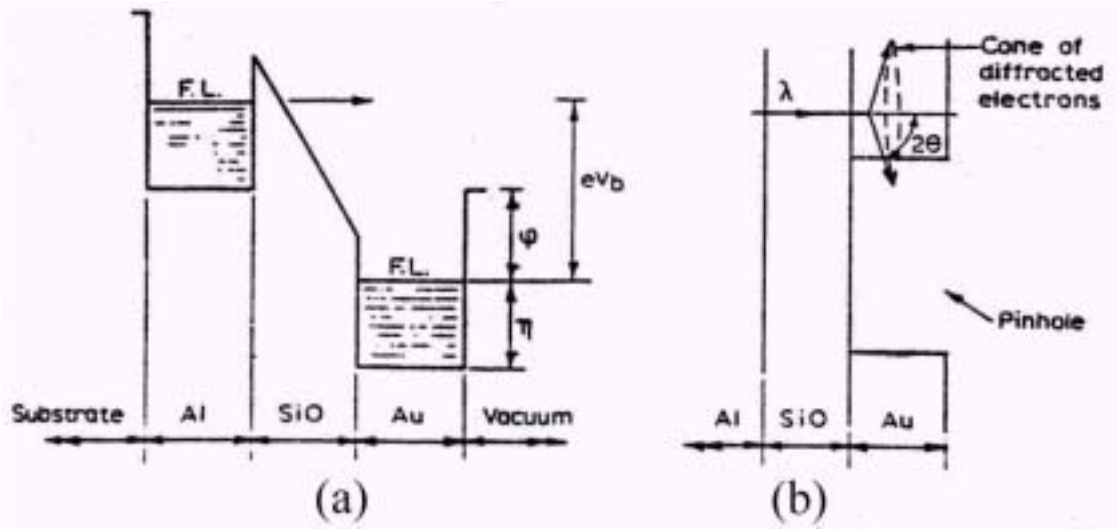


**Figure 2.10.** Electron diffraction model. (a) Energy band diagram of the cathode showing the electron transport. (b) Physical diagram of part of cathode, in the vicinity of a pinhole with the cone of diffraction of the electrons superimposed.

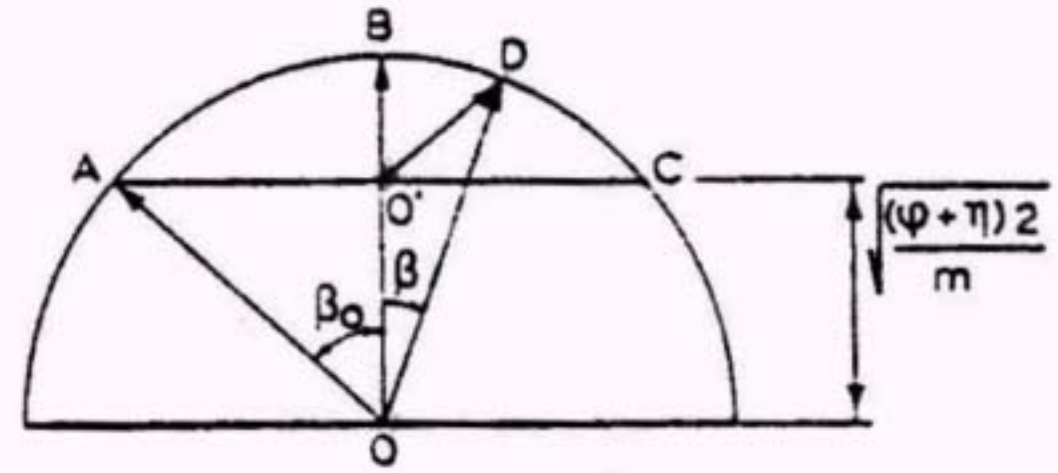


**Figure 2.11.** Velocity diagram of $v_{||}$.

According to the hot electron model, the observed electron spectra of a diamond-coated Mo cathode (FWHM~1 eV) is larger than FWHM of a clean Mo tip of ~0.23 eV. This suggests that the emitted electrons are 'hot' which means that they are likely to have been accelerated in the conduction band of the diamond film by penetrating field prior to their emission into vacuum. This implication can be referred to **Figure 2.9(b)**, where the electron energy spectra

$N_2(E)$ of the clean Mo tip is smaller compare to the energy spectra of the emitted electron N(E). In addition, the large shift in the energy spectra indicates that these electrons have suffered significant energy loss as they have been accelerated in the diamond film. This high-energy loss implies the existence of strong scattering mechanisms associated with the conduction electrons in the diamond film. The latter implication can also be referred to **Figure 2.9(b)**, where the electron spectral shift is corresponding to the difference between the center of electron energy spectra $N_2(E)$ at metal substrate-insulator junction (which is $E_F$ of the Mo substrate) and the center of emitted electron energy spectra N(E) for emitted electron. This energy difference corresponds to the potential energy loss as electrons are accelerated toward the vacuum. Since these observations seem to agree with the emission according to hot electron emission model, it therefore suggested that the emission mechanism of diamond with graphitic particles involves the creation of electroformed conducting channels via hot electron emission process similar to that of MIM graphite microstructure.

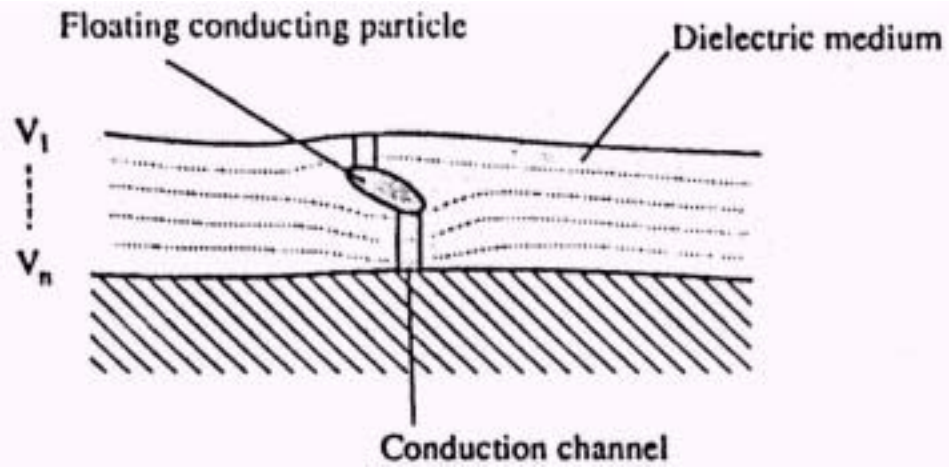


**Figure 2.12.** Electric field distribution illustrates how a floating conducting particle embedded in a dielectric medium can promote formation of an electron conduction channel.

Consequently, it was primarily concluded that the hot electron emission model of MIM graphite structure could be applied to diamond coated Mo cathodes. It is assumed that embedded carbon particles or isolated graphite crystallites in the diamond film play the role of an isolated conducting particle as illustrated in **Figure 2.12**. According to elementary electrostatic theory, a conducting particle could therefore change the field distribution as illustrated and in particular

enhances the field locally across the diamond insulator of the graphite-diamond-metal MIM microstructure. This effect increases the field enhancement factor $\beta_e$ across the diamond crystallite sitting between the graphite particle and the substrate where $\beta_e = h/d$, h is the maximum height of the graphite particle above the substrate, and d is the thickness of a single diamond crystallite. Since the insulating diamond will block the transportation of carriers from the substrate metal, this field enhancement will eventually lead to a significant voltage drop across the insulating layer sandwiched between the graphite particle and the metal substrate. According to the hot electron model, this suggests that the conduction channel will be formed preferentially in this region when electric field is applied to the gap. Therefore, electrons can get into the conduction band. The conduction electrons will be accelerated toward the interface, and subsequently escape into vacuum by going over the potential barrier. Because of the negative electron affinity property of diamond, which provides a low potential barrier, only low electric field is required to induce emission.

The further quantitative analysis of the hot electron emission model has been reported [156]. This analysis provides an alternative physical basis of the Fowler-Nordhiem equation. The energy band diagram for this analysis is shown in **Figure 2.13**. The population of hot electron shown in **Figure 2.13(c)** is assumed to obey Maxwell-Boltzmann statistics. Therefore, it could be anticipated that the emission mechanism would be analogous to the thermionic process, hence by analogy with the Richardson-Dushman relation, the emission current density would be given by

$$J = A^{*}T_e^{2}\exp(-q\chi/kT_e) \qquad (2.17)$$

where $A^{*}$ is the Richardson constant, $T_e$ is the enhanced electron temperature and $\chi$ is the height of the potential barrier at the insulator vacuum interface (i.e. the electron affinity). The potential drop $\Delta V$ across the high field surface region is given by $q\Delta V=(3/2)kT_e$ or

$$T_e = 2q\Delta V/(3k) \qquad (2.18)$$

Under the conditions depicted in **Figure 2.13(b)**, $\Delta V$ can be approximated by assuming the potential drop across the insulating inclusion:

$$\Delta V \cong (1/K_s)(\Delta d/d)V \qquad (2.19)$$

where V is the anode-cathode voltage, d is the cathode-anode separation, $\Delta d$ is the thickness of the micro-inclusion (where $\Delta d << d$) and $K_s$ is the relative dielectric constant of the insulator. Combine Eq. (2.17)-(2.19), gives

$$J = A^{*}(2q\Delta d/3kd\ K_s)^2V^2\ \exp(-\chi/V(2\Delta d/3d\ K_s)) \quad (2.20)$$

$$I = JA = A^{*}A(2q\Delta d/3kd\ K_s)^2V^2\ \exp(-\chi/V(2\Delta d/3d\ K_s)) \quad (2.21)$$

where A is the emitting area and I is the emission current. Eq. (2.21) indicates that a plot of log I/V versus 1/V gives a straight line, which is identical to a F-N plot with a slope of

$$m = -3d\ K_s\chi/2\Delta d \quad (2.22)$$

Comparing this slope to that of the F-N plot $m_{FN} = -K_2 d\Phi^{3/2}/\beta$, gives the field enhancement factor

$$\beta = 2\ K_2\ d\Phi^{3/2}\Delta d/\ K_s\chi \quad (2.23)$$

Therefore, the quantitative analysis of the hot electron emission model is similar to the analysis of the F-N plot.

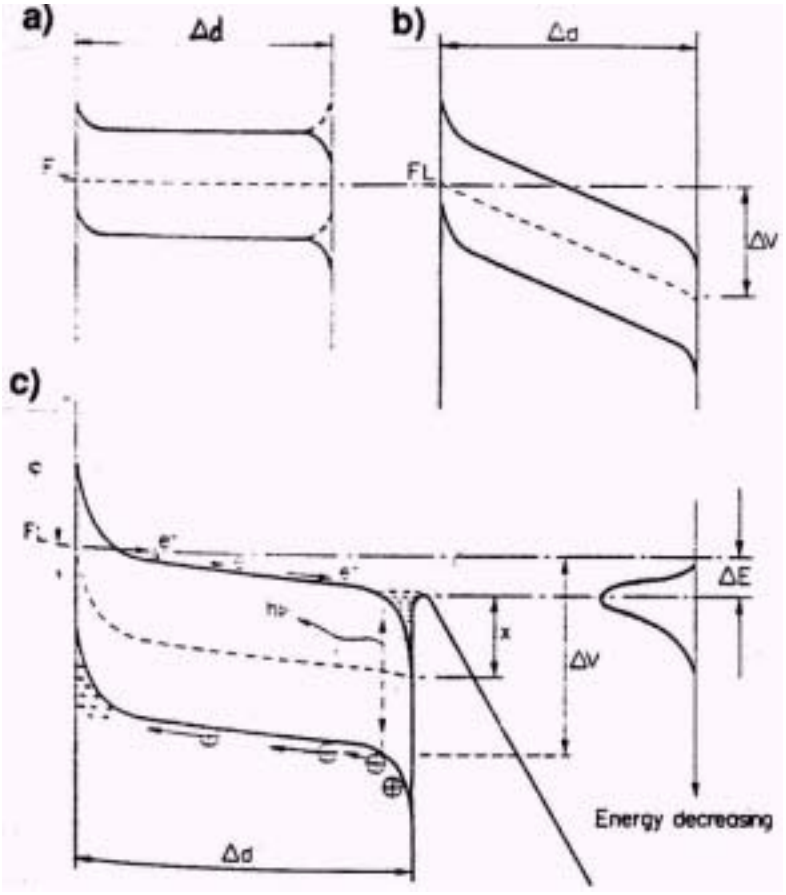


**Figure 2.13.** The energy band diagram represents of the emission regime for the hot electron emission model. (a) At thermal equilibrium. (b) Under a high applied before emission begin. (c) In the electron emission regime.

Field emission enhancement via donor and acceptor doping

In theory, the addition of n-type donor impurities into diamond is the best approach to enhance electron emission from diamond. Since diamond has small or negative electron affinity surface, if the conduction band can be directly populated with electrons via donors, very small electric field will be required to induce electron emission. On the other hand, the addition of p-type acceptor impurities into diamond should degrade emission from diamond since the addition of holes in the valence band would reduce the number of electrons in the conduction band.

The theoretical calculation of the emission current from n-type and p-type diamond has been reported to quantitatively confirm the theory [157-158]. The emission current density j calculated from an energy band is given by:

$$j=\frac{2q}{h^3}\int f(E)D(E-E_t)\frac{\partial E}{\partial p_z}dp_z dp_x dp_y$$

$$\equiv \frac{2q}{(2\pi)^3\hbar}\int f(E)P(E)dE \qquad (2.24)$$

where $P(E)=\int D(E-E_t)dk_x dk_y$ and q is the electron charge, E is the total energy of electron, $E_t$ is the transverse energy parallel to the emission surface, F(E) is the Fermi distribution function, $D(E_\perp)$ is the transmission probability with normal energy $E_\perp=E-E_t$ and $\mathbf{p}=(p_x,p_y,p_z)$ is the momentum. The zero energy is defined at the top of the valence band and at the bottom of the conduction band for hole and electron, respectively. For simplicity, the dispersion relation is taken as parabolic for both bands with the bottom of the conduction band shifted $k_c=0.7k_{\Gamma X}$ in the [100] direction because diamond is indirect band gap material:

$$E(k)=E_v+\hbar^2k_t^2/2m_p^* \qquad \text{in valence band} \qquad (2.25)$$

$$E(k)=E_c+(\hbar^2/2)(k_t^2/m_t^*+k_l^2/m_l^*) \qquad \text{in conduction band} \qquad (2.26)$$

The transmission probability D(E) is calculated from a known potential by solving the Schrodinger wave equation. The potential is obtained by solving the Poisson equation with appropriate boundary conditions. For semiconductor including diamond, it is important to consider band bending which in the absence of surface states is due to the applied field. For more accurate calculation, the total potential should also include the image interaction. If the surface states exist, it is assumed that the surface density of states is high so that the Fermi level is pinned at the highest filled surface states. In this case, the potential distribution is obtained by solving the Poisson equation with imposing the Fermi-pinning on the boundary condition. The

calculation for D(E) was done by a numerical method. From the calculated D(E) and the parabolic band Eqs. (2.25)-(2.26), the emission current density j can be calculated from Eq. (2.24).

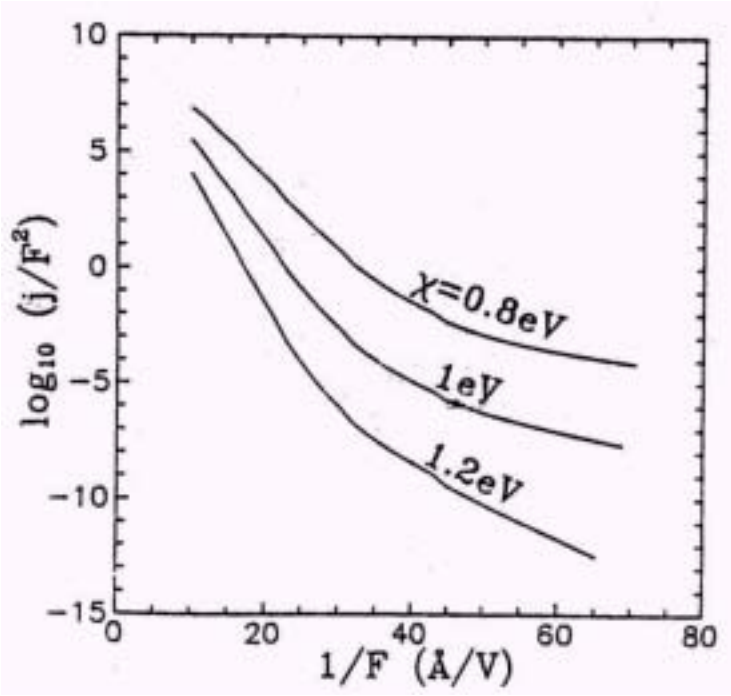


**Figure 2.14.** Calculated Fowler-Nordheim plot of emission from the conduction band for an n-type diamond (100) surface without surface state. Three curves correspond to $\chi$ =0.8, 1, and 1.2 eV, $E_g$ =5.47 eV, T=300K, and doping concentration n=$10^{19}$ $cm^{-3}$.

The F-N plot of the emission current from the theoretical calculation for n-type diamond (100) with no surface state is shown in **Figure 2.14**. The calculated results show that high emission current density j of $10^4$ A/$cm^2$ was obtained at electric field of 0.1 V/Å for n-type diamond even though positive electron affinity on diamond surface was assumed. The calculation was made on (100) surface because $\chi$ was assumed to be positive. The electron emission from (100) surface should be the largest component because the conduction band minima is located in [100] directions. On the (110) and (111) surfaces, there is negligible emission current because in one dimension tunneling calculations, the tangential component of the momentum ($k_t$) needs to be conserved.

If there are surface states, the band bending is determined by Fermi pinning. The Fermi level pinning at the midgap with band bending upward is assumed. Thus, electrons have to

tunnel through a barrier inside the bulk to reach the semiconductor-vacuum interface. In this case, the calculated results from Eq. (2.24) yields a negligibly small emission current at F=0.1 V/Å.

In practice, it is not easy to introduce impurities especially donors into diamond since diamond is a wide band gap material with very tight lattice structure. The diamond film doped with various n-type dopants such as phosphorous (P) and nitrogen (N) has currently been shown to be possible [91-92,100,103,109,144]. Ion implantation is the first successful method to introduce n-type dopants into diamond [100]. N and P have been successfully incorporated into CVD diamond films by the addition of various dopant gases such as nitrogen ($N_2$), ammonia ($NH_3$), urea ($(NH_3)_2CO$), and phosphine ($P_2H_5$) into $H_2$ plasma [91,144]. Recently, a very high concentration of $2\times10^{20}$ $cm^{-3}$ N-doped nanocrystalline diamond film has been achieved by a new CVD technique using $N_2/CH_4$ plasma [103].

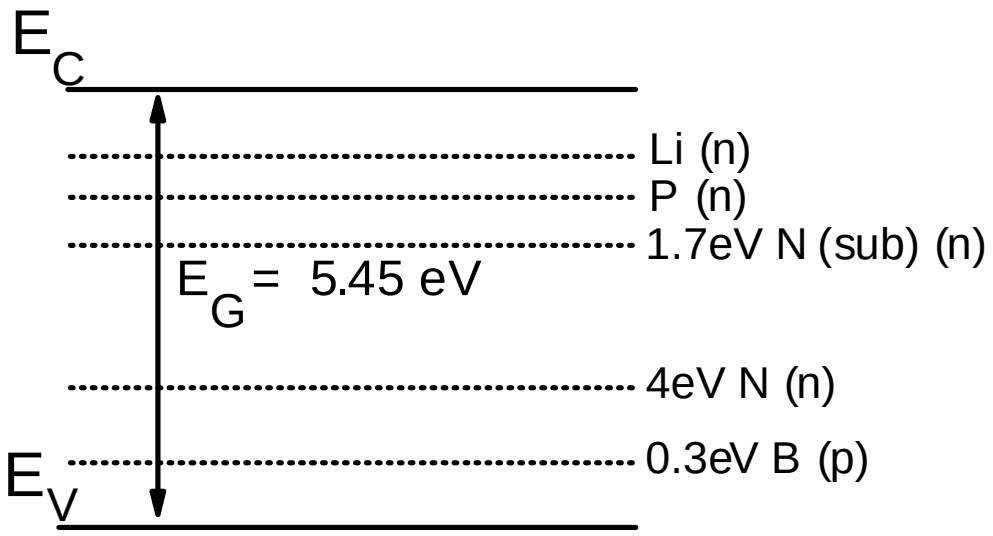


**Figure 2.15.** Energy band of diamond with dopants' energy levels.

The n-type dopants such as N, Li and P provide donor levels within the energy gap as illustrated in **Figure 2.15**. The energy levels associated with Li and P dopants are still unknown, but it has been found that the substitutional nitrogen forms a donor level ~1.7eV below the conduction band. Assuming NEA property on diamond surface, the vacuum energy level is ~0.7 eV below the conduction band. Thus, the nitrogen donor level is 1 eV below the vacuum level,

which means that the work function is approximately 1 eV. Therefore, a low electric field is required for electron emission. The effect of nitrogen doping for electron emission enhancement has been confirmed by experiment with O-Cs treatment to lower electron affinity [92,109]. The nitrogen-doped diamond field emitter with Cs treatment exhibits electron emission at the lowest reported electric field <0.2 V/μm. Furthermore, other theoretical calculations for nitrogen-doped diamond field emitter have quantitatively verified experimental results [159-160]. Other experiments [91,100,103,144] using phosphorous and nitrogen as n-type dopants with no Cs treatment have independently confirmed that an diamond emitter with n-type dopants shows a better emission characteristic than a p-type (boron-doped) diamond emitter.

Even though n-type dopants have successfully incorporated into diamond film, these donors are not electrically activated because the ionization energies for these dopants are not sufficiently small (>0.3 eV). Thus, the incorporation of these donors is not directly beneficial for electron field emission because these donors cannot effectively provide electrons for the conduction band at room temperature. The electron emission enhancement observed from diamond film doped with these n-type dopants may not arise from the intended n-type doping effect. Other mechanisms such as defects associated with these dopants to be discussed in a subsequent section are speculated to be responsible for the field emission enhancement. Thus, techniques to achieve electrically activated n-type diamond film at room temperature remain to be developed for diamond field emission enhancement.

On the other hand, the theoretical calculations show that the emission current for p-type diamond is negligible, even though negative electron affinity surface is assumed. The F-N plot of the emission current from the theoretical calculation for p-type (111) diamond surface with no surface state is shown in **Figure 2.16**. The calculation yielded maximum current density j of approximately $10^{-30}$ A/cm$^2$ at a critical electric field $F_c$=0.16 V/°A. In addition, it was interesting to see that j decreased as F increased beyond $F_c$. The explanation for this unusual behavior was that in the low fields region, the electrons in valence band only needed to tunnel through the vacuum region. As the electric field increased, the vacuum barrier reduced and thereby electron tunneling increased. As the electric field increased, band bending in diamond also increased. If the electric field exceeds $F_c$, the band bending is so large that the holes generated at the semiconductor-metal interface have to tunnel through a larger internal barrier due to greater field penetration to reach the interior of the metal. Therefore, hole transport through metal-diamond

interface that provide electrons for the valence band, reduces. Consequently, electron supply diminishes and j decreases.

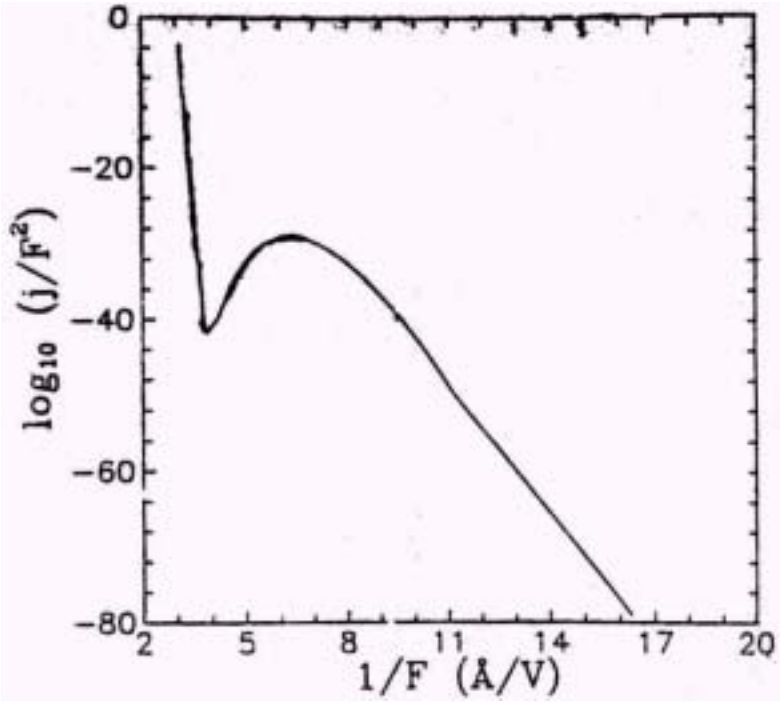


**Figure 2.16.** Calculated Fowler-Nordheim plot of emission from the valence band for a p-type diamond (111) surface. Electron affinity $\chi$ is taken to be -1 eV, $E_g$ =5.47 eV, T=300K, and doping concentration n=$10^{19}$ $cm^{-3}$.

If there are surface states, the conduction band bends down to pin the Fermi level near the midgap. Since $E_g$=5.5 eV, the band bending is significant and essentially blocks the holes tunneling into the metal. In this case negligible emission is obtained from bulk states. In addition, such a large barrier inside the bulk also eliminates the electron transport to the surface states from the bulk valence band.

On the other hand, experimental data [88,108] showed significant contradiction to the theoretical calculation. Boron-doped planar polycrystalline diamond films have lower turn-on electric fields than undoped diamond films.

Furthermore, a similar contradiction was found by using emission barrier height analysis for p-type diamond emitter [143] using Mo emitter as the reference. Using the emission barrier height of 4.24eV for Mo, the emission barrier height of B-doped diamond was estimated to be 1.87 eV. Thus, a p-type diamond emitter has low emission barrier height compare to Mo emitter.

This is a significant contradiction to the conventional band theory in which the work function is expected to be 5 eV. In addition, a recent experiment confirms that p-type diamond utilizing boron ion-implantation improves the field emission characteristic significantly [100]. From the theory, it is unlikely that low work function results from the effects of the acceptor doping and the contradiction remains to be explained.

In addition, the effect of boron doping concentration in planar diamond film on field emission has been recently studied [101]. The turn-on electric field and F-N slope were found to increase as the doping concentration increases. It was proposed that the higher boron doping concentration result in the smaller grain-size of diamond crystal. Thus the field enhancement factor decreases and field emission is degraded [101].

Field emission enhancement via surface states

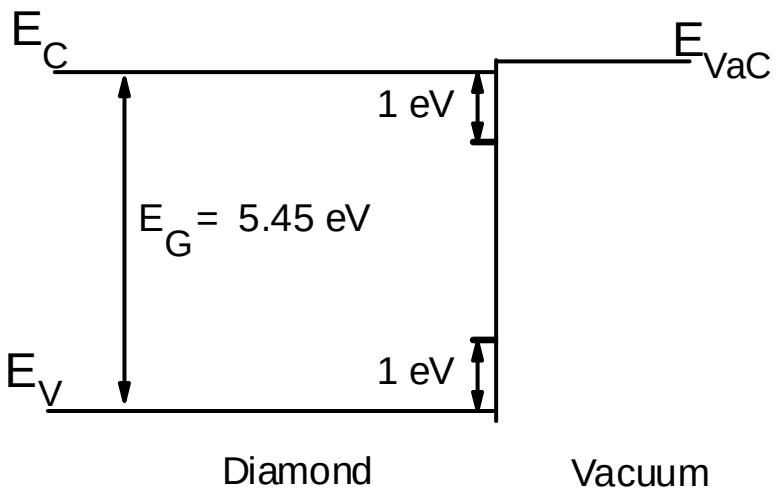


**Figure 2.17.** Energy band diagram of diamond with surface states.

Surface states could be a source that provides electrons for field emission enhancement. However, electron tunneling from a localized surface state can be different from the electron states in bands because the localized surface states do not have continuous supply of electron like electron states in bands. If it can be assumed that there is a constant supply of electrons, then the emission characteristics from the surface states should not be much different from the bulk valence band.

If a diamond surface is unreconstructed and hydrogen-passivated, no surface state exists on diamond surface. However, it has been found that on the (111) surface with 2x1 reconstruction there are occupied surface states centered at 1 eV above the valence band maximum as shown in **Figure 2.17** [157-158]. A possible continuous supply source for this surface state is the electrons from valence band. However, since the electron transmission probability from these surface states is very small due to the large barrier height for tunneling. Therefore, the surface states located at 1 eV above the valence band maximum cannot explain the electron emission at low field.

Surface states have also been found at 1 eV below the bottom of the conduction band but these states are unoccupied. If these states are occupied under an applied field under some appropriate mechanisms, electrons should be able to tunnel to vacuum easily. The current density from a surface state is given by [157-158]:

$$j=\frac{q\hbar}{2\pi m_e} N_s Q^2 \int f(E_s) D(E_s - (E_s - E_{s0}) m^* / m_e) dE_s \qquad (2.20)$$

where $N_s=m^*/(2\pi\hbar)$ is the density of states, Q is an effective wave vector, $f(E_s)=1/[1+\exp((E_s-E_F)/kT)]$ the Fermi distribution function, and D(E) is the transmission probability. It is assumed that the surface band is parabolic:

$$E_s = E_{s0} + \hbar^2 k_t^2 / 2m \qquad (2.21)$$

Assuming $E_F=E_{S0}=E_C-1$, $m^* = m_e$, Q=1, $\chi$=-0.1 to 0.1 eV and electric field of $10^{-2}$ V/°A, the calculated current density is ~1 to$10^{-3}$ A/m$^2$, which is comparable to the experimental data ~$10^{-3}$ A/m$^2$ at $10^{-2}$ V/°A. The calculation is based on the assumption that $\chi$ is negative or small positive. This assumption is applicable to the unreconstructed (111) surface. However, the assumption of small positive or negative electron affinity is not justified for the reconstructed diamond (111) surface, since it does not exhibit such a negative electron affinity due to band bending effect. Furthermore, the mechanisms how electrons are transported to the surface states still remain to be answered. Therefore, this surface states alone is not sufficient for the explanation of low field electron emission from diamond.

Field emission enhancement via defect states

Defect states or bands are very probable sources that provide electrons for field emission enhancement. It has been speculated that there exist defect states located in the energy gap close to the bottom of the conduction band [157-158] as shown in **Figure 2.18**. Defects in diamond such as vacancies and grain boundaries may be generated by chemical vapor deposition (CVD). It has been found that vacancy defects in diamond thin films are substantial [161-163]. Dangling bonds are expected to exist in the defects. In addition, defects in the form of graphite [164] and multiply twinned with quintuplet wedges [98] have also been observed. If defect concentration is significant, the electron states in these defects could form energy bands as illustrated in **Figure 2.18**. Calculation [157] shows that defect states may exist in the bulk band gap. The calculated current densities based on these bands agree with experimental results. However, more theoretical study is needed to determine how these defect states couple to each other to form a defect-induced conducting band.

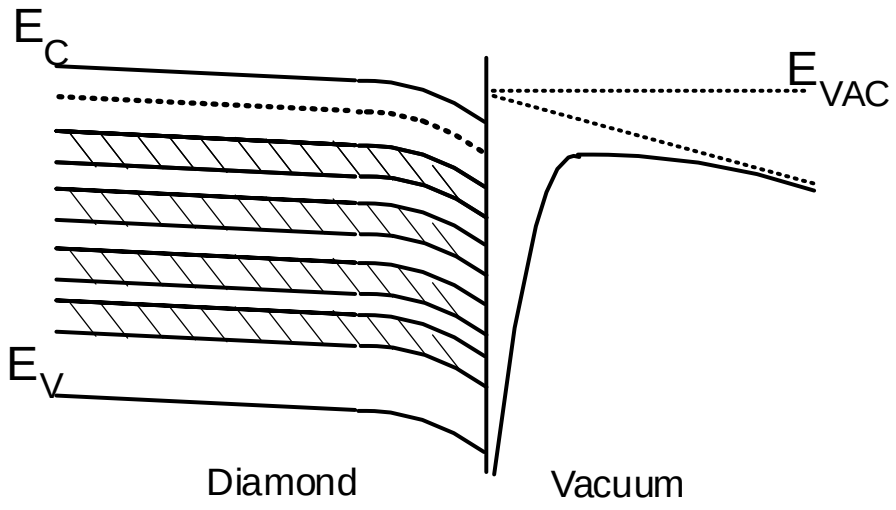


**Figure 2.18.** Energy band diagram for diamond with defect states and defect-induced bands under an applied field.

The effect of defects in diamond film generated in CVD process has been studied [93-94,105,107]. Diamond samples with varying defect densities have been synthesized by PECVD and their field emission characteristics have been analyzed. It was found that the turn-on electric field of undoped diamond films falls rapidly as the structural defect density increases. Such a strong correlation between the field emission and the structural defect density was also observed

for p-type (boron) diamond film. This indicates that the samples with higher defect density require lower fields for emission. It was also found that the emission of p-type diamond film was more stable than undoped diamond film at a lower defect density. From the result, it seems to be reasonable to believe that the enhanced field emission originates from the defect-induced energy band(s). As illustrated in **Figure 2.18**, a series of defect-induced energy bands was assumed to form throughout the band gap because of the presence of wide varieties of structural defects. If these bands are wide enough or closely spaced, electron hoping within the band(s) or excitation from the valence band could easily provide a steady follow of electrons to the surface to sustain stable emission of electrons into vacuum. Electron can emit directly from these bands or transport to the surface states for emission. The formation of these defect bands raises the Fermi level toward conduction band and thus reduces the energy barrier that the electrons must tunnel through. However the exact position of these defect-induced energy bands can not be determined from the field emission measurements because the local field enhancement factor and the emission area are not known.

The effect of defects generated by CVD process on diamond film for field emission has also been investigated using secondary electron images [84,95]. The diamond films were grown such that the percentage of non-diamond carbon was highest at the edge of the film. It was found by secondary electron images that the majority of the emission sites also occurred at the edge of the film. The results support the existing postulate that the field emission results from the composite defects of the material.

Defects may be introduced into diamond film by the incorporation of dopants. A significant field emission enhancement was observed from diamond film doped with a high nitrogen-doping concentration of $2\times10^{20}$ $cm^{-3}$ [103]. Since nitrogen is a deep donor impurity that is not ionized at room temperature, field emission enhancement may not arise from the direct effect of donor dopant but could arise from the dopant-related defect centers. The nitrogen-related defects including vacancies trapped at substitutional nitrogen atom (1.94 and 2.15 eV ), at A centers (2.3 and 2.46 eV), and at B centers (2.49 eV) were found using photoluminescence (PL) and cathodoluminescence (CL) spectroscopy measurements. The number in parenthesis denoted the energy level with respect to the valence band maximum. It was speculated that these defects might play important role for field emission enhancement. However, electrons in these defect states seem to have too low energy to couple to the vacuum or conduction band.

Defects created by ion implantation have also been studied for electron field emission [96,104]. The energetic ion implantation is known to cause structural damage and defect generation in the surface region of various materials including diamond. It was found that the threshold field falls rapidly as the dose of implantation increases. In addition, it was found that the implantation of $Si^+$ ion results in more electron emission enhancement than the implantation of $C^+$ ion because bigger atomic ions produce more defects and damage. The emission characteristics of implanted diamond films were found to be insensitive to atmospheric exposure. It is also suggested that the modified surface structure produced by the implantation process is very stable and chemically inert. It is also suggested that defects introduced in the surface regions by ion implantation increased the conductivity and altered the work function of the diamond, thus directly affecting their field emission properties. While the exact nature of the defects responsible for field emission has yet to be identified, it was suggested that the types of defects formed could include vacancies dislocations, stacking faults and second phases such as graphite and amorphous carbon components. The effect of carbon, hydrogen, argon, and xenon ion irradiation on a pure graphite carbon fiber has also been studied [112]. It was found that the turn-on electric field decreases to minimum as dose rate increase to a critical value and then increases as the dose rate increase further. It was proposed that carbon atomic displacement due to irradiation, which could result in an increase of $sp^3/sp^2$, is responsible for the improved field emission.

On the other hand, a critical theoretical examination of electron transport mechanisms in diamond did not reveal any viable process to populate these tunneling states. For example [165], the density of states for a lattice with a single vacancy has been calculated and found that there exists only defect states lie within a narrow energy range (~1-2 eV) above the top of valence band. Therefore, these defect states have too low energy to couple to the vacuum or conduction band, which can produce the tunneling current in field emission. However, defect states have been recently found at 2.0 and 4.0 eV below the conduction band minimum of diamond by photoelectron yield spectroscopy [166]. This finding suggests that these defect states could be excitation channel for electron emission from diamond.

Field emission enhancement via a complicated metal-diamond interfacial layer

A theoretical calculation of undoped diamond emitter has identified that the injection of electrons from the metallic back contact is an essential limiting factor to emission current [78,167]. Thus, it has been suggested that a possible mean to enhance electron emission is to populate the conduction band with electron injection through a complicated metal-diamond interfacial layer. It has been speculated that there is a complicated interfacial layer resulting from a chemical reaction between the metal and a treated diamond surface [168].

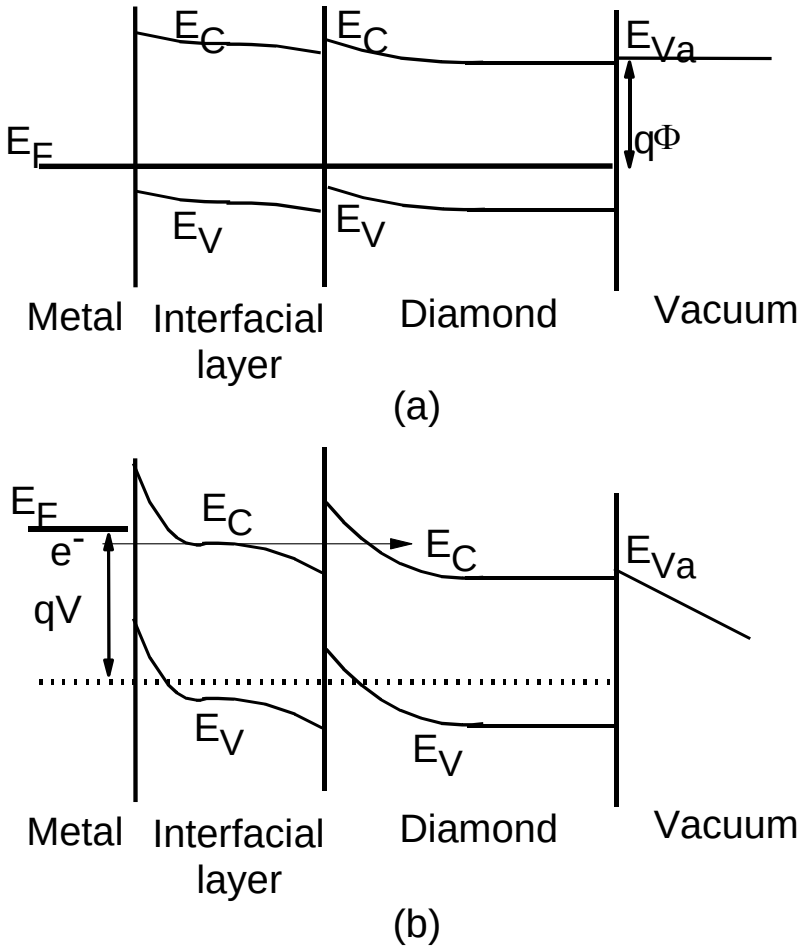


**Figure 2.19.** Energy band diagram of metal-diamond contact with an insulating interfacial layer (a) at thermal equilibrium and (b) under forward bias.

Recently, it has been found that an interfacial layer of $Mo_2C$ is formed on diamond coated Mo emitter by annealing at 500 °C for several hours [76,167]. The electron emission was found to improve after the interfacial layer formation. In addition, an interfacial layer of Au-amorphous carbon from diamond grown on gold-coated silicon substrate has also been observed

using secondary ion mass spectroscopy (SIMS) [102]. The electron emission of diamond gold-coated silicon substrate is significantly better than that of diamond on bare silicon substrate. The results suggested that the electron injection through the interfacial layer could be responsible for field emission enhancement. The electron injection through the interfacial layer can be viewed by the energy band diagram in **Figure 2.19**. The interfacial layer is assumed to be a poor conductor with a low carrier concentration such that when a DC current passes through the structure, a significant voltage drop can occur in the interfacial layer. Thus, a steep potential energy drop across the interface between the metal and diamond will be produced under applied electric field. As a result, electrons from metal states with energies near the Fermi level can tunnel through the insulating gap into the conduction band of diamond. In the case of a semiconductor-diamond interface, complicated interfacial structure has also been observed. In principle, injection of electrons into the conduction band of diamond through such an interface is also possible.

The field emission from different surfaces of diamond was calculated and the possible source of the field emission from bulk and surface state was studied by a real space Monte Carlo (MC) simulation [168-169]. In this simulation, it was assumed that electron injection via complicated interfacial layer is the mechanism by which electrons are populated in the conduction band of diamond. A real space Monte Carlo (MC) simulation was then performed to study the electron transport in the conduction band and to examine the effect of the internal electric field and the thickness of the material under a given electron energy distribution.

The scattering processes considered in the electron transport calculations [169] are acoustical (low energy mode phonon) intravalley elastic, acoustical intravalley inelastic, intravalley optical (high-energy mode phonon), and intervalley phonon scattering. The intravalley scattering needs to be included, because the constant energy surfaces near the bottom of the conduction band consist of six ellipsoids in the <100> directions (because there are six valleys of conduction band minima, the composite intravalley scattering is not negligible). Electron-electron elastic scattering in the conduction band can be omitted since it only affects the randomization of the energy distribution. For the low field approximation (<10 V/μm), the electron-plasmon (collective conduction of electron gas particle) scattering can be omitted since the plasma energy of conduction electron is small (meV) for normal electron concentrations in semiconductors.

It was found that for low internal fields (<0.1V/μm), the majority of scattering events are due to acoustical phonons since the energy gained by the electrons due to the acceleration by the internal field was dissipated through collisions with phonons. The electron energy distribution is independent of both the field and the thickness of the film and the nearly constant value of the energy distribution inferred that the electron-lattice system is in the thermal equilibrium. As the field increases, however, the energy distribution shows a tail and strongly depends on the applied field and film thickness since there is an energy gain by the electrons, resulting in some electrons with higher energies. For wider films, the accumulation of energy is larger and hence the distributions show longer tails. As electron energy and applied field increase, the contribution of optical phonon and interband scattering increases and the number of scattering decreases from several hundred at low fields to about 7 particles at 10 V/μm. Thus, there is a transition to ballistic behavior in diamond as electric field increases above a critical field (10 V/μm). In the other word, electron can travel through diamond with experiencing very few scattering events and thus it acts like it is in free flight in an electric field. Therefore, the simulation results suggest that if a realistic and viable electron injection mechanism into the conduction band of a diamond-metal or diamond-semiconductor interface exists for those NEA diamond surfaces, then a copious cold cathode electron emitter is feasible at low applied electric field.

# CHAPTER III

# FIELD EMISSION VACUUM DIODE AND TRIODE

## Field emission vacuum diode

### Structure and basic operating principles

Field emission vacuum diode is a two-electrode electronic device, which has a simple structure as shown in **Figure 3.1 (a)**. The first electrode is called cathode where electrons are emitted. The second electrode is called anode where electrons are collected. They are separated by a vacuum gap. To allow emission occurring at a low electric field, the cathode is normally made of low work function material or with a sharp structure. The circuit symbol of a vacuum diode is shown in **Figure 3.1 (b)**. The operating principle of field emission vacuum diode is as following.

Under forward bias where a positive voltage is applied to the anode with respect to the cathode, electrons emit from cathode through the triangle potential barrier into vacuum via Fowler-Nordhiem tunneling process. The emitted electrons are accelerated through vacuum gap under applied electric field and collected at the anode. When, they strike the anode, they give up most of their energy to the anode in form of heat. This loss is in the nature of $I^2R_a$, where $R_a$ is the anode resistance. Under reverse bias where a negative voltage is applied to the anode with respect to the cathode, electrons may emit from anode into vacuum via Fowler-Nordhiem tunneling process. However, the electron tunneling from anode into vacuum only occurs at a very high electric field because the anode is normally made of a high work function metal with planar structure, which does not allow emission to occur at low electric field. Therefore, field emission diode has a rectifying I-V characteristic. However at high reverse voltage, reverse breakdown occurs due to electron tunneling in the reverse direction. The reverse breakdown field and voltage depend on the anode-cathode spacing, type of anode, and condition of anode surface. It was found that the breakdown field for a highly polished chrome-steel anode increases from 45 kV/mm to 220 kV/mm as the vacuum gap decreases from 1 mm to 50 μm. However, the corresponding breakdown voltage decreases from 45 kV to 11 kV [170].

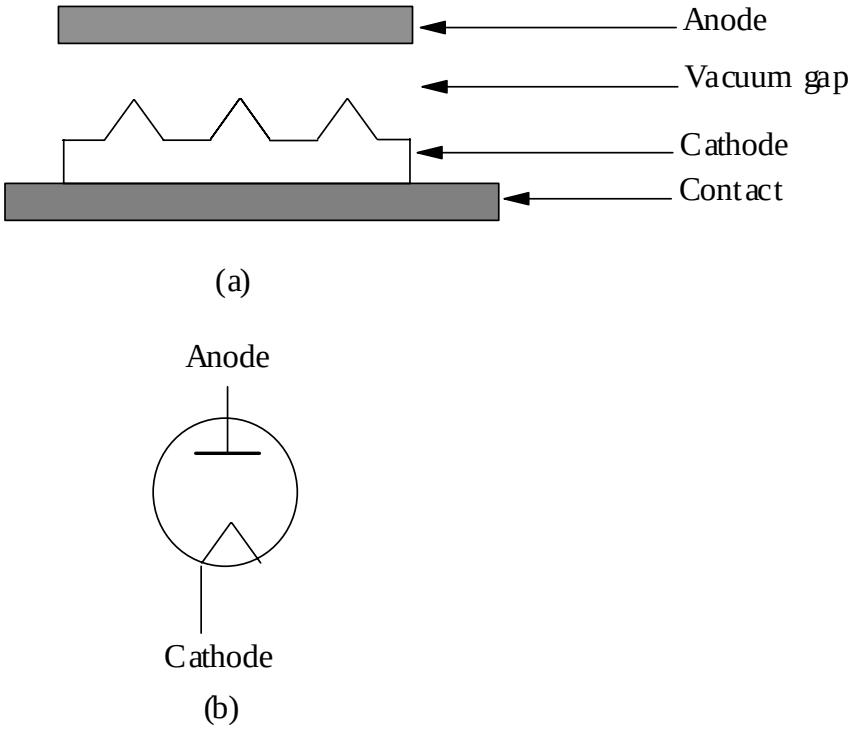


**Figure 3.1.** Field emission vacuum diode (a) structure and (b) symbol.

Field emission diode characteristics

A typical current-voltage (I-V) characteristic of a silicon field emission diode [18] is shown in **Figure 3.2**. Under forward bias, I-V characteristic follows the Fowler-Nordhiem equation. The corresponding F-N plot of $Ln(I/V^2)$ vs. 1/V as shown in **Figure 3.3** is almost linear. No deviation due to image and space charge effect can be observed because the current density is not sufficiently high. Under reverse bias, there is no emission current at low applied voltage.

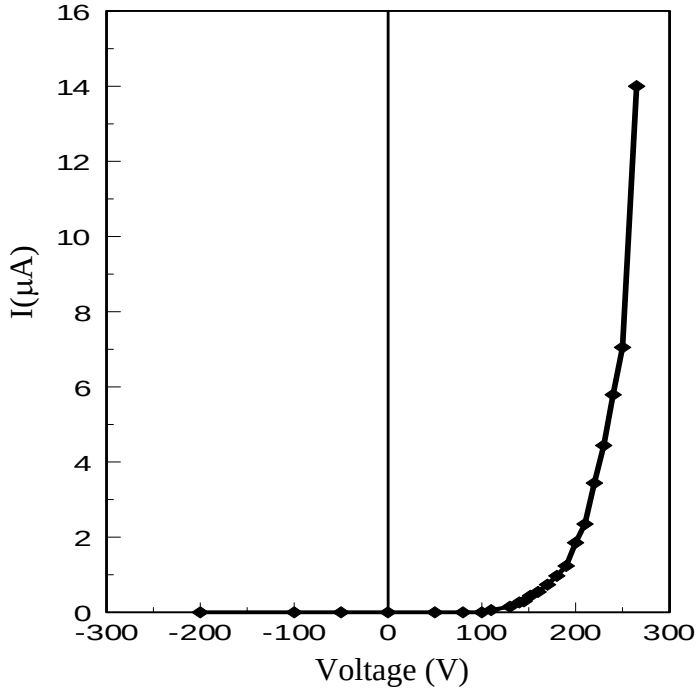


**Figure 3.2.** A typical current-voltage (I-V) characteristic of silicon field emission diode.

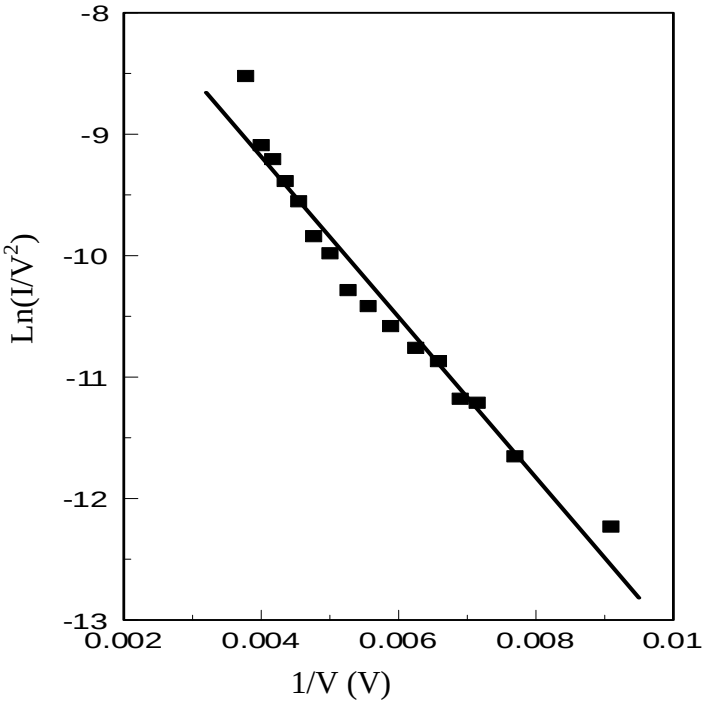


**Figure 3.3.** A typical Fowler-Nordhiem (F-N) plot of silicon field emission diode.

Field emission vacuum triode

Structure and basic operating principles

Field emission vacuum triode is a three-electrode electronic device, which has a simple structure as shown in **Figure 3.4 (a)**. The first two electrodes are cathode and anode as described for the field emission diode. The third electrode is called grid or gate. The gate is an electrode in the form of a suitable mesh, screen or circular flat structure placed between the cathode and anode. It is also often referred to as the control gate, but this distinction is only necessary in multi-electrode emitter structures containing more than one gate. The emission current flowing from the cathode to the anode must pass through the gate. The gate is, therefore, in a strategic position, and can largely control the anode current flow. The gate normally lies closer to the cathode. The addition of a gate between the anode and cathode makes it possible to control a large emission current by means of a small potential applied to the gate. Accordingly, triodes are useful in detection and amplification of small currents or voltages as well as in the generation of oscillations. The circuit symbol of a vacuum triode is shown in **Figure 3.4 (b)**.

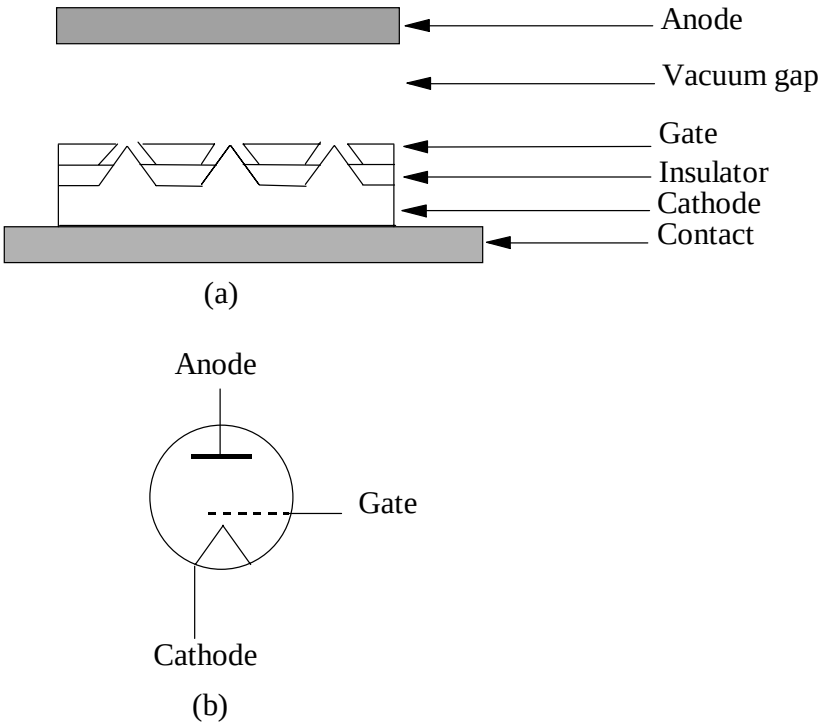


**Figure 3.4.** Field emission vacuum triode (a) structure and (b) symbol.

The function of anode and cathode for field emission vacuum triode are basically the same as that of a vacuum diode. The gate of field emission vacuum triode controls electric field at the cathode and helps to reduce space charge when operating in vacuum diode configuration. When a gate is interposed between the anode and cathode, it tends to screen the cathode from the anode field. A small change in the gate potential results in a large change in this field and hence a large change in emission current. If the gate is grounded to the cathode, the field emission behavior of a triode is the same as that of a diode because the gate contributes no effect on the electric field between anode and cathode. If the gate is made slightly positive with respect to the cathode, the gate significantly increases the electric field at the cathode, thus permitting the anode to draw a larger emission current. On the other hand, if the gate is made negative with respect to the cathode, the negative electric field of the gate significantly reduces the electric field at the cathode, which results in a smaller emission current.

The potential field at the cathode consists of two components. They are the potential field produced by the gate and the stray field provided by the anode, which act through the opening of the gate [174]. Accordingly, the characteristics of the field emission triodes depend upon many factors such as gate-cathode spacing, gate-anode spacing, size and geometry of gate. The stray potential field $V_s$ due to the applied anode voltage $V_a$ may be expressed by

$$V_s = \gamma V_a \tag{3.1}$$

where $\gamma$ is a constant determined by gate construction. This constant may be calculated from the electrostatic theory for simple geometrical design. In practice, this constant actually weakly depends on the gate and anode voltages. The electric field due to gate is the applied gate potential $V_g$ plus $V_0$, where $V_0$ is the contact difference potential between gate and cathode. The total field at the cathode therefore is [174]

$$V_t = \gamma V_a + V_g + V_0 \tag{3.2}$$

This is really an equivalent gate potential that would produce the same field at the cathode as the combined effect of gate and anode potentials. The total emission current from the cathode is therefore obtained by putting $V_t$ into the Fowler-Nordhiem equation in the place of anode-cathode voltage. Thus, the total emission current from cathode is given by

$$I_t = AK_1(\beta^2(\gamma V_a + V_g + V_0)^2 /(d^2\Phi))\exp(-K_2\, v(y)d\Phi^{3/2}/\beta(\gamma V_a + V_g + V_0)) \tag{3.3}$$

where d is cathode-gate spacing, all other variables and parameters in the equation were defined previously. The total emission current from the cathode would then be split into two

components, anode current and gate current. Let's define $\alpha$ as the fraction of the anode current to the total emission current, then the anode current and gate current are given by

$$I_a = \alpha I_t$$

$$= \alpha AK_1(\beta^2(\gamma V_a + V_g + V_0)^2 /(d^2\Phi))\exp(-K_2 v(y)d\Phi^{3/2}/\beta(\gamma V_a + V_g + V_0)) \quad (3.4)$$

$$I_g = (1-\alpha) I_t$$

$$= (1-\alpha)AK_1(\beta^2(\gamma V_a + V_g + V_0)^2 /(d^2\Phi))\exp(-K_2 v(y)d\Phi^{3/2}/\beta(\gamma V_a + V_g + V_0)) \quad (3.5)$$

where $\alpha$ is defined as transport factor similar to the transport factor of bipolar junction transistor, which take on value between 0 and 1. The $\alpha$ factor depends on several parameters. The first is the relative value between anode and gate voltages. For a given gate voltage, $\alpha$ is approaching 0 when anode voltage is much smaller than gate voltage. As anode voltage increases and becomes comparable to gate voltage, $\alpha$ takes on some values between 0 and 1. This region of triode operation is called non-saturation region. It is the region where anode current increases with anode voltage. As anode voltage increases further and becomes significantly higher than gate voltage, $\alpha$ is approaching to 1. This region of triode operation is called saturation region. It is the region where anode current is almost independent of anode voltage. This is the region where triode is normally biased for small signal amplification. Other parameters that $\alpha$ depends on are gate-cathode and anode-gate spacings. As the gate-cathode spacing decreases, higher anode voltage is required to extract electrons to the anode and hence $\alpha$ decreases at a given anode and gate voltage. On the other hand, as the anode-gate spacing decreases, lower anode voltage is required to extract electrons to the anode and hence $\alpha$ increases at a given anode and gate voltage. However, it was found that $\alpha$ is much more depending on gate-cathode spacing than it is on anode-gate spacing.

A standard thermionic field emission triode normally operates with the gate voltage made negative with respect to cathode. In this way, electrons are repelled from the gate while it is controlling the cathode-anode current. This current could also be controlled with gate voltage positive with respect to cathode. However, the electrons attracted to the gate would create a cathode-to-gate leakage current that would degrade the tube's operation. On the other hand, the field emission triode normally operates in the opposite regime as the thermionic field emission triode. If the gate were biased more negative than the cathode, there would be a possibility of having reverse field emission from the gate that would create an undesired gate-anode leakage

current. By operating the gate with positive bias, there will be no reverse field emission from the gate or cathode-gate leakage current because field emission creates high-velocity electrons at the cathode that will basically ignore the gate voltage as they travel to the anode. However, the gate voltage will change the field on the cathode, which will control the emission rate and thus the emission current as explained earlier.

Under reverse bias where a negative voltage is applied to anode with respect to cathode at a given gate voltage, there will be no emission current between anode and cathode until the reverse breakdown voltage is reached where reverse electron tunneling from anode occurs. However, if the gate is made positive with respect to the cathode, there will be emission current between gate and cathode. If the gate is made negative with respect to the cathode, there will be no emission current between gate and cathode until the reverse breakdown voltage is reached where reverse electron tunneling from gate occurs. Therefore, the gate and cathode become a field emission diode and the gate performs function as an anode. Normally, field emission triodes do not operate under these conditions.

Field emission triode characteristics

The field emission triode characteristics can be classified into two parts: static and dynamic characteristics. Static characteristics are characteristics of a triode under no load condition and dynamic characteristics are characteristics of a triode under loaded condition. Furthermore three important coefficients, amplification factor, gate-anode transconductance and anode resistance, are defined to characterize the performance and characteristics of vacuum triode [175].

Static characteristics

The static characteristic of a triode can be obtained by applying dc voltages directly on the gate and anode of a triode with no load resistor on the anode circuit. The applied voltage on gate and anode are varied and the anode and gate currents are measured to obtain a set of characteristic data. From the characteristic data, various static characteristics can be represented in three different forms as discussed below.

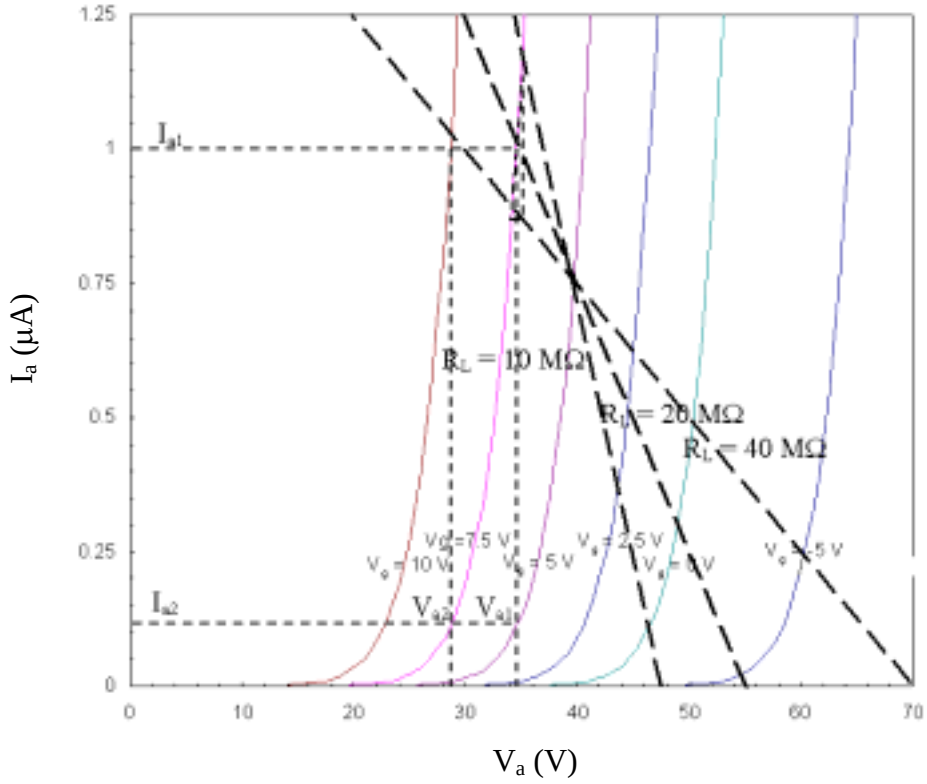


**Figure 3.5.** Calculated field emission triode $I_a$-$V_a$ characteristic of the modeled silicon field emitter triode.

The static characteristic of a triode is normally represented by the family of plots between anode current and anode voltage ($I_a$-$V_a$) with a constant gate voltage ($V_g$) in each plot. A modeled $I_a$-$V_a$ characteristic of a silicon field emission triode for various gate voltages is shown in **Figure 3.5** [16]. Under forward bias, $I_a$-$V_a$ characteristic follows the Fowler-Nordhiem triode equation. It can be seen that the turn-on anode voltage at a given gate voltage reduces as the gate voltage increases. The $I_a$-$V_a$ characteristic curves were ploted from the Fowler-Nordhiem triode equation (Eq. (3.5)) with following parameters: $A = \pi\times10^{-10}$ cm$^2$, $\alpha$=1, $\beta$ = 20, $\gamma \cong 0.42$, $\Phi$ = 4.0 eV and $d = 1.47\times10^{-5}$ cm. These parameters were assumed from a modeled silicon triode structure [16] except $\beta$, which was obtained by fitting the experimental data [15]. The modeled silicon triode structure has an anode-cathode spacing of 2 μm and a gate-cathode spacing of 0.1 μm. The parameters will be used for all subsequent discussion on the field emission triode.

Another common static characteristic representation of a triode is the family of plots between anode current and gate voltage ($I_a$-$V_g$) with a constant anode voltage ($V_a$) in each plot.

A modeled field emission triode $I_a$-$V_g$ characteristic for various anode voltages is shown in **Figure 3.6**. The turn-on gate voltage at a given anode voltage reduces as anode voltage increases. The shape of $I_a$-$V_g$ plots is similar to $I_a$-$V_a$ plots, however the turn-on gate voltage in the $I_a$-$V_g$ plot can vary from a negative to positive value unlike the turn-on anode voltage in the $I_a$-$V_a$ plot, which can only be a positive value. It should be noticed that, all curves of this family curve have the same shape and are also about equally spaced when anode voltages of consecutive curves are equally spaced.

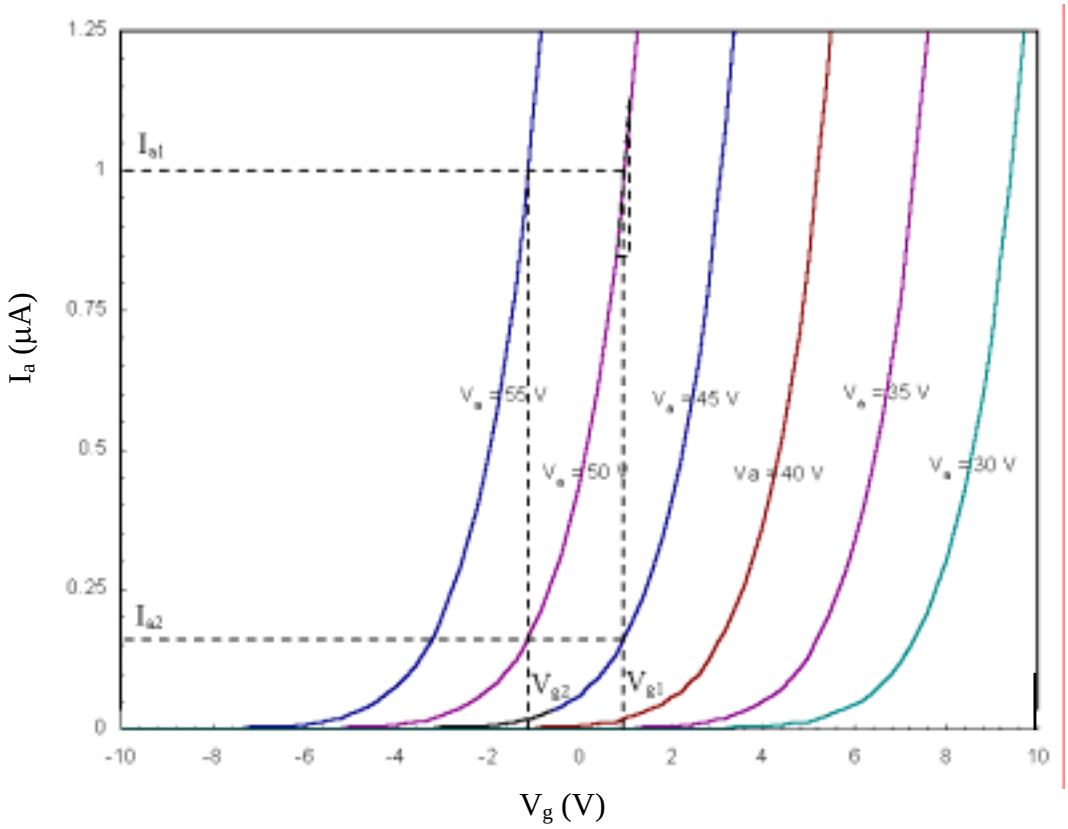


**Figure 3.6.** Calculated field emission triode $I_a$-$V_g$ characteristic of the modeled silicon field emitter triode.

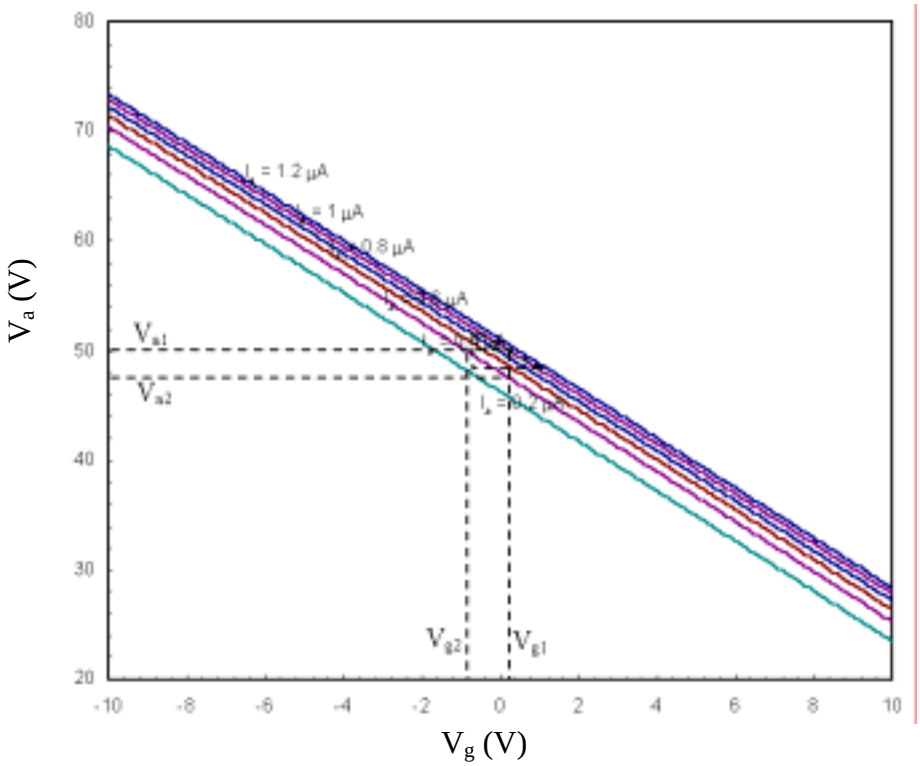


**Figure 3.7.** Calculated $V_a$-$V_g$ characteristic of the modeled silicon field emitter triode.

The transfer characteristic of a triode is a family of anode voltage vs. gate voltage ($V_a$-$V_g$) plots with a constant anode current ($I_a$) in each plot. A modeled transfer characteristic is shown in **Figure 3.7**. It is clear that $V_a$-$V_g$ curves are approximately linear. The $V_a$-$V_g$ line at a given anode voltage are shifted toward positive gate voltage as anode current increases. The transfer characteristic is useful in design work, but it is not normally used since it less clearly illustrates the operation of a triode from an electronic viewpoint.

Dynamic characteristics

The static curves of **Figures 3.5-3.7** were taken without a load resistor in the anode circuit. But, loading affects the operation of a triode and therefore must be considered. Curves taken (or calculated) with a load resistance (or impedance) in anode circuit are known as dynamic characteristic curves. Dynamic characteristic curve can be obtained by addition of a resistor in the anode circuit. With a fixed applied voltage on the anode circuit, the anode current is measured as a function of gate voltage. The dynamic characteristic is then obtained by plotting anode current vs. gate voltage with the applied voltage ($V_a$') on the anode circuit. The change in

gate voltage results in the change in anode current. With a resistor $R_L$ in series, the voltage on the anode ($V_a$) is changed according to

$$V_a = V_a' - I_a R_L \quad (3.6)$$

Hence, the presence of a resistor $R_L$ in anode circuit modifies overall characteristic of the circuit. Dynamic characteristics can be calculated from static characteristics by using Eq. (3.6). **Figure 3.8** illustrates the calculated dynamic characteristic with load resistor $R_L$ = 10, 20, and 40 MΩ on the static $I_a$-$V_g$ characteristic curve of **Figure 3.6**. Initially, a point $P_1$ ($I_{a1}$ = 0.75 μA, $V_{g1}$ = 4.9 V, and $V_{a1}$ = 40 V) on $I_a$-$V_g$ static characteristic curve was used as a starting operating point.

For the case of $R_L$ = 20 MΩ, the applied voltage on anode circuit $V_{a1}' = V_{a1}+I_{a1}R_L$ = 40+20×0.75 = 55 V. This voltage is the required supply voltage and thus is fixed throughout this calculation. If the gate voltage decreases, the anode current decreases and thus the actual voltage on anode increases. A new operating point $P_2$ of $I_a$-$V_g$ dynamic characteristic curve can be generated on another $I_a$-$V_g$ static curve with anode voltage $V_{a2}$ = 45 V and the corresponding anode current $I_{a2}$ can be calculated by

$I_{a2} = (V_{a1}' - V_{a2})/R_L$

$= I_{a1}+(V_{a1} - V_{a2})/R_L$

= 0.75+(40-45)/20 = 0.5 μA.

Likewise, another dynamic operating point $P_3$ can be generated on another $I_a$-$V_g$ static characteristic curve with anode voltage $V_{a3}$ = 35 V by calculating the corresponding anode current $I_{a3}$.

$I_{a3} =(V_{a1}' - V_{a3})/R_L$

$=I_{a1}+(V_{a1} - V_{a3})/R_L$

= 0.75 + (40-35)/20 = 1 μA.

The same calculation can be repeated to obtain a complete dynamic characteristic curve and dynamic characteristic curve for other resistance loads. It can be seen that the $I_a$-$V_g$ dynamic characteristic curve is more linear than $I_a$-$V_g$ static characteristic curve and the linearity improves as the load resistance increases. This property of $I_a$-$V_g$ dynamic characteristic curve allows triodes to be used as a linear amplifier.

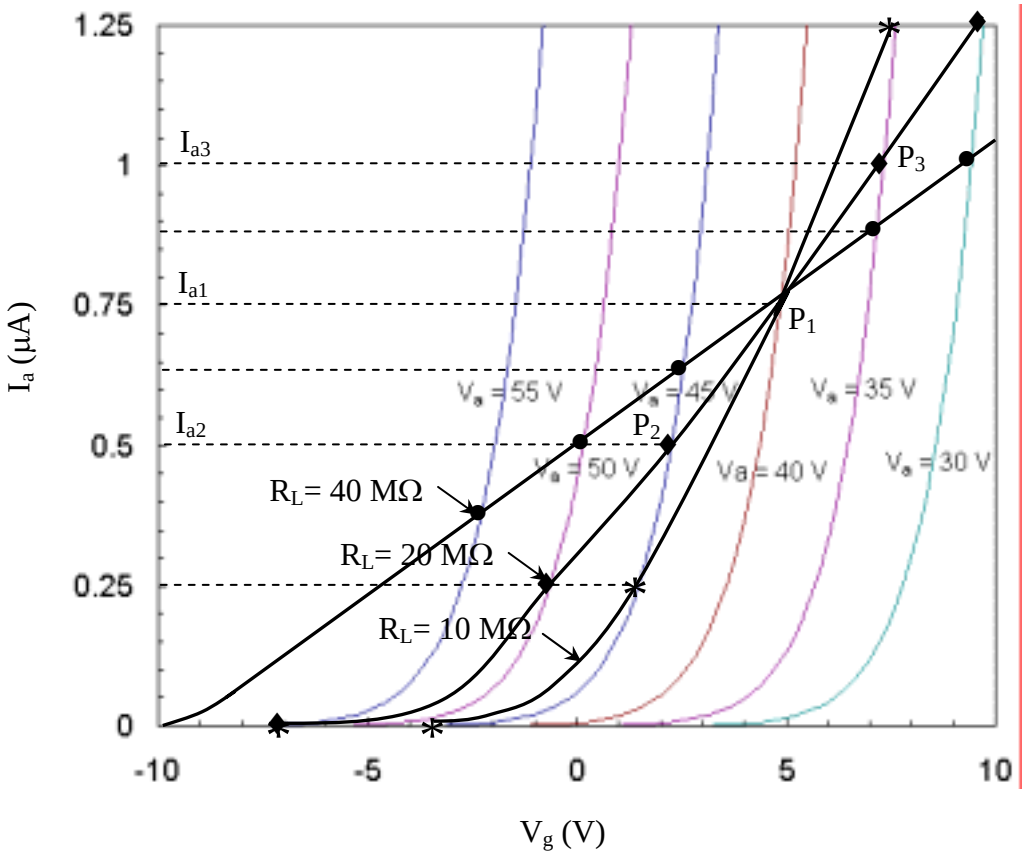


**Figure 3.8.** Dynamic characteristic curves calculated on the static $I_a$-$V_g$ characteristic of the modeled silicon field emitter triode.

Another method to obtain dynamic characteristic from static characteristics is to use load lines on $I_a$-$V_a$ characteristic curve. **Figure 3.5** also illustrates load lines corresponding to the load lines in **Figure 3.8** on the $I_a$-$V_a$ characteristic curves. The intercepts of load lines on V axis indicate the supply voltage of the anode circuits. The intercepts of load lines in **Figure 3.5** indicate that the supply voltages for $R_L$ = 10, 20, and 40 MΩ are 47.5, 55, and 70 V, respectively. Every point on the load lines is a point of dynamic characteristic. These points can be plotted to obtain the same $I_a$-$V_g$ dynamic characteristic curve as the previous method.

Three characteristic coefficients of a vacuum triode

The performance characteristics of a vacuum triode are determined by the amplification factor, gate-anode transconductance, and anode resistance, are defined to characterize. These three coefficients are particularly useful for ac equivalent circuit modeling of vacuum triode.

Amplification factor, μ, is a measure of the effectiveness of the control gate voltage relative to that of the anode voltage upon the anode current. It is also called static gain. In other words, the amplification factor is the ratio of a change in anode voltage to a change in gate voltage at constant anode current. Mathematically, the amplification factor is the negative of infinitesimal changes, as indicated by the defining equation,

$$\mu = -\frac{\partial V_a}{\partial V_g}\bigg|_{I_a = cons\tan t} \tag{3.7}$$

where μ is the amplification factor or static gain, $V_a$ is the anode voltage, $V_g$ is the gate voltage and $I_a$ is the anode current. Partial derivative is used because a third variable is held constant.

Gate-anode transconductance ($g_{ag}$) is defined as the quotient of the in-phase component of the alternating current of the anode by the alternating voltage of gate under the conditions that all other electrode voltages remain constant. It is also called mutual conductance, $g_m$, or shortly transconductance. Mathematically, the gate-anode transconductance or mutual conductance is the infinitesimal amplitudes, as indicated by the defining equation,

$$g_{ag} = g_m = \frac{\partial I_a}{\partial V_g}\bigg|_{V_a = cons\tan t} \tag{3.8}$$

where $g_{ag}$ is the gate-anode transconductance, $g_m$ stands for mutual conductance, $V_a$ is the anode voltage, $V_g$ is the gate voltage and $I_a$ is the anode current. The mutual conductance generally also depends on gate and anode voltages.

Anode resistance, $r_a$, is derived from anode conductance which is defined as the quotient of the in-phase component of the alternating current of the anode by the alternating voltage of anode under the conditions that all other electrode voltages maintain constant. Mathematically, the anode conductance is the infinitesimal amplitudes, as indicated by the defining equation,

$$g_a = \frac{\partial I_a}{\partial V_a}\bigg|_{V_g = cons\tan t} \tag{3.9}$$

where $g_a$ is the anode conductance, $V_a$ is the anode voltage, $V_g$ is the gate voltage and $I_a$ is the anode current. The values of anode resistance are ordinarily used instead of anode conductance. The anode conductance generally depends on gate voltage and anode voltage. Anode resistance is defined as the reciprocal of the anode conductance. Symbolically,

$$r_a = \frac{1}{g_a} = \left.\frac{\partial V_a}{\partial I_a}\right|_{V_g = \text{constant}} \tag{3.10}$$

The values of $\mu$, $g_a$ and $r_a$ are usually referred to as coefficients. They are not constant, in the strict sense, because these values vary with the operating conditions. For a given set of conditions, however, a useful relation exists among these coefficients. If equation (3.8) and (3.10) are multiplied together, the result is

$$r_a \cdot g_m = \frac{\partial V_a}{\partial I_a} \cdot \frac{\partial I_a}{\partial V_g} = \frac{\partial V_a}{\partial V_g} = \mu$$

according to equation (3.9). The relations

$$\mu = r_a \cdot g_m, \quad g_m = \frac{\mu}{r_a}, \text{ and } \quad r_a = \frac{\mu}{g_m} \tag{3.11}$$

are often useful for design work since one coefficient can be found from the other two. There are three basic methods to determine these three coefficients. The first method is the graphical method. In this method, these coefficients are calculated from characteristic curves. The second method is the direct calculation from characteristic equation. The last method is the direct experimental method. In this method, these coefficients are measured directly by dynamic measurement techniques.

The graphical method for determining the amplification factor can be obtained from any kind of characteristic curves. The amplification factor can be approximately determined from the $I_a$-$V_a$ characteristic curve as following. From two consecutive $I_a$-$V_a$ characteristic curves with gate voltages $V_{g1}$ and $V_{g2}$, two anode voltages $V_{a1}$ and $V_{a2}$ at the same anode current $I_a$ can be read from these two curves. From the definition, the amplification factor $\mu$ is approximately equal to $(V_{a1}-V_{a2})/(V_{g2}-V_{g1})$. For example (**Figure 3.5**), the anode voltage $V_{a1}$ is approximately 34.5 V at gate voltage $V_{g1}$ = 7.5 V, and the anode voltage $V_{a2}$ is approximately 28.5 V at gate voltage $V_{g2}$ = 10 V on the constant anode current line of $I_a$ = 1 μA. Therefore, the amplification factor $\mu$ is approximately equal to (34.5-28.5)/(10-7.5) = 2.4. This amplification factor value should only be applied for the operating range of gate voltage from 7.5 V to 10 V, anode voltage from 28.5 V to 34.5 V and at anode current of 1 μA.

The amplification factor can also be estimated from the $I_a$-$V_g$ characteristic curve in similar manner as following. From two successive $I_a$-$V_g$ characteristic curves with anode voltages $V_{a1}$ and $V_{a2}$, two gate voltages $V_{g1}$ and $V_{g2}$ at the same anode current $I_a$ can be obtained

from these two curves. From the definition, the amplification factor μ is again approximately equal to $(V_{a1}-V_{a2})/(V_{g2}-V_{g1})$. For instance (**Figure 3.6**), the gate voltage $V_{g1}$ is circa 1.05 V at anode voltage $V_{a1}$ = 50 V, and the gate voltage $V_{g2}$ is circa -1.1 V at anode voltage $V_{a2}$ = 55 V on the constant anode current line of $I_a$ = 1 μA. Therefore, the amplification factor μ is approximately equal to (55-50)/(1.05-(-1.1) = 2.32. This amplification factor value should only be assumed for the operating range of gate voltage from 1.05 V to –1.1 V, anode voltage from 50 V to 55 V and at anode current of 1 μA.

The amplification factor can also be calculated from the $V_a$-$V_g$ characteristic curve. However, the calculation in this case is simpler and more accurate than the previous cases, because the amplification factor is the negative slope of this curve at the point of operation by definition. For illustration (**Figure 3.7**), the negative of slope of the curve at anode current $I_a$= 1 μA and anode voltage $V_a$ = 50 V is approximately 2.35. This amplification factor value should only be used for the operating point at anode voltage of 50 V and anode current of 1 μA. However since $V_a$-$V_g$ curves are almost linear the amplification factor is almost the same for other operating points along the same line.

The transconductance can also be graphically estimated from all kinds of characteristic curves. The transconductance can be approximately acquired from the $I_a$-$V_a$ characteristic curve as following. From two successive $I_a$-$V_a$ characteristic curves with gate voltages $V_{g1}$ and $V_{g2}$, two anode currents $I_{a1}$ and $I_{a2}$ , at the same anode voltage $V_a$, can be attained from these two curves. From the definition, the transconductance $g_m$ is approximately equal to $(I_{a2}-I_{a1})/(V_{g2}-V_{g1})$. For example (**Figure 3.5**), the anode current $I_{a1}$ is approximately 1 μA at gate voltage $V_{g1}$ = 7.5 V and the anode current $I_{a2}$ is approximately 0.11 μA at gate voltage $V_{g2}$ = 5 V on the constant anode voltage line of $V_a$ = 34.5 V. Therefore, the transconductance $g_m$ is approximately equal to (1-0.11)/(7.5-5) = 0.356 μS. This transconductance value should only be assumed for the operating range of gate voltage from 5 V to 7.5 V, anode current from 1 μA to 0.11 μA and at anode voltage of 35 V.

The transconductance can also be approximately computed from the $I_a$-$V_g$ characteristic curve. The calculation in this case is easier and more precise than the previous case, since by definition the transconductance is the slope of this curve at the point of operation. For instance (**Figure 3.6)**, the slope of the curve at anode current $I_a$= 1 μA, gate voltage $V_g$ = 7.5 V, and anode voltage $V_a$ = 34.5 V is approximately 1.15 μS. This transconductance value should only

be applied for the operating point at anode voltage of 34.5 V, gate voltage of 7.5 V, and anode current of 1 μA.

The transconductance can also be approximately attained from the $V_a$-$V_g$ characteristic curve in similar manner as following. From two consecutive $V_a$-$V_g$ characteristic curves with anode voltages $I_{a1}$ and $I_{a2}$, two gate voltages $V_{g1}$ and $V_{g2}$, at the same anode voltage $V_a$, can be acquired from these two curves. From the definition, the transconductance $g_m$ is approximately equal to $(I_{a2}-I_{a1})/(V_{g2}-V_{g1})$. For illustration (**Figure 3.7**), the gate voltage $V_{g1}$ is approximately 0.3 V at anode current $I_{a1}$= 1 μA, and the gate voltage $V_{g2}$ is approximately –0.8 V at anode current $I_{a1}$= 0.4 μA on the constant anode voltage line of $V_a$=50 V. Therefore, the transconductance $g_m$ is approximately equal to (1-0.4)/(0.3-(-0.8)) = 0.54 μS. This transconductance value should be only assumed for the operating range of gate voltage from 6 V to 10 V, anode current from 0.4 μA to 1 μA and at anode voltage of 50 V.

Anode resistance can also be acquired manually from any kind of characteristic curves described above. The anode resistance can be approximately determined from the $I_a$-$V_a$ characteristic curve. In this case, the calculation is straightforward, because the anode resistance is the reciprocal of the slope of this curve at the point of operation by definition. For example (**Figure 3.5**), the slope of the curve at anode current $I_a$ = 1 μA and gate voltage $V_g$ = 7.5 V is approximately 0.3 μS. Thus, the anode resistance is approximately 3.3 MΩ. This anode resistance value should only be applied for the operating point at gate voltage of 7.5 V, and anode current of 1 μA.

The anode resistance can be approximately calculated from the $I_a$-$V_g$ characteristic curve as following. From two successive $I_a$-$V_g$ characteristic curves with anode voltages $V_{a1}$ and $V_{a2}$, two anode currents $I_{a1}$ and $I_{a2}$, at the same gate voltage $V_{g1}$, can be acquired from these two curves. From the definition, the anode resistance $r_a$ is approximately equal to $(I_{a2}-I_{a1})/(V_{a2}-V_{a1})$. For instance (**Figure 3.6**), the anode current $I_{a1}$ is approximately 1 μA at anode voltage $V_{a1}$ = 55 V and the anode current $I_{a2}$ is approximately 0.17 μA at anode voltage $V_{a2}$ = 50 V on the constant gate voltage line of $V_g$ = 1.05 V. Therefore, the anode resistance $r_a$ is approximately equal to (1-0.17)/(55-50) = 6 MΩ. This anode resistance value can be only used for the operating range of anode voltage from 50 V to 55 V, anode current from 0.17 μA to 1 μA and at gate voltage of 1.05 V.

The anode resistance can also be estimated from the $V_a$-$V_g$ characteristic curve in similar manner as following. From two consecutive $V_a$-$V_g$ characteristic curves with anode voltages $I_{a1}$ and $I_{a2}$, two anode voltages $V_{a1}$ and $V_{a2}$, at the same gate voltage $V_{g1}$, can be attained from these two curves. From the definition, the anode resistance $r_a$ is approximately equal to $(V_{a2}-V_{a1})/(I_{a2}-I_{a1})$. For illustration (**Figure 3.7**), the anode voltage $V_{a1}$ is approximately 50 V at anode current $I_{a1}$= 1 μA and the anode voltage $V_{a2}$ is approximately 47.5 V at anode current $I_{a1}$= 0.4 μA on the constant gate voltage line of $V_g$ = 0.3 V. Therefore, the anode resistance $r_a$ is approximately equal to (50-47.5)/(1-0.4) = 4.17 MΩ. This anode resistance value should be only assumed for the operating range of anode voltage from 47.5 V to 50 V, anode current from 0.4 μA to 1 μA and at gate voltage of 0.3 V.

It is apparent that these graphical methods give different results, largely due to errors in taking data, plotting curves, and reading curves. However, this method is useful for hand calculation and design work and they agree fairly closely with the more exact method, which will be described below.

Direct calculation of triode coefficients from characteristic equation is a more accurate method than the graphical method. This method can be done by performing partial differentiation according to the defining equation of these coefficients on the characteristic equation of triodes Eq. (3.4). By performing partial differentiation according to the definition in Eq. (3.7), the amplification factor of a field emission triode in saturation region ($\alpha$=1) was found to be

$$\mu = 1/\gamma \tag{3.12}$$

According to Eq. (3.12), the amplification factor of a field emission triode is constant independent of gate and anode voltages. However, this is not true for practical real devices because $\gamma$ is not a true constant. It actually weakly depends on gate and anode voltages. The amplification factor of a typical field emission triode calculated using Eq. (3.12) along with $\gamma$ computed by an electrostatic simulation code is plotted as a function of gate and anode voltage in **Figure 3.9** [16]. It can be seen that the amplification factor is approximately an increasing linear function of gate voltage and it linearly decreases as the anode voltage increase. The dependency of amplification factor on anode and gate voltage can be qualitatively explained as followed. As the gate voltage increases, the effectiveness of gate in shielding anode electric field increases because of the stronger gate electric field and thereby the amplification factor increases.

Conversely as the anode voltage decreases the effectiveness of gate in shielding anode electric field increases because of the weaker anode electric field and hence the amplification factor also increases.

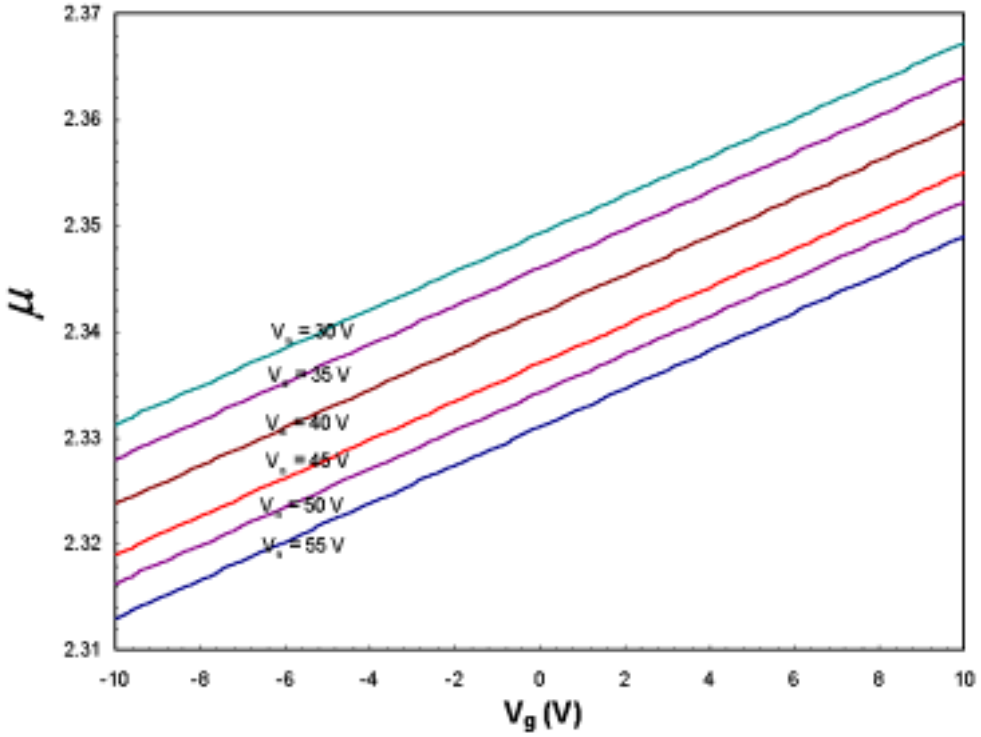


**Figure 3.9.** Amplification factor vs. gate voltage for various anode voltages of the modeled silicon field emitter triode.

By performing partial differentiation on Eq. (3.4) according to the definition in Eq. (3.8), the transconductance of a field emission triode in saturation region ($\alpha$=1) was found to be [16]

$$g_m = \frac{AK_1\beta}{d\Phi}\exp\left\{-\frac{K_2\Phi^{3/2}v(y)d}{\beta(\gamma V_a + V_g + V_0)}\right\}\left[\frac{2\beta(\gamma V_a + V_g + V_0)}{d} + K_2\Phi^{3/2}s(y)\right] \qquad (3.13)$$

**Figure 3.10** shows the transconductance as a function of gate and anode voltages of the modeled field emission triode calculated using Eq. (3.13) [16]. The values of transconductance increase from a very small value at negative gate voltage to a few μS at large positive gate voltages. These transconductances are quite low compared to those typically found in standard thermionic vacuum tubes, which range form a few hundred to over ten thousand μS. The

transconductance can be increased by increasing the number of tip or by decreasing the cathode-gate spacing for a given anode spacing.

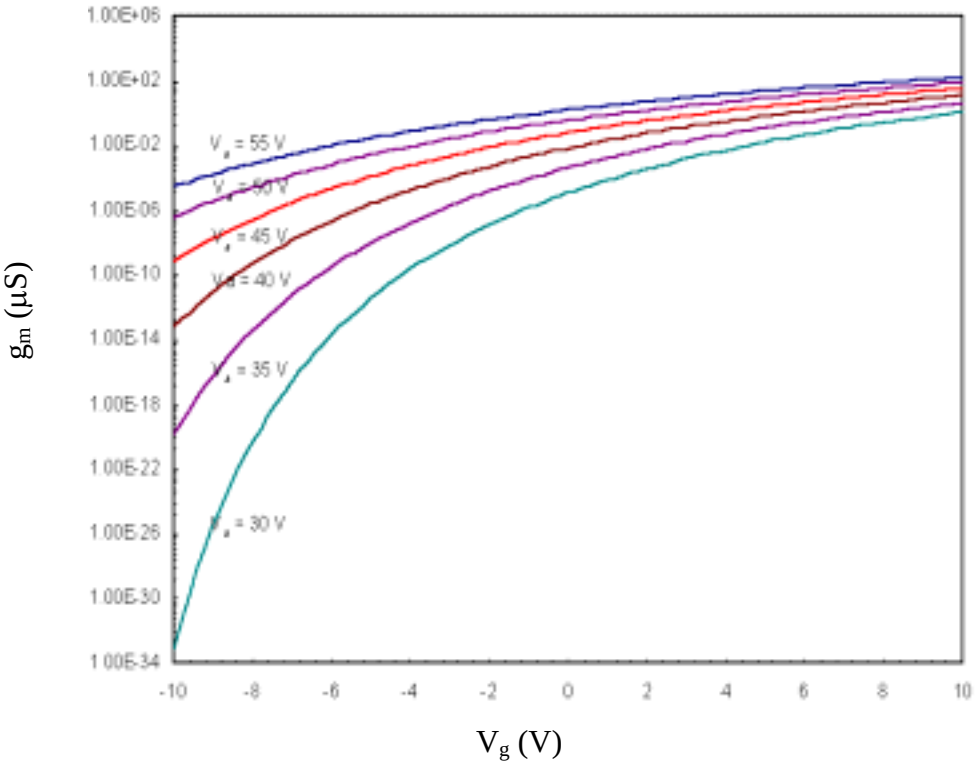


**Figure 3.10.** Transconductance vs. gate voltage for various anode voltages of the modeled silicon field emitter triode.

By performing similar partial differentiation on Eq. (3.4) according to the definition in Eq. (3.9), the anode conductance of a field emission triode in saturation region ($\alpha$=1) was found to be [16]

$$g_a = \frac{AK_1\beta\gamma}{d\Phi}\exp\left\{-\frac{K_2\Phi^{3/2}v(y)d}{\beta(\gamma V_a + V_g + V_0)}\right\}\left[\frac{2\beta(\gamma V_a + V_g + V_0)}{d} + K_2\Phi^{3/2}s(y)\right] \qquad (3.14)$$

The anode resistance is the inverse of the anode conductance as in Eq (3.10). The anode resistance of a typical field emission triode calculated using the inverse of Eq. (3.14) is plotted as a function of gate and anode voltages as shown in **Figure 3.11** [16]. The values of anode resistance decreases from a very large value at negative gate voltage to a few hundred kΩ at large positive gate voltages. These anode resistances are quite large compared to those typically

found in standard thermionic vacuum tubes, which range form a few hundred to over ten kΩ over wide range of operating condition. The anode resistance can be reduced by increasing the number of tip.

To perform the direct calculation method, a complete knowledge of the characteristic equation is required. This includes the value of all coefficients in the equation. Furthermore, the calculation of these coefficients from the characteristic equation of field emission triode is fairly complicated because of the complexity of the characteristic equation (Fowler-Norhiem equation).

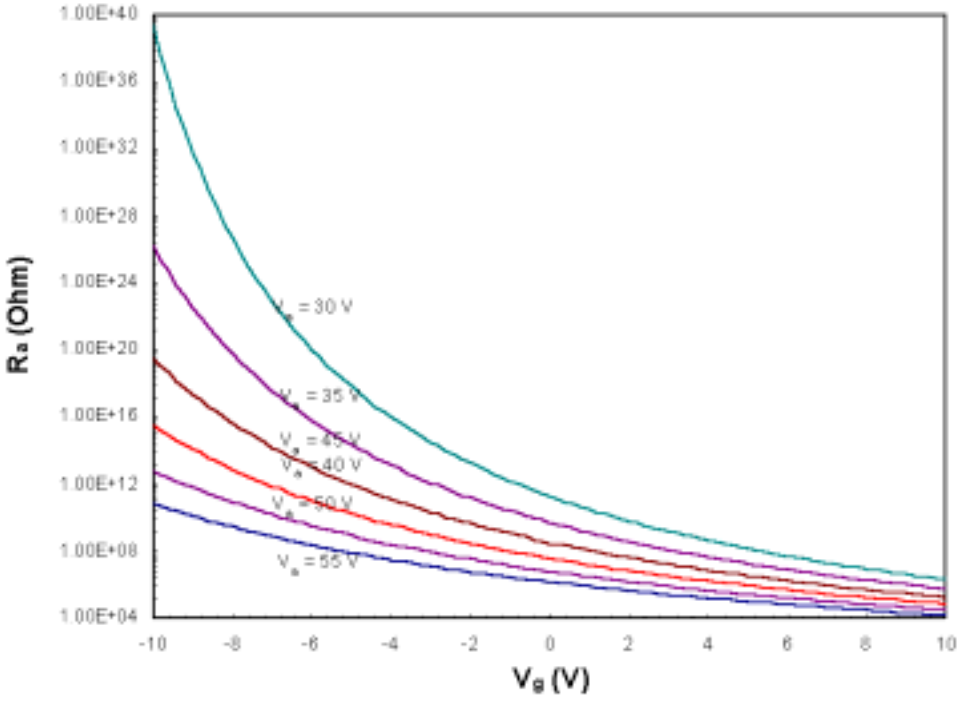


**Figure 3.11.** Calculated anode resistance vs. gate voltage for various anode voltages of the modeled silicon field emitter triode.

Dynamic measurements of coefficient [174] are experimental methods used to determine the true values these coefficients. The direct dynamic measurements, in which alternating current bridge circuit are used, give accurate results that include all non-ideal behaviors of the real devices. Furthermore, a complete knowledge of the characteristic equation is not required and it is less complicated. In performing these measurements, it is important that the following precautions must be taken. First, the value of the alternating voltage should be sufficiently small

that the results are unaffected by a reduction of the applied voltage. Second, the bridge circuit should be arranged such that stray capacitive and inductive couplings do not cause errors or make balancing of the bridge difficult. Third, grounding and shielding of the circuits may be required. Last, it is usually necessary to make allowances for direct-current voltage drops in the bridge circuit so that the correct voltage values are impressed on the electrodes of the triode. A frequency of 1 kHz is very satisfactory for this measurement. This frequency can be readily detected and the bridge balance with an ac ammeter or a simple telephone receiver. It is sufficiently low so that stray coupling usually gives little trouble. Furthermore, since the coefficients are unaffected by the value of the testing frequency, at least up to several MHz, the coefficient determined at 1 kHz are satisfactory for all except very high frequency radio applications. The details of dynamic measurements can be found in the literature [174].

AC equivalent circuit of a triode at low frequency

For low frequency ac amplifier applications, two simple forms of ac equivalent circuits, **Figure 3.12(a)-(b)**, can be used for field emission triode. Both forms can be shown to be equivalent by Thevenin-Norton theorem. A basic application of a triode for a class A amplifier is illustrated in **Figure 3.12(c)**. In operation, an alternating voltage $v_g$ is applied on the gate of the triode. This voltage is then amplified by the amplification factor via the control of gate on anode current. This is equivalent to an induce voltage $\mu v_g$ appear across anode and cathode. This voltage acts in series with the anode resistance $r_a$ and the load resistance $R_L$. The ac current flowing through this simple series circuit is

$$i = \mu v_g /(r_a+R_L) \tag{3.15}$$

Thus, the output ac voltage across the load is

$$v_{out} = i R_L= \mu v_g R_L /(r_a+R_L) \tag{3.16}$$

and the voltage amplification factor $A_v$ for the circuit is

$$A_v == \mu R_L /(r_a+R_L) \tag{3.17}$$

Furthermore, the power output for the circuit is

$$p_{out} = i^2 R_L= \mu^2 v_g^2 R_L /(r_a+R_L)^2 \tag{3.18}$$

Other than this basic amplifier, the equivalent circuit has varieties of applications in other triode circuits such as power amplifier, and modulator.

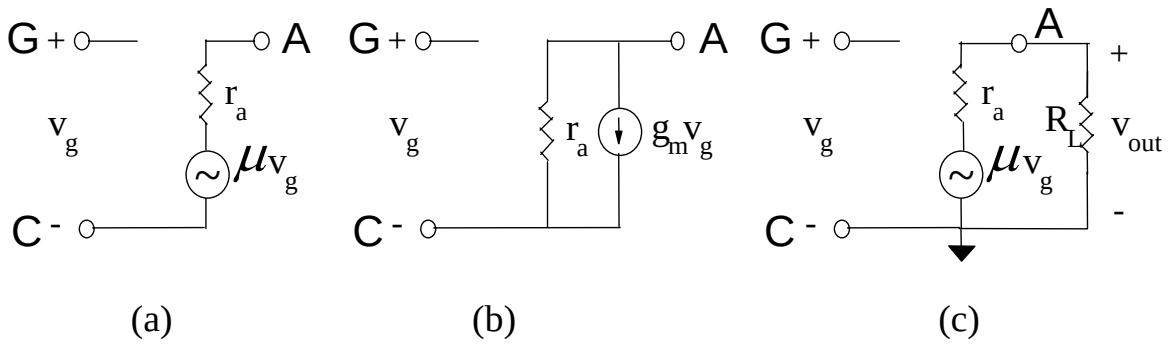


**Figure 3.12.** AC equivalent circuit at low frequency. (a) and (b) A triode. (c) Class A amplifier.

AC equivalent circuit of a triode at high frequency

The complete ac equivalent circuit of a triode for ac amplifier applications at all frequency is shown in **Figure 3.13(a)** [176]. In the circuit, T is the internal node that is supposed to be located at the apex of the cathode. The dependent current source $g_m v_g$ and the anode resistance $r_a$ are described earlier. $R_C$, $R_G$, and $R_A$ represent the line resistances of cathode, gate, and anode, respectively, which are typically less than 10 Ω. $R_{GC}$ is the modeling resistor for leakage current component through the gate dielectric, which is a non-linear resistor and a typical value is 1 GΩ. $R_{GT}$ is the modeling resistor for stray emission current component from cathode to the gate via the gate opening, which is also a non-linear resistor and is typically very large. The resistance of the tip, $R_{tip}$, is the internal resistance of cathode, which may be calculated from geometry and resistivity of the cathode material. $R_{tip}$, is very small for metal tip but is not negligible for other materials.

The gate-tip capacitance, $C_{GT}$, is the capacitance formed by gate electrode, vacuum gap, and tip that can be calculated from the total surface charge induced on the tip by gate voltage, which is equal to the surface integral of the electric flux density due to the gate voltage [177]. Similarly, the anode-tip capacitance, $C_{AT}$, is the capacitance formed by anode electrode, vacuum gap, and tip that can be calculated from the total surface charge induced on the tip by anode voltage, which is equal to the surface integral of the electric flux density due to the anode voltage. The gate-anode capacitance, $C_{GA}$, is the capacitance formed by gate electrode, vacuum gap, and anode electrode, which may be estimated from the gate geometry and the gate-anode spacing. Finally, the gate-cathode capacitance, $C_{GC}$, is the capacitance formed by gate electrode, gate dielectric, and planar portion of the cathode, which may be determined from the gate

geometry and the gate-cathode spacing and $C_{GC}$ is almost independent of bias voltage. $C_{GC}$ is the largest capacitance in the circuit because the gate-cathode spacing is much smaller than anode-gate spacing and the area of flat portion of cathode is large compared to the gate opening area. $C_{GA}$, is the second largest capacitance, which is typically smaller by 1 order of magnitude compared to $C_{GC.}$ $C_{AG}$ and $C_{AT}$ are very small compared to $C_{GC}$ and $C_{GA}$.

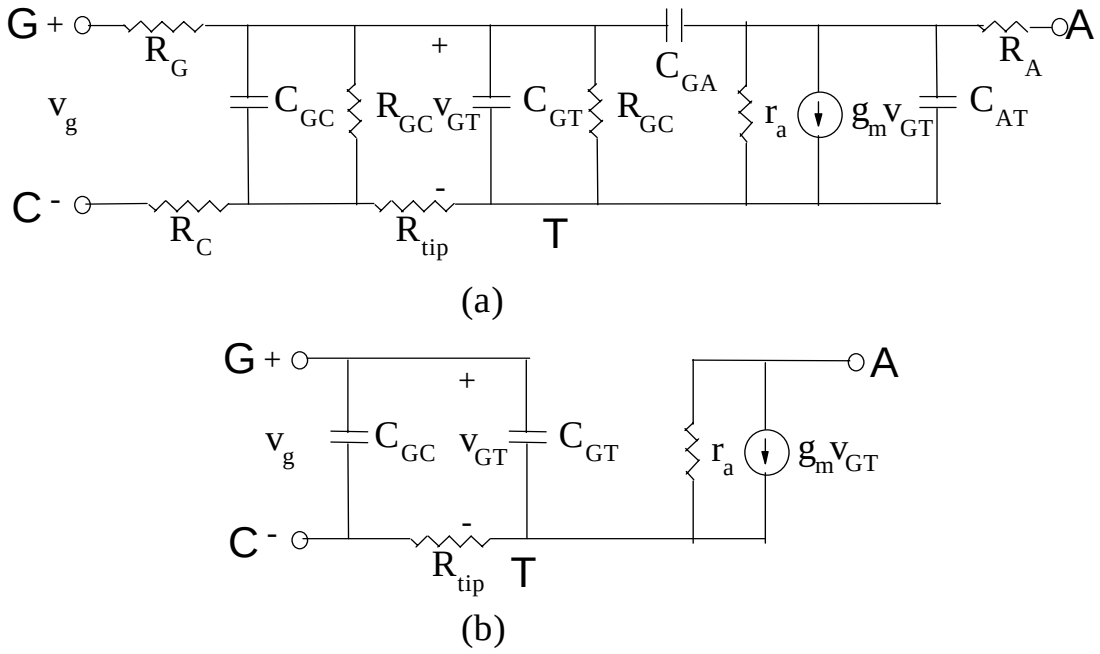


**Figure 3.13.** AC equivalent circuit of a triode. (a) Complete circuit for all frequency. (b) Simplified form for medium high frequency.

In normal operation of triode at a normally high frequency, $C_{GC}$, $C_{GA}$, $R_G$, and $R_C$ are very small, and $R_{GC}$ and $R_{GA}$ are very large so that they can be ignored. Thus, the equivalent circuit of a field emission triode at a medium high frequency can be simplified as illustrated in **Figure 3.13(b)**. From the simplified circuit, it can be seen that the combination of $C_{GC}$, $C_{GA}$, and $R_{tip}$ determines the limit of speed at which the gate voltage can be modulated and the gain attenuation due to the reduction of gate input voltage operating at high frequency.

The key parameter, which determines the maximum operating frequency for small signal amplification, is the cut-off frequency $f_T$. $f_T$ is generally defined as the frequency at which the common source short circuit current gain comes to unity. Using the simplified equivalent circuit, $f_T$ is found to be

$$f_T = \frac{g'_m}{2\pi(C'_{GC} + C_{GT})} \tag{3.19}$$

where $g'_m$ and $C'_{GC}$ are defined as

$$g'_m = g_m + 4\pi^2 f_T^2 R_{tip} C_{GC} C_{GT} \tag{3.20}$$

$$C'_{GC} = C_{GC}(1 + g_m R_{tip}) \tag{3.21}$$

$g'_m$ and $C'_{GC}$ are the corrected values of $g_m$ and $C_{GC}$ because of the tip resistance $R_{tip}$. The deviations of $g'_m$ and $C'_{GC}$ from $g_m$ and $C_{GC}$ are typically less than 1% for normal field emission triode. Thus, in practice the correction may not be necessary. From the equation to the first order, $f_T$ does not depend on the sample area since $g_m$ and $C_{GC}$ are both proportional to the area. Thus a simple increasing in the area and hence the number of tips does not improve $f_T$. There are two simple techniques that can improve $f_T$. The first technique is to optimize $g_m$ by choosing the operating point of higher gate bias voltage. By this technique, $C_{GC}$ does not increase at the same time because it does not depend on gate bias voltage. The other technique is to reduce $C_{GC}$ by reducing the area of flat region of the cathode or in the other word increasing the tip packing density.

Potential applications for field emission diode and triode

Field emission vacuum diode and triode have numerous potential applications in vacuum microelectronics. The vacuum diode and triode can be used as electronic switch, signal or power amplifier, oscillator, modulator, and control devices completely analogous to conventional solid-state p-n diodes and bipolar or MOSFET transistors. However, the field emission vacuum diode and triode have several advantages over solid-state semiconductor devices. First of all, the field emission vacuum diode and triode can operate at a much higher speed than the p-n diode and transistor. This makes them suitable for high frequency applications such as microwave power generation and microwave and plasma electronics [178-179]. In addition, field emission devices are suitable for high current density and high power electronic applications. Metal field emission triodes have shown to be able to operate at high emission current density of $10^{10}$ A/cm$^2$ [9,12]. Diamond field emitters are supposed to be able to operate at even higher current density due to its higher thermal conductivity. Furthermore, radiation does not affect the performance of the

vacuum device because it has no p-n junction. Thus, field emission diode and triode can be used for radiation-hardened devices in space and other hostile environments.

The vacuum diode and triode can be used for a number of applications that require electron gun such as scanning and transmission electron microscopy (SEM, TEM, and STM), electron beam microscopy, electronic lithography, and Auger electron spectroscopy (AES) microprobes [72, 180-181]. A major problem of using cold metal and silicon field emitters as electron guns is the requirement of ultra high vacuum operating condition to ensure emission stability. On the other hand, the use of diamond field emitter as electron gun has been demonstrated high emission stability under relatively low vacuum condition due to its robust material property [70]. This leads to more economical electron microscopes with simplified pumping systems. In addition, since diamond field emitter can operate at low voltage, it can be used as electron gun for low voltage electron microscopy such as low voltage SEM.

Field emission flat panel displays (FEDs) is another potential application of field emission diode and triode [51,182-183]. The application of diamond field emitters for low voltage FEDs has been widely studied [71,82,89-90]. Other potential applications include novel pressure sensors and accelerometers.

# CHAPTER IV

# PROPOSED RESEARCH AND APPROACH

## Proposed Research

The purpose of this research is to develop, for the first time, micropatterned polycrystalline diamond field emission devices operable at low voltage for vacuum microelectronic applications. To achieve this goal, the research has been focused on two main parts. The first part of the research is to develop diamond microtip for use as field emission cathode. This part of the research involves design, fabrication, characterization, and developing practical techniques to enhance and maximize field emission performances of diamond microtips. The second part of the research is to develop monolithic micro-patterned diamond field emission devices, diodes and triodes. This later part of the research includes design, fabrication, characterization, and modeling of monolithic micro-patterned diamond field emission diodes and triodes. The following sections describe the proposed research methods. Details of device fabrications, implementations, and characterization methods will be presented in chapter V.

### Part I: Design and development of diamond microtips for use as field emission cathode

#### Design concept for diamond field emission cathode

An understanding of the physics of diamond field emission is essential for diamond field emitter design. Conceptually, the physics of diamond field emission can be summarized and illustrated in **Figure 4.1**.

For electron field emission from diamond to occur electrons must:

1) Tunnel through the metal-diamond interface. Electron tunneling at the metal-diamond interface depends on the barrier height, $\Phi_b$, and hence the choice of metal contact.

2) Conduction through the diamond layer. The conduction through diamond plays an important role in the diamond field emission characteristics and this conduction is primarily controlled by diamond's composition ($sp^2/sp^3$ and doping).

3) Tunneling through the diamond-vacuum interface. The geometry of diamond emitter controls the electric field and the electron tunneling probability through the diamond-vacuum interface.

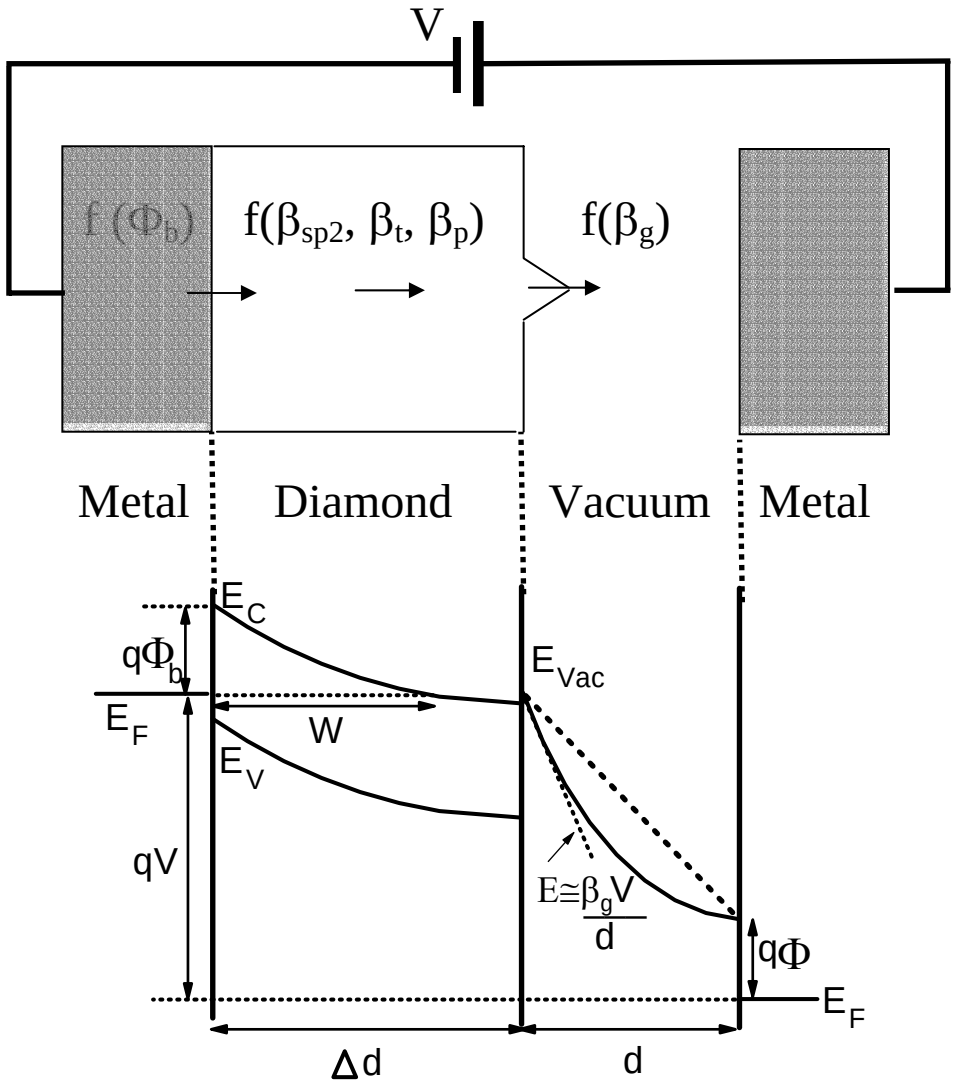


**Figure 4.1.** A summary of the physics of diamond field emission.

The electron emission from the diamond emitters were found to obey the modified Fowler-Nordhiem equation:

$$\mathrm{Ln}(I/E_0^2) = \mathrm{Ln}(A^* K_1 \beta^2/\Phi) - (K_2 \Phi^{1.5}/\beta)(1/E_0) \qquad (4.1)$$

where $K_1$ and $K_2$ are constants, I is the emission current, $\Phi$ is the work function of the emitting surface (in eV), $\beta$ is the total field enhancement factor, A is the emitting area, and $E_0$ is

the macroscopic applied electric field (Volts/cm). $E_0=V_D/d$ where $V_D$ and d are the anode-cathode voltage and spacing, respectively.

Furthermore, we have identified the unique behavior of the total field enhancement factor β of the diamond tip. The β can be expressed as the product of the following field enhancement components:

$$\beta = \beta_g \beta_{sp2} \beta_t \beta_p \quad (4.2)$$

where $\beta_g$, $\beta_{sp2}$, $\beta_t$, and $\beta_p$ are field enhancement components due to the tips' geometry, $sp^2$ content, surface treatment, and boron doping, respectively.

Design of diamond tip parameters

Examining these parameters of the physics of diamond field emission allows one to design an optimized tip structure and composition. An effective way of enhancing diamond electron emission is maximizing the field enhancement factor components, $\beta_g$, $\beta_{sp2}$, $\beta_t$, and $\beta_p$. A systematic approach to improve the diamond emission behavior was conducted.

I. Tip geometry design, $\beta_g$

Diamond microtips were achieved via silicon molding technique [184]. The molding technique can produce well-controlled micro-patterned diamond emitters with a well-defined diamond microtip structure and uniformity over a large area that cannot be achieved by other techniques. Diamond pyramidal microtips have been successfully fabricated by PECVD diamond deposition on inverted pyramidal silicon molds. The inverted pyramidal silicon molds can be reproducibly formed by anisotropic etching of micron-size square patterns on a (100) single crystal silicon wafer. The inverted pyramidal cavity, which comprised of 4 (111) planes of silicon, is the inverted trapezoidal shape with a 70.5° angle at the apex.

The diamond pyramidal microtips with normal trapezoidal geometry having quite large angle and radius curvature at the apex and thus have low geometrical field enhancement factor. With such a low geometrical field enhancement factor, optimum emission characteristics from diamond microtips may not be achieved. Thus, pyramidal microtips with sharper apex should be designed to increase the geometrical field enhancement factor, hence improving field emission characteristics.

Pyramidal diamond tips with sharp apex have been designed utilizing mold sharpening technique. The sharpened silicon mold can be fabricated by dry thermal oxidation of the

anisotropic etched silicon cavities. Sharpened diamond tips having very sharp apex and small radius curvature of 5 nm have been successfully fabricated. The results of the effect of tip geometry on diamond field emission will be presented in chapter VI.

II. $sp^2/sp^3$ composition control, $\beta_{sp2}$

The $sp^2/sp^3$ composition in diamond film can be controlled by varying PECVD process parameters. The most critical process parameter that controls $sp^2$ formation in diamond film is the ratio of methane ($CH_4$) to hydrogen ($H_2$) concentration. The higher the $CH_4/H_2$ ratio, the higher the $sp^2$ content incorporated into the diamond film. A systematic study on the effect of $sp^2/sp^3$ composition on diamond field emission was performed. The results of the effect of $sp^2/sp^3$ composition on diamond field emission will be presented in chapter VI.

III. Tip treatment, $\beta_t$

The vacuum-thermal-electric (VTE) treatment is a post-fabricated treatment in which the diamond microtips were simultaneously treated at low emission current under moderate heat and applied electric field. The results of the effect of VTE treatment on diamond field emission will be presented in chapter VI.

IV. Doping of diamond microtips, $\beta_p$

Incorporation of boron dopant in diamond tips changes the diamond bulk conductivity. The effect of boron dopants on the field emission characteristics of micropatterned diamond microtips has been investigated. Boron doping was performed *in-situ* by the introduction of solid boron source during PECVD diamond growth process. The results of the effect of p-type doping on diamond field emission will be presented in chapter VI.

Part II: Design and development of monolithic diamond vacuum diodes and triodes

Design of monolithic diamond vacuum diodes

A monolithic micro-patterned diamond vacuum diode can be achieved by integrating diamond microtips with a built-in anode (gate). There are two main configurations of built-in anode: planar suspended anode and self-aligned anode.

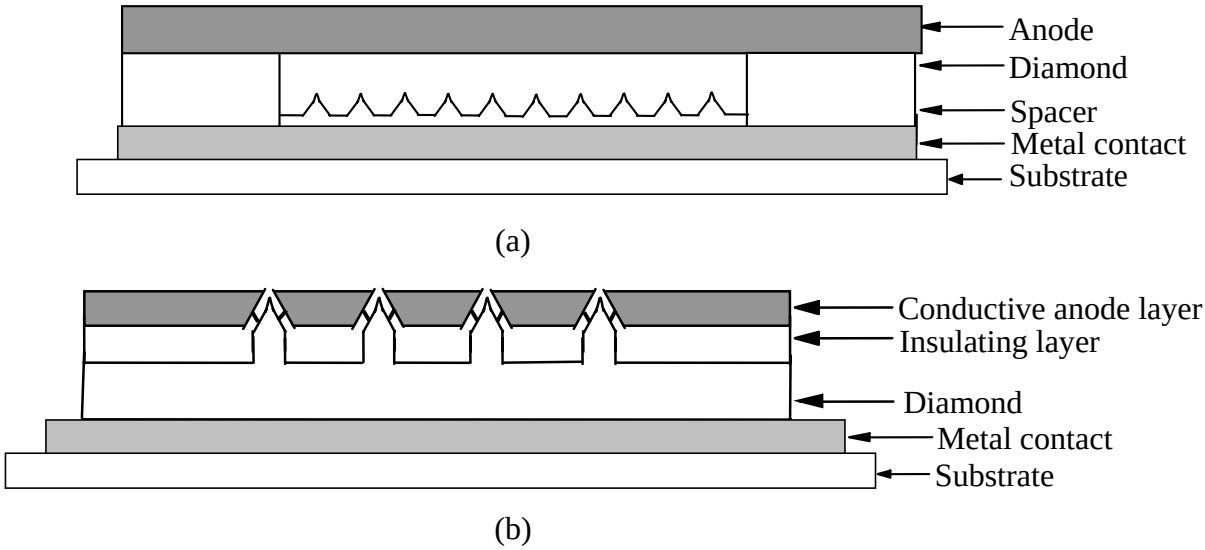


**Figure 4.2.** Monolithic diamond vacuum diode with (a) planar suspended anode and (b) self-aligned anode.

For the first case, a planar anode is aligned and placed directly over the diamond tips via a solid spacer as illustrated in **Figure 4.2(a)**. A cap anode attached via electrostatic bonding technique has been constructed to achieve this type of monolithic diamond diode. A major problem in achieving this type of monolithic diamond diode is the coplanar alignment of the anode-cathode spacing.

For the self-aligned anode case, an anode that is normally a layer of conductive material is self-aligned to the diamond tips via an insulating layer as illustrated in **Figure 4.2(b)**. This structure is also called “gated diode” because the self-align conductive layer can also be used as the gate of a triode. Self-align volcano process and self-align gate molding have been employed to accomplish monolithic diamond field emission diodes with built-in anode. The detail fabrication process will be present in Chapter V.

The key parameter for diamond vacuum diode design is the turn-on voltage. For most applications, the turn-on voltage should be as low as possible. Since the turn-on voltage depends on the turn-on electric field of diamond cathode and the anode-cathode spacing, it is desired that diamond cathode with low turn-on electric field and small anode-cathode spacing be fabricated. Diamond cathode with low turn-on electric field, as discussed previously, can be achieved by a

proper design of diamond cathode with a high field enhancement factor (β). Anode-cathode spacing of less than a micron can be realized with the self-align fabrication techniques.

Design of monolithic diamond vacuum triodes

Monolithic micro-patterned diamond triode can be achieved by integrating gated diamond emitters with an anode via a spacer as illustrated in **Figure 4.3**. An important parameter for diamond vacuum triode design is the gate turn-on voltage. For most practical applications, the gate turn-on voltage is desired to be small. Similar to diamond vacuum diode, the gate turn-on voltage relies on the turn-on electric field of diamond cathode and the gate-cathode spacing. Proper diamond cathode design and self-align fabrication techniques are the approaches to achieve the desired goals. We achieved micro-patterned diamond vacuum triodes with a low operating voltage and high emission current by these approaches.

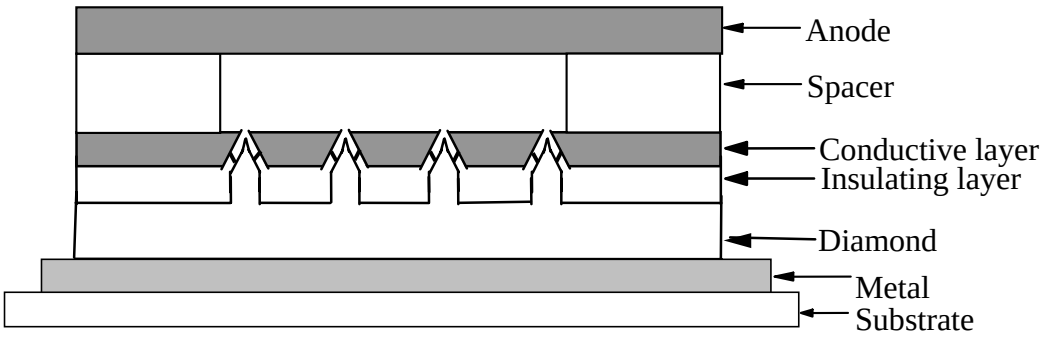


**Figure 4.3.** Monolithic diamond vacuum triode.

Other important parameters for diamond vacuum triode design are amplification factor and transconducance. Amplification factor determines the ultimate voltage gain and transconductance signifies current driving capability when a diamond triode is operated as an amplifier. For transistor application, the amplification factor and transconductance are desired to be high. To achieve high amplification factor, gate-anode spacing and the gate positioning must be properly chosen such that cathode is effectively shield from the anode by the gate but anode potential is still capable of collecting all electrons emitted from the cathode. High emission current at low gate voltage from diamond triode is the key requirement to achieve high

transconductance. High transconductance can be achieved by proper design and high packing density of diamond triode structure.

# CHAPTER V

## DEVICE FABRICATION AND EXPERIMENTATION

This chapter describes various fabrication processes developed for achieving diamond field emission cathodes, diodes, and triodes. This chapter also presents field emission characterization methods for the fabricated devices.

### Fabrication of the micro-patterned diamond field emission cathode

Two types of diamond field emission cathode structures have been successfully fabricated, the pyramidal microtip and the pyramidal microtip with sharpened apex.

#### I. Mold transfer technique for fabrication of pyramidal diamond microtips

The fabrication scheme of pyramidal diamond microtips is shown in **Figure 5.1**. First, a 0.2 μm $SiO_2$ layer was grown on (100) silicon wafer. Conventional photolithographic patterning was then used to define a mask array of diamond microtips. The base width of pyramidal microtip was defined by a square pattern of 2 μm x 2μm. Next, $SiO_2$ in the pattern was etched away by buffered oxide etching (BOE) solution. To form an inverted pyramidal structure, the silicon wafer was anisotropically etched with an etch-stopped process using potassium hydroxide: normal propanol:deionized water solution. Due to anisotropic etching behavior of KOH solution, the etching rate on silicon (111) plane is smaller than that on (100) plane and hence an inverted pyramidal cavity that comprised of four (111) planes was formed. The remaining $SiO_2$ was then removed by the buffered oxide etch (BOE) solution. Next, diamond was deposited in and on the inverted pyramidal silicon mold by plasma enhanced chemical vapor deposition (PECVD). Finally, the silicon mold was completely etched away by HF:$HNO_3$ etching solution and micropatterned polycrystalline pyramidal diamond microtips were obtained.

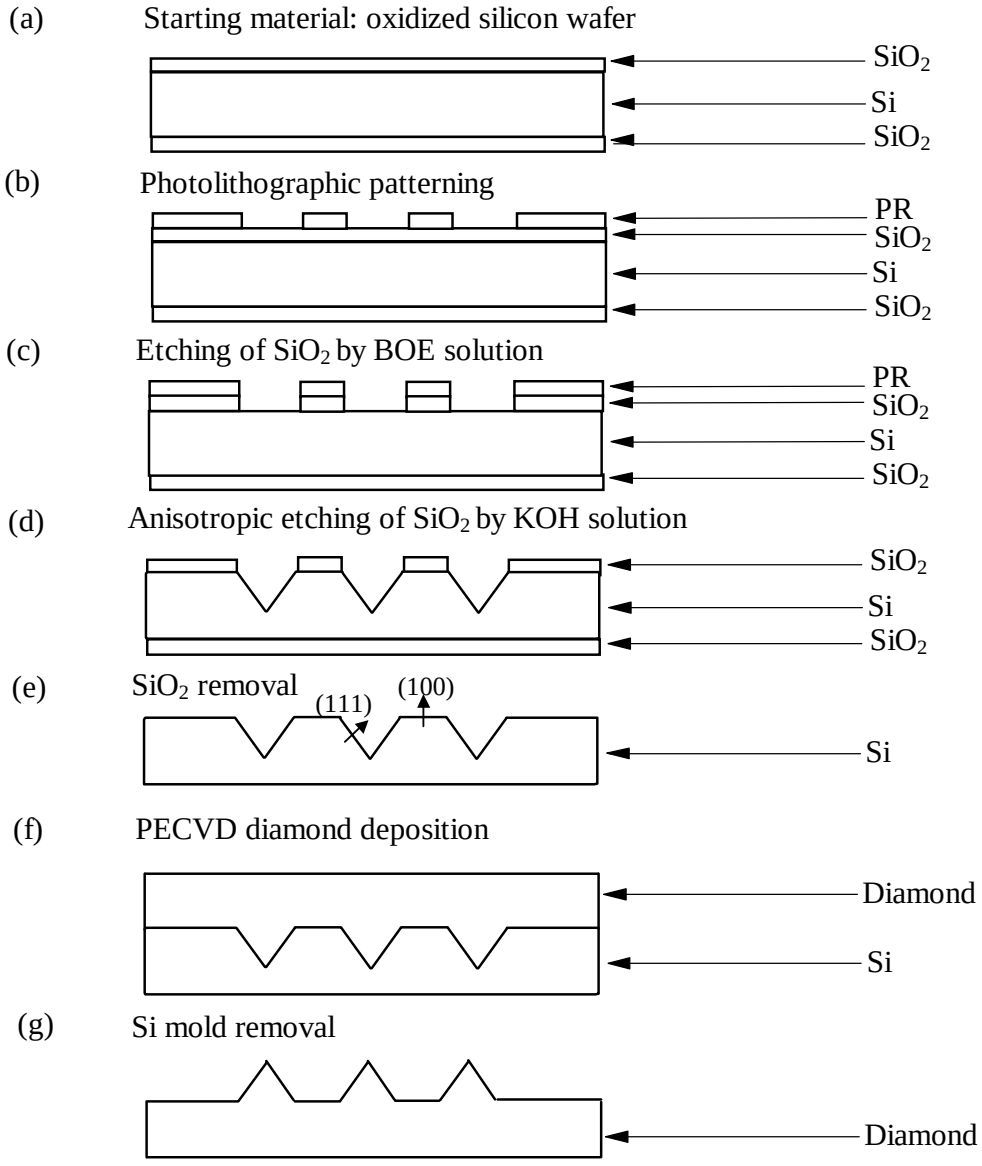


**Figure 5.1.** The fabrication process of pyramidal (trapezoidal) diamond microtips

In order to study diamond-processing parameters on field emission characteristic of diamond tips, PECVD fabrication parameters were varied to obtain diamond tips with different $sp^2/sp^3$ compositions and doping concentrations. The most critical process parameter that controls $sp^2$ content formation in diamond film is the ratio of methane to hydrogen concentration. The higher methane concentration, the higher $sp^2$ content in diamond film was obtained. The second critical process parameter that controls $sp^2$ content formation in diamond film is the microwave power level. The microwave power determines the power of the hydrogen plasma.

The higher power of hydrogen plasma, the more $sp^2$ etching occurs. The substrate temperature also has an effect on $sp^2$ formation in diamond film. A low substrate temperature was used for all-$sp^2$-content steps in order to prevent the secondary effect of hydrogen plasma etching. Lastly, the chamber pressure also affects $sp^2$ formation in diamond film. The higher pressure, the more $sp^2$ etching by the hydrogen plasma occurred because the plasma was condensed by pressure so that its effective power increased. Boron doping was performed *in-situ* by gas or solid boron source during PECVD diamond growth process.

For this investigation, five types of diamond films with different $sp^2$ contents and doping conditions were grown on the silicon mold: i) undoped diamond film with no $sp^2$ content, ii) undoped diamond film with trace $sp^2$ content, iii) undoped diamond film with low $sp^2$ content, iv) p-type diamond film with trace $sp^2$ content, and v) p-type diamond film with low $sp^2$ content. The detailed processing parameters of each type of film are proprietary information of Vanderbilt diamond technology laboratory.

II. Mold sharpening technique for fabrication of pyramidal diamond microtips with ultra sharp apex

The fabrication scheme of pyramidal diamond microtip with ultra sharp apex is shown in **Figure 5.2**. After the inverted pyramidal cavities in Si were formed by anisotropic etching as previously described in the mold transfer process, a 0.2 μm thick $SiO_2$ layer was then thermally grown on the pyramidal cavities by dry thermal oxidation for inverted apex sharpening. This ultra-sharp apex occurs because the thermal oxidation rate on the (111) planes of the inverted pyramidal silicon surface is faster than that on the (100) plane of the silicon base and the oxidation rate at the apex is smallest due to limited oxidation reaction in this confined region. Next, diamond was deposited in and on the sharpened inverted pyramidal mold by PECVD. Finally, the mold was completely etched away by $HF:HNO_3$ solution to obtain pyramidal diamond microtips with ultra sharp apexes.

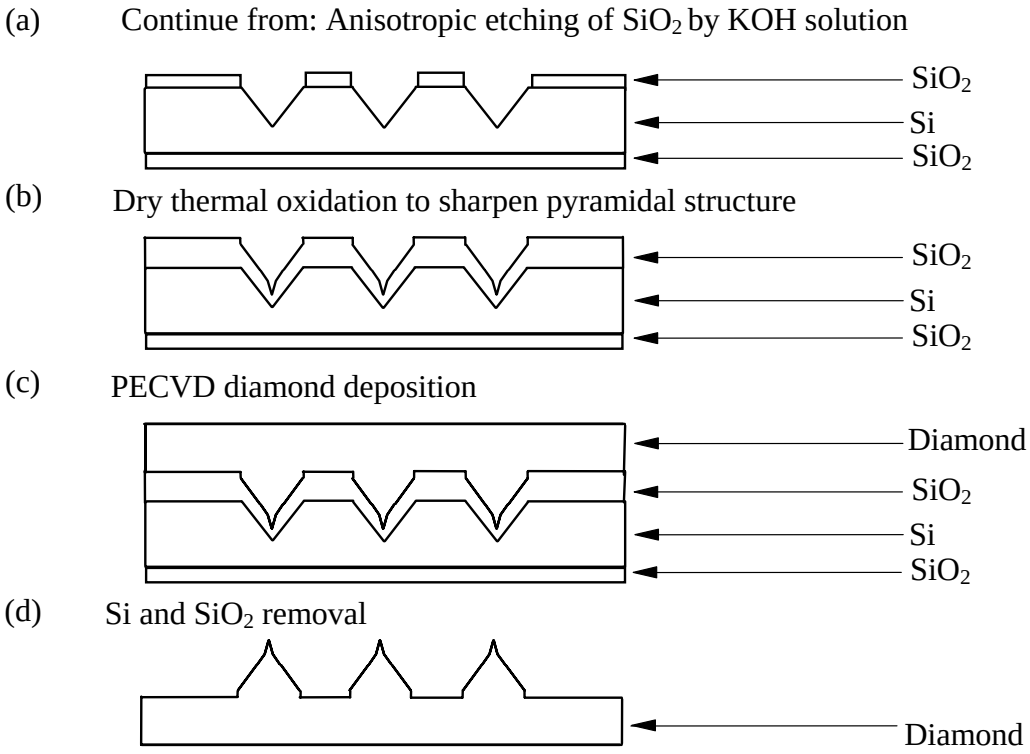


**Figure 5.2.** The fabrication process of pyramidal diamond microtips with ultra sharp apex.

Fabrication of monolithic diamond vacuum diodes

Five fabrication methods for monolithic diamond vacuum diode structures have been explored and developed: i) capped vacuum diode by electrostatic bonding technique, ii) diamond vacuum diode by self-aligned volcano anode technique, iii) self-align-anode-molding technique utilizing standard silicon wafer, iv) self-align-anode-molding technique utilizing epitaxial wafer, and v) self-align-anode-molding technique utilizing SOI wafer.

I. Capped vacuum diode by electrostatic bonding technique

The fabrication process of capped diamond vacuum diode by electrostatic bonding is shown in **Figure 5.3**. First, micropatterned diamond field emitter arrays were fabricated by PECVD diamond deposition in and on the inverted pyramidal silicon mold as previously described. Next, a metal layer was deposited on the diamond film and bonded to a glass substrate via a metal layer by electrostatic bonding technique with an applied voltage of 800 V at 300 °C. The silicon mold was then completely etched away. An anode (cap) comprised of heavily doped

silicon was then prepared by photolithographic $SiO_2$ masking and silicon anisotropic etching techniques. The conventional ethylenediamine (EDP) etching solution was used for silicon anisotropic etching. To complete construction of the capped diamond field emitter diode, the silicon anode was electrostatically bonded to the glass substrate via the $SiO_2$ dielectric layer. The electrostatic bonding was conducted at an applied voltage of 500 V at 200 °C in an open environment. The emitter-anode spacing was designed to be 2 μm.

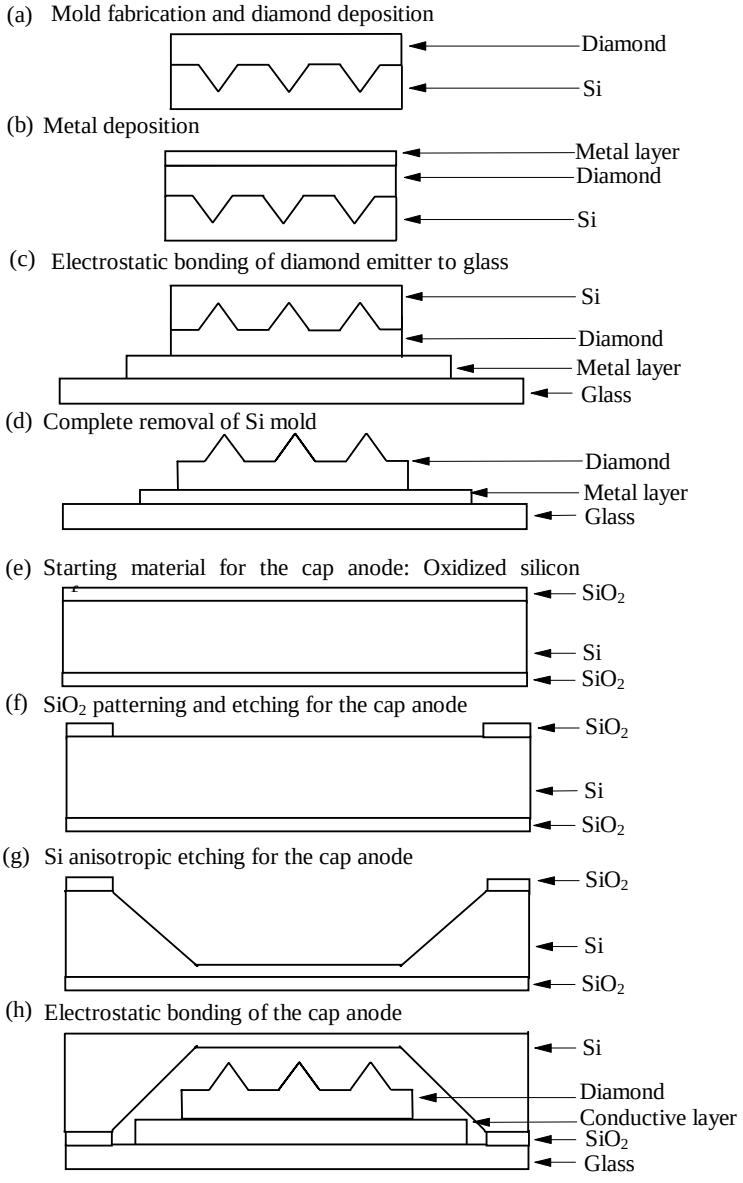


**Figure 5.3.** The fabrication process of capped vacuum diode by electrostatic bonding technique.

II. Diamond vacuum diode by self-aligned volcano anode technique

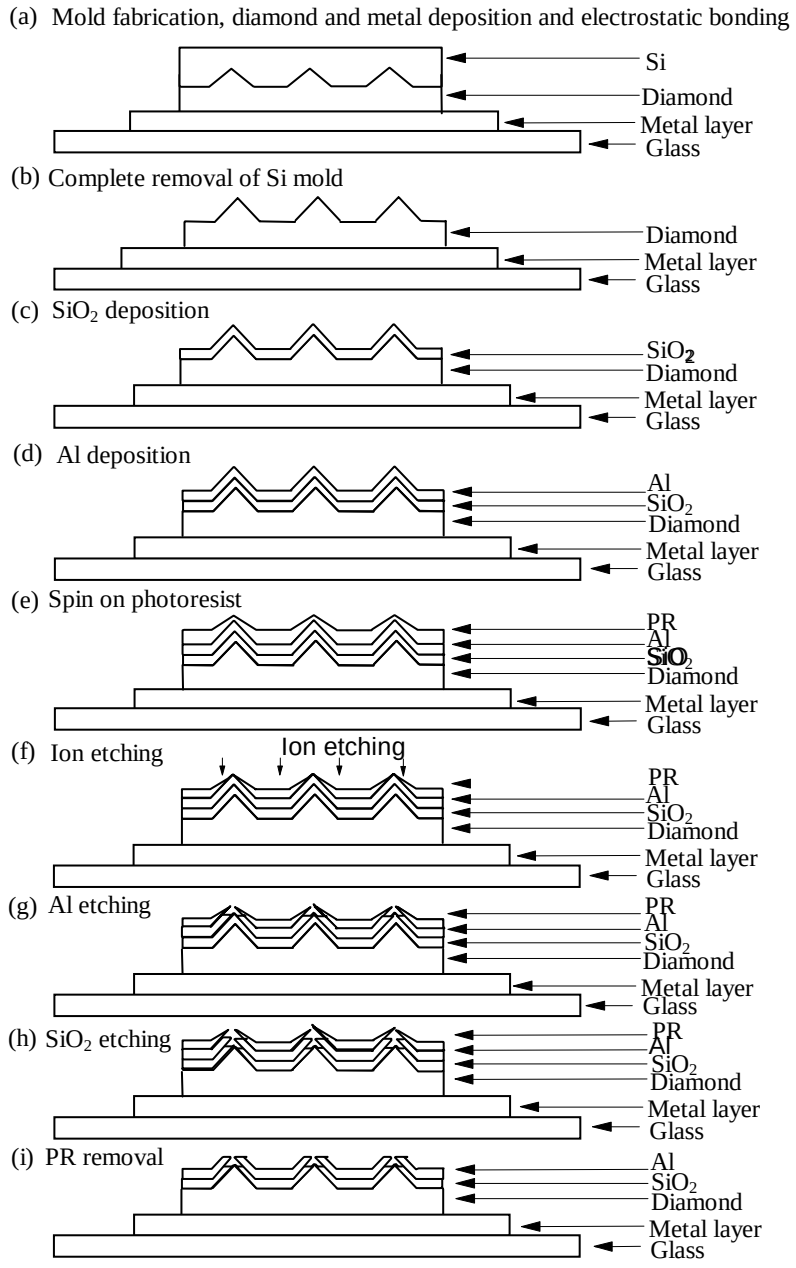


**Figure 5.4.** The fabrication process of diamond vacuum diode with self-aligned volcano anode.

The fabrication scheme of diamond vacuum diode with self-aligned volcano anode is shown in **Figure 5.4**. First, micropatterned diamond field emitter was fabricated from PECVD diamond deposition in and on the silicon mold as previously described. Next, the diamond field

emitter was bonded to a glass substrate via a metal layer and the silicon mold was then etched away. To construct the self-aligned volcano anode, a 1 μm-thick $SiO_2$ as an insulating spacer and a 1 μm-thick Al as an anode layer were subsequently deposited on the diamond field emitter. Photoresist (PR) was then spun on the Al layer. Next, PR was partially etched by ion-etching technique to expose the tip apexes. Finally, Al and $SiO_2$ at the tip apexes were etched away to complete the construction of the self-aligned volcano anode structure with $SiO_2$ as the anode-cathode dielectric and Al as the anode.

III. Self-align-anode-molding technique utilizing standard silicon wafer

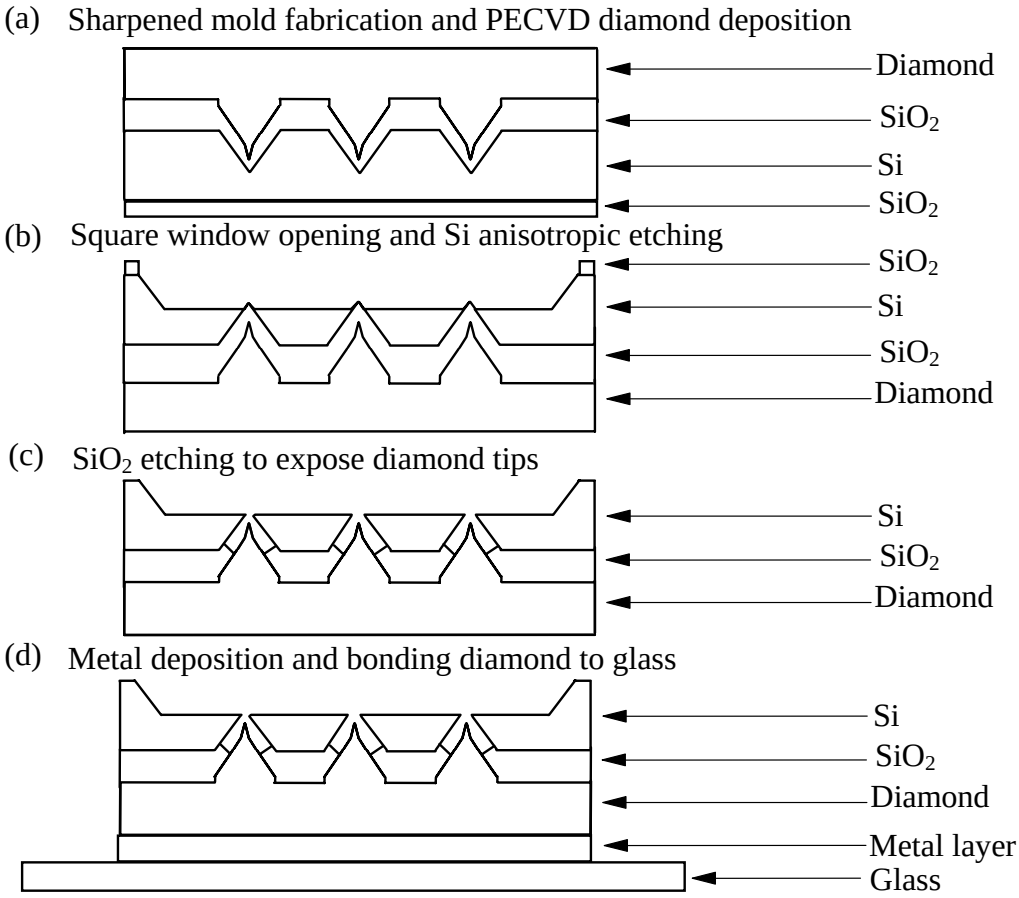


**Figure 5.5.** The fabrication process of self- align-anode-molding technique utilizing standard silicon wafer.

The fabrication scheme of the self-align-anode-molding technique is shown in **Figure 5.5**. First, PECVD diamond was deposited in and on the $SiO_2$ inverted pyramidal cavities as previously described. A square window was then opened on the backside of the mold and silicon was then anisotropically etched by ethylenediamine (EDP) solution until $SiO_2$ covered diamond apexes were exposed. Finally, the $SiO_2$ near the apex region was etched away to expose the naturally sharpened diamond tips. The remaining $SiO_2$ and Si form dielectric spacer and anode, respectively. To provide support and electrical contact, the diamond field emitters were bonded to a glass substrate via a conductive layer.

IV. Self-align-anode-molding technique utilizing epitaxial silicon wafer

The fabrication diagram of diamond vacuum diode with self- aligned silicon anode utilizing epitaxial silicon wafer is shown in **Figure 5.6**. For this fabrication, specifically design epitaxial wafer was used as the starting material. The epitaxial wafer comprises of 2.2 μm-thick (100) n-type silicon epitaxial layer with resistivity of 0.02 Ω-cm on (100) p-type silicon substrate with resistivity of 10 Ω-cm and thickness of 525 μm. A 0.2 μm-thick $SiO_2$ layer was then grown on the wafer surface. Inverted pyramidal cavities were then formed on the Si active layer (as anode layer) by photolithographic patterning of square patterns on 0.2 μm-thick $SiO_2$ layer and anisotropic etching of Si as previously described in the molding process. The square patterns were sized such that the apex of inverted pyramidal cavities would be protruded into the p-type substrate as illustrated in **Figure 5.6 (c)**. A high quality 1 μm thick silicon dioxide layer as a dielectric spacer was then grown on the silicon inverted pyramidal mold using dry thermal oxidation, which concurrently produced well-sharpened apex on the inverted mold as previously described. Next, diamond was deposited by plasma enhance chemical vapor deposition (PECVD) on the $SiO_2$ inverted pyramidal mold. The p-type silicon substrate was then selectively etched away by electrochemical etching in KOH solution.

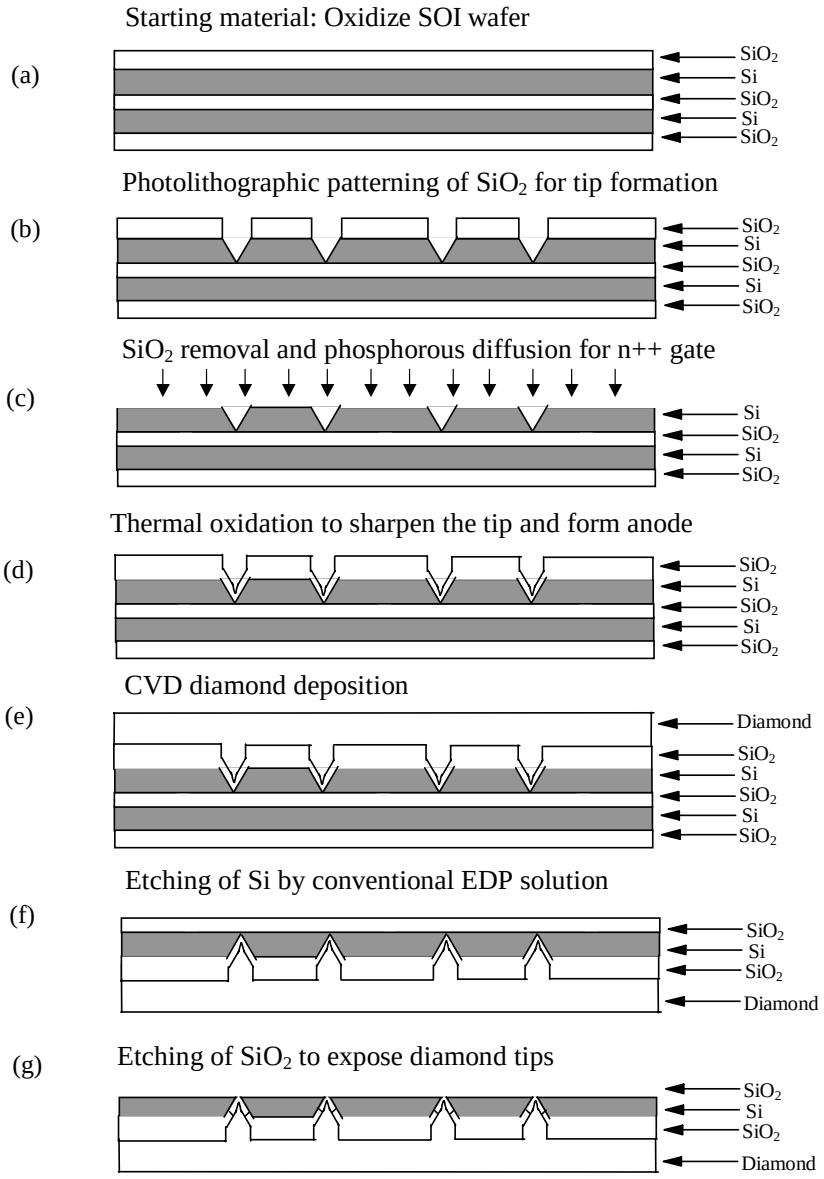


**Figure 5.6.** The fabrication diagram of the self- align-anode-molding technique utilizing epitaxial silicon wafer.

An experimental scheme for electrochemical etching is shown in **Figure 5.7**. The designed electrochemical etch-stop technique utilizes anodic passivation characteristics of silicon with a reverse-bias p-n junction to provide a large etching selectivity of p-type silicon over the n-type in anisotropic etchant such as KOH or EDP. The etching is designed to stop at the well-defined p-n junction. A positive bias voltage is applied directly to the n-type silicon via an ohmic electrical contact while the electrical contact to the p-type silicon is accomplished via the etching solution with an appropriated counter electrode (CE). Since the majority of potential

drop is across the reverse-biased p-n junction, the p-type silicon remains at open circuit potential (OCP) and is etched. When the p-type silicon is completely removed, the diode is destroyed and the n-type silicon becomes directly exposed to the etch solution. The positive potential applied to the n-type silicon passivates the etching by forming a thin oxide layer and the etching terminates. Samples were specially prepared in order to obtain a direct electrical contact to the n+ epitaxial layer. The molding sample was masked with a small silicon stripe during PECVD diamond deposition such that diamond grew everywhere except the thin stripe placed on the edge of the sample. The exposed $SiO_2$ layer of the diamond covered $n^+$ silicon layer was then etched away to make electrical contact to $n^+$ silicon. The sample was then mounted in a U-shape tube fixture. Viton O-rings, Teflon tapes, and Vinyl caps were used to seal the sample from the solution and the electrical contact was achieved by attaching a thin aluminum wire to the $n^+$ epitaxial layer on the backside.

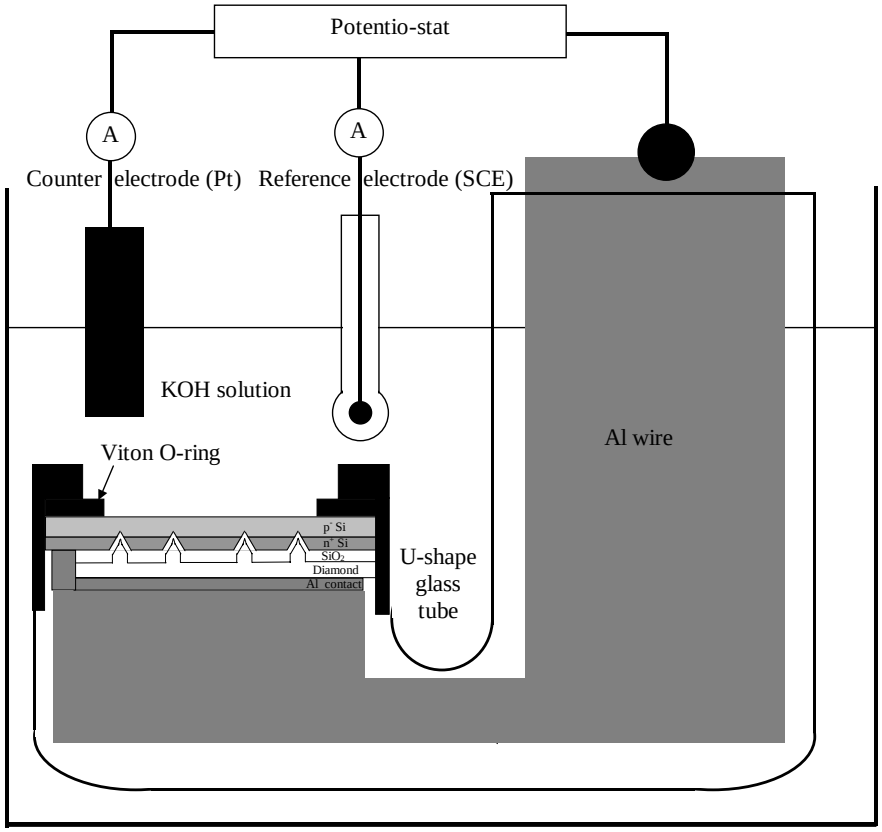


**Figure 5.7.** Schematic apparatus for electrochemical etching of gated diamond emitter on epitaxial silicon based wafer.

The sample in the U-shape tube fixture along with additional 2 electrodes: saturated calomel reference electrode (SCE) and a platinum counter electrode (CE) were then immersed into the KOH solution (40%). The sample and the electrodes are connected to a potentiostat as illustrated in **Figure 5.7**. In this three-electrode configuration, the SCE was included in order to stabilize the solution potential, which would be ill-defined and current dependent if only CE was used. The current through the CE was adjusted by the potentiostat to zero the SCE current. The interface potential of SCE with solution was stabilized because SCE was made currentless and having high input impedance. The etching was performed at 60 °C and the SCE current was monitored during etching process. SCE current determines the condition for etch-stop. During substrate etching, SCE current is at some low value. When etch-stop junction is reached, the SCE current increases for a short period of time and then reduces to a lower value than that observed during the substrate etching. After etch-stop was accomplished, the sample was disconnected from the setup and proceed for $SiO_2$ etching to expose the sharpened diamond pyramidal apexes. The remaining $SiO_2$ and n-type epitaxial silicon layers form the dielectric spacer and the anode, respectively.

V. Self-align-anode-molding technique utilizing SOI wafer

The fabrication diagram of self-align-anode-molding technique utilizing SOI wafer is shown in **Figure 5.8**. The fabrication process begins with wafer bonding of two pieces of oxidized (100) silicon wafers followed by etchback and electropolishing. The resulting SOI wafer is comprised of 2.2 μm-thick silicon active layer, 1 μm-thick $SiO_2$ layer, and 525 μm-thick silicon substrate. A 0.2 μm-thick $SiO_2$ layer was then grown on the wafer surface. Inverted pyramidal cavities were then formed on the silicon active layer (as anode layer) by photolithographic patterning and anisotropic etching of silicon using KOH solution. The square patterns are sized such that complete inverted pyramidal cavities are formed within the silicon active layer. To achieve highly conductive silicon anode, the silicon active layer was diffused with phosphorous using spin-on doping process at 1050 °C. The resulting gate resistivity of less than $10^{-3}$ Ω-cm was achieved. Next, a silicon dioxide layer was grown on the active silicon layer to form the gate dielectric, which concurrently produces a well-sharpened apex on the inverted pyramidal $SiO_2$ layer. And the growth proceeded until it touched the embedded 1 μm-thick $SiO_2$ layer (as the etch-stop layer). Diamond was then deposited on the mold by plasma enhanced

chemical vapor deposition (PECVD). The PECVD fabrication parameters were controlled to achieve a small but deliberate $sp^2$ content in the diamond film. Next, the backside of the silicon was etched away and stopped at the embedded $SiO_2$ layer. Finally, the $SiO_2$ layer was etched and the sharpened diamond pyramidal apexes were exposed. However, a slight thinning down of silicon gate layer may be performed to adjust and optimize the gate opening. The remaining $SiO_2$ and silicon form the dielectric spacer and the gate, respectively.

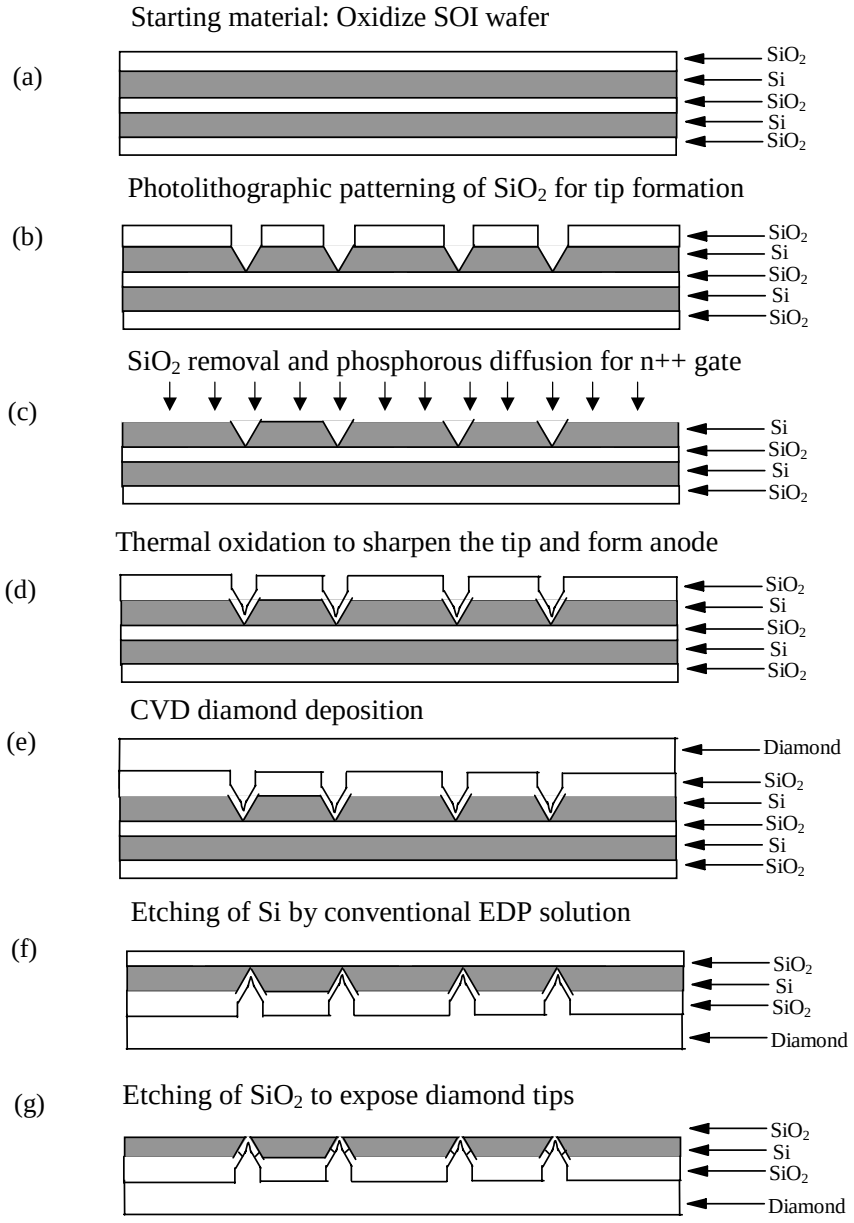


**Figure 5.8.** The fabrication diagram of the self-aligned anode diamond field emitter utilizing SOI wafer.

Fabrication of monolithic diamond vacuum triode

Two fabrication methods for micro-patterned diamond vacuum triode structures have been explored. First, electrostatic bonding technique was used to obtain a self-align gated triode with a cap anode structure. Subsequently, integrated anode utilizing SOI bulk layer was investigated to achieve self-align gated diamond emitters with an integrated suspending anode.

I. Cap-anode electrostatic bonding technique on gated diamond emitter

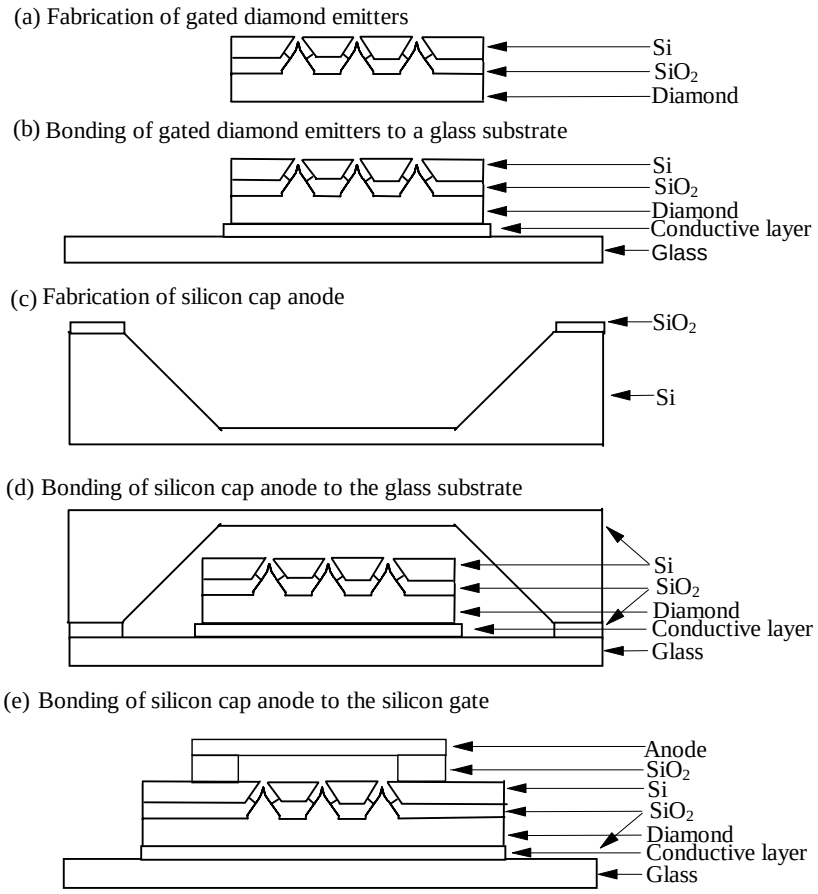


**Figure 5.9.** The fabrication process of diamond field emitter triode with a cap anode.

This technique is similar to that of capped diodes. The only difference is that ungated diamond emitter is replaced with gated diamond emitter. The fabrication process of a self-align gated triode with electrostatic bonded cap anode is shown in **Figure 5.9**. Upon the fabrication of self-align gated diamond field emitters, the gated diamond tips were bonded to a glass substrate.

Next, an anode (cap) comprised of heavily doped silicon described previously was electrostatically bonded to the glass substrate via the $SiO_2$ dielectric layer over the self-align gated diamond field emitter as shown in **Figure 5.9 (d)**. The emitter-anode spacing was designed to be 50-100 μm. Alternatively, a cap anode may be bonded directly on the silicon gate layer as shown in **Figure 5.9 (e)**. The second configuration is preferred for better anode-cathode co-planarity.

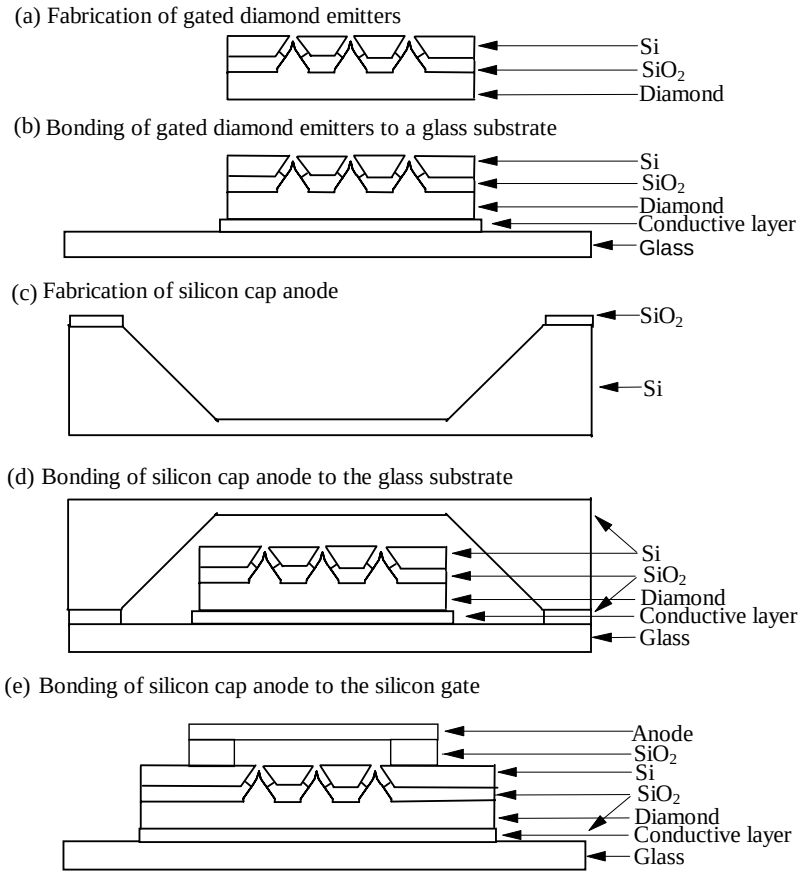


**Figure 5.9.** The fabrication process of diamond field emitter triode with a cap anode.

II. Integrated anode utilizing SOI bulk layer

The fabrication scheme of self-align gated diamond field emission triode with self-aligned anode utilizing SOI bulk layer is shown in **Figure 5.10**. The fabrication process begins with PECVD diamond deposition on sharpened SOI molds described previously. Next, $SiO_2$ layer on the backside was patterned and etched. The pattern should be aligned such that the opening areas are the regions between tips arrays. Si bulk layer was then anisotropically and selectively etch-stopped at the $SiO_2$ embedded layer by EDP solution. Finally, the $SiO_2$ embedded layer was laterally etched to exposed the sharpened $SiO_2$-covered diamond tips. The remaining $SiO_2$ embedded layer and silicon bulk form the anode-gate spacer and the suspended anode, respectively.

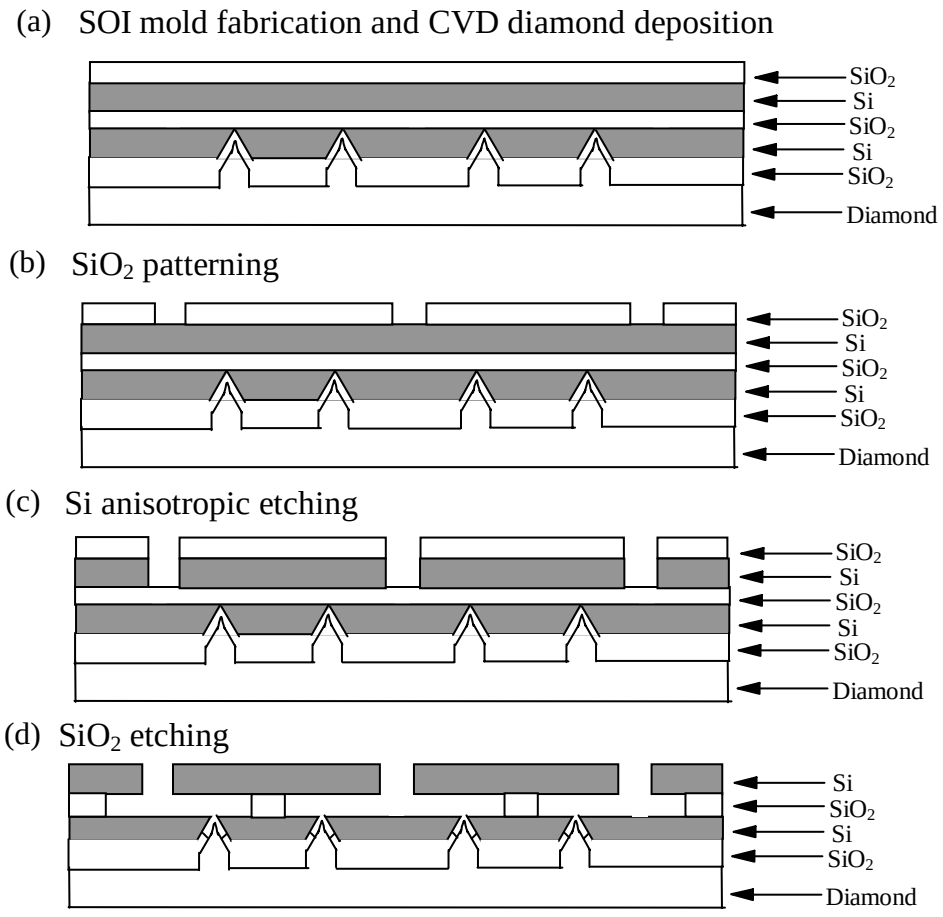


**Figure 5.10.** The fabrication process of self-align gated diamond field emitter triode with built-in anode utilizing SOI bulk layer.

Device characterization techniques

Emission characterization of diamond microtips and diamond vacuum diodes

Emission characteristics of diamond microtips were investigated in diode configuration with an external phosphorous anode as shown in **Figure 5.11(a)**. The phosphorous anode was used to confirm electron emission by observing the light generated on the screen. The insulating spacers (Kapton or Teflon) with thickness of 30 μm or 15 μm were used in this experiment. The anode-cathode spacing was determined by the spacer thickness. The glass slide coated with metal was used for electrical contact and support. For monolithic diamond vacuum diode, as-fabricated device was ready to test and the anode-cathode spacing was measured by SEM.

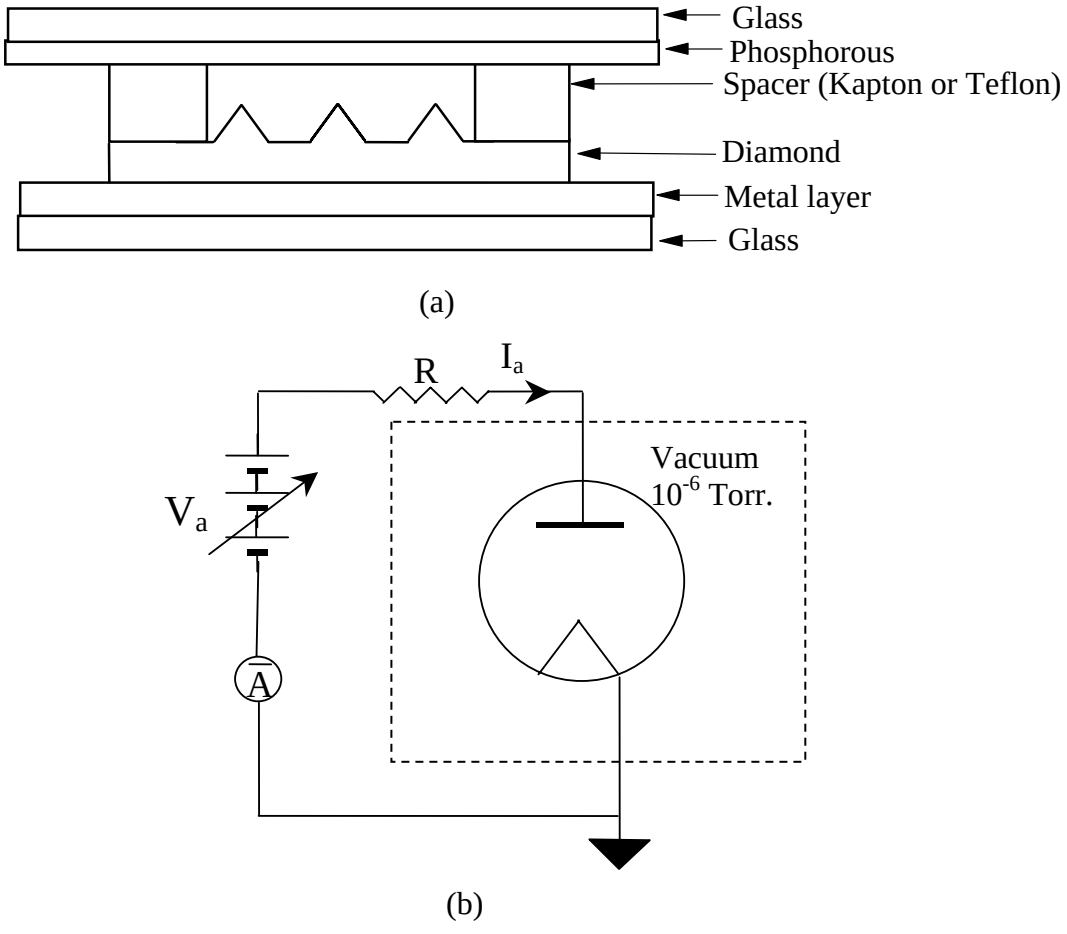


**Figure 5.11.** (a) Tested structure for diamond mictrotips and (b) Emission testing circuit for diamond vacuum diodes.

The emission characteristics of diamond microtips and monolithic diamond vacuum diodes were characterized by a simple diode test circuit as shown in **Figure 5.11(b)**. A resistor R (10MΩ-100MΩ) was used to limit the current in the case of short circuit. Anode and cathode were electrically connected to the circuit via metal probes in a vacuum chamber. The emission testing was performed at room temperature and in vacuum environment of $10^{-6}$ Torr. To begin emission testing, the anode voltage was gradually increased from zero until a significant emission current was detected. At the beginning stage, the emission was usually unstable because there was contamination on the tip surface. Therefore, tip self-cleaning process was conducted by adjusting the anode voltage to keep the emission current below 2 μA. After the emission became stable, the emission current versus time, at a fixed anode voltage, was taken by a computer. The stability of emission current at a given anode voltage can be characterized by the current versus time plot. An average value of emission current at a fixed anode voltage was then computed and the voltage drop on the limiting current resistor was subtracted from the applied voltage to obtain the true anode voltage. The anode voltage was then scanned manually in both forward and reverse directions to obtain complete set of current versus voltage characteristics. The emission characteristic was obtained by plotting the emission current versus the anode voltage.

Vacuum-thermal-electric (VTE) treatment was conducted on the device by heating the device slowly to ~150 °C in vacuum environment of $10^{-6}$ Torr. The device was maintained at 150 °C for several hours while the emission current was kept below 2 μA by adjusting the anode voltage. The VTE treatment was terminated when a stable current was obtained for a considerable period of time, usually 1 hour. The device was then cooled down slowly to room temperature. The same procedure as before VTE treatment was then repeated to obtain the emission characteristic after VTE treatment.

Emission characterization of diamond vacuum triodes

Static characteristic emission measurements

The testing circuit for static emission characteristic of monolithic diamond vacuum triode, in a common emitter configuration, is shown in **Figure 5.12**. In this case the resistor, $R_a$, as a dc load in the anode circuit is omitted. The resistor $R_g$ is used to limit the gate leakage

current in the case of short circuit in the gate circuit. Anode, gate, and cathode were electrically connected to the circuit via tungsten probes in a vacuum chamber. The anode emission current was then measured as a function of gate and anode voltages in a vacuum environment ($10^{-6}$ Torr).

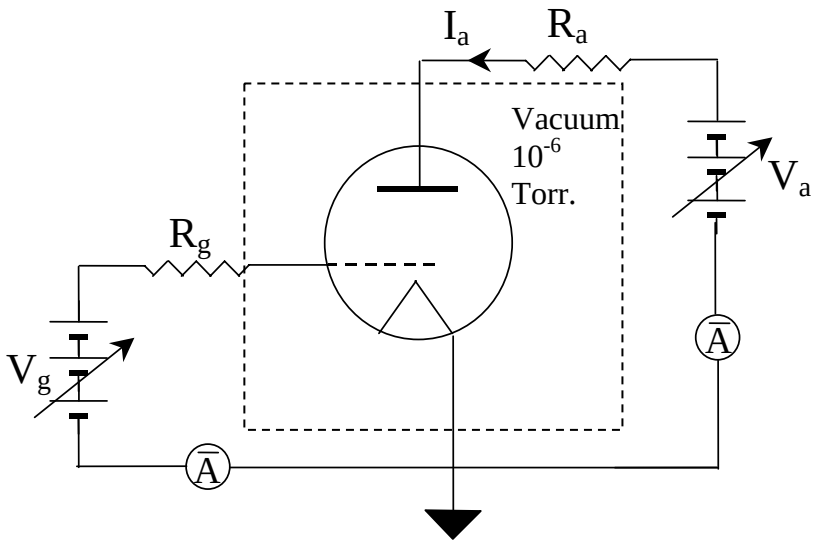


**Figure 5.12.** Emission testing circuit for diamond field emitter triodes.

The procedures for triode testing were as followed. Initially, a fixed anode voltage (~ 400 V) was applied to attract electrons extracted by the gate voltage. Next, the gate voltage was gradually increased from zero until a significant anode emission current was perceived. The anode emission currents versus time were taken semi-manually by a computer data acquisition system. For each set of emission current ($I_a$) measurement, the anode voltage was scanned manually while keeping the gate voltage constant. The gate voltage was then changed to a new value and the same emission measurement was repeated until a complete data set for all gate voltages in the range of interest were attained. The emission characteristics of triodes were obtained by plotting the anode emission current versus gate and anode voltages.

Vacuum-thermal-electric (VTE) treatment was also conducted on the device by heating the device slowly to ~150 °C in vacuum environment of $10^{-6}$ Torr. The device was maintained at 150 °C for several hours while the emission current was kept below 2 μA by adjusting the applied gate voltage. The VTE treatment was terminated when a stable anode current was

obtained for a considerable period of time, usually 1-2 hour. The devices were then cooled down slowly to room temperature. The anode emission currents after VTE treatment were then acquired by the same procedure as the pre-VTE emission measurement.

Measurement of dynamic emission characteristics

The testing circuit for dynamic emission characteristics of diamond field emitter triode is a same circuit as that for static characteristic but with an additional load resistor $R_a$ into the anode circuit. The $R_a$ is also useful to limit the current in the case of short circuit in the anode circuit.

Upon the emission testing for static characteristic, the variable load resistor $R_a$ into the anode circuit was then inserted. The anode emission current and gate current for dynamic characteristics were then acquired by the same procedure as the static emission measurement. The load resistance $R_a$ may be varied and the previous procedure was repeated to obtained dynamic characteristics for various load resistance values.

AC characteristic measurements

AC characteristics of diamond triode were measured in a basic common emitter amplifier circuit as shown in **Figure 5.13**. The capacitor, C, in the circuit, is for AC coupling (high pass filter). The C value is designed according to the high-pass cut-off frequency, $f_H$, which is given by

$$f_H = \frac{1}{2\pi C(R_L // R_a)}$$

where $R_L//R_a$ is the parallel of ac load resistor ($R_L$) and dc load resistor ($R_a$). $f_H$ was designed to be less than 10 Hz in this triode amplifier circuit. Choosing a minimum $R_L//R_a$ of 50 kΩ, C value of ~0.3 μF is obtained. Conservatively, a C value of 1 μF is used in this circuit. It should be noted that the capacitor used is a high voltage capacitor that can withstand the high voltage on the anode circuit.

The procedures for triode amplifier testing were as follows. Initially, all applied voltages are set to zero. First, the capacitor, C, is charged up slowly by gradually increasing $V_a$ until desired anode bias is reached. $V_a$ must increase slowly in order to protect the digital oscilloscope from a surge voltage. Next, a gate bias voltage, $V_g$, is applied until the desired operating

emission current is reached and stabilized. Finally, a sine-wave gate input voltage, $v_{in}$, from a function generator is applied. Both ac input and output voltages are simultaneously monitored and recorded using the digital oscilloscope.

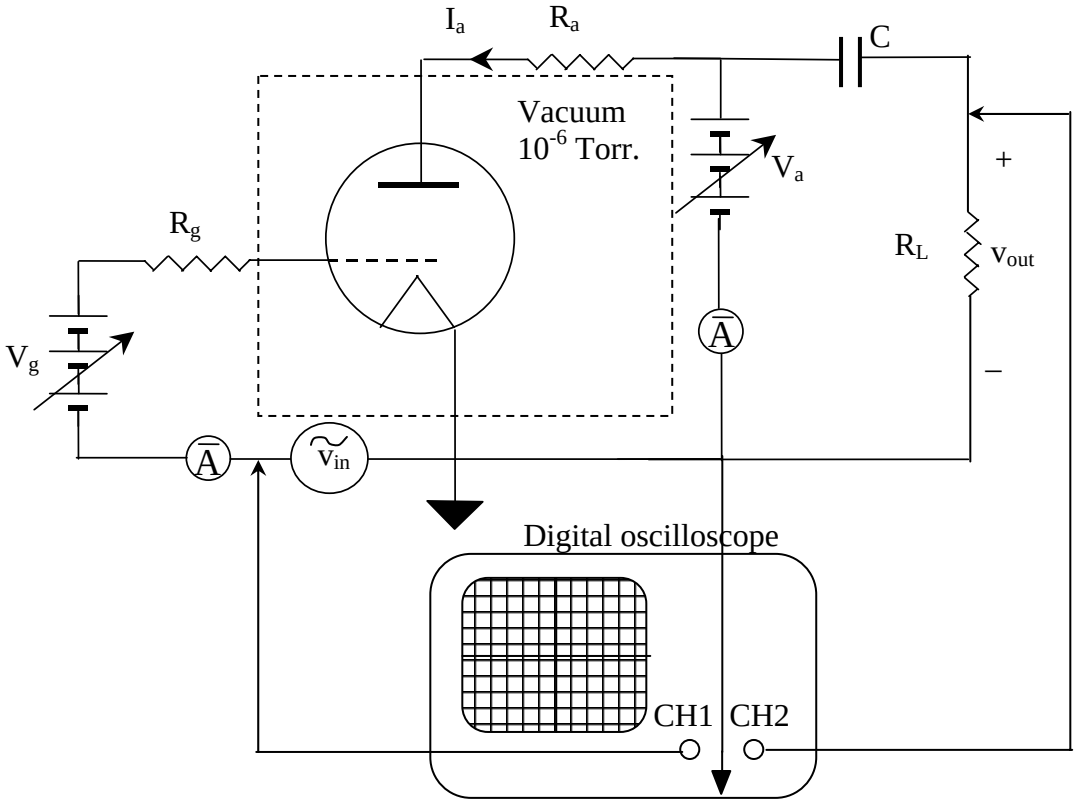


**Figure 5.13.** A common emitter diamond vacuum triode amplifier circuit.

# CHAPTER VI

# EXPERIMENTAL RESULTS AND DISCUSSION

## Part I: Micro-patterned pyramidal diamond field emission cathode

### Design and fabrication issues for diamond field emission cathode

In order to achieve a highly efficient and reliable field emission cathode, the cathode must have a designed (not stochastic) geometry with a sharp apex. Metal and silicon cathodes with such geometry are achieved from the available material processing technology. On the other hand, it is difficult to fabricate a well-defined structured diamond cathode because of challenge in diamond processing technology. For example, there is no available wet or dry chemical etching for diamond. We have overcome these problems and developed a practical, reliable, and efficient mold transfer technique for diamond field emitter fabrication. This mold transfer technique can produce well controlled micropatterned diamond emitters with a well-defined microtip structure and uniformity over a large area.

#### Design of diamond pyramidal microtip by mold transfer technique

In the mold transfer technique, a cathode structure is produced by deposition of the cathode material into a mold having an inverse shape of the cathode geometry. We have successfully fabricated diamond pyramidal microtips by PECVD diamond deposition into inverted pyramidal silicon cavities, which can be reproducibly formed by anisotropic etching of micron-size square patterns on (100) silicon wafer. The inverted pyramidal cavity, which comprised of 4 {111} planes of silicon, has an inverted trapezoidal shape with a 70.5° angle at the apex as illustrated in **Figure 6.1**.

The relationship between the base width (W) and the height (H) of a pyramid is given by

$$W = \sqrt{2}\, H \qquad (6.1)$$

The base width of the pyramid is determined by the size of the square pattern. The nominal height of diamond pyramidal microtip with a base of 2 μm is approximately 1.4 μm.

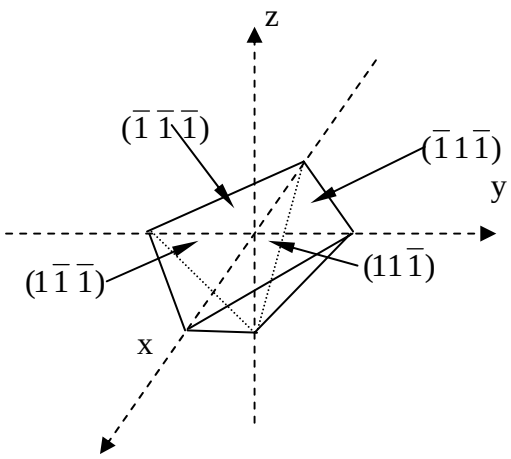


**Figure 6.1.** Crystallographic structure of inverted pyramidal cavity.

Design of diamond pyramidal microtips with ultrasharp apex

Since the tip radius of curvature of the pyramidal diamond tip is still quite large, the field enhancement factor is low and optimum emission behavior may not be achieved. Thus, it is beneficial to sharpen pyramidal diamond tips to achieve the highest performance. However, post-fabrication tip sharpening for diamond is nearly impossible because diamond is inert, hard, and cannot be etched by any regular chemical etchants. To overcome this problem, we have developed a novel mold sharpening technique for the fabrication of ultra-sharp pyramidal diamond microtips.

We have achieved the mold sharpening by dry thermal oxidation of the inverted pyramidal silicon mold. **Figure 6.2** shows an SEM of a sharpened mold formed by dry thermal oxidation versus that of an as-etched, unsharpened pyramidal mold. This ultra-sharp apex happens because thermal oxidation rate on the (111) planes of the inverted pyramidal silicon surface is faster than that on the (100) plane of the silicon base and the oxidation rate at the inverted apex is smallest due to limited oxidation reaction in this confined region. Dry thermal oxidation is used to achieve high quality $SiO_2$ dielectric, which is later used as a gate dielectric.

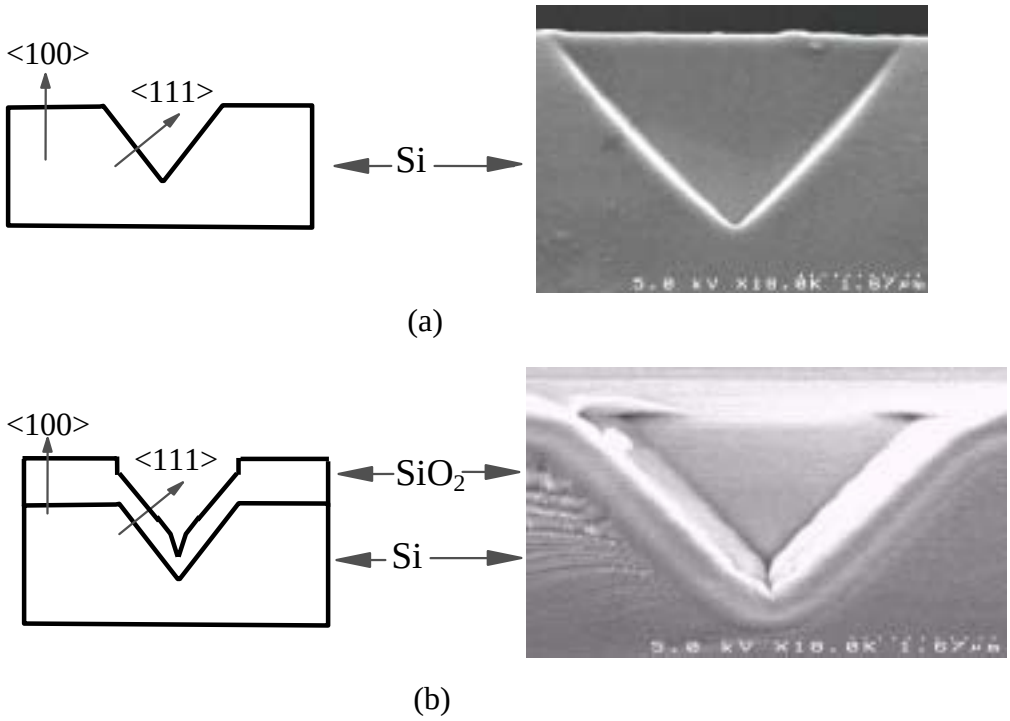


**Figure 6.2.** Structure and SEM micrograph of (a) unsharpened and (b) sharpened pyramidal mold.

Oxidation process parameters for fabrication of pyramidal mold

There are two oxidation process parameters that define the fabrication of pyramidal mold: 1) oxide layer thickness for patterning and 2) oxide layer thickness for tip sharpening.

1) The oxide layer thickness ($T_1$) for pattering needs to be thin in order to minimize lateral etching and better control the tip size. The minimum $T_1$ is determined by the etching process used. However, $T_1$ must be sufficiently thick to prevent complete removal of $SiO_2$ masking layer by KOH during silicon etching process. The etching selectivity of Si over $SiO_2$ for KOH is nominally 10-100 depending on KOH concentration and etching temperature. Thus, the minimum $T_1$ should be equal to the depth of mold cavity (H), which is the depth of silicon etching divided by the minimum selectivity of KOH etching solution. For a typical cavity depth of 1.5 μm and a minimum etching selectivity of 10, the minimum $T_1$ is approximately 1.5/10 = 0.15 μm. Conservatively, a $T_1$ of 0.2 μm is nominally chosen for our fabrication process.

2). The tip sharpening oxide thickness ($T_2$): $T_2$ determines the sharpness of the inverted mold apex. It was found experimentally that increasing $T_2$ would improve the sharpness of the inverted mold apex. Thus, $T_2$ should be as large as possible for tip sharpening. However, there

are two main factors that limit $T_2$. The first limiting factor is the dry oxidation process. Since silicon dry oxidation is a very slow process, it is not practical to grow dry oxide layer thicker than 1 μm. The time required for dry thermal oxidation of 1 μm-thick oxide at the standard growth temperature of 1100 °C is ~ 48 hours, which is very time consuming. Second, $T_2$ determines the gate-cathode spacing of gated diamond emitter and hence $T_2$ should be as thin as possible in order to reduce turn-on voltage. Therefore, a trade off between the two competing issues needs to be taken into consideration for the choice of $T_2$. Thus, $T_2$ of 1 μm was nominally chosen for optimum tip sharpness and moderate gate-cathode spacing.

Physical characteristics of micro-patterned diamond field emission cathode

The microstructures of diamond field emission cathodes were examined by scanning electron microscopy (SEM). **Figures 6.3-6.4** show the SEM micrograph of unsharpened pyramidal diamond microtips. A detailed topology, geometry, and dimension of a single unsharpened diamond microtip can be seen in **Figure 6.3**. It shows a pyramidal diamond tip with base dimension of 2 μm x 2 μm and a tip radius of curvature ~ 20 nm. It also can be seen that the diamond tip comprises of polycrystalline structures separated by grain boundaries. The average grain size is ~ 0.2 μm. **Figure 6.4** shows arrays of 7x7 diamond tips with different magnifications. It demonstrates good uniformity among tips with tip spacing of ~ 20 μm and array spacing of ~ 50 μm.

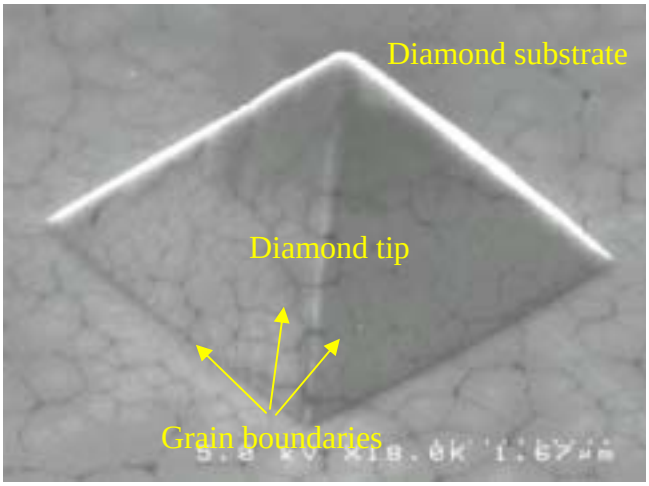


**Figure 6.3.** An SEM micrograph of a single pyramidal (trapezoidal) diamond microtip

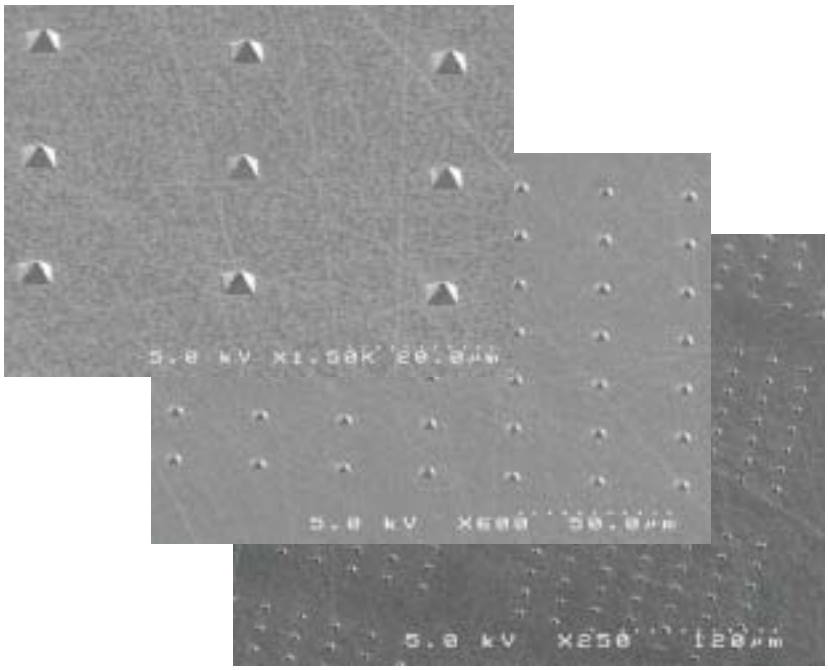

**Figure 6.4.** SEM micrographs of arrays pyramidal diamond microtips.

Typical structures of sharpened pyramidal diamond microtips are shown in **Figures 6.5-6.6**. An SEM micrograph, **Figure 6.5**, shows a single diamond microtip with ultra sharp apex and base dimension of 2 μm x 2 μm. The radius of curvature at the apex was estimated to be less than 5 nm, representing the sharpest as-grown diamond tip reported in the literature. **Figure 6.6**

shows a large array of high-density sharpened diamond tips with different magnifications. It can be seen that ultra sharp diamond tips with good uniformity in size and shape can be reproducibly fabricated by mold sharpening technique.

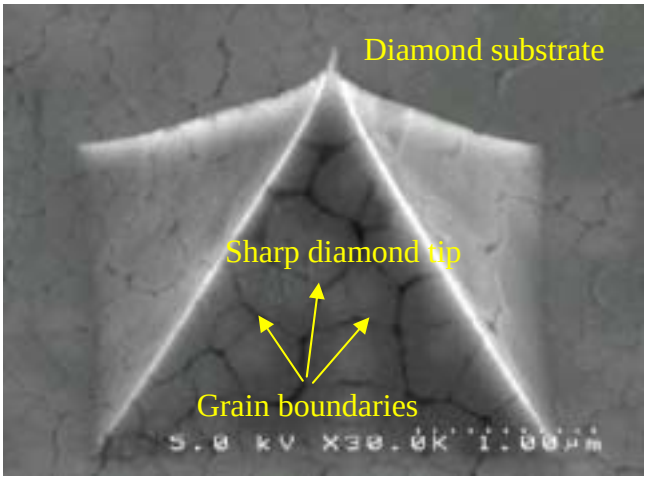


**Figure 6.5.** An SEM micrograph of a single pyramidal diamond microtips with ultra sharp apex.

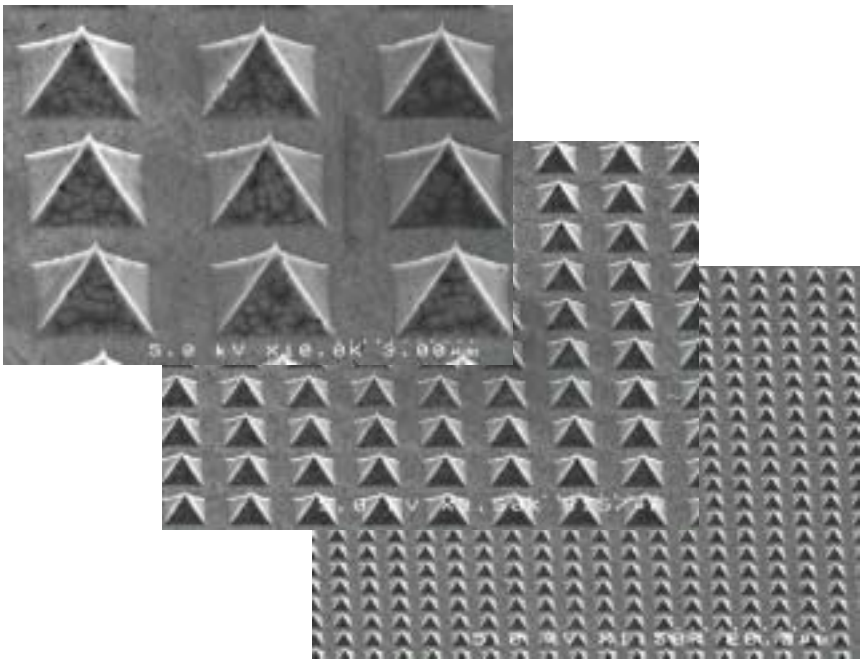

**Figure 6.6.** SEM micrographs of arrays pyramidal diamond microtips with ultra sharp apex.
Raman spectra of diamond microtips

The quality of diamond film, $sp^2/sp^3$ composition, was characterized using Raman spectroscopy. **Figure 6.7** shows Raman spectra of diamond films on the tip side for no, trace, and low $sp^2$ content, respectively. From these Raman spectra, it can be seen that the ratio of the peak-height of $sp^2$ peak (at 1580 $cm^{-1}$) to diamond peak (at 1332 $cm^{-1}$) of no $sp^2$ content diamond tips is smaller than that of trace $sp^2$ content diamond tips. Likewise, the peak-height ratio of trace $sp^2$ content diamond tips is smaller than that of low $sp^2$ content diamond tips. This indicates that the higher the $sp^2$ content, the higher the peak-height ratio is obtained. Furthermore, the corresponding diamond peak at 1332 $cm^{-1}$ becomes broader as the $sp^2$ content increases. Although the exact $sp^2/sp^3$ composition cannot be determined from the Raman spectra, it can be assumed that the $sp^2/sp^3$ ratio of low $sp^2$ content diamond tip is only in the order of few percents. This is because the areas under $sp^2$ and $sp^3$ peaks are approximately the same and the $sp^2$ bonding has about 50 times higher scattering efficiency than $sp^3$ bonding. Similarly, it can be implied that the $sp^2/sp^3$ ratio of trace $sp^2$ content diamond tip is less than one percent and the $sp^2/sp^3$ ratio of no $sp^2$ content diamond tip is negligible.

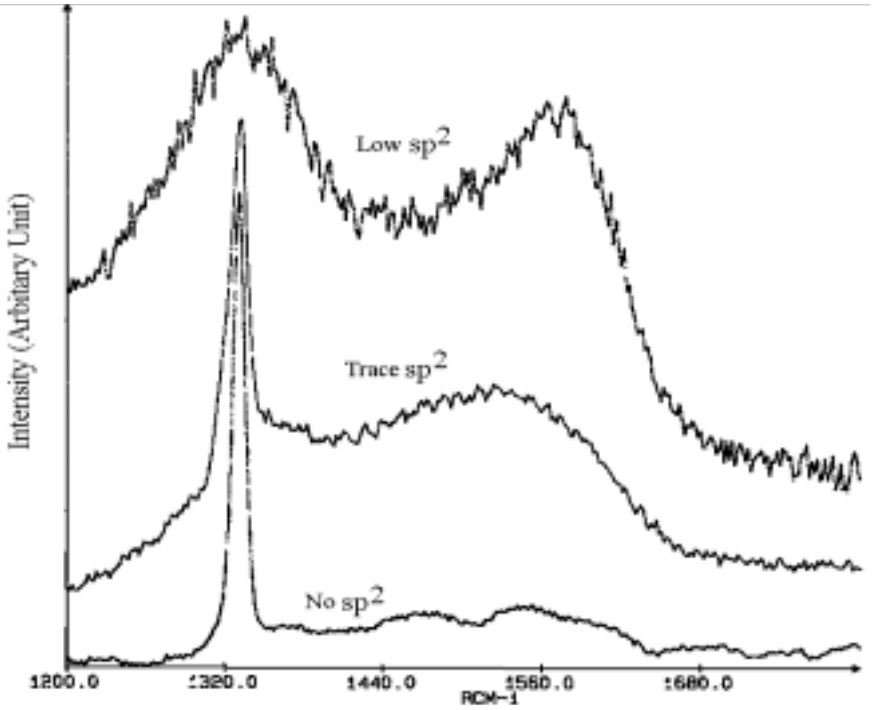


**Figure 6.7.** Raman spectra of diamond tips with different $sp^2$ content.

Emission characteristics of diamond microtips

Emission characteristics, current vs. electric field (I-E), of unsharpened diamond tips with different $sp^2$ contents before VTE treatment are shown in **Figures 6.8-6.12**. I-E emission characteristics of unsharpened diamond tips with different $sp^2$ contents after VTE treatment are shown **Figures 6.13-6.17**. I-E emission characteristics of sharpened diamond tips with low $sp^2$ contents before and after VTE treatment are shown **Figures 6.18-6.19**.

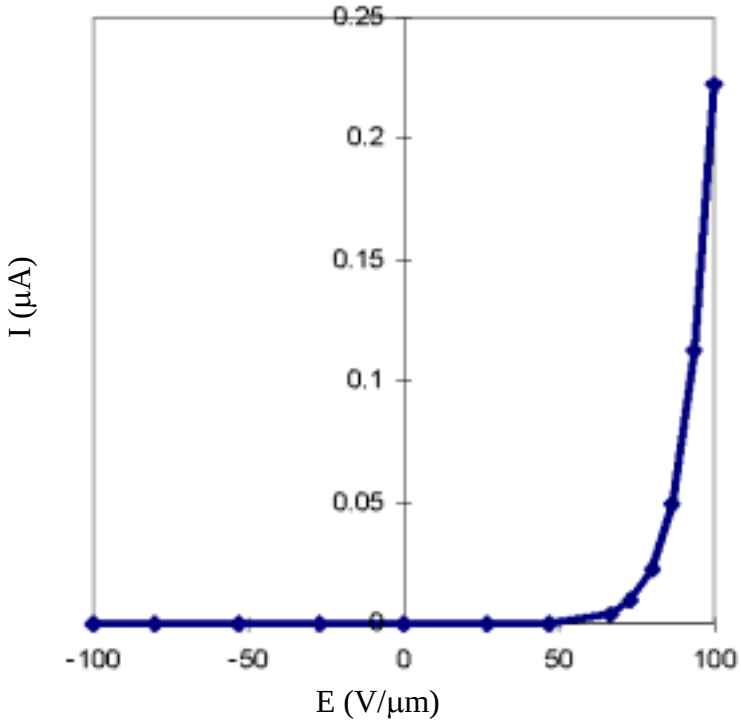


**Figure 6.8.** I-E emission characteristics of unsharpened undoped diamond tips with no $sp^2$ contents before VTE treatment.

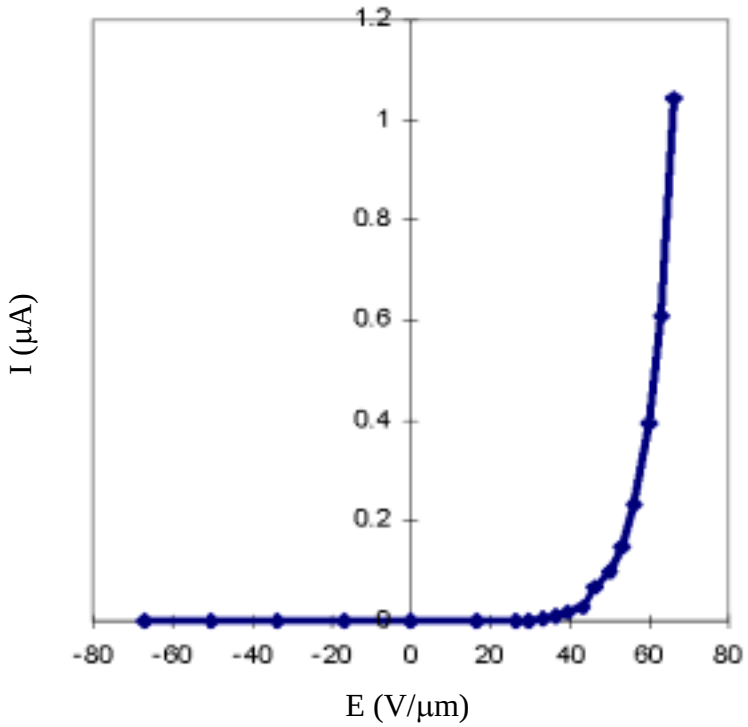


**Figure 6.9.** I-E emission characteristics of unsharpened undoped diamond tips with trace $sp^2$ contents before VTE treatment.

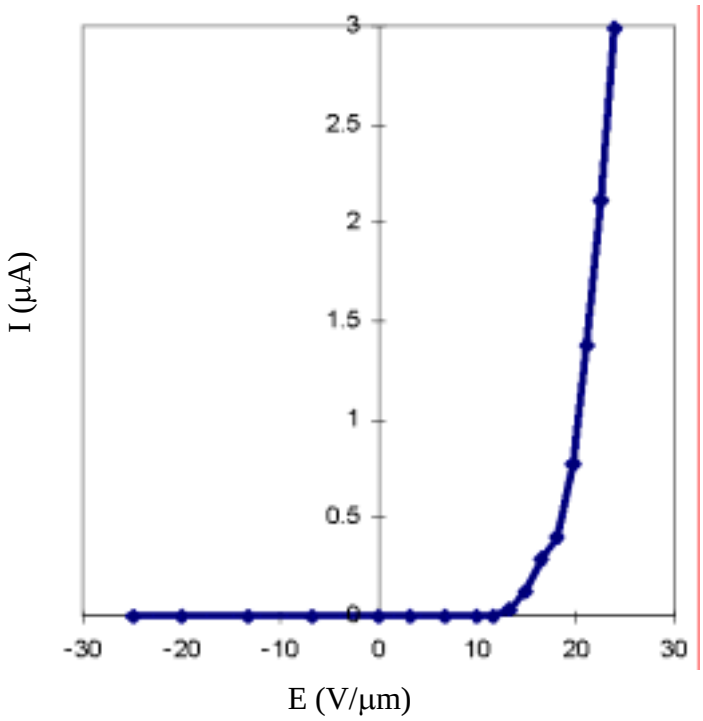


**Figure 6.10.** I-E emission characteristics of unsharpened undoped diamond tips with low $sp^2$ contents before VTE treatment.

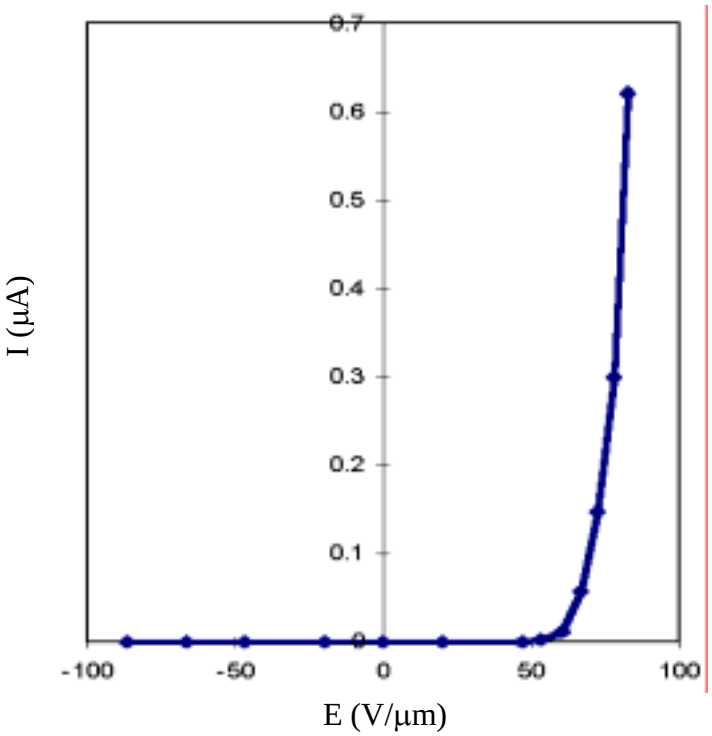


**Figure 6.11.** I-E emission characteristics of unsharpened boron-doped diamond tips with trace $sp^2$ contents before VTE treatment.

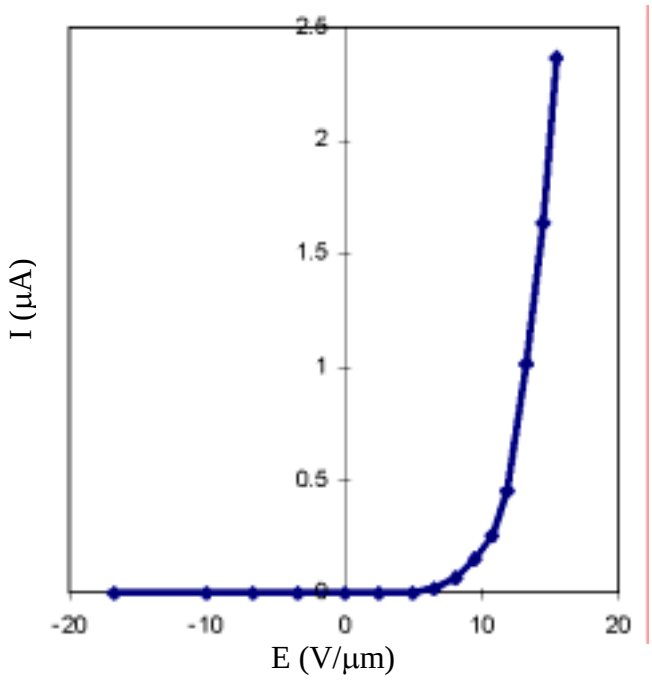


**Figure 6.12.** I-E emission characteristics of unsharpened boron-doped diamond tips with low $sp^2$ contents before VTE treatment.

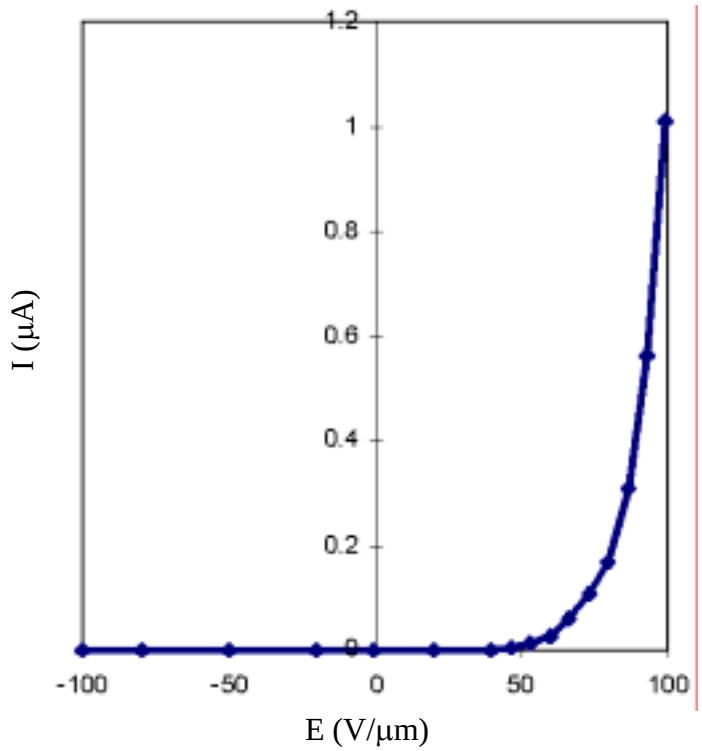


**Figure 6.13.** I-E emission characteristics of unsharpened undoped diamond tips with no $sp^2$ contents after VTE treatment.

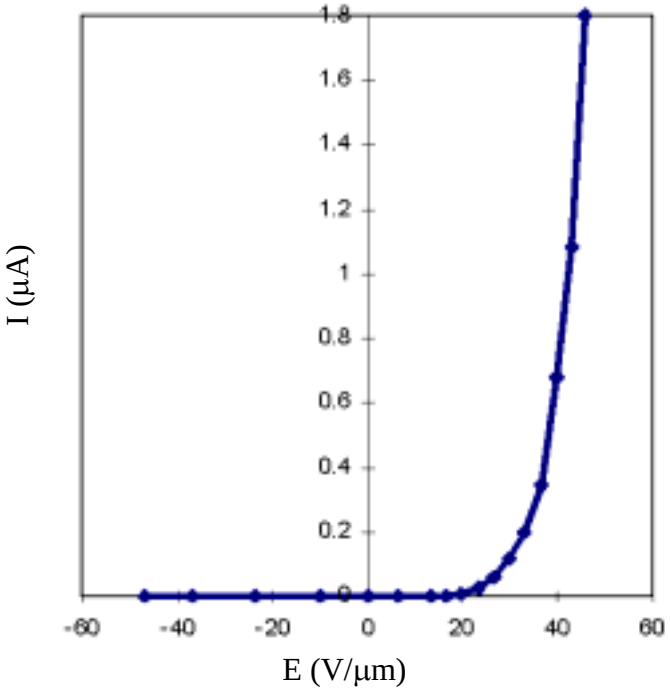


**Figure 6.14.** I-E emission characteristics of unsharpened undoped diamond tips with trace $sp^2$ contents after VTE treatment.

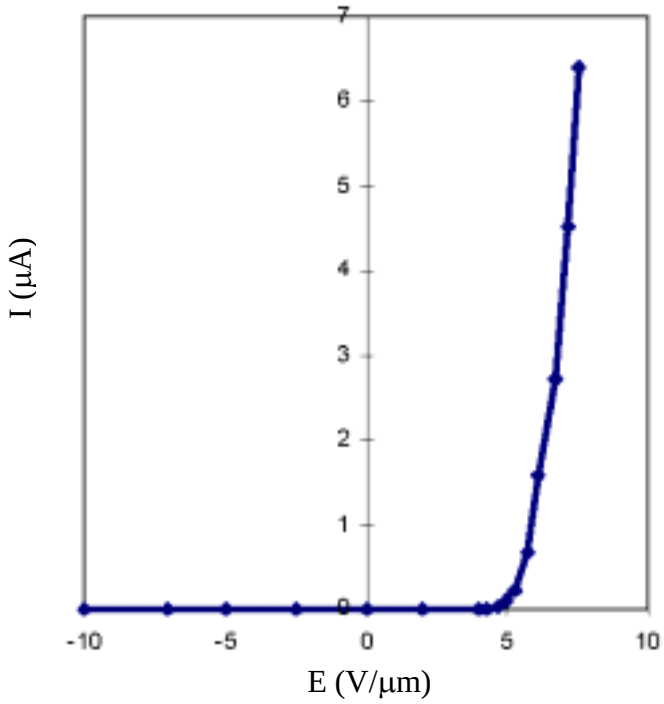


**Figure 6.15.** I-E emission characteristics of unsharpened undoped diamond tips with low $sp^2$ contents after VTE treatment.

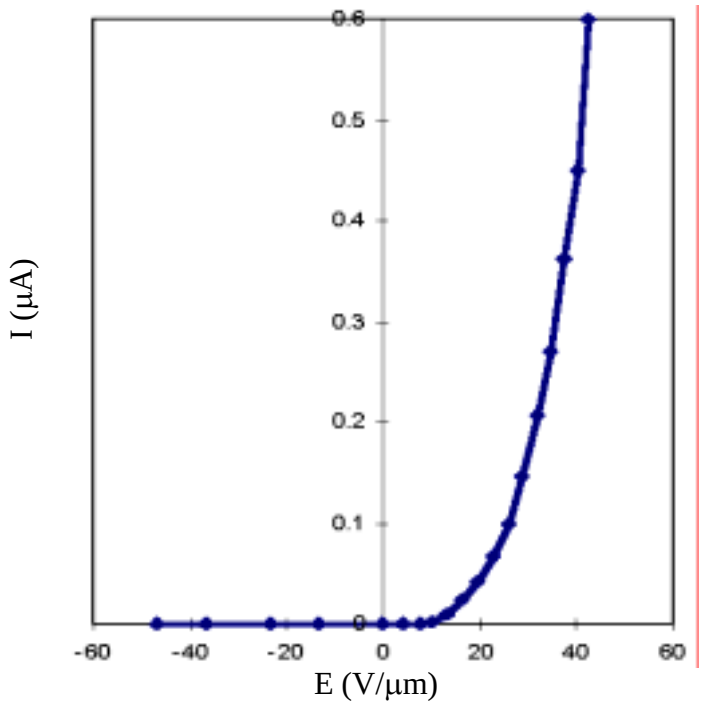


**Figure 6.16.** I-E emission characteristics of unsharpened boron-doped diamond tips with trace $sp^2$ contents after VTE treatment.

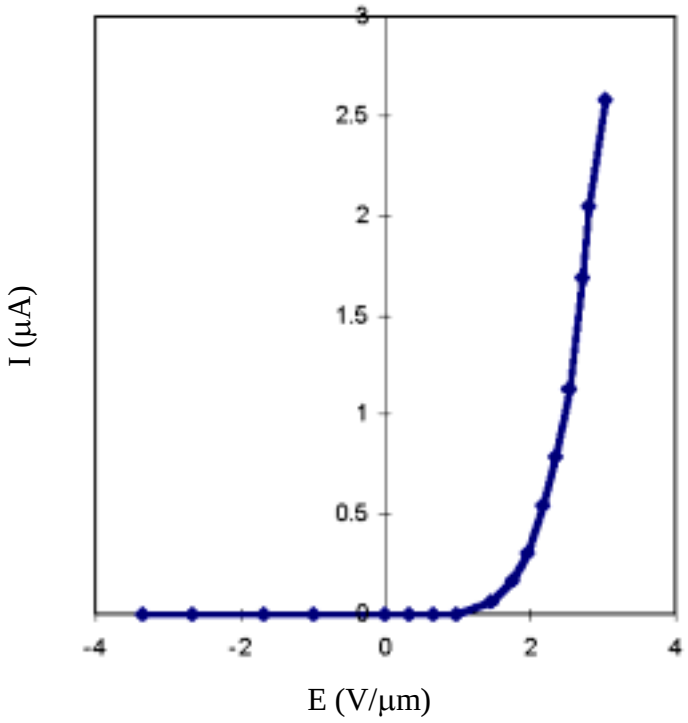


**Figure 6.17.** I-E emission characteristics of unsharpened boron-doped diamond tips with low $sp^2$ contents after VTE treatment.

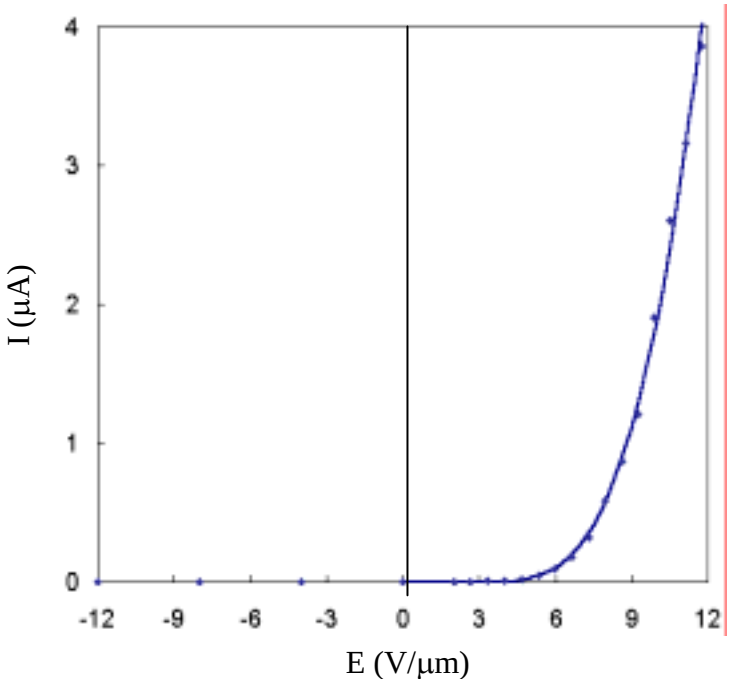


**Figure 6.18.** I-E emission characteristics of sharpened undoped diamond tips with low $sp^2$ contents before VTE treatment.

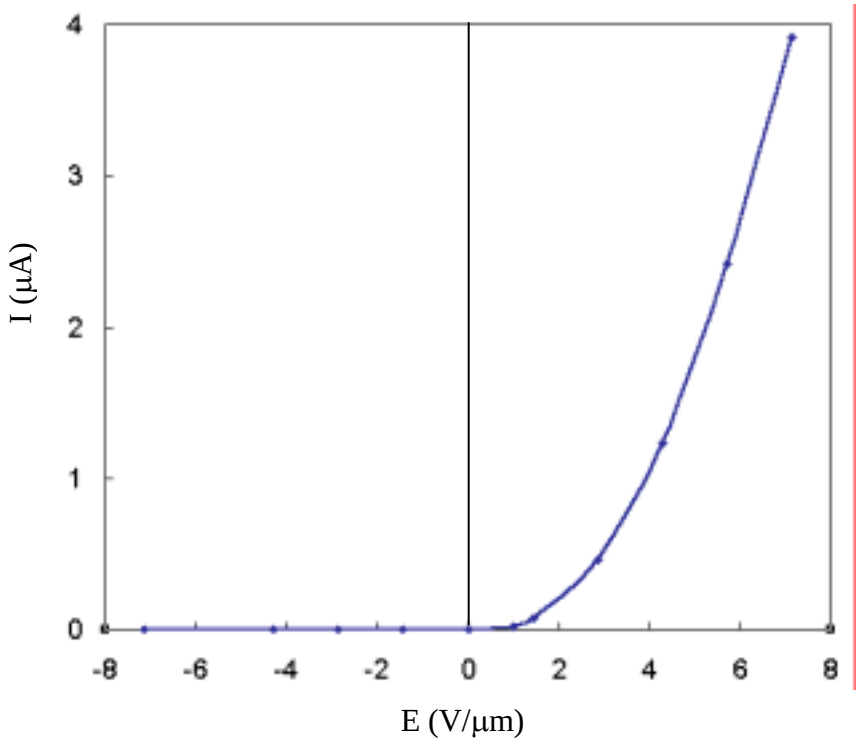


**Figure 6.19.** I-E emission characteristics of sharpened undoped diamond tips with low $sp^2$ contents after VTE treatment.

Discussion and analysis of emission results from diamond field emitter cathode

All emission data of diamond microtips were primarily examined using Fowler-Nordhiem (F-N) analysis. Emission characteristics based on F-N model were then compared and discussed into four categories: (I) the effect of $sp^2/sp^3$ composition on diamond field emission, (II) the effect of VTE treatment on diamond field emission, (III) the effect of doping on diamond field emission, and (IV) the effect of tip sharpening on diamond field emission.

Preliminary Fowler-Nordhiem analysis for diamond field emission

The emission data of the diamond microtips were analyzed by the modified Fowler-Nordhiem equation:

$$\mathrm{Ln}(I/E^2) = \mathrm{Ln}(AK_1\beta^2/\Phi) - (K_2\Phi^{1.5}/\beta)(1/E) \qquad (6.2)$$

where $K_1$ and $K_2$ are constants: $K_1 = 1.54\times10^{-6}$ A·eV/V$^2$, $K_2 = 6.83\times10^{7}$ V/(cm·eV$^{3/2}$), I is the emission current, $\Phi$ is the work function of the emitting surface (in eV), $\beta$ is the field

enhancement factor, A is the emitting area, and E is the macroscopic applied electric field (Volts/cm). E=V/d where V and d are the anode-cathode voltage and spacing, respectively.

According to this equation, a plot of $Ln(I/E^2)$ versus 1/E should be linear with the slope equals to $-K2\Phi^{1.5}/\beta$ and the intercept at $Ln(I/E^2)$ axis equals to $Ln(AK_1\beta^2/\Phi)$. This plot is generally referred to the F-N plot. The F-N plots of the experimental data are in good agreement with the F-N equation. Detail discussions for each type of diamond film will be shown in next section.

There are three unknown device parameters involved in the slope and intercept of F-N plot: the emitting area (A), the work function ($\Phi$), and the field enhancement factor ($\beta$). However, these three parameters cannot primarily be determined, because only two equations can be obtained from the slope and intercept of the F-N plot. For field emission analysis, the work function and field enhancement factor of diamond tips needs to be determined. Additional experiment must be conducted to determine one of these unknown parameters. Since the emitting area (A) is the area where electrons emitted from the diamond cathode, the exact area is difficult to be measured and there has been no experimental technique to directly measure the emitting area of field emission cathodes. The work function ($\Phi$) of diamond is also an unknown parameter that is difficult to determine because diamond is a wide band gap material. In addition, $\Phi$ of diamond depends on diamond composition and surface structure. The field enhancement factor ($\beta$) depends on geometry of cathode, and hence it may be estimated from the measurement of diamond tip geometry using SEM.

Geometrical field enhancement factor approximation of pyramidal diamond tip

The unsharpened pyramidal diamond tip was approximated as a single conical tip with tip height of $h_1$ and tip radius curvature of $r_1$ as illustrated in **Figure 6.20(a)**. From the simple field enhancement model described in chapter II, the geometrical field enhancement factor of a conical tip is given by:

$$\beta_{g,\ unsharpened} = \frac{h_1}{r_1} \tag{6.3}$$

Using $h_1 \approx 2.5$ μm obtained from the low magnification SEM micrograph (**Figure 6.3**) and $r_1 \approx 25$ nm obtained from the high magnification SEM micrograph of the tip apex as illustrated in **Figure 6.20(b)**, $\beta_{g,\ unsharpened} \approx 100$ was acquired. Primarily, the simple field

enhancement model were used because from the SEM pictures of all pyramidal microtips, the surface of pyramidal microtip is smooth, thus the simple field enhancement model should be valid.

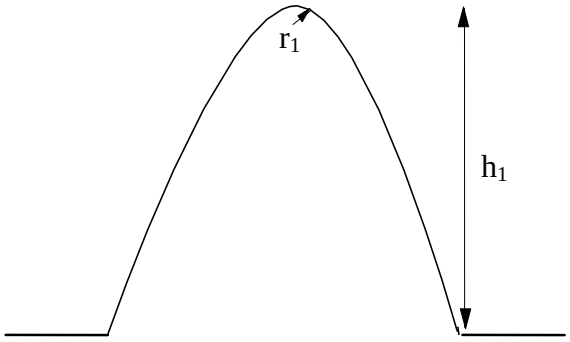


(a)

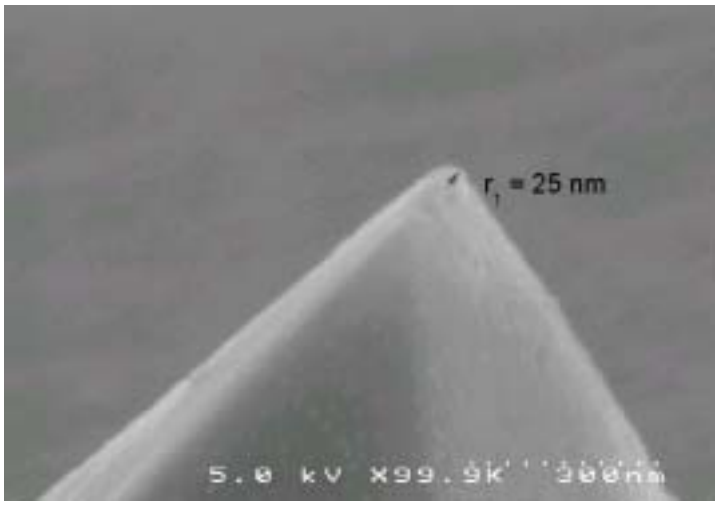


(b)

**Figure 6.20.** (a) the model of an unsharpened diamond tip and (b) high magnification SEM micrograph of an unsharpened diamond tip focused at the tip apex.

Based on this $\beta_{g,\ unsharpened}$ value, the work function Φ was obtained from the slope of the F-N plot. Theoretically, A can be determined from F-N intercept since both field enhancement factor and work function values are known. However, the emitting areas is not meaningful for the comparison of the results because the exact number of tips that participated in the field emission process can not be determined in the experimental setup. Thus, the calculation of emitting area is omitted. **Table 6.1** shows the results obtained for diamond tips with different $sp^2$

contents and different treatments. It is important to note that the work function based on constant β value is for primary comparison purpose. This assumption may be changed based on the subsequent discussion.

**Table 6.1.** Calculated results from Fowler-Nordhiem plots based on simple field enhancement model.

| Treatment | Doping | $sp^2$ content | F-N slope | Φ(eV) | β |
|---|---|---|---|---|---|
| Before VTE treatment | no | no | -651.08 | 2.13 | 100 |
| | no | trace | -268.53 | 1.18 | 100 |
| | no | low | -114.04 | 0.67 | 100 |
| | p | trace | -685.72 | 2.20 | 100 |
| | p | low | -35.04 | 0.30 | 100 |
| After VTE treatment | no | no | -328.14 | 1.35 | 100 |
| | no | trace | -127.79 | 0.72 | 100 |
| | no | low | -58.21 | 0.43 | 100 |
| | p | trace | -44.07 | 0.35 | 100 |
| | p | low | -6.10 | 0.09 | 100 |

Discussion of the effect of $sp^2/sp^3$ composition

The detail discussion on the effect of $sp^2$ content on diamond field emission is separated into the following four cases.

The effect of $sp^2$ content on undoped diamond tips before VTE treatment

The effect of $sp^2$ content on the I-E and F-N plots of undoped diamond tips before VTE treatment are shown in **Figures 6.21-6.22**. From **Figure 6.21**, it can be seen that the turn-on electric field of diamond tips tends to reduce as $sp^2$ content increases. The turn-on electric field is defined as the electric field at which a threshold emission current of ~10 nA is obtained. The turn-on electric field of no, trace, and low $sp^2$ content diamond tips are approximately 67, 30, and 12 V/ μm, respectively. From **Figure 6.22**, it can be seen that the slope of F-N plots also tends to be shallower as $sp^2$ content increases. **Figure 6.23(a)** and **Figure 6.24(a)** show the effect of $sp^2$ content on the F-N slope ratio and work function ratio of undoped diamond tips (from **Table 6.1**) using undoped no $sp^2$ content diamond tip as a reference. From these figures, it can be seen that the F-N slope ratio and work function ratio of diamond tips tend to reduce as $sp^2$ content increases. F-N slope ratio and work function ratio of diamond tips will be further discussed and analyzed in the subsequent theoretical discussion.

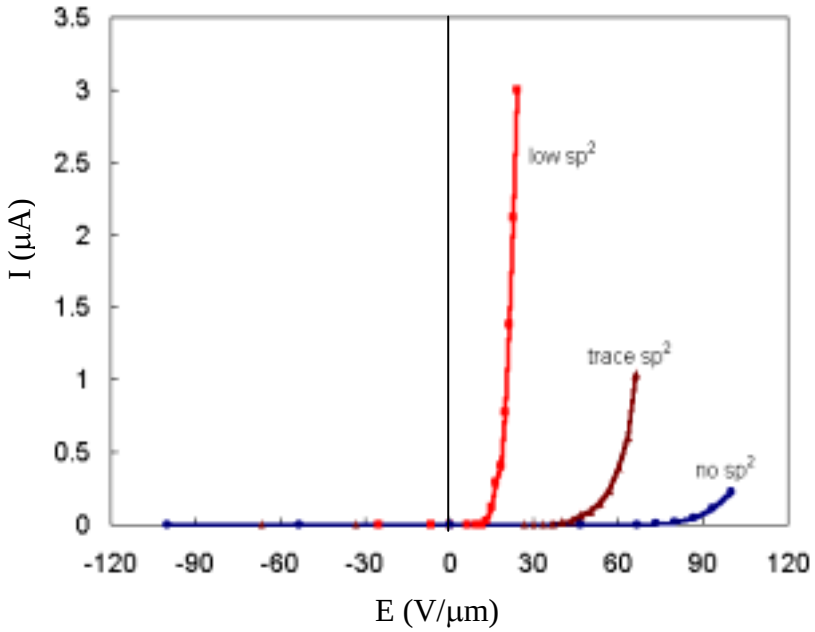


**Figure 6.21.** The effect of $sp^2$ content on I-E plot of undoped diamond tips before VTE treatment.

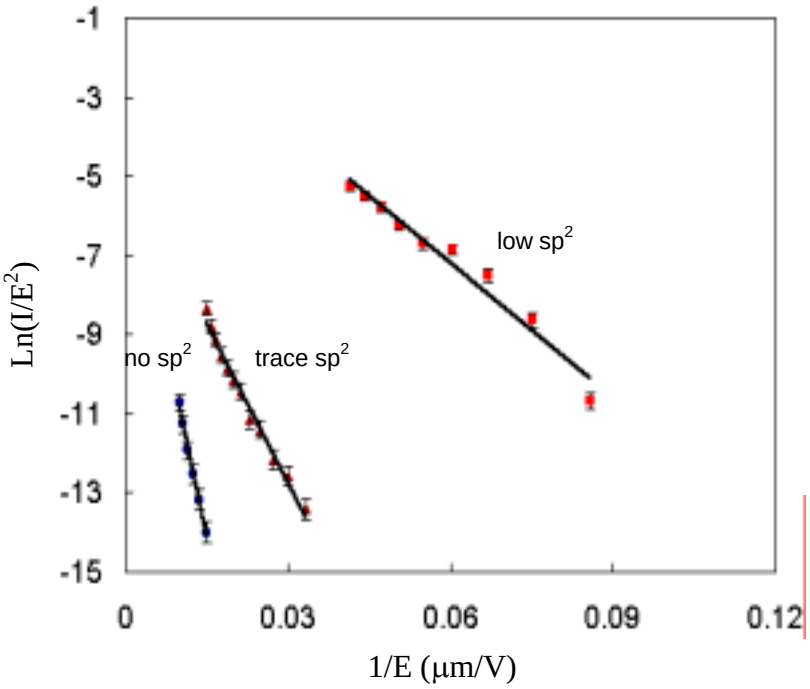


**Figure 6.22.** The effect of $sp^2$ content on F-N plot of undoped diamond tips before VTE treatment.

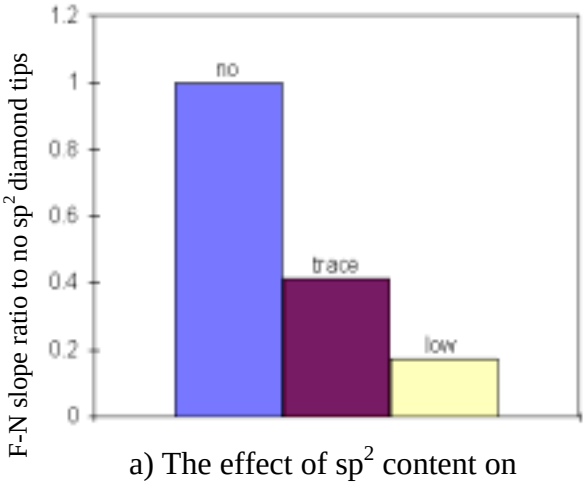


a) The effect of $sp^2$ content on undoped diamond tips before V-T-E treatment.

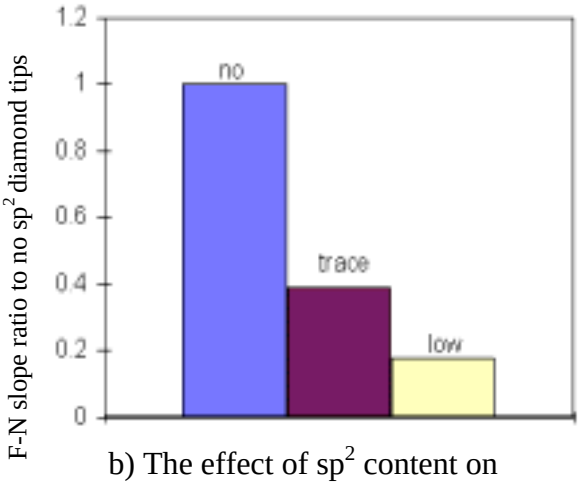


b) The effect of $sp^2$ content on undoped diamond tips after V-T-E treatment.

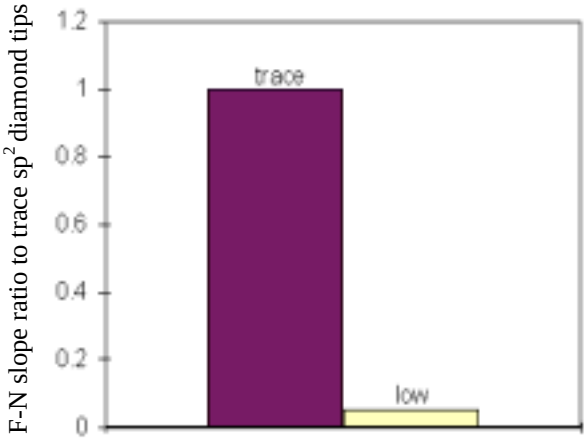


c) The effect of $sp^2$ content on p-type diamond tips before V-T-E treatment.

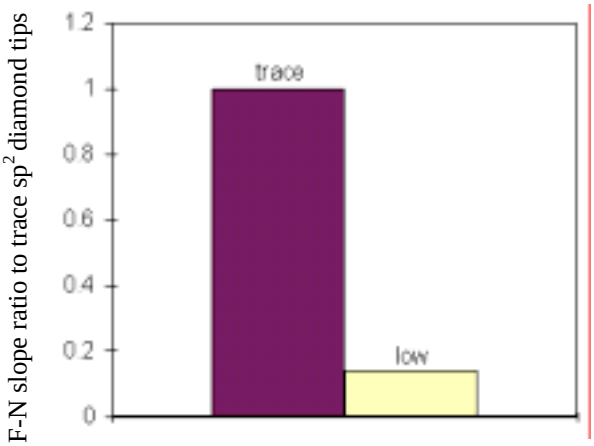


d) The effect of $sp^2$ content on p-type diamond tips after V-T-E treatment.

**Figure 6.23.** The effect of $sp^2$ content on the F-N slope ratio of diamond tips for the same doping and same treatment.

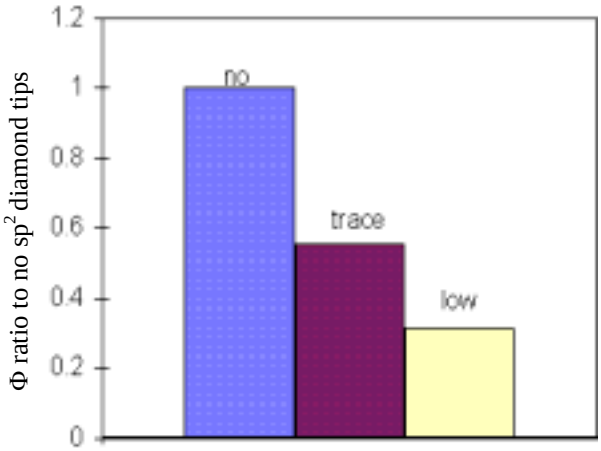


a) The effect of $sp^2$ content on undoped diamond tips before V-T-E treatment.

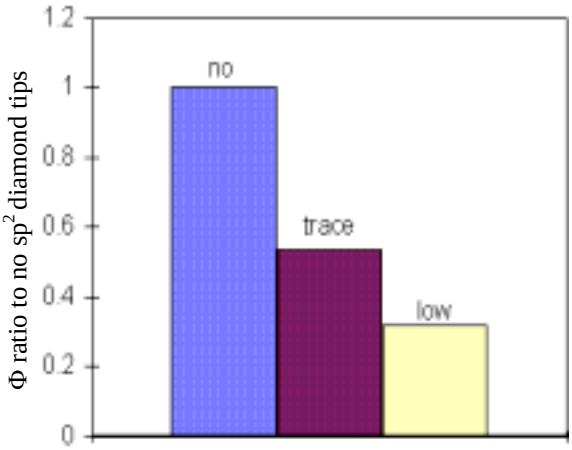


b) The effect of $sp^2$ content on undoped diamond tips after V-T-E treatment.

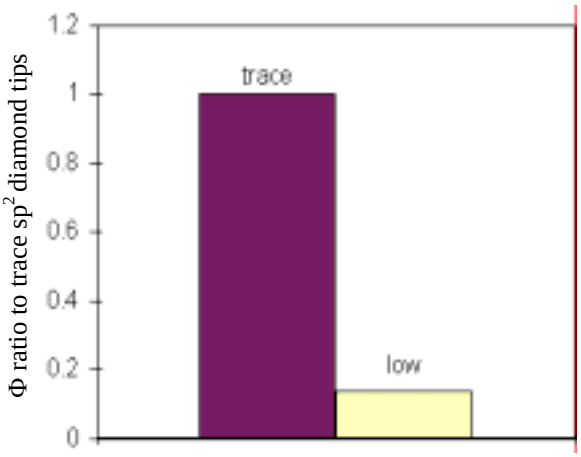


c) The effect of $sp^2$ content on p-type diamond tips before V-T-E treatment.

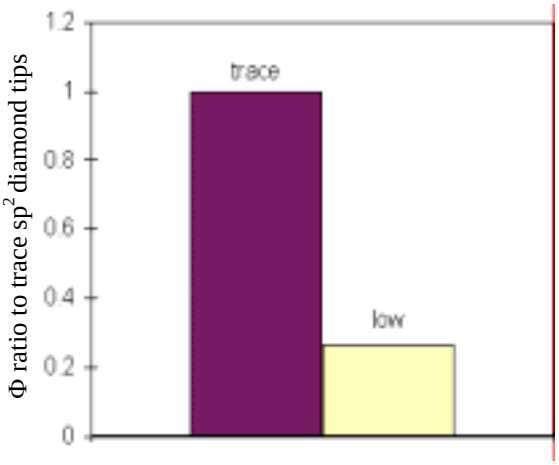


d) The effect of $sp^2$ content on p-type diamond tips after V-T-E treatment.

**Figure 6.24.** The effect of $sp^2$ content on the Φ ratio of diamond tips for the same doping and same treatment.

The effect of $sp^2$ content on undoped diamond tips after VTE treatment

The effect of $sp^2$ content on the I-E and F-N plots of undoped diamond tips after VTE treatment are shown in **Figures 6.25-6.26**. From **Figure 6.25**, it can be seen that the turn-on electric field of the diamond tips tends to reduce as $sp^2$ content increases. The turn-on electric field of no, trace, and low $sp^2$ content diamond tips are approximately 40, 17, and 4 V/μm, respectively. From **Figure 6.26**, it can be seen that the slope of F-N plots also tends to be shallower as $sp^2$ content increases. **Figure 6.23(b)** and **Figure 6.24(b)** show the effect of $sp^2$ content on the F-N slope ratio and work function ratio of undoped diamond tips using undoped no $sp^2$ content diamond tip as a reference. From these figures, it can be seen that the F-N slope ratio and work function ratio of diamond tips tend to reduce as $sp^2$ content increases.

It is interesting to note that the F-N slope ratio and work function ratio of diamond tips as a function of $sp^2$ content before and after VTE treatment remain almost the same. This suggests that the F-N slope ratio and work function ratio of diamond tips have correlation with $sp^2$ content independent of VTE treatment. This interesting result will be further discussed in the theoretical discussion of the effect of $sp^2$ content on diamond tips.

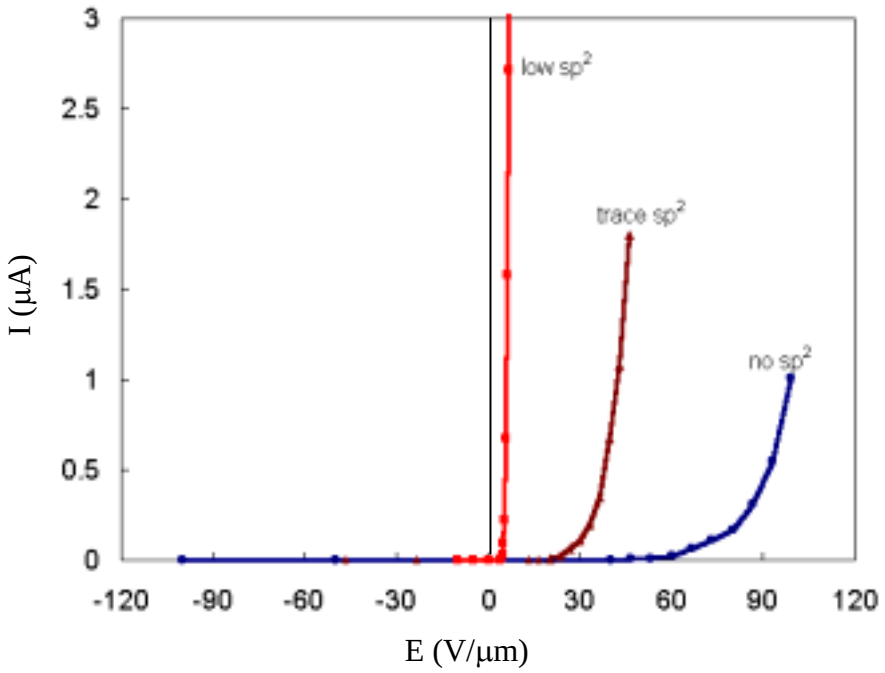


**Figure 6.25.** The effect of $sp^2$ content on I-E plot of undoped diamond tips after VTE treatment.

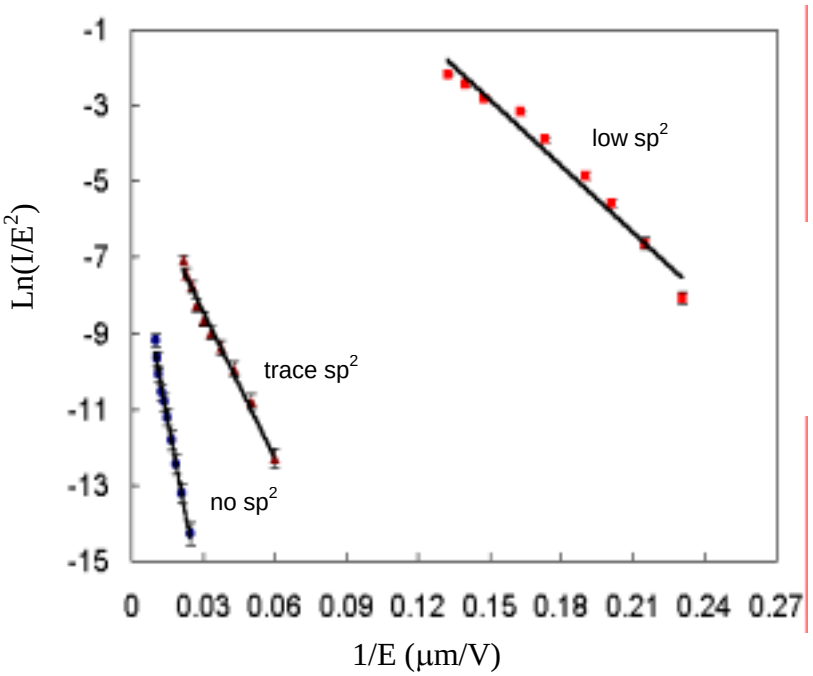


**Figure 6.26.** The effect of $sp^2$ content on F-N plot of undoped diamond tips after VTE treatment.

The effect of $sp^2$ content on p-type diamond tips before VTE treatment

The effect of $sp^2$ content on the I-E and F-N plots of p-type diamond tips before VTE treatment are shown in **Figures 6.27-6.28**. From **Figure 6.27,** it is obvious that the turn-on electric field of the diamond tips reduces as $sp^2$ content increases. The turn-on electric field of trace and low $sp^2$ content diamond tips are approximately 53 and 7 V/μm, respectively. From **Figure 6.28**, it can be seen again that the slope of F-N plots is shallower as $sp^2$ content increases. **Figure 6.23(c)** and **Figure 6.24(c)** show the effect of $sp^2$ content on the F-N slope ratio and work function ratio of p-type diamond tips using p-type trace $sp^2$ content diamond tip as a reference. From these figures, it can be seen that the F-N slope ratio and work function ratio of diamond tips reduce as $sp^2$ content increases.

It is interesting to observe that the F-N slope ratio and work function ratio of low to trace $sp^2$ content p-type diamond tip are much lower compare to those for undoped diamond tip. This suggests that p-type doping has some secondary effects so that the role of $sp^2$ content in undoped and p-type diamond are different. This interesting result will be further discussed in the theoretical discussion of the effect of doping on diamond tips.

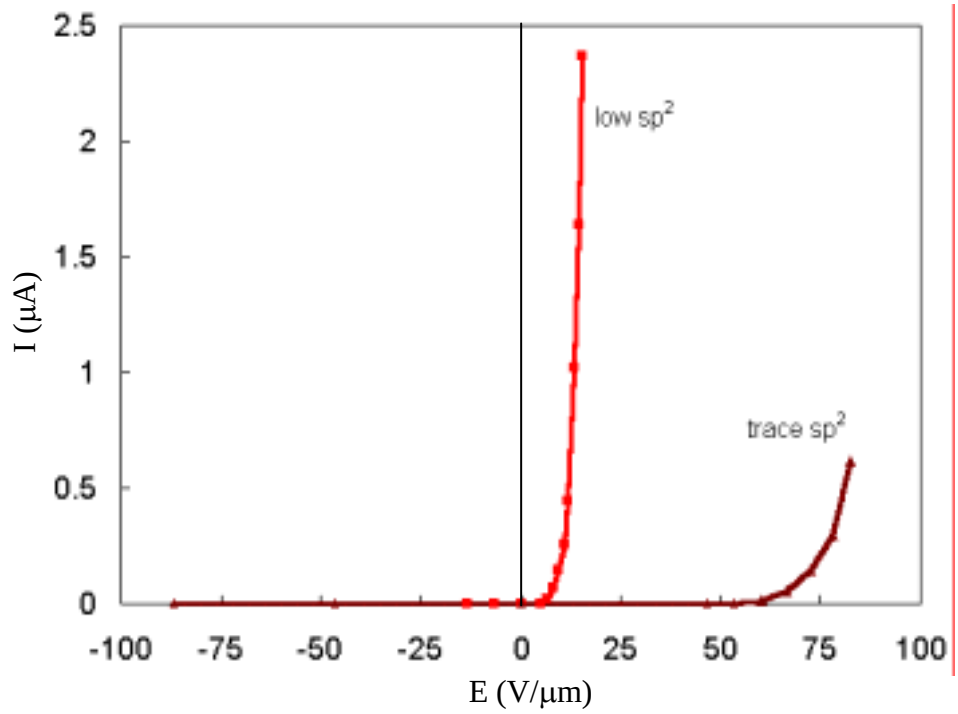


**Figure 6.27.** The effect of $sp^2$ content on I-E plot of p-type diamond tips before VTE treatment.

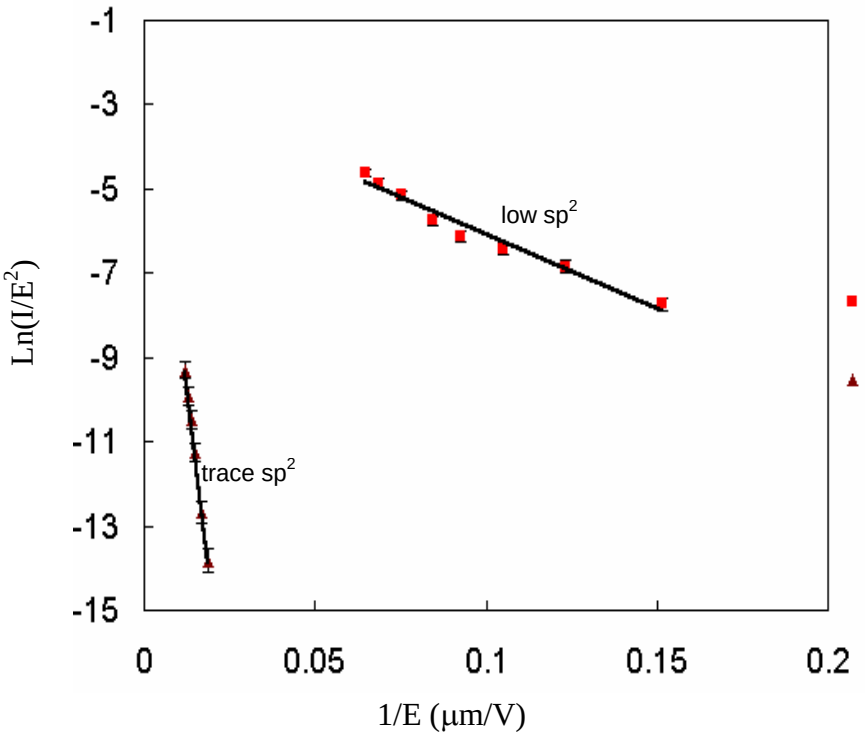


**Figure 6.28.** The effect of $sp^2$ content on F-N plot of p-type diamond tips before VTE treatment.

The effect of $sp^2$ content on p-type diamond tips after VTE treatment

The effect of $sp^2$ content on the I-E and F-N plots of p-type diamond tips before VTE treatment are shown in **Figures 6.29-6.30**. From **Figure 6.29,** it is obvious that the turn-on electric field of the diamond tips reduces as $sp^2$ content increases. The turn-on electric field of trace and low $sp^2$ content diamond tips are approximately 6 and 1 V/μm, respectively. From **Figure 6.30**, it can be seen again that the slope of F-N plots is shallower as $sp^2$ content increases. **Figure 6.23(d)** and **Figure 6.24(d)** show the effect of $sp^2$ content on F-N slope ratio and the work function ratio of p-type diamond tips using p-type trace $sp^2$ content diamond tip as a reference. From these figures, it can be seen that the F-N slope ratio and work function ratio of diamond tips reduce as $sp^2$ content increases.

It is interesting to see that the F-N slope ratio and work function ratio of low $sp^2$ content diamond tips before and after VTE treatment are very different. This suggests that the F-N slope ratio and work function ratio have correlation with $sp^2$ content that depend on VTE treatment for p-type diamond tips, which is in contrast to undoped diamond tips. This interesting result will be further discussed in the theoretical discussion of the effect of $sp^2$ content on diamond tips.

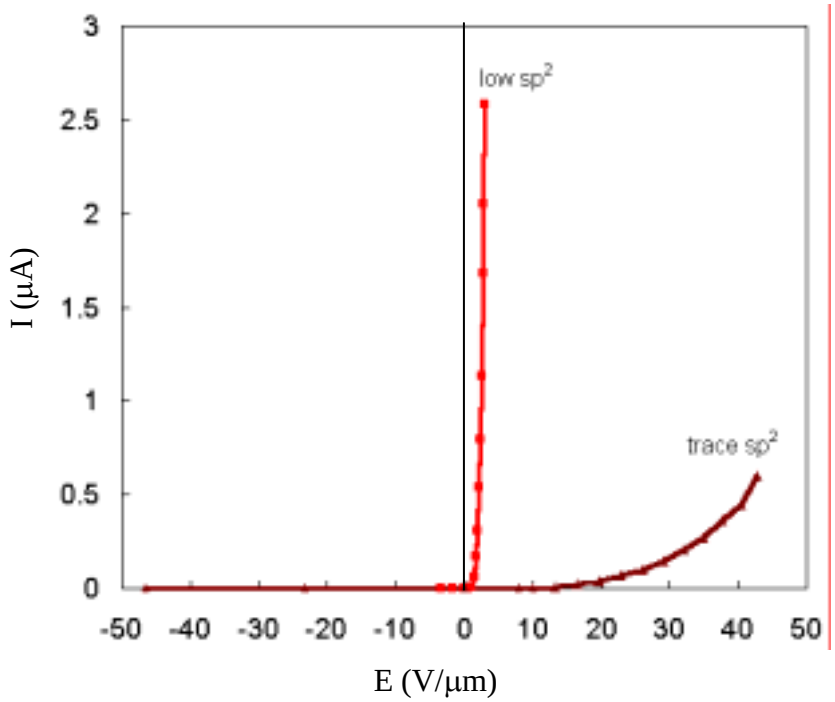


**Figure 6.29.** The effect of $sp^2$ content on I-E plot of p-type diamond tips after VTE treatment.

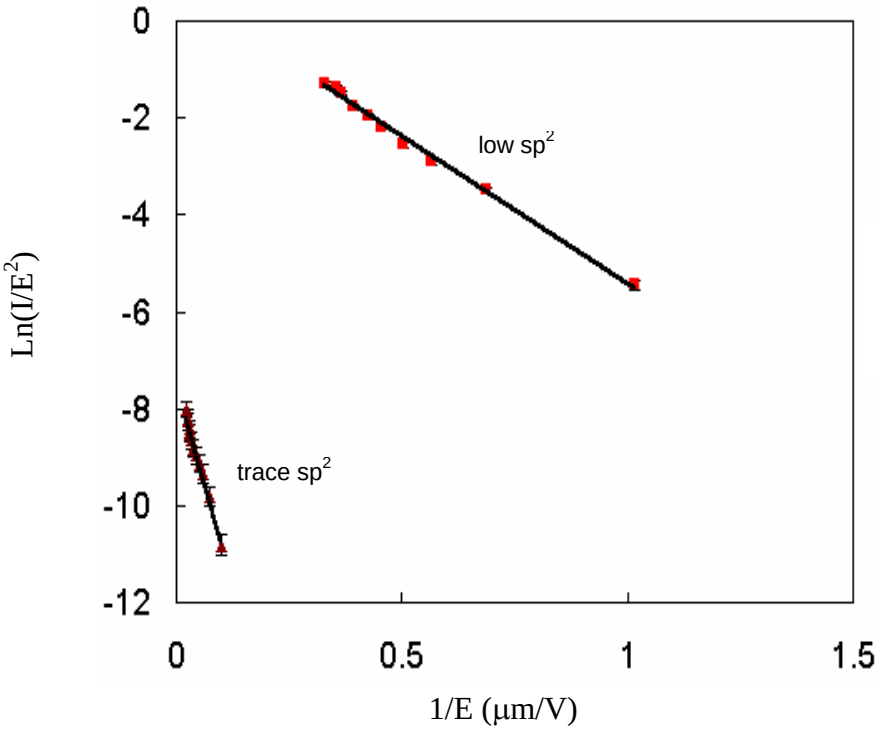


**Figure 6.30.** The effect of $sp^2$ content on F-N plot of p-type diamond tips after VTE treatment.

Modeling of the effect of $sp^2/sp^3$ composition on diamond field emission

From the overall results, it can be primarily concluded that the turn-on electric field of the undoped diamond tips tends to reduce as $sp^2$ (graphitic) content increases. These results are in agreement with other researches on diamond coated tip or planar diamond film [85-88, 94-95]. According to the experimental results, we have proposed two hypotheses to explain how $sp^2$ content improves field emission of diamond tip.

The first hypothesis: Defect-induced band due to $sp^2$ content

The first hypothesis proposes that the enhanced field emission may originate from the defect-induced energy band(s) formed within the energy gap of the diamond bulk [85-88] as previously described in **Figure 3.9**. A series of defect-induced bands is assumed to form throughout the energy gap due to the presence of structural defects created by the embedded carbon particles or $sp^2$ nano-crystallites. If these defect bands are wide enough or closely spaced, electron hoping within the band(s) or excitation from the valence band could easily provide a steady flow of electrons to the surface to sustain stable emission of electron in vacuum under low

applied electric field. The formation of defect bands moves the Fermi level toward the conduction band, thereby reduces the work function, and enhances electron emission. Therefore, this hypothesis is a lowering of work function model. Since diamond has small electron affinity [56], it may be assumed that $E_c$ coincides with $E_{vac}$. Thus, the relative Fermi level due to defect-induced band of different $sp^2$ contents can be shown in the energy band of diamond, **Figure 6.31**. It should be noted that the energy bands are not drawn to scale and the Fermi level denoted corresponding to the calculated work function values. The detail of defect-induced band is omitted for clarity. From the energy band diagram, these work function values seem to be unreasonably low. Thus, this model is highly improbable.

Moreover, the calculated work function ratios in terms of $sp^2$ content for undoped diamond tips remain the same after VTE treatment. In order to correlate this experimental result with the hypothesis, let's consider the energy band diagram of diamond tip before VTE and after VTE treatment as shown in **Figure 6.32**. In the energy band diagram, it is assumed that VTE treatment causes a change in surface band bending due to the change in surface states at the diamond-vacuum interface. Thus, the effective work function of low and no $sp^2$ content diamond tips change from $\Phi_{H1}$, $\Phi_{L1}$ (as shown in **Figure 6.32(a)**) to $\Phi_{H2}$, $\Phi_{L2}$ (as shown in **Figure 6.32(b)**). From the diagram, it can be seen that the work function difference between the different $sp^2$ contents should not be affected by VTE treatment, i.e., $\Delta\Phi_1 = \Phi_{L1} - \Phi_{H1} = \Delta\Phi_2 = \Phi_{L2} - \Phi_{H2}$, which is not true from the calculated results. In addition, the work function ratio in terms of $sp^2$ content diamond tips should depend on VTE treatment, since it can be shown that if $\Delta\Phi_1 = \Delta\Phi_2$, then the work function ratio $\Phi_{H1}/\Phi_{L1} = \Phi_{H2}/\Phi_{L2}$ only if $\Phi_{L1} = \Phi_{L2}$ and $\Phi_{H1} = \Phi_{H2}$, which means that the work function does not change due VTE treatment. This reassures disagreement with the experimental results. Therefore, it is clear that this hypothesis fails to explain the experimental result that the work function ratios for undoped diamond tip remain the same after VTE treatment.

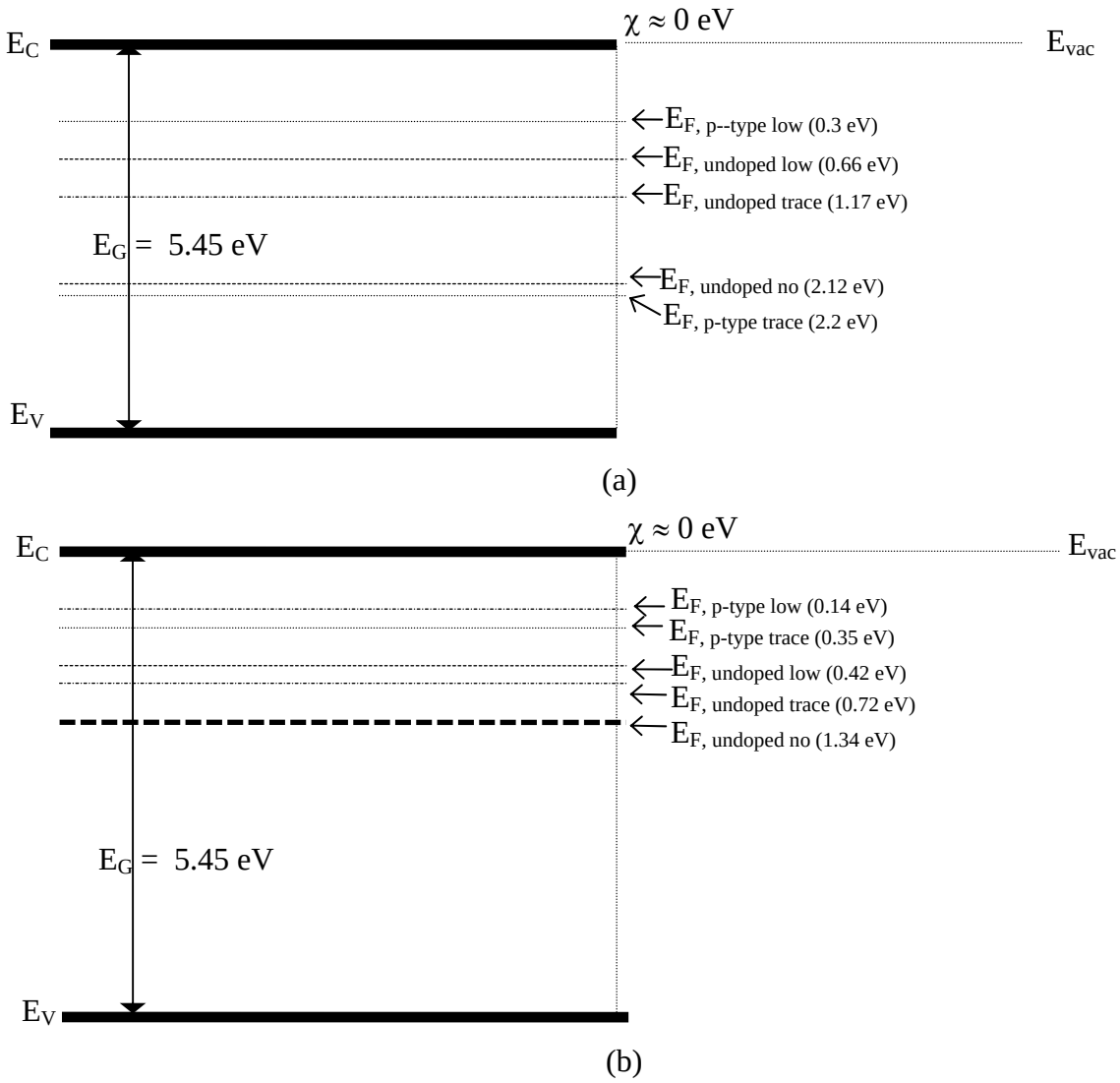


**Figure 6.31.** Fermi level relative to conduction band and vacuum level of diamond tips based on defect induced band model (a) before VTE treatment, and (b) after VTE treatment. Note: The Fermi levels obtained are unreasonable, see discussion in the text.

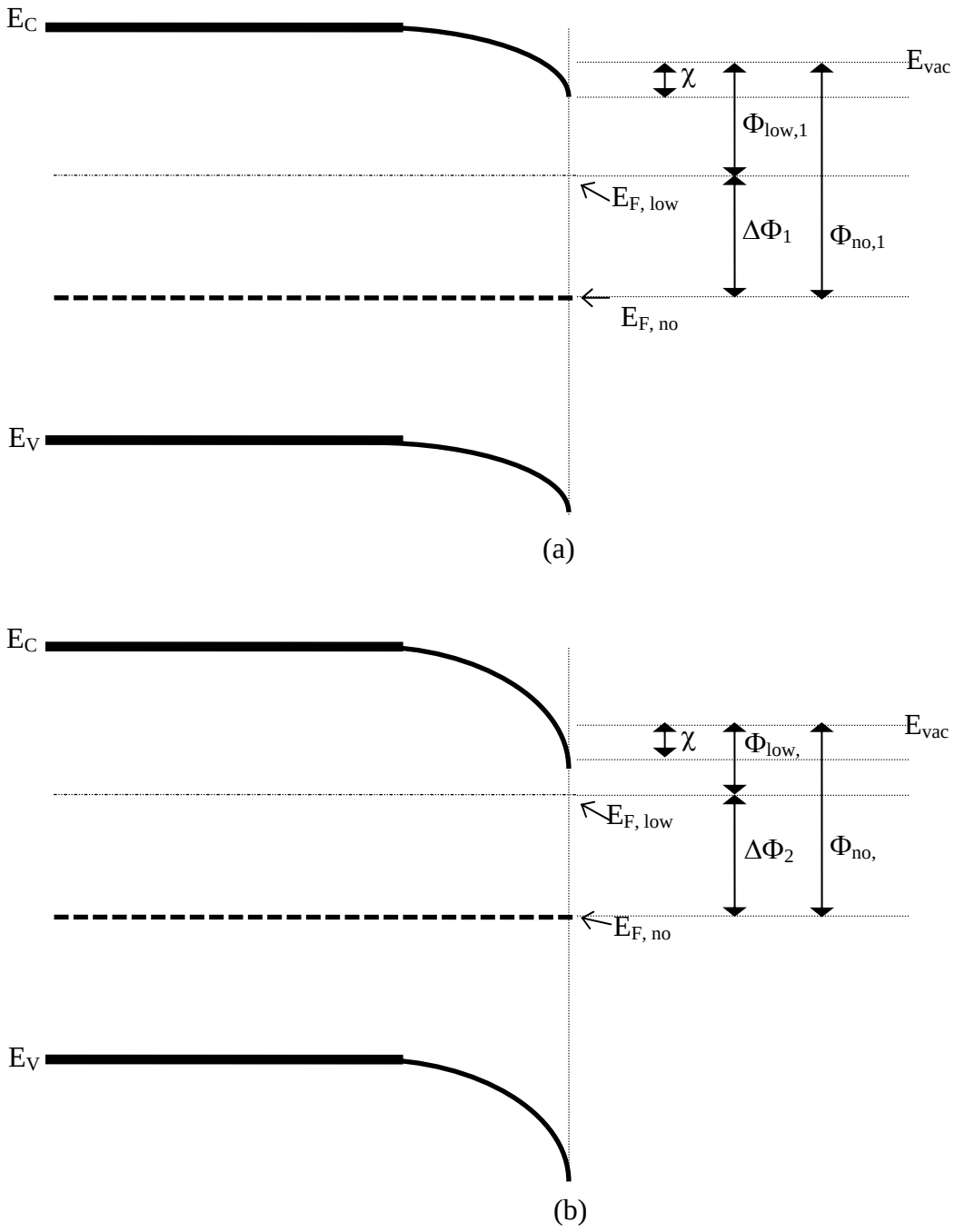


**Figure 6.32.** Energy band diagram of diamond tip with two different $sp^2$ contents. (a) Before VTE treatment. (b) After VTE treatment.

The second hypothesis: Cascaded MIM microstructures formed by $sp^2$ nano-particles

The second hypothesis proposes that isolated conducting $sp^2$ nano-particles in the diamond film form a series of cascaded MIM microstructures, which enhance the electric field inside diamond film and thereby increases the field enhancement factor. This model is derived from the hot electron emission model, which has been proposed to explain field emission from MIM microstructures [153-154].

The application of hot electron emission model to the diamond tips needs a major modification because the original model treats $sp^2$ content [154] as a floating conducting particle at the vacuum interface, whereas in our case the $sp^2$ content is considered as embedded conducting particles in the insulating diamond. The energy band diagram of diamond film that we proposed is based on the hot electron diffraction model with an embedded $sp^2$ state as illustrated in **Figure 6.33**. In this energy band diagram, it is assumed that the energy band diagram of diamond has a small electron affinity.

The energy band diagram of the undoped diamond emitter system, with no $sp^2$ conducting particles in the diamond under applied electric field is shown in **Figure 6.33(a)**. From electrostatic calculation, voltage drop across diamond under a moderate applied electric field is sufficient to bend down the conduction band of diamond as illustrated. This allows electrons to tunnel into conduction band of diamond. However, electric field in diamond is small compared to vacuum field because $E_d \approx E_0/K_s \approx 0.17E_0$, where $E_d$, $E_0$, and $K_s$ are electric field in diamond, electric field in vacuum, and diamond dielectric constant, respectively. As a result, the electron tunneling distance, W, is very wide. This leads to a very small electron tunneling probability and low electron emission current.

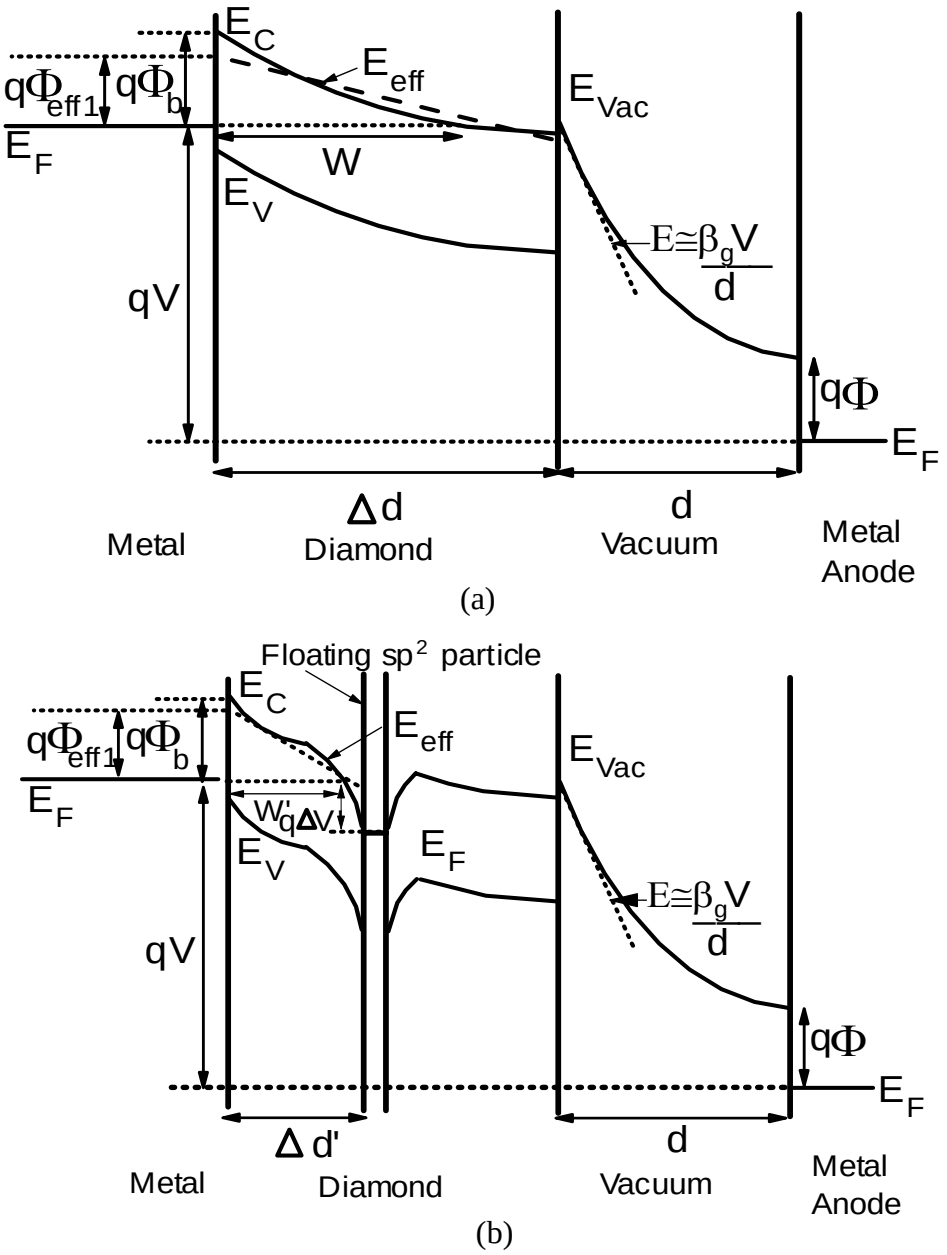


**Figure 6.33.** Energy band diagram for MIM microstructure model. (a) The energy band without a conducting particle. (b) The energy band with a conducting particle.

With $sp^2$ conducting particles embedded in the diamond tip, the energy band diagram under the same applied electric field is shown in **Figure 6.33(b)**. The $sp^2$ (graphite) conducting particle may be represented in the energy band diagram by a metal energy level similar to the metal back contact but with a very small dimension. This metallic particle has some finite conductivity and does not have as high electron density as the metal bulk. The approximation

should be reasonable because the conductivity of graphite is very high. From electrostatic principle, $sp^2$ conducting particles would introduce a potential between the $sp^2$ conducting particle and the metal contact, $\Delta V' \cong (1/K_s)(\Delta d'/d)V$, (where V is the anode-cathode voltage, d is the cathode-anode separation, $\Delta d'$ is the separation between the floating conducting particle and the metal-diamond interface (where $\Delta d' << d$), and $K_s$ is diamond dielectric constant). Furthermore, the image effect at the diamond-$sp^2$ interface causes band bending in the conduction band of diamond as illustrated in **Figure 6.33(b)**. Thus, the electric field in the metal-diamond-$sp^2$ region is enhanced by the MIM structure. The enhanced electric field decreases the width of tunneling distance, W', at the metal-diamond interface significantly, and thereby increases the electrons tunneling probability from metal into the conduction band of diamond. The electrons in the conduction band of diamond are then accelerated toward the next floating $sp^2$ particle under the induced electric field. Thus, the $sp^2$ particles would enhance diamond field emission.

At the floating $sp^2$ particle, it is assumed that electrons will undergo coherent scattering process by the electron diffraction [154-155]. In this case, electrons undergo a coherent scattering inside $sp^2$ particle embedded in the insulating diamond and surmount the barrier between the $sp^2$ metallic level and the conduction band of diamond. In order to apply the electron diffraction model, the embedded $sp^2$ particle should have configuration similar to a pinhole of a metallic film so that it can provide a favorable configuration allowing electrons to be diffracted and tunnel through the potential well under relatively low field. In this case, the edges of $sp^2$ nano-crystallite may be treated as the edge of pinholes where electrons can tunnel through. As a result, the conduction channel will be formed preferentially in this region when electric field is applied to the structure. A portion of electrons that can tunnel through the successive $sp^2$-$sp^3$ (graphite-diamond) potential barrier will be accelerated toward the vacuum interface. Furthermore, for diamond, the low electron affinity at diamond-vacuum interface promotes the emission of electrons from the conduction channel because of small potential barrier at the vacuum interface. Therefore, the electron emission at low electric field is feasible.

In **Figure 6.33(b)**, only single $sp^2$ conducting particle has been shown for simplicity, however in the real diamond film there are a lot of such conducting particles. However, the concept of emission mechanism is essentially the same as the discussion of a $sp^2$ conducting particle. The modification can be extended by the use of cascading effects of conducting

particles as illustrated in **Figure 6.34**. In this figure, the diamond regime is enlarged for illustrating purpose.

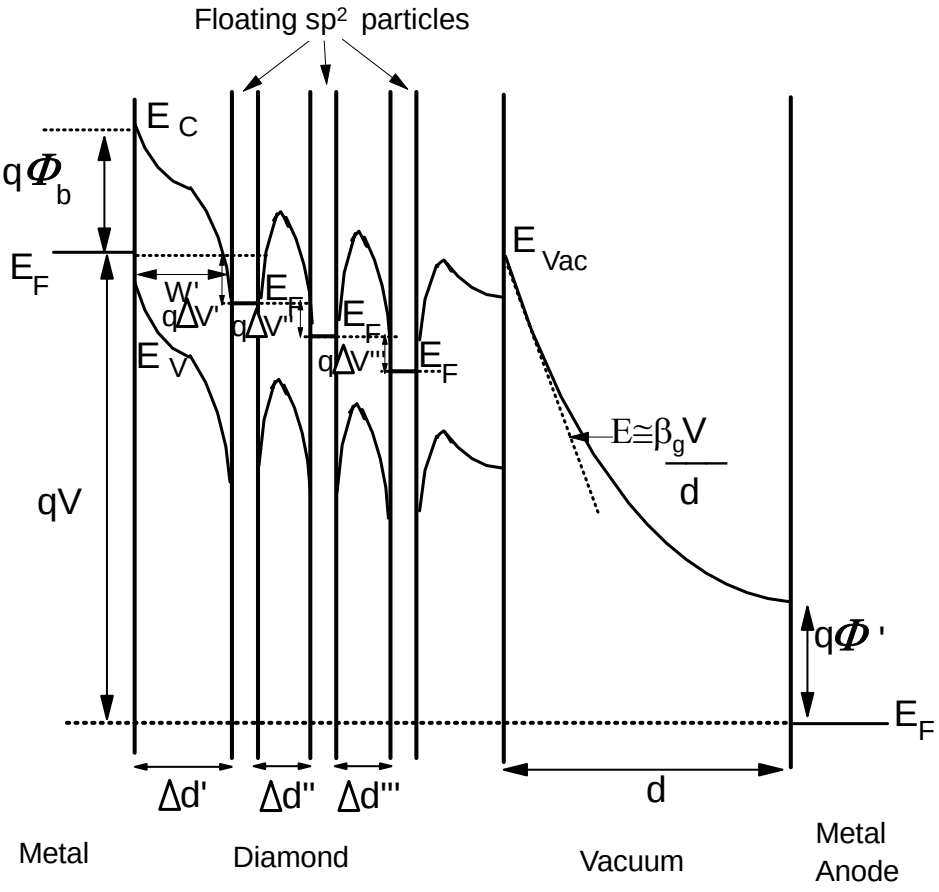


**Figure 6.34.** Energy band diagram for cascaded MIM microstructure model illustrates how a series of floating conducting particles embedded in a dielectric medium can cooperate in formation of an electron conduction channel.

Based on this hypothesis, the embedded $sp^2$ conducting particles do not affect the work function of diamond film. Therefore, it may be assumed that the work functions of diamond tip with different $sp^2$ contents remain the same, but with different field enhancement factors. The effect of electric field enhancement due to $sp^2$ particles may be accounted into Fowler-Nordhiem equation by a new field enhancement component, $\beta_{sp2}$. Therefore, the previous calculated work function and field enhancement factor based on constant $\beta$ need to be revised.

As described below, a new field enhancement component, $\beta_{sp2}$, due to the effect of the cascaded $sp^2$–diamond-$sp^2$ microstructures can be included in the total field enhancement factor,

$\beta$, of the F-N equation. It is assumed that for the no $sp^2$ content diamond tips, the effect of the cascaded MIM microstructures is negligible. Thus, there is no $\beta_{sp2}$ contribution to the total $\beta$. Hence, $\beta_{sp2}$ =1 for diamond tips contain no $sp^2$ content. For the same token, an additional field enhancement component due to the effect of VTE treatment, $\beta_t$, is introduced into the total field enhancement factor, $\beta$. Likewise, it is assumed that $\beta_t$ = 1 prior to VTE treatment. The detail discussion of VTE treatment will be presented later. Therefore, the total field enhancement factor can be expressed in terms of the product of each of field enhancement component as

$$\beta = \beta_g \beta_{sp2} \beta_t \quad (6.4)$$

where $\beta_g$ is the field enhancement component due to the tips' geometry ($\beta_g$ = h/r = 100 in our case).

Based on these assumptions, the work function for no $sp^2$ content diamond tip before VTE treatment was used to obtain the new field enhancement factors for diamond tips with various $sp^2$ contents. The calculated results are shown in **Table 6.2**. **Figure 6.35** shows the effect of $sp^2$ content on the field enhancement component, $\beta_{sp2}$, (from **Table 6.2**) of diamond tips for the same doping and the same treatment.

According to this hypothesis, the field enhancement component, $\beta_{sp2}$, due to the effect of $sp^2$ content should be the same for diamond tips with the same $sp^2$ content because the same $sp^2$ content should result in the same field enhancement factor. From **Table 6.2** and **Figure 6.35**, $\beta_{sp2}$ of the undoped diamond tips before and after VTE treatment remains the same. This means that $\beta_{sp2}$ does not depend on VTE treatment and depends only on $sp^2$ content. In addition, $\beta_{sp2}$ of p-type diamond tips before VTE treatment are quite the same except the low $sp^2$ case. Therefore, this hypothesis provides a reasonable explanation for the observed experimental results that the F-N slope ratios are constant independent of VTE treatment. Hence, it can be preliminarily concluded that this hypothesis is more likely than the first one. On the other hand, $\beta_{sp2}$ is not constant for p-type low $sp^2$ diamond tips before and after VTE treatment. This result seems to contradict to this hypothesis. However, it is possible that the p-type doping may modified the total field enhancement factor in conjunction with $sp^2$ particles, so that $\beta_{sp2}$ appeared to be different. The detail of the effect of p-type doping will be further discussed in the subsequent section.

**Table 6.2.** Calculated results from Fowler-Nordhiem plots based on the field enhancement due to cascaded MIM microstructure model

| Treatment | Doping | $sp^2$ content | Φ(eV) | β | $\beta_g$ | $\beta_t$ | $\beta_{sp2}$ |
|---|---|---|---|---|---|---|---|
| Before VTE treatment | no | no | 2.13 | 100 | 100 | 1 | 1 |
| | no | trace | 2.13 | 242.46 | 100 | 1 | 2.42 |
| | no | low | 2.13 | 570.91 | 100 | 1 | 5.71 |
| | p | trace | 3.97 | 242.46 | 100 | 1 | 2.42 |
| | p | low | 3.97 | 4744.37 | 100 | 1 | 47.44 |
| After VTE treatment | no | no | 2.13 | 198.41 | 100 | 1.98 | 1 |
| | no | trace | 2.13 | 509.49 | 100 | 1.98 | 2.57 |
| | no | low | 2.13 | 1118.51 | 100 | 1.98 | 5.64 |
| | p | trace | 3.97 | 3772.70 | 100 | 14.69 | 2.57 |
| | p | low | 3.97 | 27255.03 | 100 | 14.69 | 18.55 |

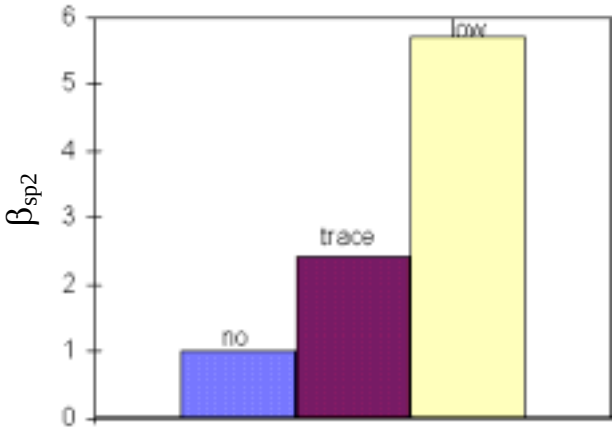


a) The effect of $sp^2$ content on undoped diamond tips before V-T-E treatment.

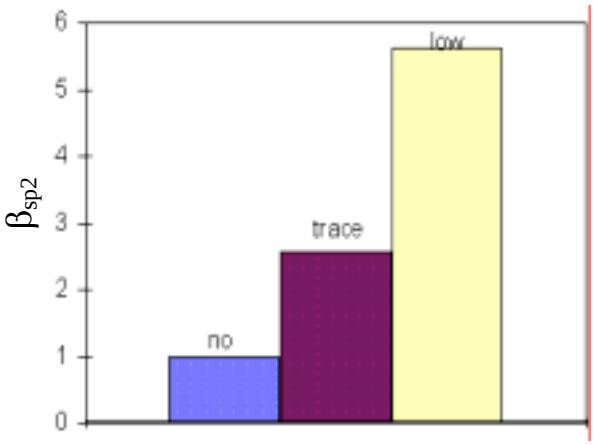


b) The effect of $sp^2$ content on undoped diamond tips after V-T-E treatment.

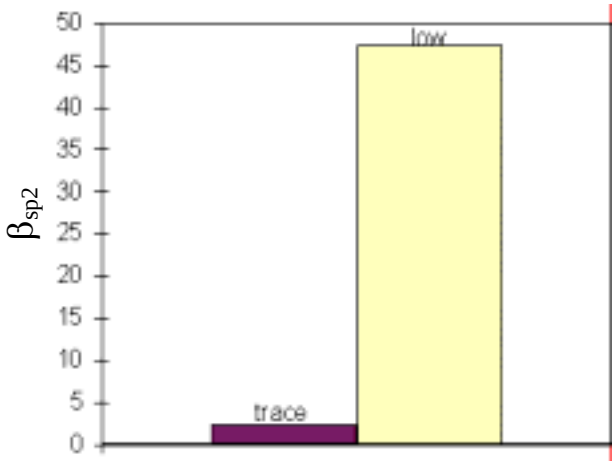


c) The effect of $sp^2$ content on p-type diamond tips before V-T-E treatment.

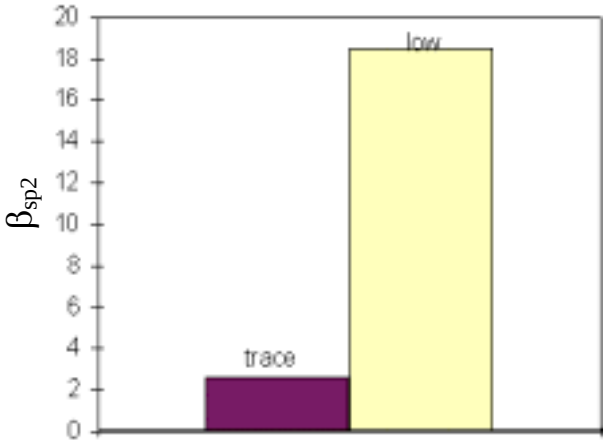


d) The effect of $sp^2$ content on p-type diamond tips after V-T-E treatment.

**Figure 6.35.** The effect of $sp^2$ content on $\beta_{sp2}$ of diamond tips for the same doping and same treatment.

Discussion of the effect of VTE treatment

The detail discussion on the effect of VTE treatment is separated into two following main cases.

The effect of VTE treatment on undoped diamond tips

The effect of VTE treatment on I-E and F-N plots of undoped diamond tips with no, trace, and low $sp^2$ content are shown in **Figures 6.36-6.41**. From **Figures 6.36, 6.38,** and **6.40**, it is obvious that the turn-on electric field of undoped diamond tips reduces after VTE treatment. The turn-on electric field of undoped diamond tips with no $sp^2$ content before and after VTE treatment are approximately 67 and 40 V/μm, respectively. The turn-on electric field of undoped diamond tips with trace $sp^2$ content before and after VTE treatment are approximately 30 and 17 V/μm, respectively. The turn-on electric field of undoped diamond tips with low $sp^2$ content before and after VTE treatment are approximately 12 and 4 V/μm, respectively. From **Figures 6.37**, **6.39** and **6.41**, it is clear that the slopes of F-N plots are shallower after VTE treatment. **Figure 6.42(a-c)** and **Figure 6.43(a-c)** show the effect of treatment on F-N slope ratio and the work function ratio of undoped diamond tips with no, trace, and low $sp^2$ content, respectively using the corresponding undoped diamond tip before VTE treatment as a reference. It can be seen that the F-N slope ratio and work function ratio of diamond tips reduce after VTE treatment.

It is interesting to notice that the F-N slope ratio and work function ratio of undoped diamond tips with no, trace and low $sp^2$ content after VTE treatment remain almost the same. This suggests that the F-N slope ratio and work function ratio of diamond tips have correlation with VTE treatment independent of the $sp^2$ content of undoped diamond tips. This is the converse of the results in the previous discussion. This interesting result will be further discussed in the modeling of the effect of treatment on diamond tips.

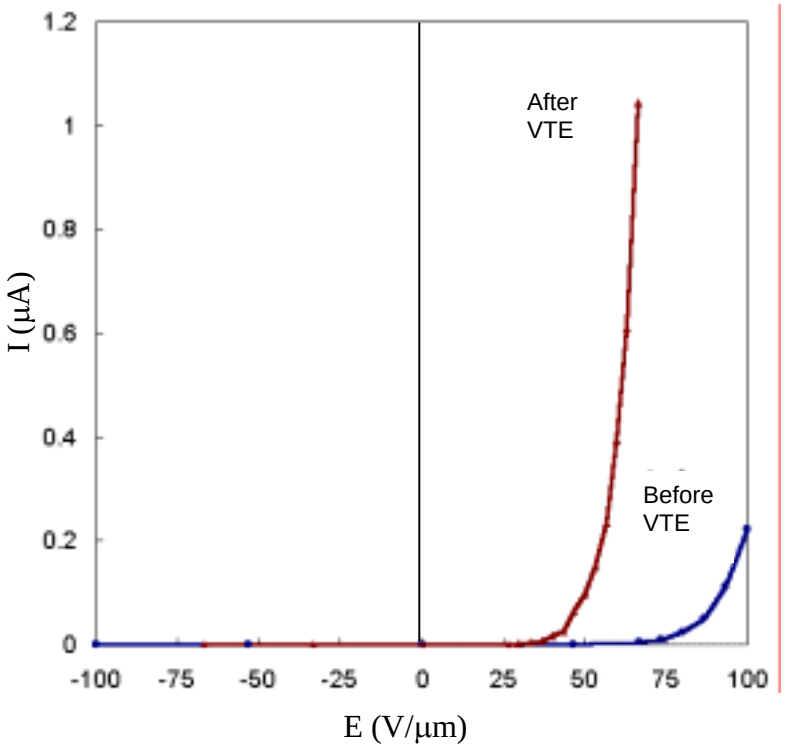


**Figure 6.36.** The effect of VTE treatment on I-E plot of no $sp^2$ undoped diamond tips.

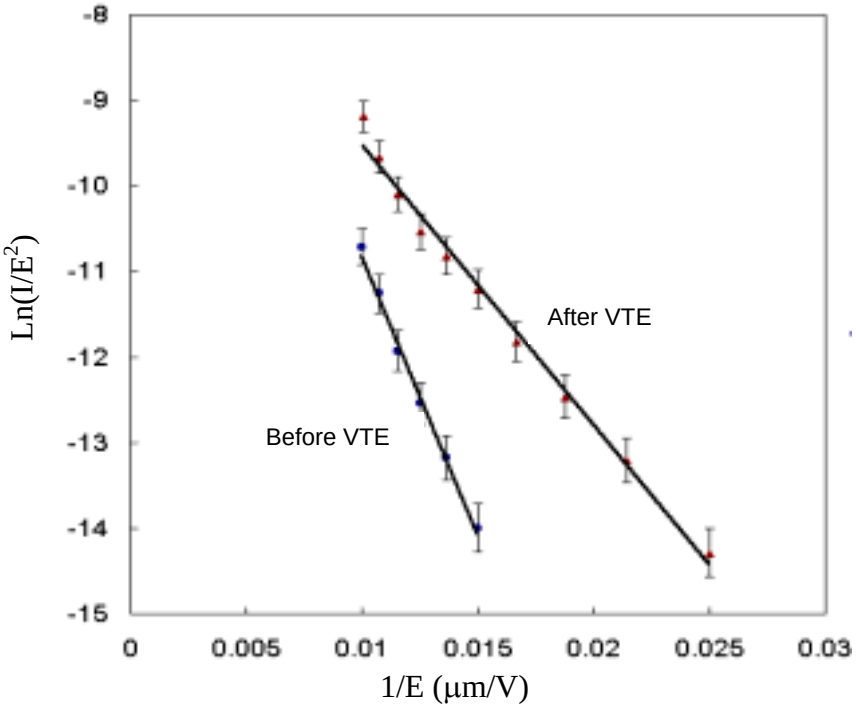


**Figure 6.37.** The effect of VTE treatment on F-N plot of no $sp^2$ undoped diamond tips.

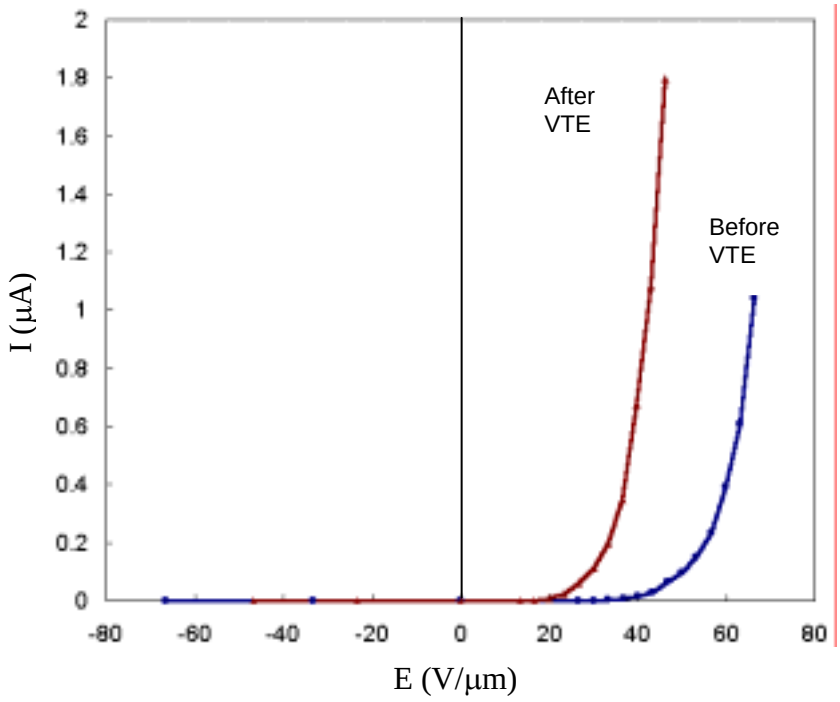


**Figure 6.38.** The effect of VTE treatment on I-E plot of trace $sp^2$ undoped diamond tips.

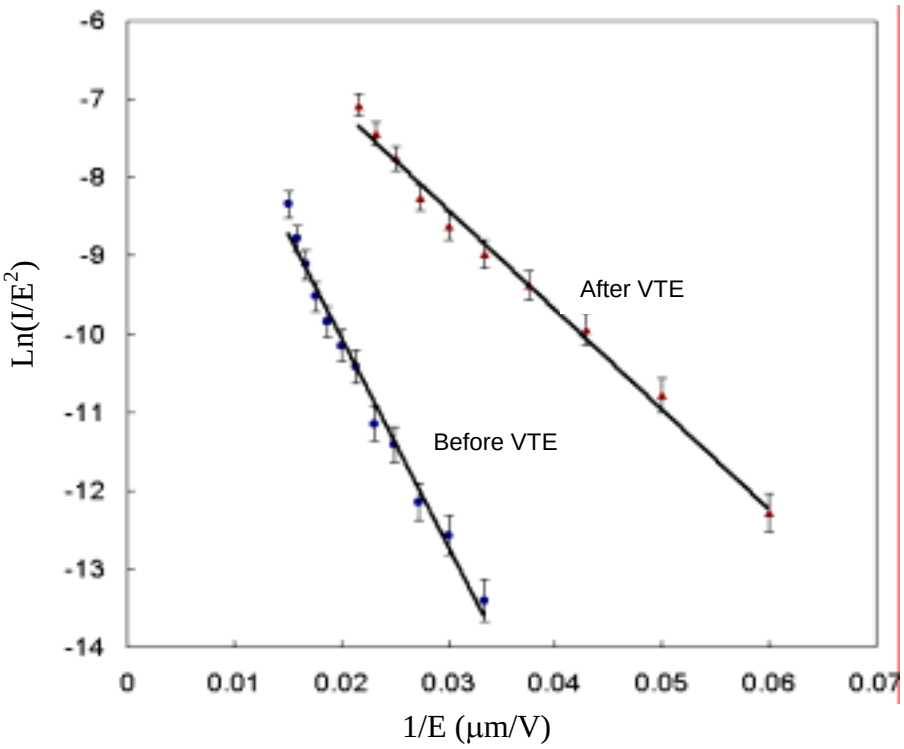


**Figure 6.39.** The effect of VTE treatment on F-N plot of trace $sp^2$ undoped diamond tips.

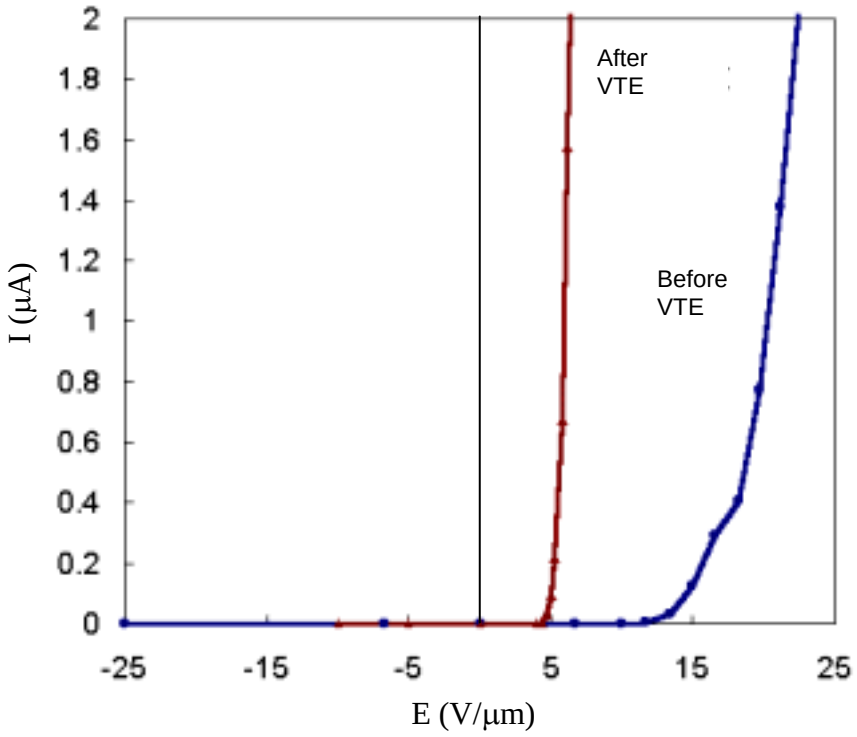


**Figure 6.40.** The effect of VTE treatment on I-E plot of low $sp^2$ undoped diamond tips.

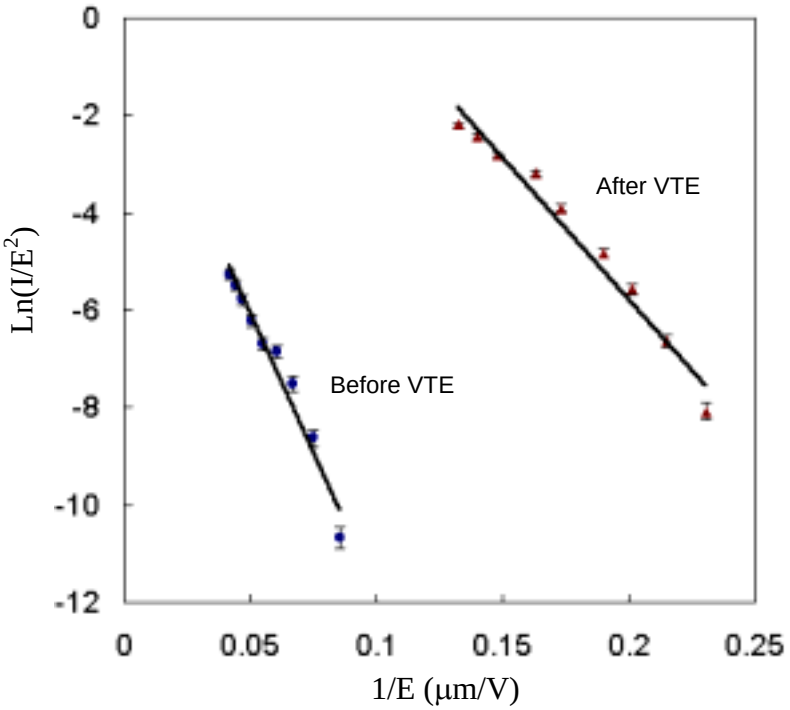


**Figure 6.41.** The effect of VTE treatment on F-N plot of low $sp^2$ undoped diamond tips.

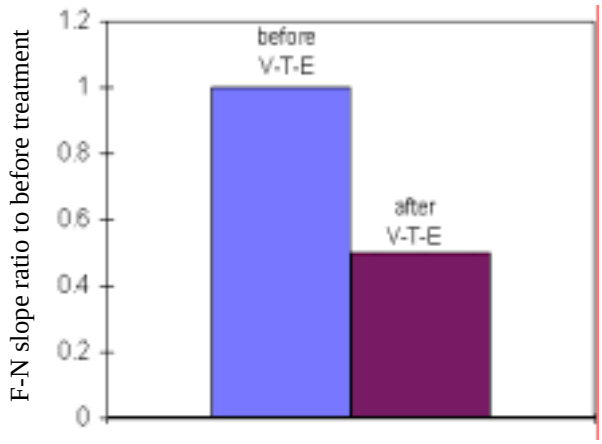


a) The effect of treatment on undoped no $sp^2$ content diamond tips.

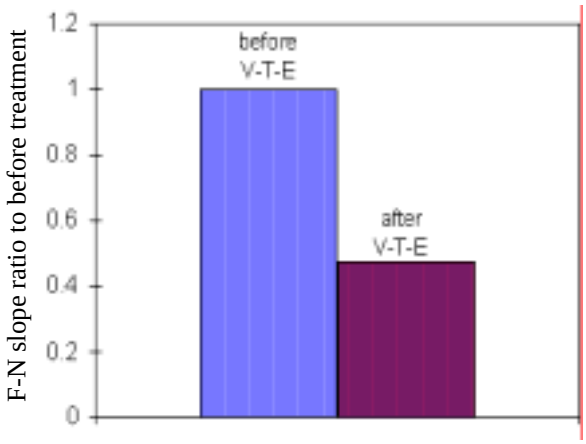


b) The effect of treatment on undoped trace $sp^2$ content diamond tips.

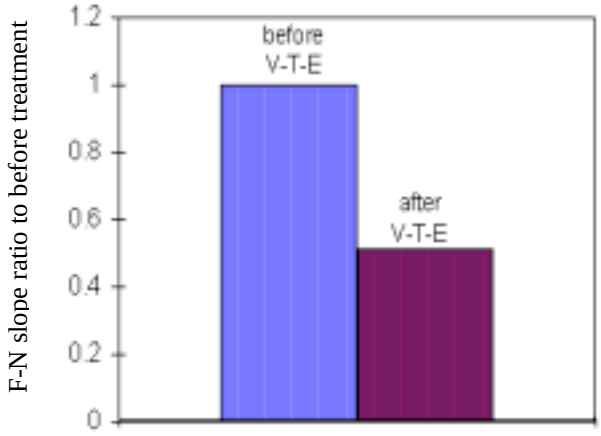


c) The effect of treatment on undoped low $sp^2$ content diamond tips.

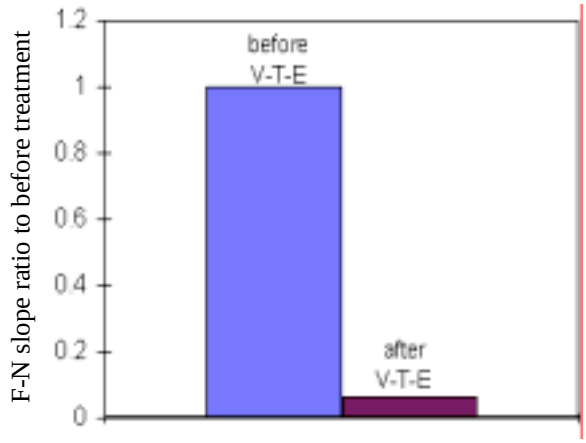


d) The effect of treatment on p-type trace $sp^2$ content diamond tips.

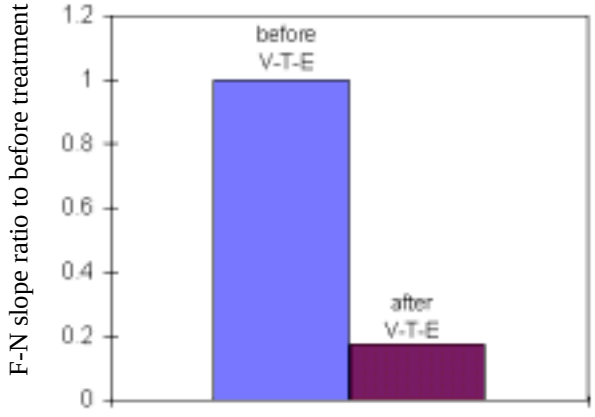


e) The effect of treatment on p-type low $sp^2$ content diamond tips.

**Figure 6.42.** The effect of treatment on the F-N slope ratio of diamond tip for the same $sp^2$ content and same doping.

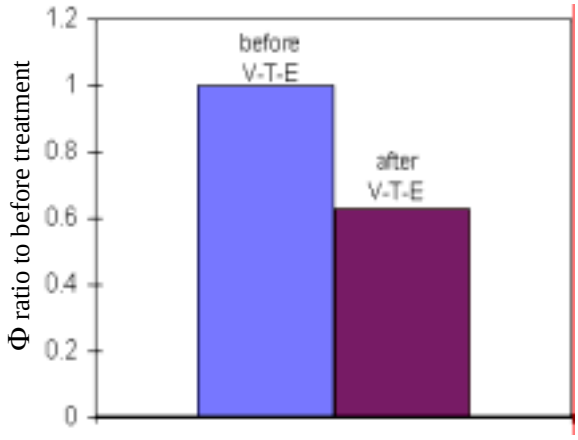


a) The effect of treatment on undoped no $sp^2$ content diamond tips.

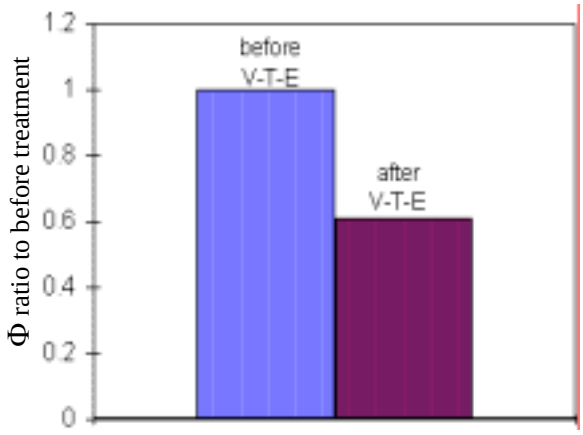


b) The effect of treatment on undoped trace $sp^2$ content diamond tips.

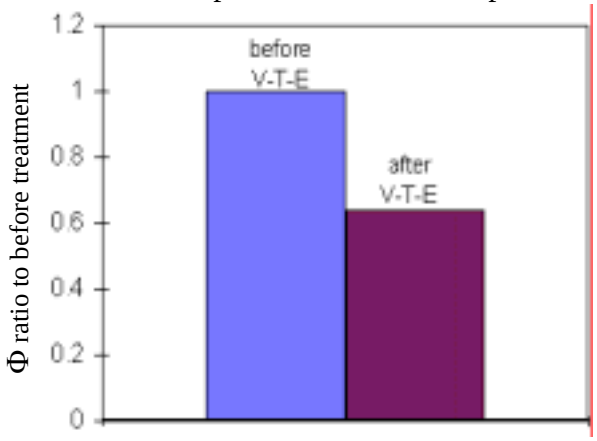


c) The effect of treatment on undoped low $sp^2$ content diamond tips.

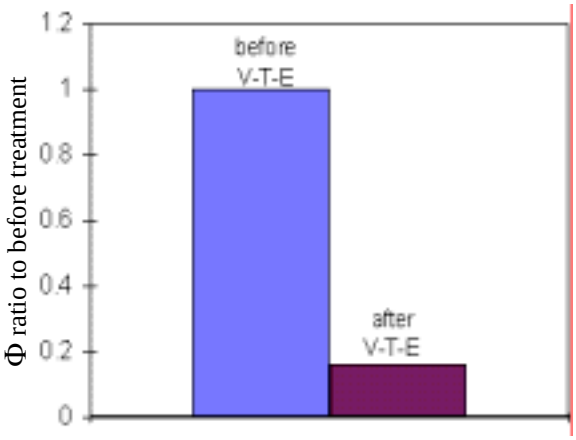


d) The effect of treatment on p-type trace $sp^2$ content diamond tips.

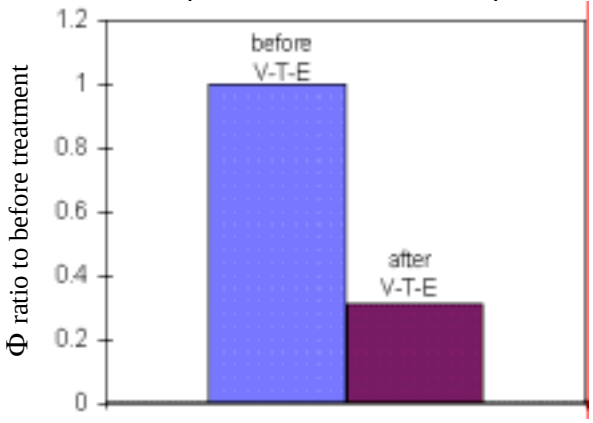


e) The effect of treatment on p-type low $sp^2$ content diamond tips.

**Figure 6.43.** The effect of treatment on the Φ ratio of diamond tip for the same $sp^2$ content and same doping.

The effect of VTE treatment on p-type diamond tips

The effect of VTE treatment on I-E and F-N plots of p-type diamond tips with trace and low $sp^2$ content are shown in **Figures 6.44-6.47**. From **Figure 6.44** and **Figure 6.46**, it is obvious that the turn-on electric field of the p-type diamond tips reduces after VTE treatment. The turn-on electric field of p-type diamond tips with trace $sp^2$ content before and after VTE treatment are approximately 53 and 6 V/μm, respectively. The turn-on electric field of p- type diamond tips with low $sp^2$ content before and after VTE treatment are approximately 7 and 1 V/μm, respectively. From **Figure 6.45** and **Figure 6.47**, it is clear that the slopes of F-N plots are significantly shallower after VTE treatment. **Figure 6.42(d-e)** and **Figure 6.43(d-e)** show the effect of treatment on the F-N slope ratio and work function ratio of p-type diamond tips with trace and low $sp^2$ content using the corresponding p-type diamond tip before VTE treatment as a reference. It can be seen that the F-N slope ratio and work function ratio of diamond tips reduce after VTE treatment.

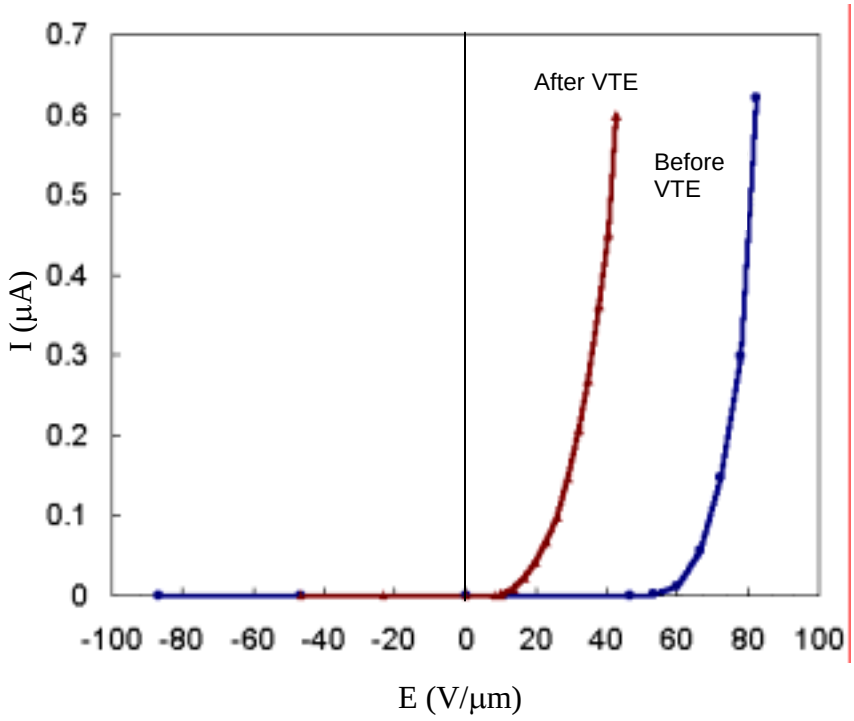


**Figure 6.44.** The effect of VTE treatment on I-E plot of trace $sp^2$ p-type diamond tips.

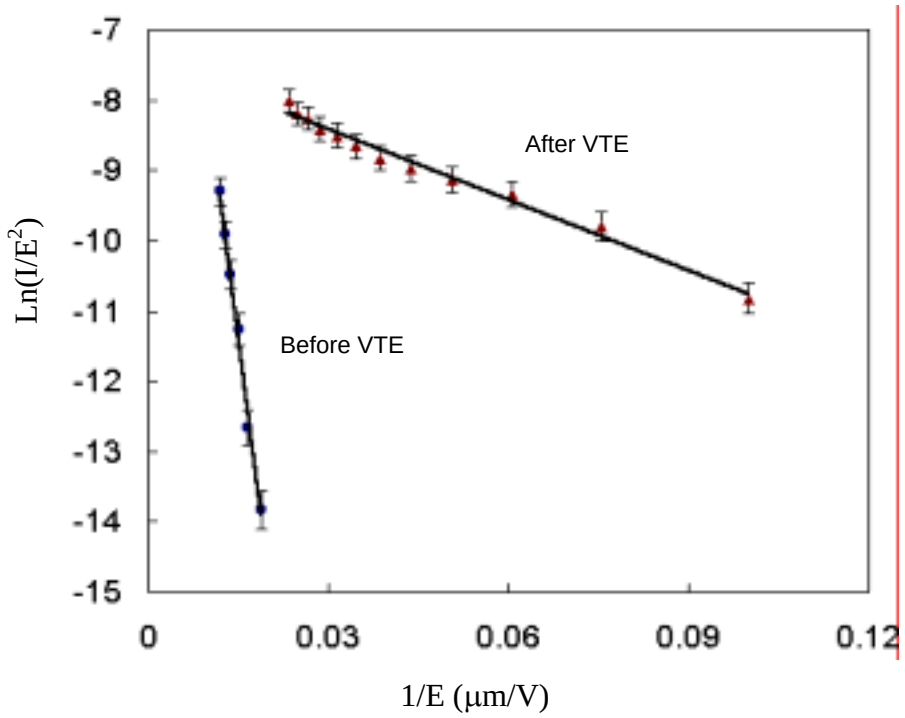


**Figure 6.45.** The effect of VTE treatment on F-N plot of trace $sp^2$ undoped diamond tips.

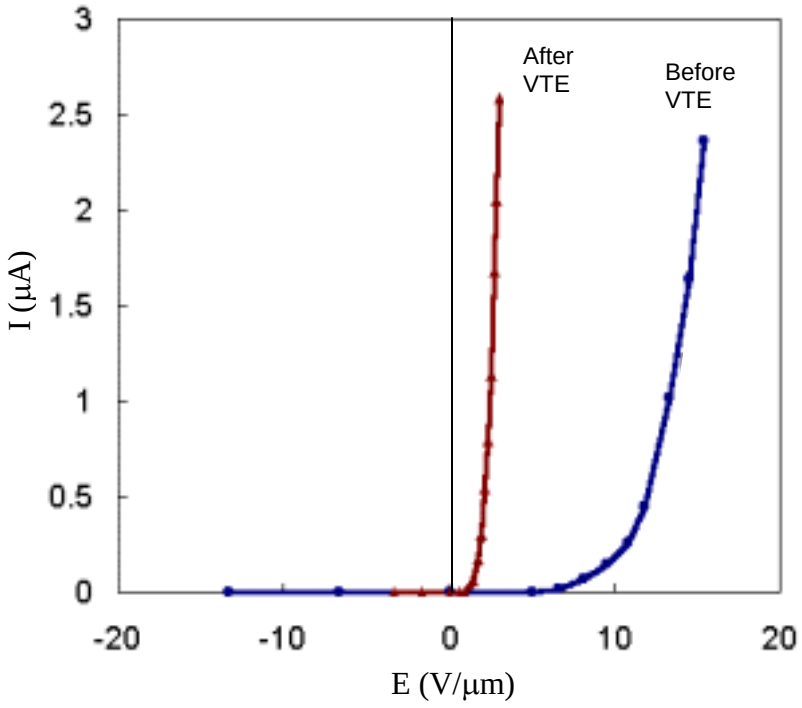


**Figure 6.46.** The effect of VTE treatment on I-E plot of low $sp^2$ p-type diamond tips.

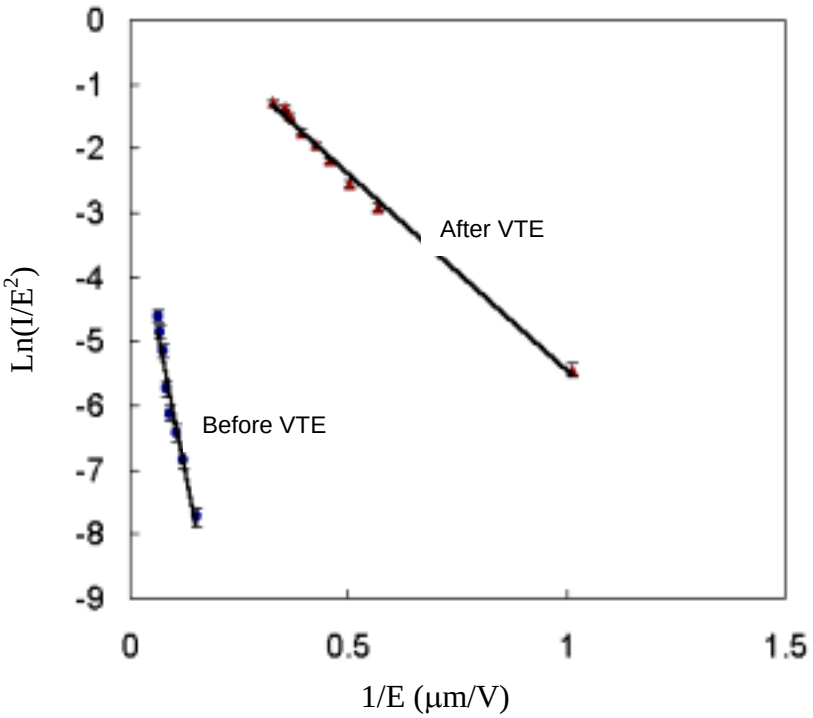


**Figure 6.47.** The effect of VTE treatment on F-N plot of low $sp^2$ p-type diamond tips.

It is interesting that the F-N slope ratio and the work function ratio of p-type diamond tips with trace and low $sp^2$ content after VTE treatment do not remain the same. This suggests that the F-N slope ratio and work function ratio have correlation with VTE treatment that depends on the $sp^2$ content of p-type diamond. This interesting result will be further discussed in the modeling of the effect of treatment on diamond tips.

Modeling on the effect of VTE treatment on diamond tips

From the overall results, it can be concluded primarily that the turn-on electric field of the diamond tips reduces after VTE treatment in all cases. In addition, it should be noted that the stability of the field emission characteristic is also improved after this treatment. According to the experimental results, we propose two hypotheses to explain how VTE treatment improves the field emission characteristics.

The first hypothesis: the reduction of work function due to impurity desorption

The first hypothesis proposes that VTE treatment reduces the surface work function due to impurity desorption. In vacuum-thermal-electric treatment, the cathode is heated while the tips

are under electric field stress. The emission under heat and electric field results in surface cleaning process. The surface cleaning helps to improve field emission enhancement and stabilizes field emission characteristic of diamond field emitters. During fabrication process, adsorption of impurities may occur on the diamond surface. The adsorption of impurity on diamond surface increases the surface work function because the additive impurities influence the surface potential and electronic surface states. Therefore, the impurities are able to shift and populate or depopulate surface states. Consequently, the surface work function is changed due to impurity adsorption.

Even though, diamond is chemically inert, it does not exclude surface adsorption to some impurities or gases such as oxygen. It has been known that oxygen adsorption on diamond surface results in positive electron affinity due to the effect of C-O or C-$O_2$ bonding on the diamond surface. It has been reported [148-149,186], when diamond (100) surfaces were cleaned and annealed in ultrahigh vacuum to a high temperature >1050°C, a reduction of oxygen on the diamond surface occurred and a lowering of the work function and electron affinity (from positive to negative) were observed. For our case, even though VTE treatment was conducted at a relatively low temperature (150°C), but the effect of applied electric field and electron emission may accelerate the impurity desorption process to occur at low temperature. Therefore, the observed field emission enhancement may result from the reduction of surface work function due to impurity (e.g., oxygen) desorption. However, according to **Figure 6.43**, the effect of VTE treatment resulted in the work function reduction of more than 40% in all cases, it is unlikely that the effect of surface cleaning alone would cause drastic reduction in the surface work function because the adsorption problem on diamond surface is not as severe as Si or metal surfaces.

The second hypothesis: the tip deformation due to field forming process.

The second hypothesis proposes that VTE treatment results in tip deformation due to field forming process. The field forming process has been successfully done to provide field emission enhancement for metal (i.e., Mo) cathode tips [6]. According to the field forming process for a metal cathode, the enhanced emission is achieved by heating the cathode to a high temperature (>1000°C) while the tips are under high electric field stress. The tips were found to be reformed, due to the field-forming process, into a configuration that increases the electric

field locally on the tip surface for a given applied field. As a result, the geometrical field enhancement factor $\beta$ is increased.

Primarily, it can be seen that the vacuum-thermal-electric treatment process is similar to the field forming process. The differences between VTE treatment and field forming process are that the applied electric field stress and temperature are low for VTE treatment. However, the field forming process concept may be applicable to the VTE treatment because in the VTE treatment the moderate electric field was applied for a very long period of time. It is also possible that field forming process may occur on diamond tips at a relatively low temperature.

For our case, a similar observations in VTE treatment as explained in the field forming process have been observed: (i) while under VTE treatment, the emission current of the diamond tips increases and shifts toward a lower operating voltage and (ii) upon completion of VTE treatment and the cathode cooled to room temperature, the diamond tips retained the low voltage performance. Therefore, it is likely that the effect of VTE treatment on field enhancement may be explained by the similar way as the field forming process in the metal cathode and it may be the major contribution to the observed field enhancement. In order to verify this hypothesis, further morphology and physical characterization of the diamond tips after VTE treatment should to be conducted.

Based on this hypothesis, the work function for all diamond tips remains the same and the field enhancement factor is improved due to the change in the tip geometry. The effect of the enhanced electric field due to the tip deformation may be accounted into Fowler-Nordhiem equation by an additional field enhancement factor due to VTE treatment $\beta_t$, which has been introduced in eq. (6.5). Therefore, the previous calculated work functions and field enhancement factors, in **Table 6.2** based on constant $\beta$, need to be revised.

The $\beta_t$ for this discussion is estimated from eq. (6.5) using slightly different assumption from the previous case. As in the previous case, $\beta_t$ is 1 for the diamond tips before VTE treatment because there is no treatment. The work function of undoped diamond tips with no $sp^2$ content before VTE treatment is used as the reference for all undoped diamond tips. Similarly, the work function of p-type diamond tips with trace $sp^2$ content before VTE treatment is used as the reference for all p-type diamond tips. However, in order to consider the effect of VTE treatment only, the field enhancement component $\beta_{sp2}$ due to the effect of $sp^2$ content are assumed to be the same for the same $sp^2$ content for all treatments and these values are obtained

from before VTE treatment cases. Based on this assumption, the new additional field enhancement component $\beta_t$ are obtained. The calculated results are shown in **Table 6.3**. **Figure 6.48** shows the effect of treatment on $\beta_t$ (from **Table 6.3**) of diamond tips for the same doping and the same $sp^2$ content.

According to this hypothesis, the additional field enhancement factor due to the effect of VTE treatment ($\beta_t$) should be the same for the same treatment because the VTE treatment should cause tips deformed in similar manner so that the geometrical field enhancement factor should be changed by the same factor. From **Table 6.3** and **Figure 6.48**, $\beta_t$ due to VTE treatment of the undoped diamond tips are approximately the same for different $sp^2$ contents. Therefore, it is likely that this hypothesis provides a reasonable explanation for the experimental results that the F-N slope ratios (F-N slope before VTE treatment/F-N slope after VTE treatment) for all undoped diamond tips are constant independent of $sp^2$ content. However, this explanation does not agree with the results of p-type diamond tips. The results in **Figure 6.48(d)-(e)** indicate a variation in the F-N slope ratios of p-type diamond tips with trace and low $sp^2$ content. The detail of the effect of p-type doping will be further discussed in the modeling of the effect of p-type on diamond tips.

**Table 6.3.** Calculated results from Fowler-Nordhiem plots based on the field forming process.

| Doping | $sp^2$ content | Treatment | Φ(eV) | β | $\beta_g$ | $\beta_t$ | $\beta_{sp2}$ |
|---|---|---|---|---|---|---|---|
| no | low | before VTE | 2.13 | 100.00 | 100 | 1 | 1 |
| | | after VTE | 2.13 | 198.41 | 100 | 1.98 | 1 |
| no | trace | before VTE | 2.13 | 242.46 | 100 | 1 | 2.42 |
| | | after VTE | 2.13 | 509.49 | 100 | 2.10 | 2.42 |
| no | low | before VTE | 2.13 | 570.91 | 100 | 1 | 5.71 |
| | | after VTE | 2.13 | 1118.51 | 100 | 1.96 | 5.71 |
| p | trace | before VTE | 3.97 | 242.46 | 100 | 1 | 2.42 |
| | | after VTE | 3.97 | 3772.70 | 100 | 15.56 | 2.42 |
| p | low | before VTE | 3.97 | 4744.37 | 100 | 1 | 47.44 |
| | | after VTE | 3.97 | 27255.0 | 100 | 5.74 | 47.44 |

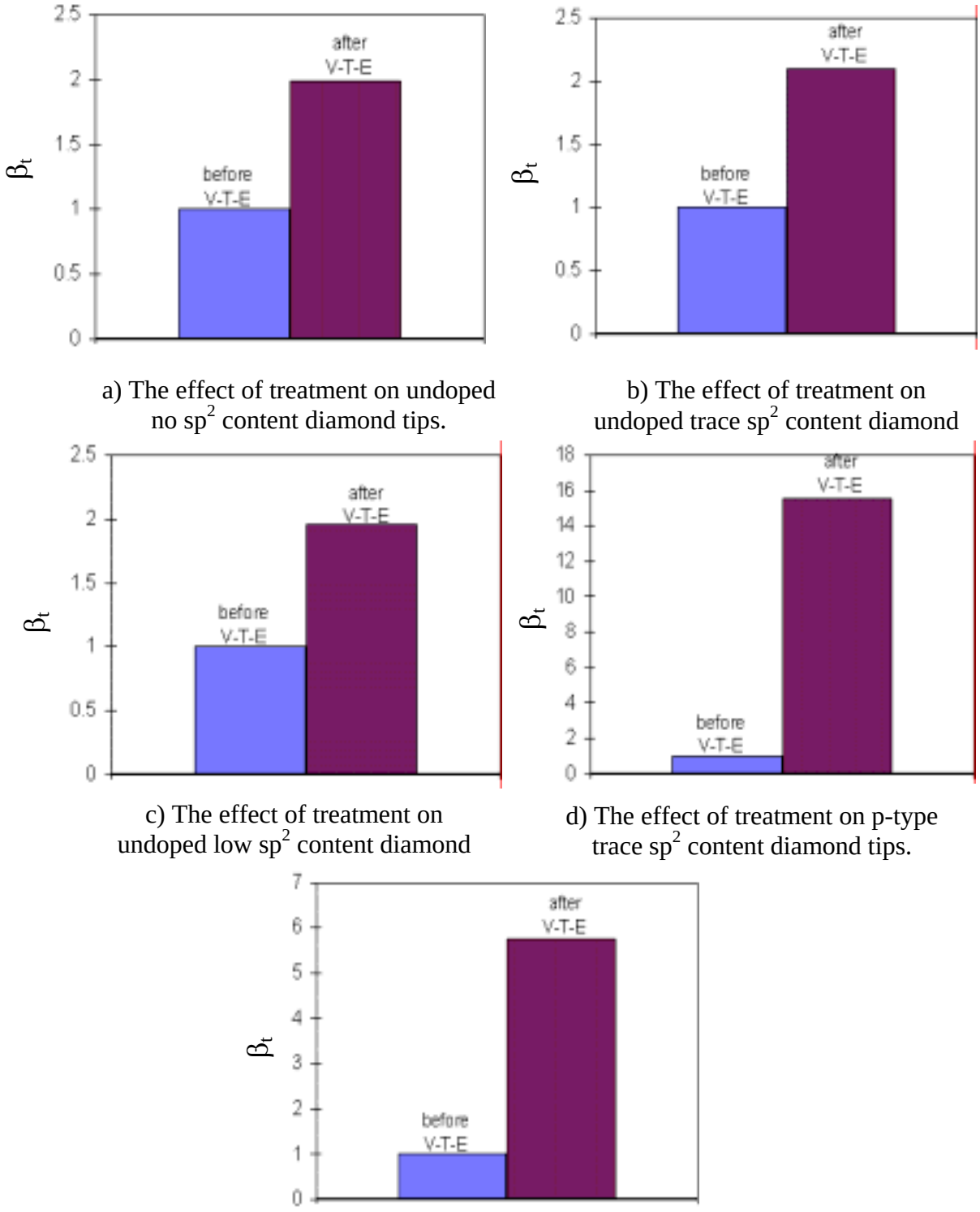


a) The effect of treatment on undoped no $sp^2$ content diamond tips.

b) The effect of treatment on undoped trace $sp^2$ content diamond

c) The effect of treatment on undoped low $sp^2$ content diamond

d) The effect of treatment on p-type trace $sp^2$ content diamond tips.

e) The effect of treatment on p-type low $sp^2$ content diamond tips.

**Figure 6.48.** The effect of treatment on the $\beta_t$ of diamond tip for the same $sp^2$ content and same doping.

Discussion of the effect of boron (p-type) doping

The detail discussion is separated into the following two main cases:

The effect of doping on diamond tips with trace $sp^2$ content

The effect of doping on I-E and F-N plots of diamond tips with trace $sp^2$ content before and after VTE treatment are shown in **Figures 6.49-6.52**. **Figure 6.53** shows the effect of doping on the F-N slope ratios of diamond tips (from **Table 6.1**) for the same $sp^2$ content and the same treatment. **Figure 6.54** shows the effect of doping on the work function ratios of diamond tips (from **Table 6.1**) for the same treatment and the same $sp^2$ content. From **Figure 6.49,** it can be seen that the turn-on electric field of diamond tips with trace $sp^2$ content before VTE treatment increases with p-type doping. The turn-on electric field of undoped and p-type diamond tips with trace $sp^2$ content are approximately 40 and 60 V/ μm, respectively. From **Figure 6.50**, it can be seen that the slope of F-N plots tends to be steeper with p-type doping. **Figure 6.53(a)** and **Figure 6.54(a)** show the effect of doping on the F-N slope ratio and work function ratio of diamond tips with trace $sp^2$ content using undoped diamond tip with trace $sp^2$ content before VTE treatment as a reference. From these figures, it can be seen again that the F-N slope ratio and work function ratio of diamond tips increase with p-type doping.

On the other hand, it can be seen from **Figure 6.51** that the turn-on electric field of diamond tips with trace $sp^2$ content after VTE treatment decreases with p-type doping. The turn-on electric field of undoped and p-type diamond tips with trace $sp^2$ content are approximately 17 and 10 V/ μm, respectively. From **Figure 6.52**, it can be seen that the slope of F-N plots tends to be shallower with p-type doping. **Figure 6.53(b)** and **Figure 6.54(b)** show the effect of doping on the F-N slope ratio and work function ratio of diamond tips with trace $sp^2$ content using undoped diamond tip with trace $sp^2$ content after VTE treatment as a reference. From these figures, it can be seen that the F-N slope ratio and work function ratio of diamond tip decrease with p-type doping. It is interesting that this result shows a strong contradiction to the previous case. This interesting result will be further discussed in the modeling of the effect of doping on diamond tips.

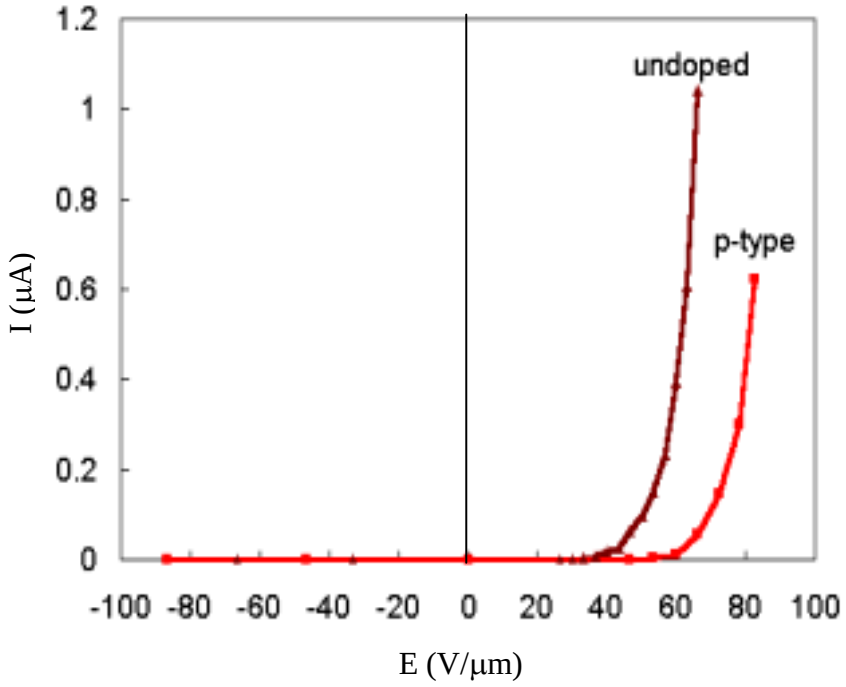


**Figure 6.49.** The effect of doping on I-E plot of trace $sp^2$ diamond tips before VTE treatment.

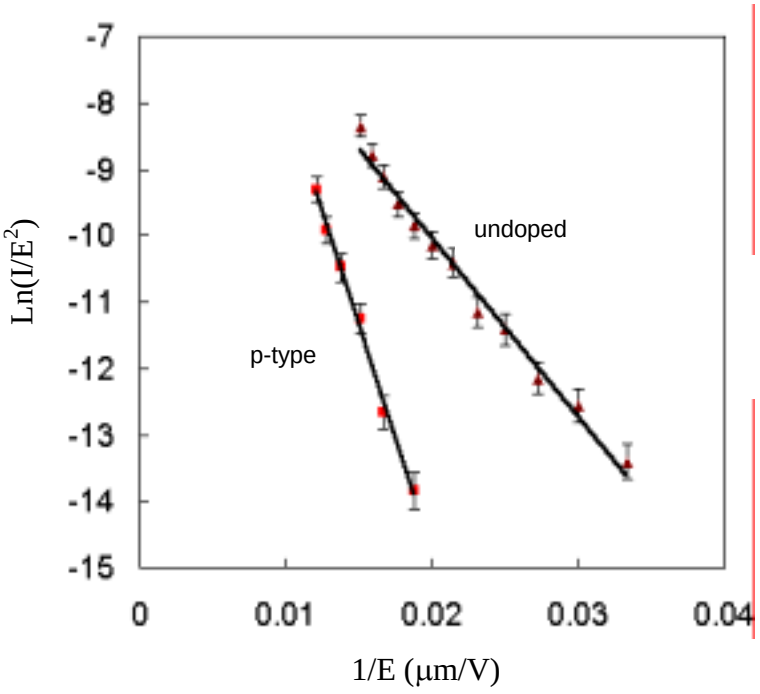


**Figure 6.50.** The effect of doping on F-N plot of trace $sp^2$ diamond tips before VTE treatment.

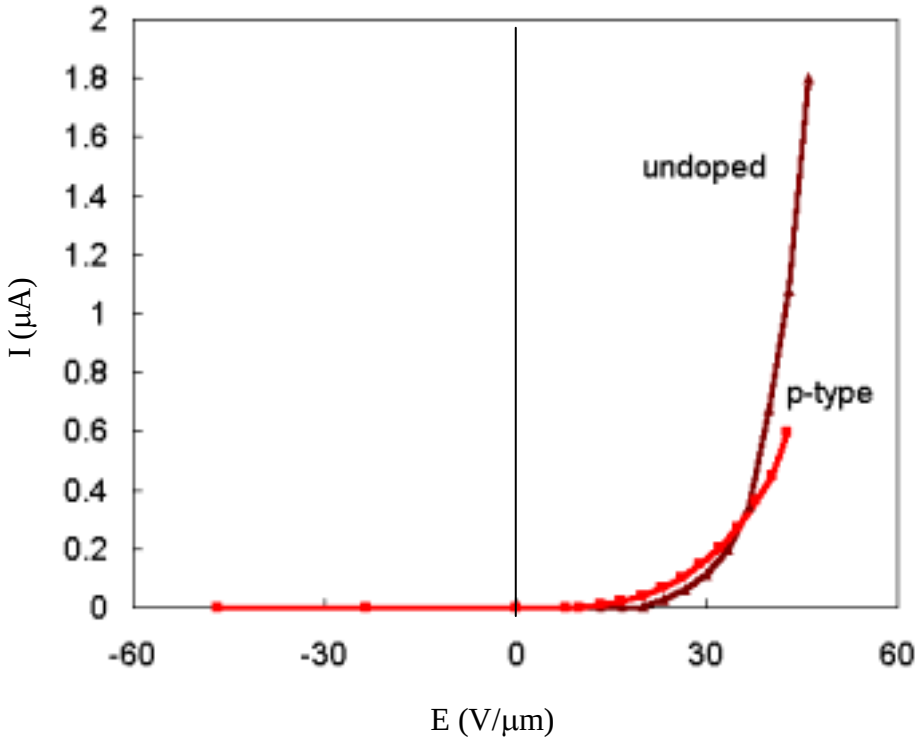


**Figure 6.51.** The effect of doping on I-E plot of trace $sp^2$ diamond tips after VTE treatment.

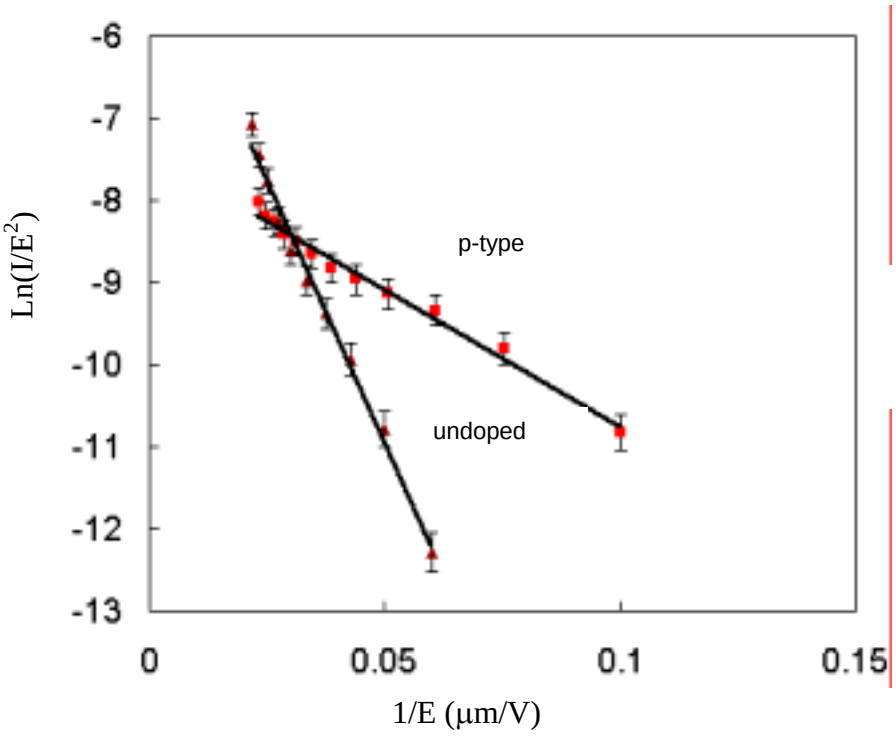


**Figure 6.52.** The effect of doping on F-N plot of trace $sp^2$ diamond tips after VTE treatment.

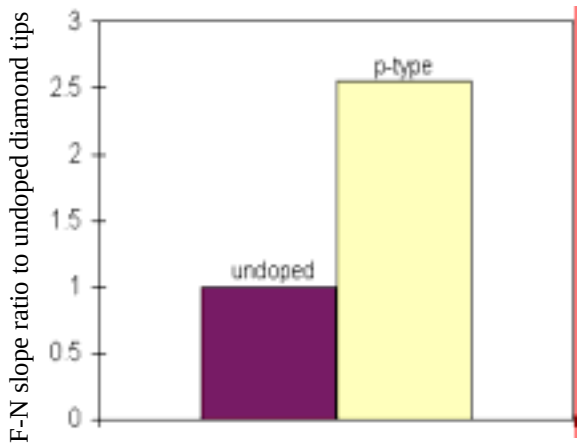


a) The effect of doping on trace $sp^2$ content diamond tips before V-T-E treatment.

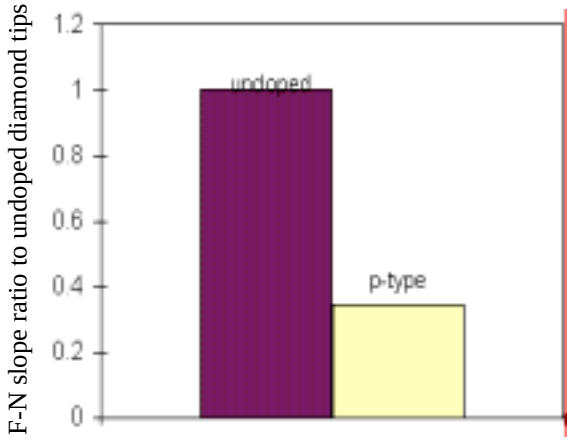


b) The effect of doping on trace $sp^2$ content diamond tips after V-T-E treatment.

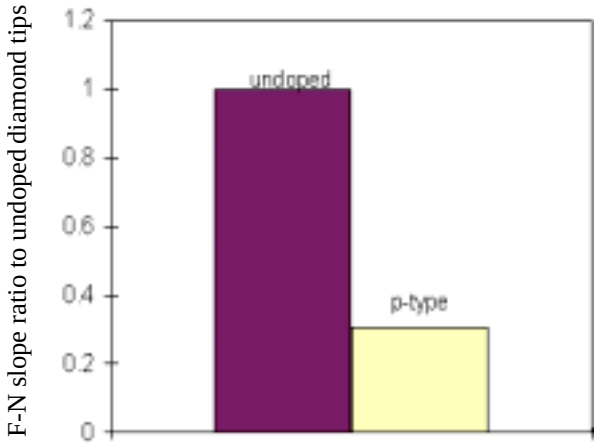


c) The effect of doping on low $sp^2$ content diamond tips before V-T-E treatment.

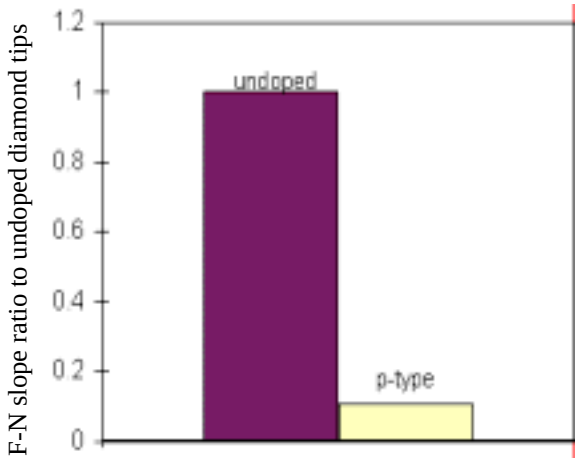


d) The effect of doping on low $sp^2$ content diamond tips after V-T-E treatment.

**Figure 6.53.** The effect of doping on the F-N slope ratio of diamond tips for the same $sp^2$ content and same treatment.

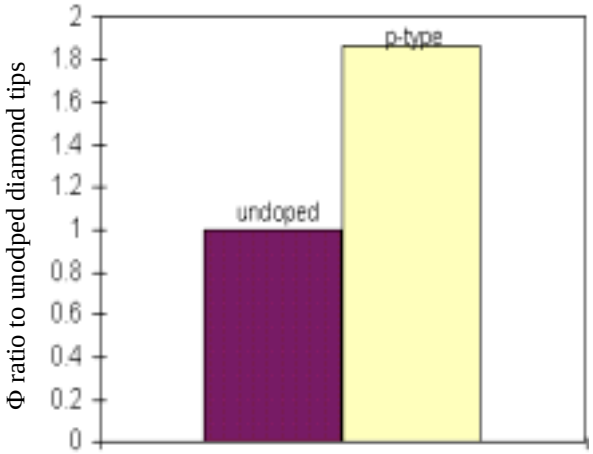


a) The effect of doping on trace $sp^2$ content diamond tips before V-T-E treatment.

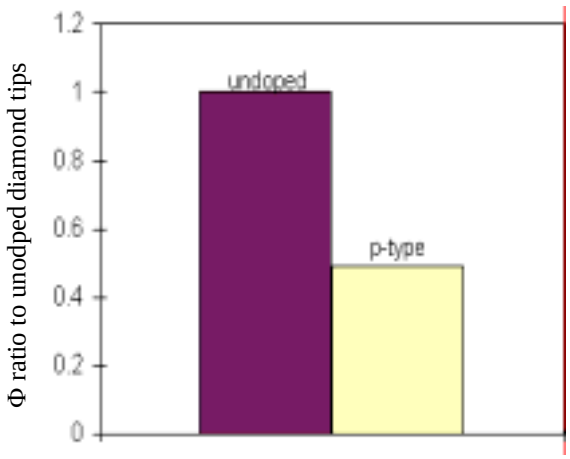


b) The effect of doping on trace $sp^2$ content diamond tips after V-T-E treatment.

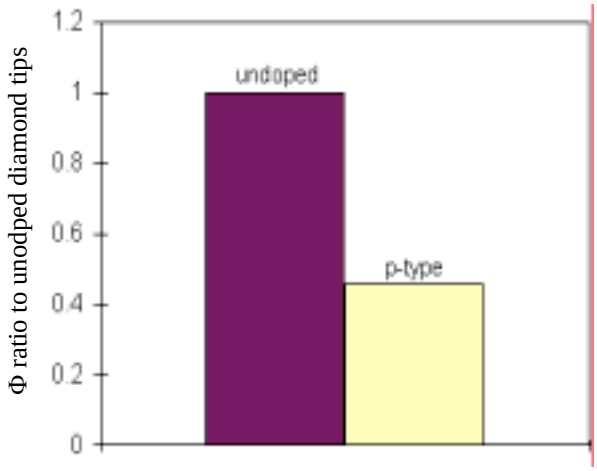


c) The effect of doping on low $sp^2$ content diamond tips before V-T-E treatment.

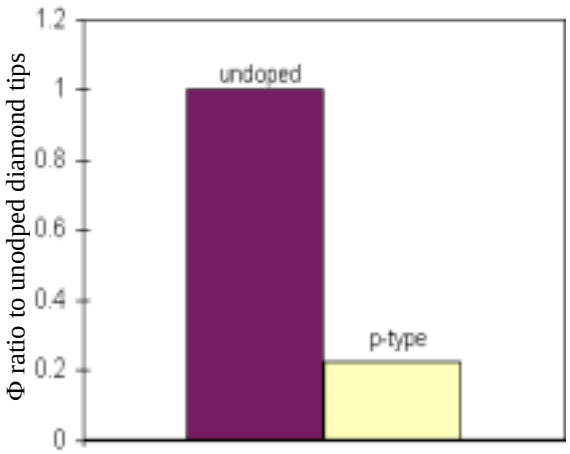


d) The effect of doping on low $sp^2$ content diamond tips after V-T-E treatment.

**Figure 6.54.** The effect of doping on Φ ratio of diamond tips for the same $sp^2$ content and same treatment.

The effect of doping on diamond tips with low $sp^2$ content

The effect of doping on I-E and F-N plots of diamond tips with low $sp^2$ content before and after VTE treatment are shown in **Figures 6.55-6.58**. From **Figure 6.55,** it can be seen that the turn-on electric field of the low $sp^2$ content diamond tips before VTE treatment decreases with p-type doping. The turn-on electric field of the undoped and p-type diamond tips with low $sp^2$ content are approximately 12 and 7 V/ μm, respectively. From **Figure 6.56**, it can be seen

that the slope of F-N plot tends to be shallower with p-type doping. **Figure 6.53(c)** and **Figure 6.54(c)** show the effect of doping on F-N slope ratio and the work function ratio of diamond tips with low $sp^2$ content using undoped diamond tip with low $sp^2$ content before VTE treatment as a reference. From these figures, it can be seen that the F-N slope ratio and work function ratio of diamond tips decrease with p-type doping. It is interesting that this result shows a strong contradiction to the diamond tips with trace $sp^2$ content. This interesting result will be further discussed in the modeling of the effect of doping on diamond tips.

From **Figure 6.57**, it can also be seen that the turn-on electric field of diamond tips with low $sp^2$ content after VTE treatment decreases with p-type doping. The turn-on electric fields of the undoped and p-type diamond tips with low $sp^2$ content are approximately 4 and 1 V/ μm, respectively. From **Figure 6.58**, it can be seen that the slope of F-N plots tends to be shallower with p-type doping. **Figure 6.53(d)** and **Figure 6.54(d)** show the effect of doping on the F-N slope ratio and work function ratio of diamond tips with low $sp^2$ content using undoped diamond tip with low $sp^2$ content after VTE treatment as a reference. From these figures, it can be seen that the F-N slope ratio and work function ratio of diamond tips decrease significantly with p-type doping.

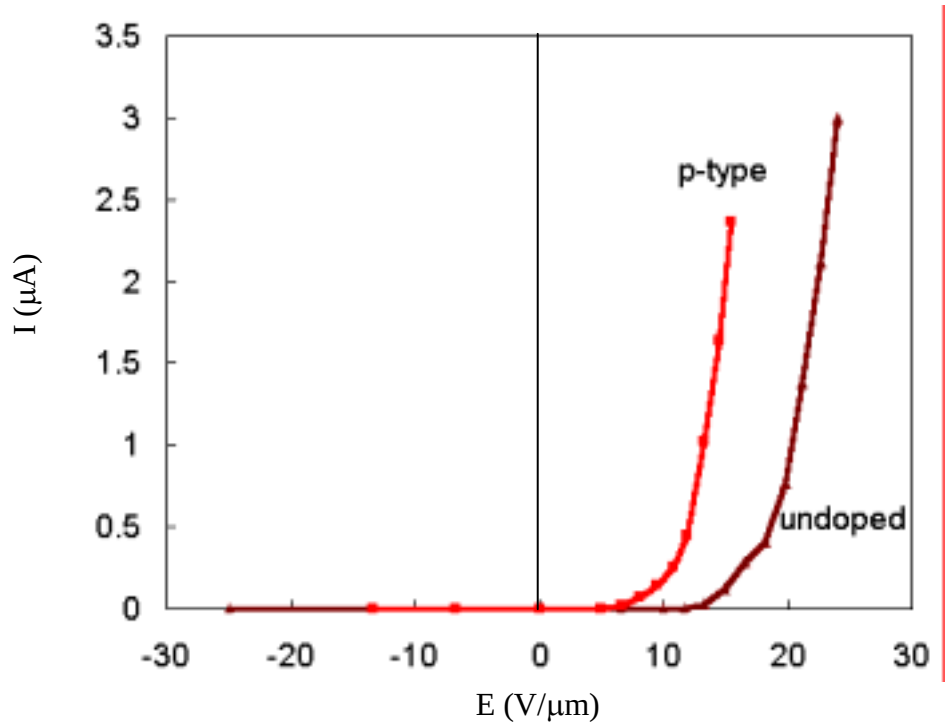


**Figure 6.55.** The effect of doping on I-E plot of low $sp^2$ diamond tips before VTE treatment.

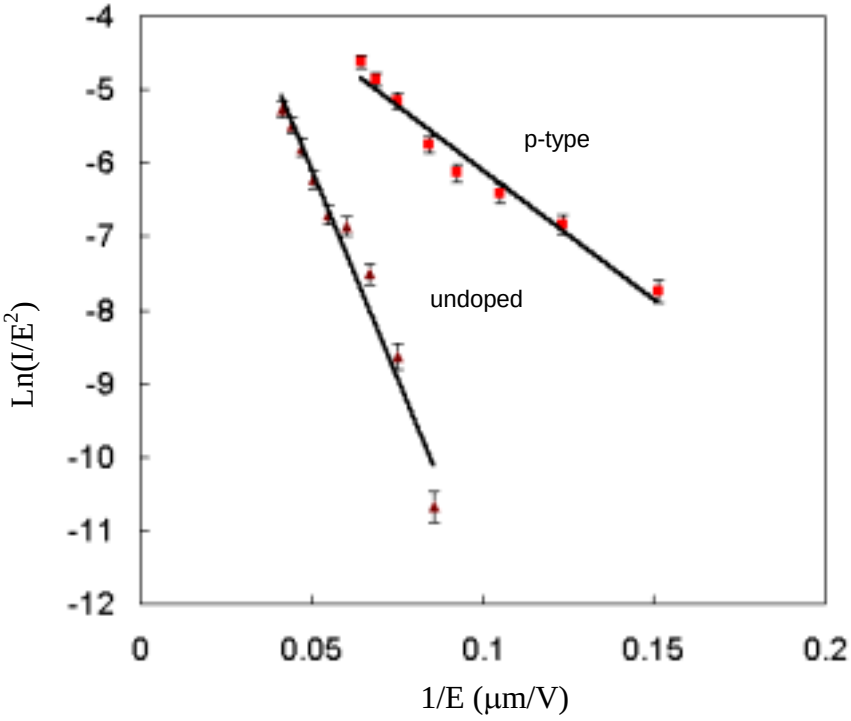


**Figure 6.56.** The effect of doping on F-N plot of low $sp^2$ diamond tips before VTE treatment.

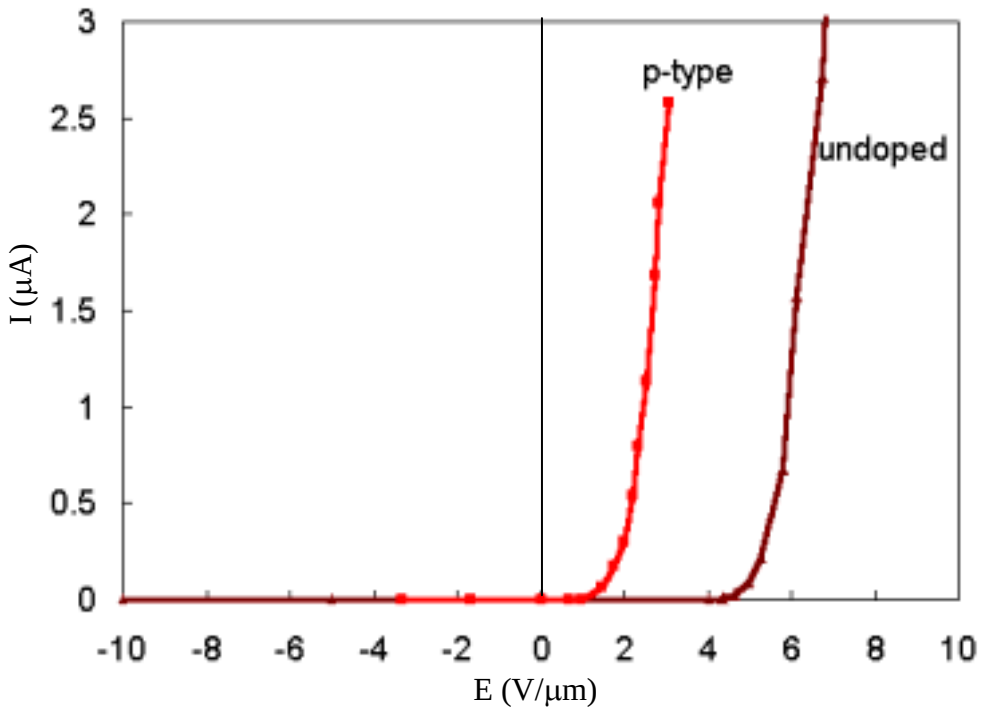


**Figure 6.57.** The effect of doping on I-E plot of low $sp^2$ diamond tips after VTE treatment.

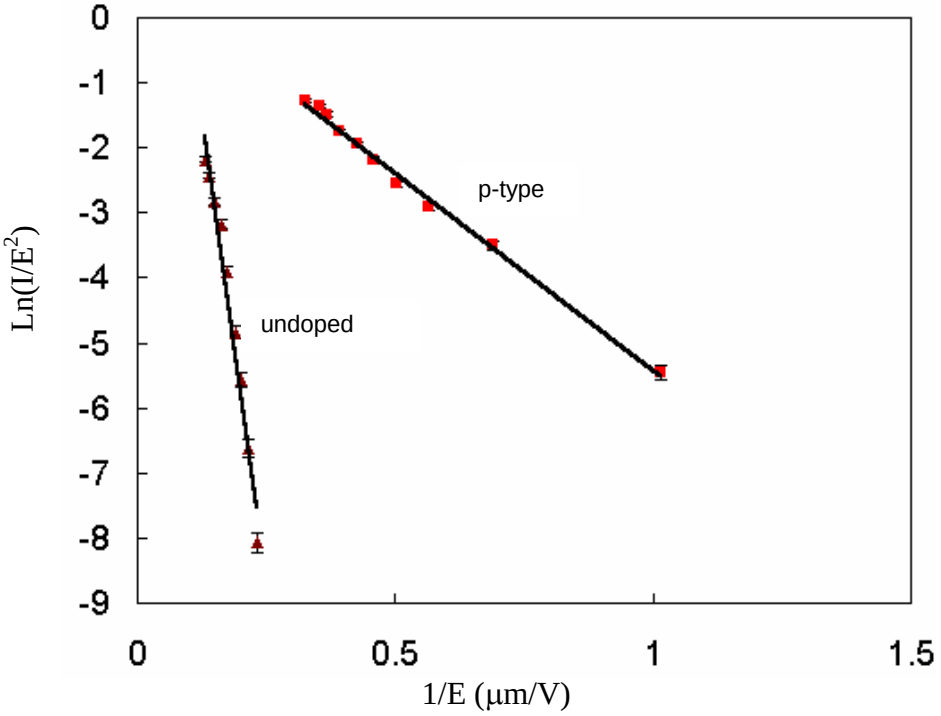


**Figure 6.58.** The effect of doping on F-N plot of low $sp^2$ diamond tips after VTE treatment.

Modeling of the effect of p-type doping on diamond tips

From the overall results, p-type doping shows an inconsistent effect on field emission characteristics of diamond tips. For the p-type diamond tip with trace $sp^2$ content before VTE treatment, the turn-on electric field increases with p-type doping. This result is in agreement with the conventional theory based on energy band diagram. P-type doping lowers the Fermi-level of the bulk and hence increases the work function. On the other hand, for the p-type low $sp^2$ content, the turn-on electric field decreases with p-type doping. This result contradicts to the conventional theory based on energy band diagram.

To explain this contradiction, we have proposed that emission enhancement is due to hole accumulation in MIM ($sp^2$-diamond $sp^2$) microstructure of the diamond tips. The concept of this model was expanded from the MIM model previously developed and is related to hole accumulation in valence band in this structure [156] that enhances internal electric field and hence improved in electron emission in this structure. **Figure 6.59** demonstrates the concept of this model on diamond tip. It should be noted that the metal and boron-doped diamond forms an ohmic contact for holes, not a Schottky contact as one might expect and the barrier height at the contact ($\Phi_b$) indicated in the diagram is the barrier height for electrons. The ohmic contact was obtained because gold with work function of ~5.1 eV was used for back contact. The ohmic Au/p-diamond interface was confirmed by conductivity measurement.

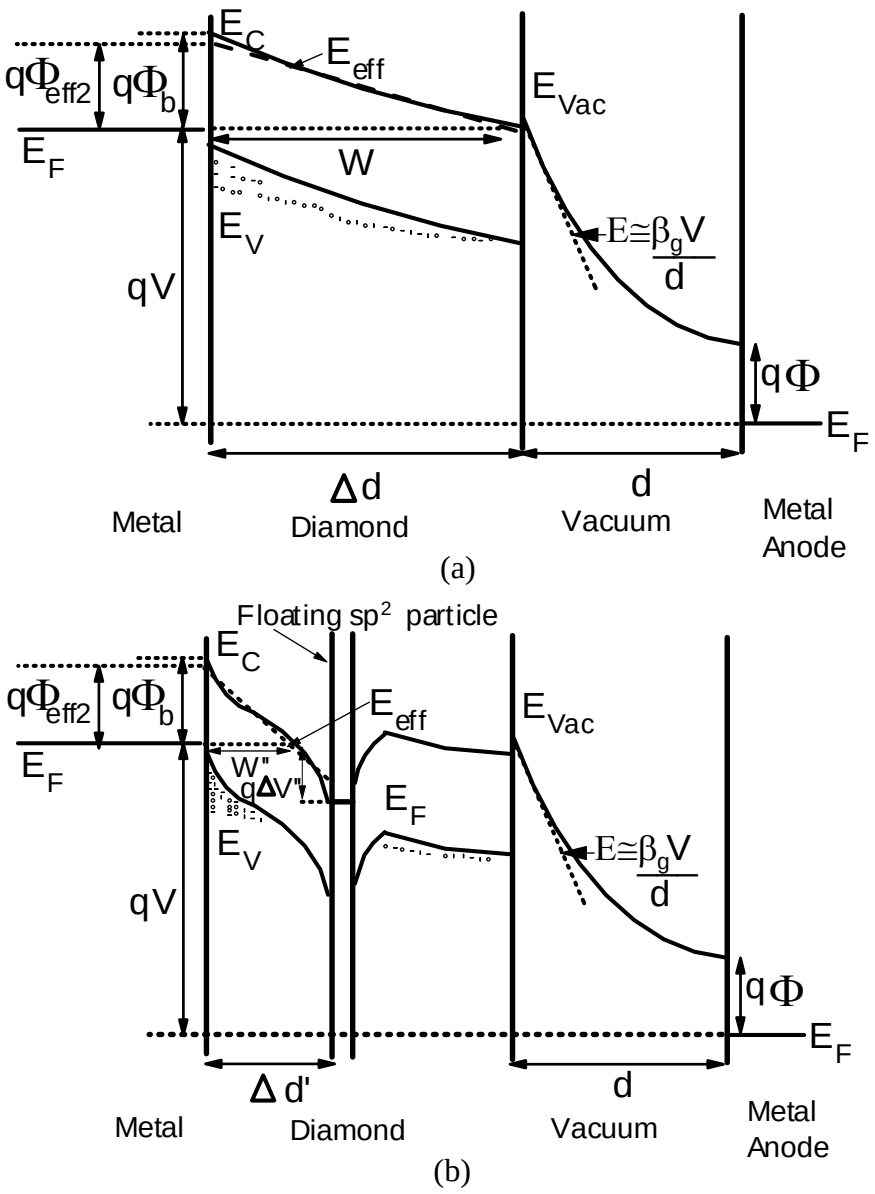


**Figure 6.59.** Energy band diagram of holes accumulation model (a) Energy band without a $sp^2$ conducting particle. (b) Energy band with a $sp^2$ conducting particle.

Without a $sp^2$ conducting particle (**Figure 6.59 (a)**), the electric field inside diamond film is small. Thus, it is not enough to accelerate holes toward metal-diamond interface. Holes in valence band are distributed throughout the neutral region in diamond and do not contribute any effect on field emission. Thus, holes do not contribute any enhanced effect on field emission, but do result in increasing the effective work function and hence degrade electron field emission.

With a $sp^2$ conducting particle (**Figure 6.59 (b)**), the enhanced electric field between particles and the metal contact accelerates most of holes toward the metal-diamond interface. According to elementary electrostatics, the accumulation of holes at the metal-diamond interface further increases the electric field at the junction. The enhanced electric field causes more band bending of the conduction band, thereby reduces the width of tunneling distance W" (<<W). Therefore, electron tunneling into the diamond is increased and the field emission is enhanced due to boron dopants in the cascaded MIM microstructures. This may be the reason why the p-type low $sp^2$ content diamond tips show a better field emission enhancement than that of undoped low $sp^2$ content diamond tips.

According to this assumption, p-typed doping leads to field emission enhancement that depends on $sp^2$ content. For no $sp^2$ content, p-type dopant does not play any role for field emission enhancement, but it results in higher work function and degrade field emission behavior. On the other hand, for low $sp^2$ content, p-type dopant plays an important role for field emission enhancement because of the cascading enhancement process through the floating $sp^2$ particle.

After VTE treatment, the turn-on electric field decreases with p-type doping for both trace and low $sp^2$ content diamond tips. A possible mechanism for the field emission enhancement by boron after VTE treatment is proposed. At room temperature, boron may be partially ionized because boron is a deep acceptor. During VTE treatment, the acceptor state is completely ionized due to thermal energy. Thus, more holes are generated in the valence band. According to hot electron model, the presence of holes leads to field emission enhancement via the accumulation of holes at metal-$sp^2$-diamond interface. Therefore, the electric field inside the diamond film particularly at the tip region is enhanced significantly. Thus, the field forming process is accelerated and improved. This may be the reason why the VTE treatment for p-type diamond tips produces a better field emission behavior than undoped diamond tips.

The effect of field emission enhancement by p-type dopant due to hole accumulation at $sp^2$-diamond $sp^2$ interface can be accounted for in Fowler-Norheim equation by introducing an additional field enhancement component, $\beta_p$, to the total field enhancement factor, $\beta$. Thus, $\beta$ in eq. (6.4) becomes:

$$\beta = \beta_g \beta_{sp2} \beta_t \beta_p \qquad (6.5)$$

Hence, the previously calculated work function and field enhancement factor based on constant work function Φ and β using eq. (6.4) need to be revised. The calculated field enhancement factor due to p-type doping $\beta_p$ is based on constant $\beta_{sp2}$ and $\beta_t$ for diamond tip with the same $sp^2$ content and treatment. Based on constant $\beta_{sp2}$ and $\beta_t$, Φ of p-type diamond tips would be different from that of undoped diamond tips. Φ of p-type diamond tips was estimated to be ~4 eV. The revised Φ of p-type diamond tips is reasonable and in agreement with a typical work function of p-type diamond [147]. The calculated results based on this model are shown in **Table 6.4**. **Figure 6.60** shows the effect of p-type doping on $\beta_p$ (from **Table 6.4**) for the same treatment and the same $sp^2$ content. From **Table 6.4** and **Figure 6.60**, it can be seen that $\beta_p$ depends on doping and $sp^2$ content. For p-type diamond tips, $\beta_p$ of diamond tips with low $sp^2$ content is higher than that of diamond tips with trace $sp^2$ content. This result agrees with the hypothesis that the effect of p-type dopant on field emission enhancement depends on $sp^2$ content.

**Table 6.4.** Calculated results from Fowler-Nordhiem plots based on field enhancement due to hole accumulation and the associated field forming process.

| Treatment | $sp^2$ Content | Doping | Φ(eV) | β | $\beta_g$ | $\beta_t$ | $\beta_{sp2}$ | $\beta_p$ |
|---|---|---|---|---|---|---|---|---|
| before VTE treatment | trace | no | 2.13 | 242.5 | 100 | 1 | 2.42 | 1 |
| | | p | 3.97 | 242.5 | 100 | 1 | 2.42 | 1 |
| after VTE treatment | trace | no | 2.13 | 509.5 | 100 | 1.98 | 2.57 | 1 |
| | | p | 3.97 | 3772.7 | 100 | 1.98 | 2.57 | 7.4 |
| before VTE treatment | low | no | 2.13 | 570.9 | 100 | 1 | 5.71 | 1 |
| | | p | 3.97 | 4744.4 | 100 | 1 | 5.71 | 8.3 |
| after VTE treatment | low | no | 2.13 | 1118.5 | 100 | 1.98 | 5.64 | 1 |
| | | p | 3.97 | 27255 | 100 | 1.98 | 5.64 | 24.4 |

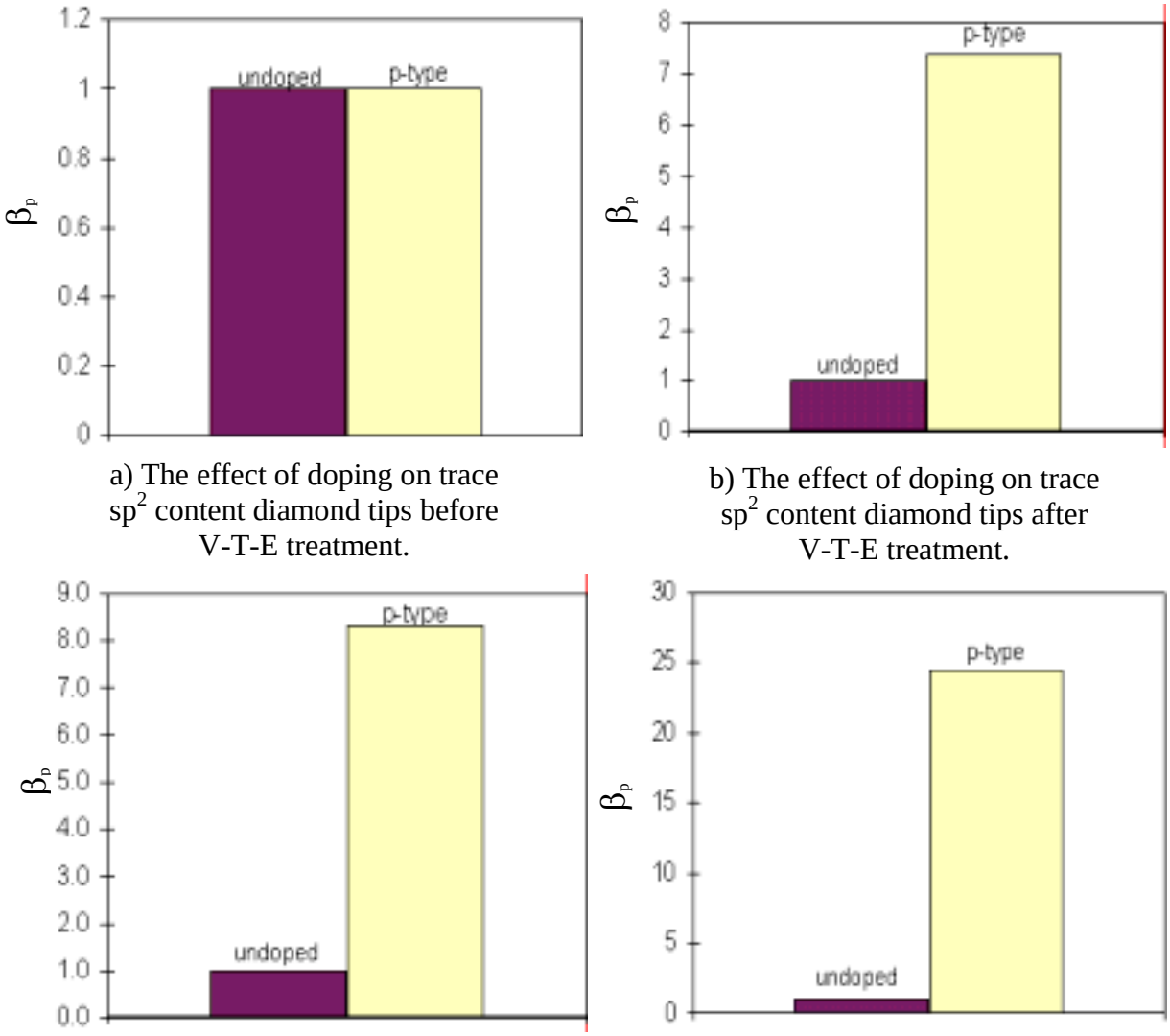


a) The effect of doping on trace $sp^2$ content diamond tips before V-T-E treatment.

b) The effect of doping on trace $sp^2$ content diamond tips after V-T-E treatment.

c) The effect of doping on low $sp^2$ content diamond tips before V-T-E treatment.

d) The effect of doping on low $sp^2$ content diamond tips after V-T-E treatment.

**Figure 6.60.** The effect of doping on $\beta_p$ of diamond tips for the same $sp^2$ content and same treatment.

Discussion on the effect of tip sharpening

The I-E plots of unsharpened and sharpened undoped diamond tips with low $sp^2$ contents after VTE treatment are shown in **Figure 6.61**. It can be seen that the turn-on electric field reduces from 14 V/μm to 1 V/μm, and the emission current is significantly increased with tip sharpening. The corresponding F-N plots of the emission data are shown in **Figure 6.62**. It can

be seen that the F-N slope reduce significantly due to tip sharpening. The experimental results demonstrate that turn-on electric field can be significantly reduced by tip sharpening.

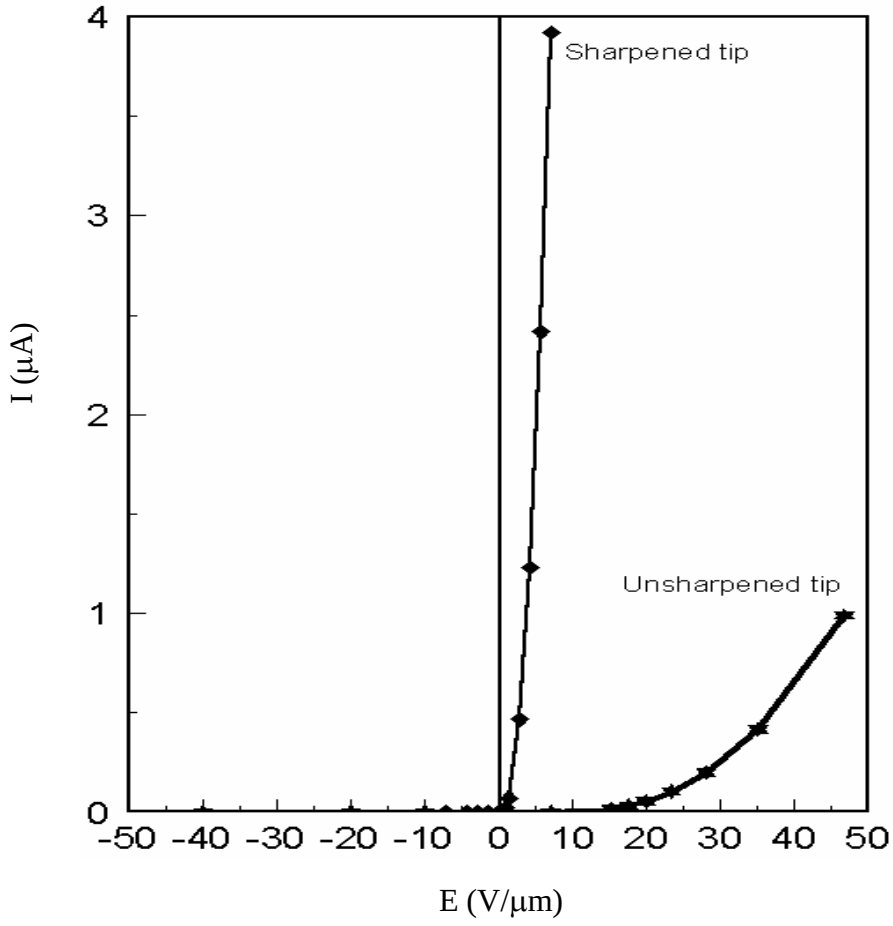


**Figure 6.61.** I-E plots of unsharpened and sharpened undoped diamond tips with low $sp^2$ contents after VTE treatment.

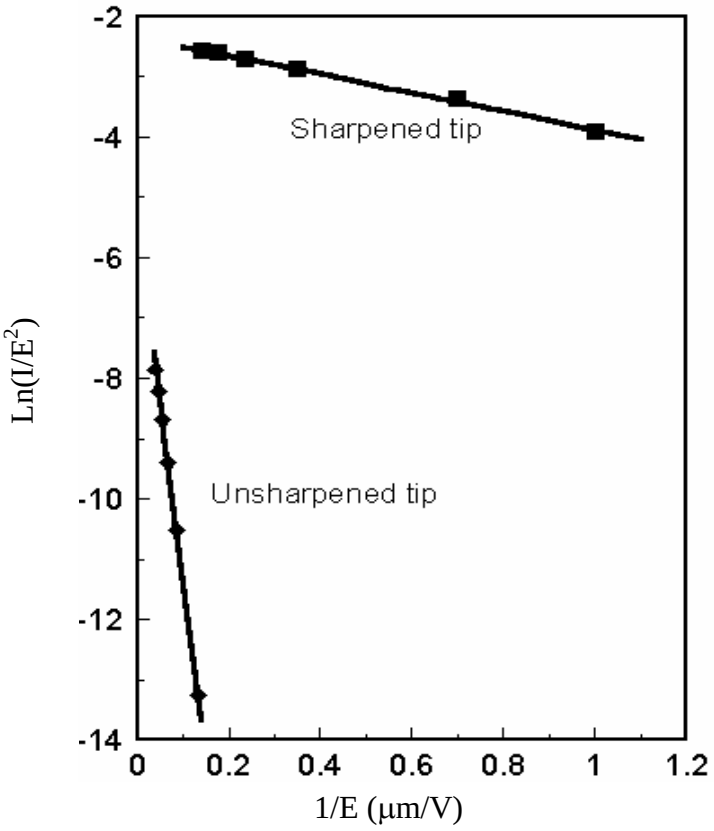


**Figure 6.62.** F-N plots of unsharpened and sharpened undoped diamond tips with low $sp^2$ contents after VTE treatment.

Modeling on the effect of tip sharpening

The observed field emission enhancement by tip sharpening can be explained by the increasing of geometrical field enhancement factor of diamond tips due to tip sharpening. This can be deduced from the observation that the F-N slope decreases significantly with tip sharpening. The reduction of F-N slope should mainly arise from the geometric effect because both diamond tip has the same $sp^2$ content, doping, and VTE treatment and thus should have the same $\Phi$, $\beta_{sp2}$, $\beta_t$ and $\beta_p$. Assuming that $\Phi$, $\beta_{sp2}$, $\beta_t$ and $\beta_p$ are the same for both diamond tips, $\beta_g$ can be found from the F-N slopes of emission data. It was found that

$$\frac{\beta_{g,\,sharpened}}{\beta_{g,\,unsharpened}} = 37$$

where $\beta_{g,\,sharpened}$ and $\beta_{g,\,unsharpened}$ are the geometrical field enhancement components for the sharpened and unsharpened diamond tips, respectively. This means that the geometrical field enhancement component increases by the factor of 37 due to the tip sharpening by the self-align-

gate-sharpened molding technique. Given $\beta_{g,\ unsharpened} = 100$ from previous analysis, $\beta_{g,\ sharpened} \approx$ 3700. This high field enhancement factor value confirms that tip sharpening is an effective mean to enhance electron emission from diamond tips.

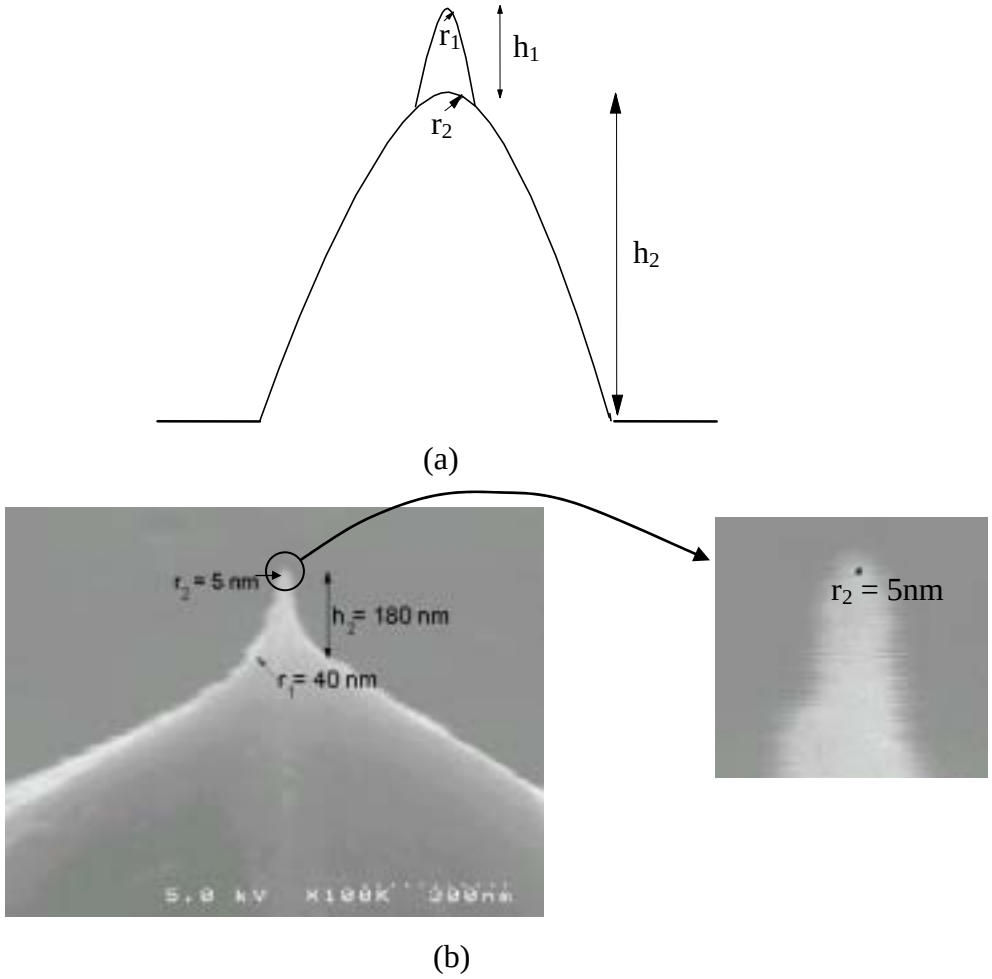


**Figure 6.63.** (a) the model of an sharpened diamond tip and (b) high magnification SEM micrograph of a sharpened diamond tip focused at the tip apex.

Alternatively, the field enhancement factor of the sharpened diamond tip can be estimated using two-step field emission enhancement model (TSFE) described in chapter II. In this model [68], the sharpened diamond tip is modeled as a large conical tip with tip height of $h_1$ and tip radius curvature of $r_1$ superimposed with a sharp tiny conical tip with tip height of $h_2$ and tip radius curvature of $r_2$ illustrated in **Figure 6.63(a)**. In other words, the electric field at the sharpened tip apex arises from two-cascaded tip structure. In the first step, the electric field at the apex of large conical tip is enhanced by the factor of $h_1/r_1$ from the planar base. In the second

step, the electric field at the apex of the sharp tiny conical tip is enhanced by the factor of $h_2/r_2$ from the apex of large conical tip. Thus, the total geometrical field enhancement factor of the sharpened tip is the product of field enhancement factor of two cascaded tip structure:

$$\beta_{\text{g, sharpened}} = \left(\frac{h_1}{r_1}\right)\left(\frac{h_2}{r_2}\right) \tag{6.6}$$

using $h_1 \approx 3.4$ μm as obtained from the low magnification SEM micrograph (**Figure 6.3**), $r_1 \approx 25$ nm, $h_2 \approx 180$ nm, and $r_2 \approx 5$ nm as obtained from the high magnification SEM micrograph, **Figure 6.63(b)**, the calculated $\beta_{\text{g, sharpened}}$ is 3060. From the above result, $\frac{\beta_{g,\,sharpened}}{\beta_{g,\,unsharpened}} = 30.6$ , which is in good agreement with the result obtained from F-N analysis.

Part II: Monolithic diamond vacuum diode

Design and fabrication issues of monolithic diamond vacuum diode

Fabrication of monolithic diamond vacuum diode is considerably more complicated than stand-alone diamond microtips. There are four main issues involving design and fabrication of monolithic diamond vacuum diode by molding technique: 1) the practicality of the fabrication process for diamond emitter with built-in anode, 2) the quality of anode-cathode dielectric spacer, 3) small anode-cathode spacing for low operating voltage, and 4) uniform-planarity of anode-cathode structure over large area. To achieve these goals, five fabrication methods: electrostatic bonding, self-align volcano anode, and self-align-anode molding (utilizing standard, epitaxial, and SOI wafers) have been developed for the fabrication of monolithic diamond field emission diode structures.

Discussion of fabrication methods developed for monolithic diamond vacuum diode

I. Electrostatic bonding method

This method, described in chapter V, was used to fabricate a capped diamond emitter diode. However, there were some deficiencies and practical problems encountered. First, it was difficult to align a cap anode perfectly coplanar to cathode arrays. A small coplanar misalignment would result in anode-cathode touching. Second, it was also difficult to achieve

micron-scale anode-cathode spacing because of co-planarity problem. Last, the capped diode structure could only be used for diode application only. Most practical applications require a three-terminal triode configuration.

II. Self-align volcano anode method

Volcano diode structure with self-aligned anode, described in chapter V, was fabricated. This fabrication method was complicated and inefficient because it required many fabrication steps. In addition, the poor quality of deposited $SiO_2$ dielectric spacer resulted in high leakage current and degraded the diode performances.

III. Self-align-anode-molding method utilizing standard silicon wafer

As described in chapter V, this method is practical and efficient because it requires few processing steps. Moreover, the anode is self-align to the cathode, and it utilizes part of the mold for the fabrication of anode and anode-cathode dielectric. However, some practical problems were encountered after the implementation of this technique. Anode-cathode spacing (anode opening and height) was difficult to control. The anode etching process needed to be very closely monitored in order to successfully etch-stop at a suitable silicon thickness. The etching time was much dependent on the wafer thickness, etching temperature, and concentration of etchants. Hence, it was difficult to control the process. In addition, uniform diode array over large area could not be accomplished by this technique because of imperfect anisotropic etching properties of EDP or KOH etchants. The largest array with good uniformity that we had achieved from this method was a diamond diode structure with 8x8 tips. We have found that the silicon anode layer was reduced to a very small island with non-uniform thickness when silicon layer was thinned down to exposed diamond tips. A small island of silicon anode was formed because the etchant etched faster on the edges of the window than the center region. **Figure 6.64** shows the failure of this fabrication process on a large array of diamond diode structure. Due to non-uniform etching, a portion of diamond tip array is over etched (**Figure 6.64 (a)**) while the other portion is under etched (**Figure 6.64 (b)**). In order to overcome these problems, an etch-stop process needed to be employed for silicon-anode etching. Electrochemical etching technique utilizing $n^+/p^-$ epitaxial wafer (described in Chapter V) was then experimented as an etch-stop process.

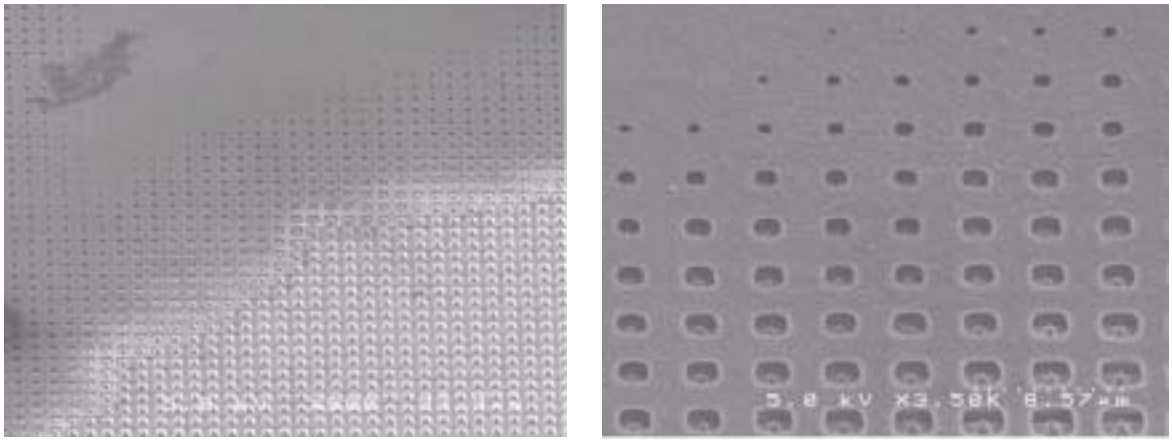

(a) (b)

**Figure 6.64.** The problem of fabricating high-density gated diamond field emitter array using standard Si or epitaxial wafer (a) over etched and (b) under etched.

IV. Self-align-anode-molding technique utilizing $n^+/p^-$ epitaxial Si wafer

Some practical problems were found after the implementation of self-align-gate-molding technique utilizing epitaxial based wafer. First, electrochemical etching was complicated because special sample preparation and etching apparatus were required. Second, reproducibility was poor because good p-n junction (low leakage current) was required for this technique to work. Last, it was found that the design of the epitaxial layer thickness and hence p-n junction depth was more complicated than reality due to further diffusion of dopants during thermal oxidation and CVD diamond deposition steps. From our electrochemical etching experiment, the silicon thickness after etch-stop (5 μm) was larger than the desired thickness (2 μm). As a result, the silicon layer must be further thinned down by regular anisotropic etching and hence a similar non-uniform etching problem as seen in the process using standard silicon wafer occurred. Self-align-molding technique utilizing SOI based wafer was then explored to overcome these problems.

V. Self-align-molding technique utilizing SOI wafer

This is the most successful method that we have developed for the fabrication of self-align gated diamond emitter. It is a highly efficient approach because the integral parts of field emitter device (gate and anode) can be designed on the SOI substrate. In addition, the fabrication yield is high (more than 90%) because the etch-stop by $SiO_2$ layer is highly reproducible.

Moreover, uniform self-aligned anode structure over large area can be achieved. The only drawback of this technique is the high cost of SOI wafer. However, the high cost problem will be lessening as the SOI technology becomes more developed.

Design of diamond diode structure with self-aligned anode utilizing SOI wafer

Fabrication of self-aligned anode diamond diode structure utilizing SOI wafer requires a careful design of pattern size, active silicon layer thickness of SOI wafer, and oxide parameters. The active silicon layer thickness (S) of SOI wafer must be properly designed to match the base width of pyramid (W), which defines the square patterns on the mask. A practical relationship between S and W is given by

$$S = 0.46\times(T_1+T_2)+(W+0.8\times T_1)/\sqrt{2} \quad (6.7)$$

where $T_1$ is the thickness of the $SiO_2$ masking layer for square patterning and $T_2$ is the desired thickness of the $SiO_2$ gate dielectric layer. This relation was derived from the process consideration along with diamond tip geometry contemplation. The first term is the active silicon layer thickness that is required to compensate the depletion of silicon layer due to the masking oxidation and the gate oxidation. The factor of 0.46 comes from the well-known fact that a silicon layer is depleted by 46% of the oxide thickness for conventional thermal oxidation. The second term is the active silicon layer thickness that is required to accommodate the height of inverted pyramidal cavities, which was given in eq. (6.1). The additional internal term of $0.8\times T_1$ accounts for the lateral etching of the oxide masking layer. The factor 0.8 is due to the fact that lateral etching of oxide by conventional wet etching is approximately 80% of the vertical etching [192]. If reactive ion etching (RIE) is used instead of wet etching, then the term $0.8\times T_1$ can be omitted because there is negligible lateral etching [192].

It should be noted that for the design based on eq. (6.7), the apex of $SiO_2$ gate dielectric is designed to meet the buried oxide etch stop layer and the resulting SOI mold structure would be as illustrated in **Figure 6.65 (a)** so that diamond tip apexes would be automatically exposed after buried oxide etching. In practice, the gate dielectric oxidation would slightly proceed so that the apex of $SiO_2$ gate dielectric is completely joined with the buried oxide layer. For the design of self-aligned anode diamond tips with W = 2 μm, $T_1$ = 0.2 μm, $T_2$ = 1 μm, S should be approximately 2 μm. The fabricated mold based on this design is shown in **Figure 6.65 (b)**. It can be seen that the apex of $SiO_2$ gate dielectric is almost joined with the buried oxide layer. The

apex of $SiO_2$ gate dielectric was not completely joined with the buried oxide layer because the active silicon layer thickness (S) was actually slightly bigger than 2 μm. This discrepancy was very small and can be adjusted by slight thinning of silicon anode layer to expose the $SiO_2$ apex.

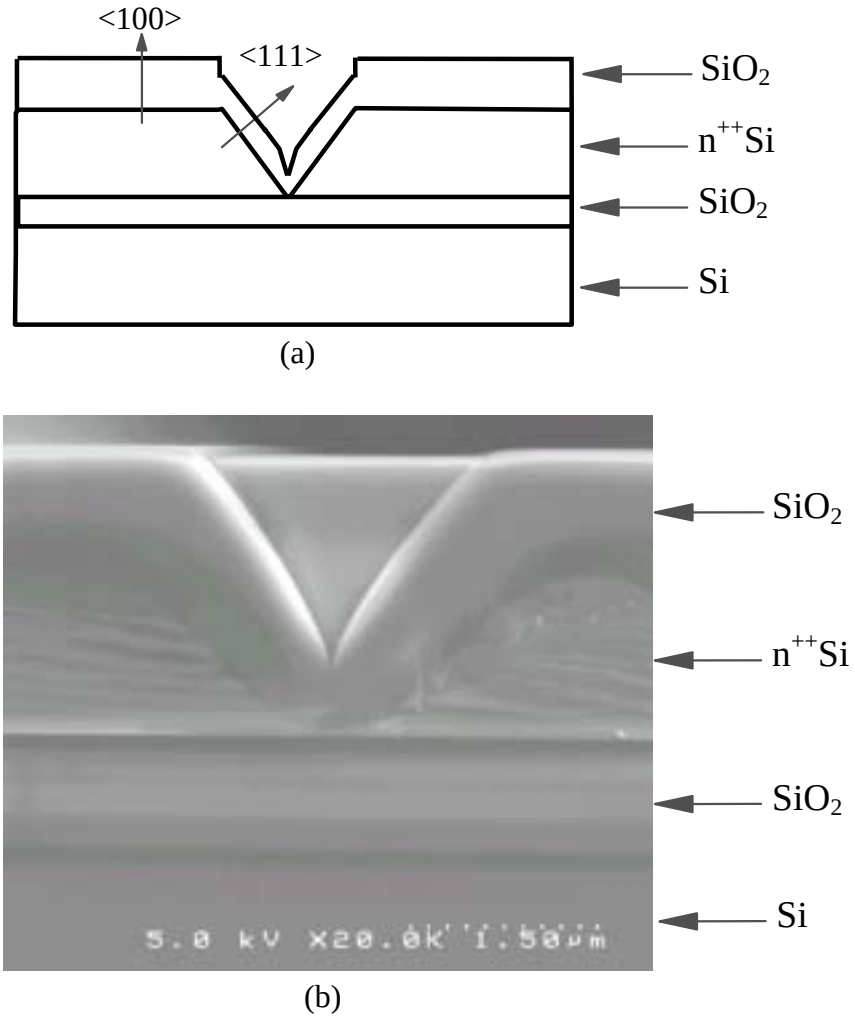


**Figure 6.65.** (a) Structure and (b) SEM micrograph of SOI inverted pyramidal mold.

Physical structure of monolithic diamond vacuum diode

Physical structures of monolithic diamond vacuum diodes fabricated by various fabrication techniques are shown in **Figures 6.66-6.70**. An SEM micrograph of capped diamond field emitter diode is shown **Figure 6.66.** It illustrates a diamond microtip with base dimension of 2 μm x 2 μm sitting on diamond film with an integrated silicon anode located 2 μm above the diamond tip. An SEM micrograph, **Figure 6.67**, shows a volcano self-aligned anode diamond microtip with base dimension of 2μm x 2μm and an aluminum anode supported by a $SiO_2$ layer. An SEM micrograph of diamond field emitter diode with self-aligned silicon anode separated by 0.7 μm thick $SiO_2$ dielectric spacer is demonstrated in **Figure 6.68**. An SEM micrograph, **Figure 6.69**, shows a single diamond vacuum diode with self-aligned silicon anode fabricated from SOI sharpened mold. **Figure 6.70** is an SEM micrograph of a large array of diamond vacuum diode with self-aligned silicon anode fabricated from SOI sharpened mold.

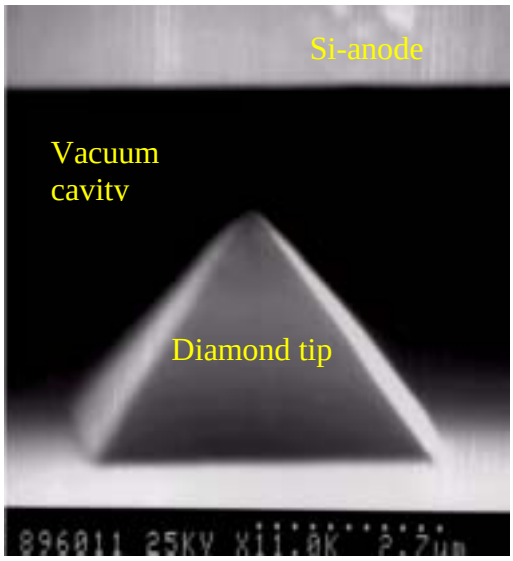


**Figure 6.66.** SEM micrograph of capped diamond vacuum diode.

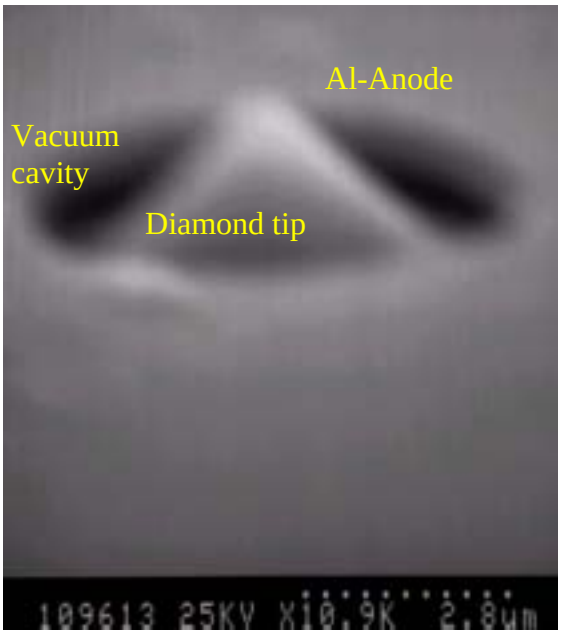


**Figure 6.67.** SEM micrograph of volcano diamond diode structure with self-align Al anode.

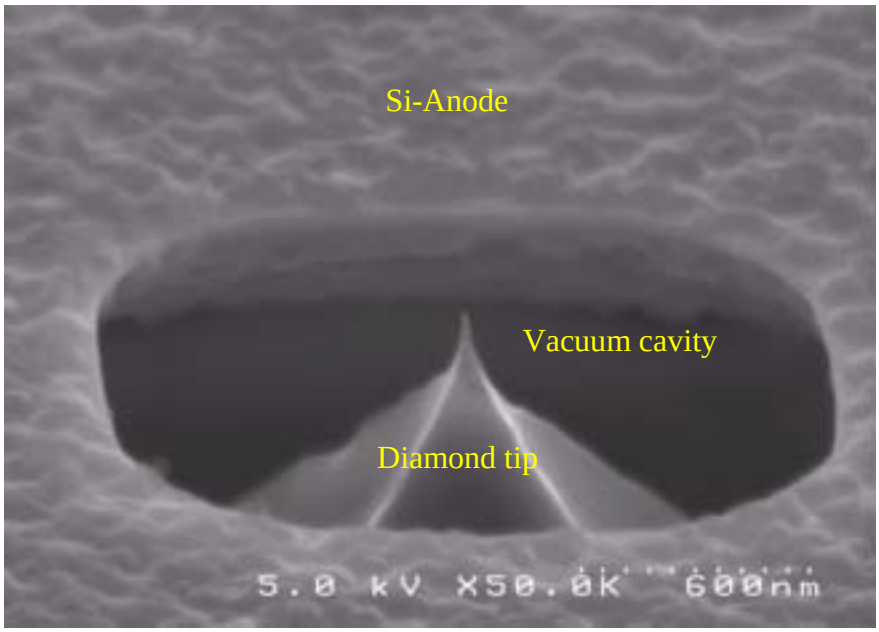


**Figure 6.68.** SEM micrograph of a diamond vacuum diode with self-aligned Si anode fabricated by self-align-anode-molding technique.

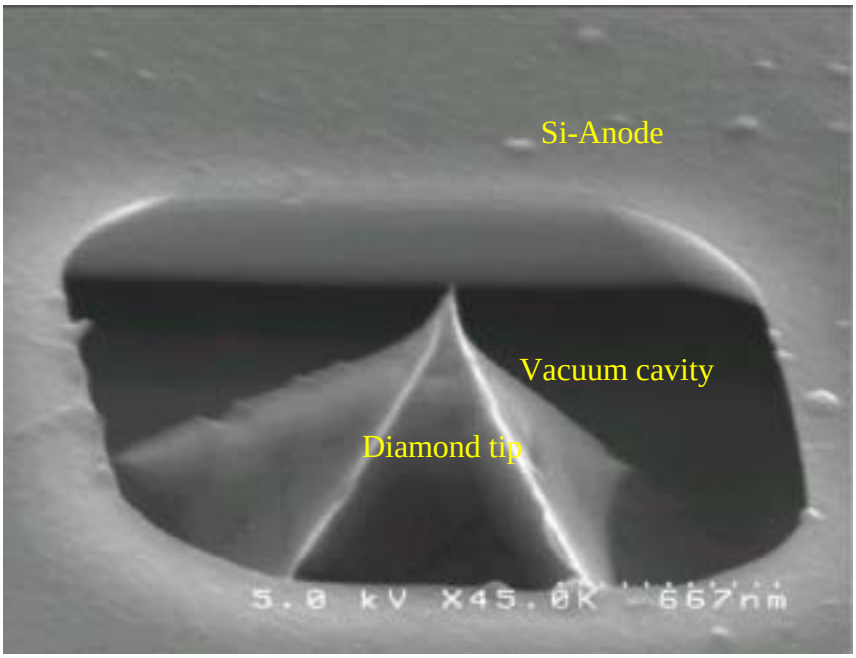


**Figure 6.69.** SEM micrograph of a diamond vacuum diode with self-aligned Si anode fabricated by self-align-anode-molding technique utilizing SOI wafer.

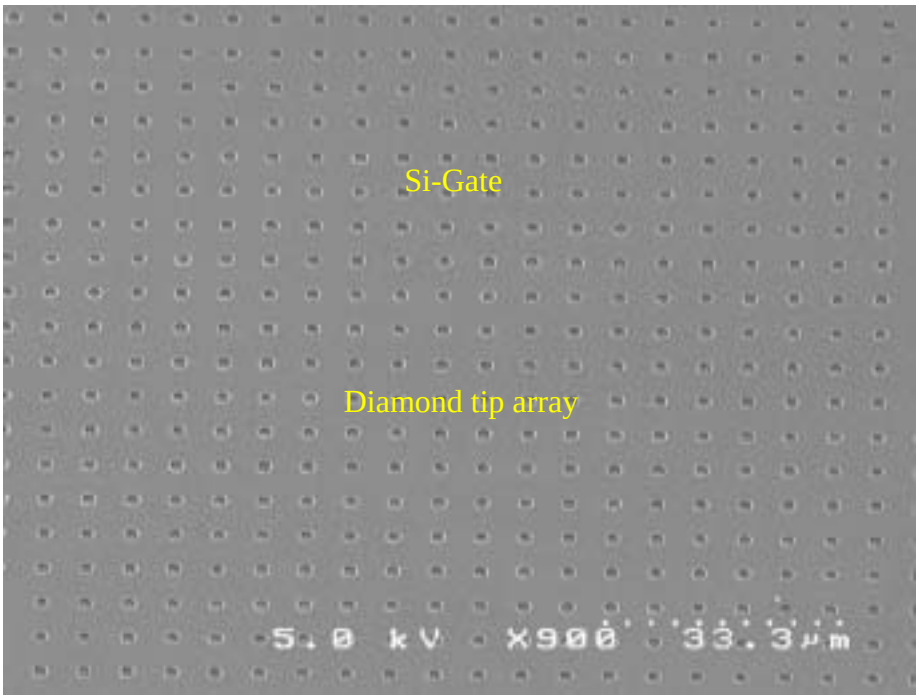


**Figure 6.70.** SEM micrograph of a large array of diamond vacuum diodes with self-aligned Si anode fabricated by self-align-anode-molding technique utilizing SOI wafer.

Emission characteristics of monolithic diamond vacuum diodes

A typical I-V characteristic of volcano type diamond vacuum diode (undoped diamond tips with no $sp^2$ content before VTE treatment) is shown in **Figure 6.71**. A nominal I-V characteristic of capped diamond vacuum diode (boron-doped diamond tips with low $sp^2$ content after VTE treatment) is demonstrated in **Figure 6.72**. A distinctive I-V characteristic of diamond vacuum diode with self-aligned Si anode (undoped sharpened diamond tips with low $sp^2$ content after VTE treatment) is shown in **Figure 6.73**.

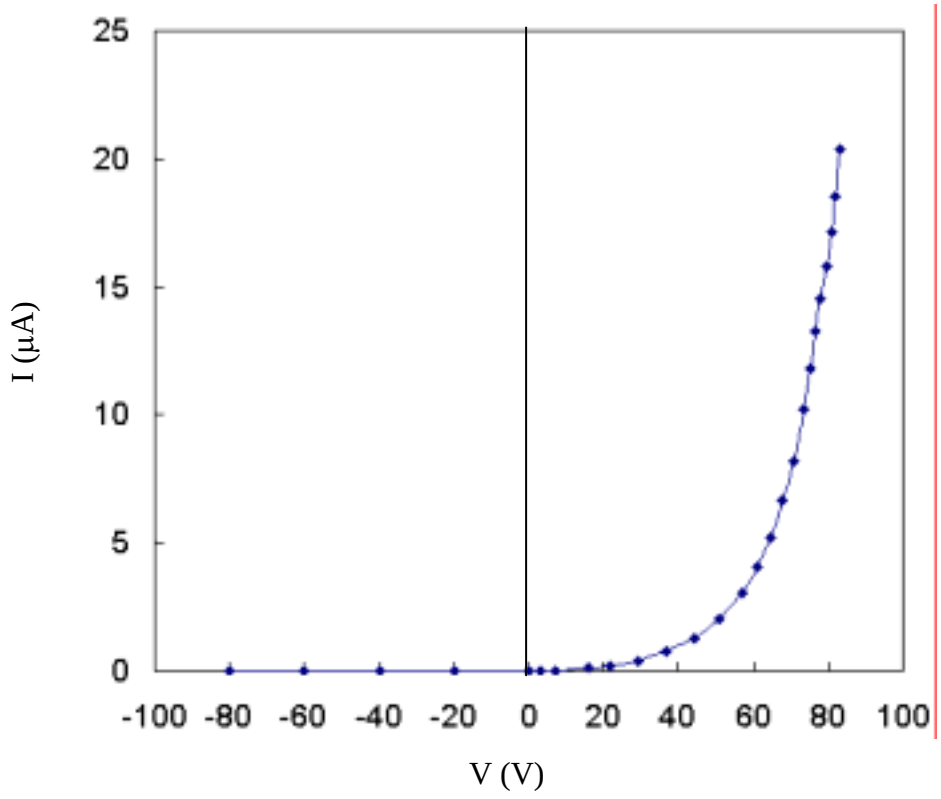


**Figure 6.71.** I-V plot of volcano type diamond vacuum diode (undoped diamond tips with no $sp^2$ content before VTE treatment).

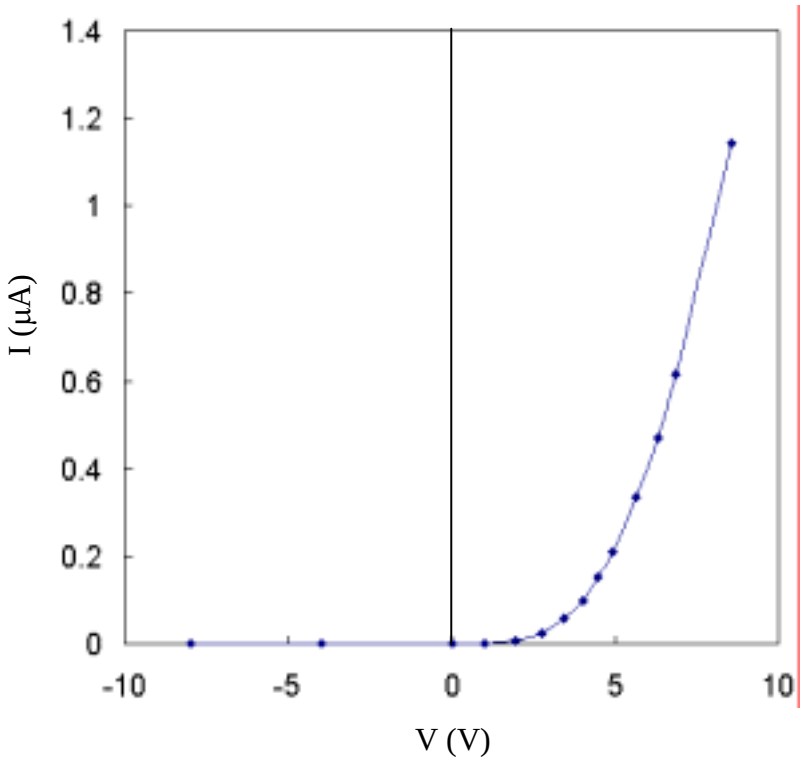


**Figure 6.72.** I-V plot of capped diamond vacuum diode (boron-doped diamond tips with low $sp^2$ content after VTE treatment)

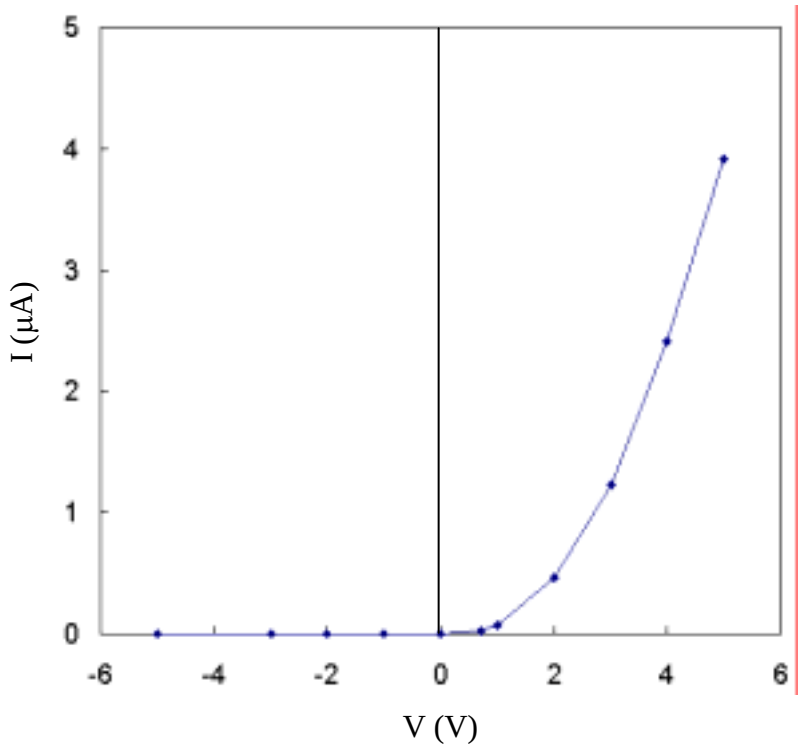


**Figure 6.73.** I-V plot of diamond vacuum diode with self-aligned Si anode (undoped sharpened diamond tips with low $sp^2$ content after VTE treatment).

Discussion of emission results from monolithic diamond vacuum diodes

Typical I-V characteristics of various types of diamond vacuum diode structures (normalized to a single tip) are shown in **Figure 6.74**, and the corresponding F-N plots are shown in **Figure 6.75**. It should be noted that these monolithic diodes were fabricated with different diamond cathode structures, diamond compositions, anode-cathode spacing, and anode configurations. First, the volcano diamond vacuum diode utilized unsharpened undoped diamond tips with no $sp^2$ content and volcano Al anode sitting on $SiO_2$ spacer with anode-cathode spacing of ~1 μm. Second, the capped diamond vacuum diode composed of boron-doped unsharpened diamond tips with low $sp^2$ content and Si suspending cap anode bonded via $SiO_2$ spacer with anode-cathode spacing of ~2 μm. Last, the self-aligned Si-anode diamond vacuum diode comprised of ultra sharp undoped diamond tips with low $sp^2$ content and silicon anode sitting on $SiO_2$ spacer with anode-cathode spacing of ~0.7 μm. From **Figure 6.74**, the turn-on voltage of volcano, capped, and self-aligned Si-anode diamond vacuum diodes are approximately 30 V, 2 V, and 0.7 V with emission current of 1 μA per tips at an anode voltage of 80 V, 10 V, and 5 V, respectively. Therefore, diamond vacuum diodes have excellent emission characteristics with low turn-on voltages. The turn-on voltages of diamond vacuum diodes (even for the worst case: volcano diode) are significantly lower than silicon field emission diode whose turn-on voltage is typically higher than 60 V even with submicron anode-cathode spacing [18-22].

Since the emission from the monolithic diodes cannot be directly confirmed from the fluorescent screen, additional experiments were conducted to affirm that the measured current is indeed a field emission current from diamond tips not a leakage current or hopping conduction current via the inter electrode silicon dioxide layer. Conductivity measurements of the devices in an open-air environment before and after emission testing were conducted to examine the quality of the silicon dioxide layer. No conduction current was observed for normal operating voltage up to ±80V. On the other hand, the measured current, **Figure 6.74**, shows a distinct asymmetric I-V characteristic for all diamond vacuum diode in vacuum environment ($10^{-6}$ Torr.). If the measured current is a leakage current or hopping conduction current via $SiO_2$, it must remain unchanged in open-air as well as vacuum environment because it is conduction current in solid-state device. In addition, current conduction due to F-N tunneling through silicon dioxide is highly unlikely, because tunneling through a 0.7 μm thick silicon dioxide layer would occur at a much higher electric field typically 1000 V/μm [193], contradicting to the low turn-on of 1 V/μm obtained

from **Figure 6.74**. Moreover, the measured current (**Figure 6.74**) is in good agreement with the emission current obtained from a similar diamond tip tested with an external phosphorous anode as described in part I. One may also speculate that the measured current at low electric field could be a result of Frenkel-Poole conduction via $SiO_2$ defects or emission through $SiO_2$/diamond Schottky barrier. These types of conduction currents, according to solid-state physics, are temperature dependent. Thus, we can distinguish these types of conduction currents from field emission current by temperature sensitivity measurement. **Figure 6.76** shows I-V plots of diamond vacuum diode with self-aligned Si-anode for various temperatures up to 200 °C. From **Figure 6.76**, it can be seen that the measured current is temperature in sensitive up to 200 °C, thus ruled out Frenkel-Poole and Schottky barrier conduction. All other diamond diodes have the same temperature insensitivity characteristics. Furthermore, it should be noted that leakage conduction currents via $SiO_2$ layer were observed from defective samples. These leakage conduction currents through the oxide were found to be strongly temperature sensitive, symmetric under applied voltage, and remained the same in both vacuum and open-air environment. More importantly, all of emission currents from monolithic diamond diodes conform to F-N behavior as evident from **Figure 6.75**. Therefore, it is confident to conclude from these experimental observations that these measured currents are indeed the emission currents from diamond into vacuum.

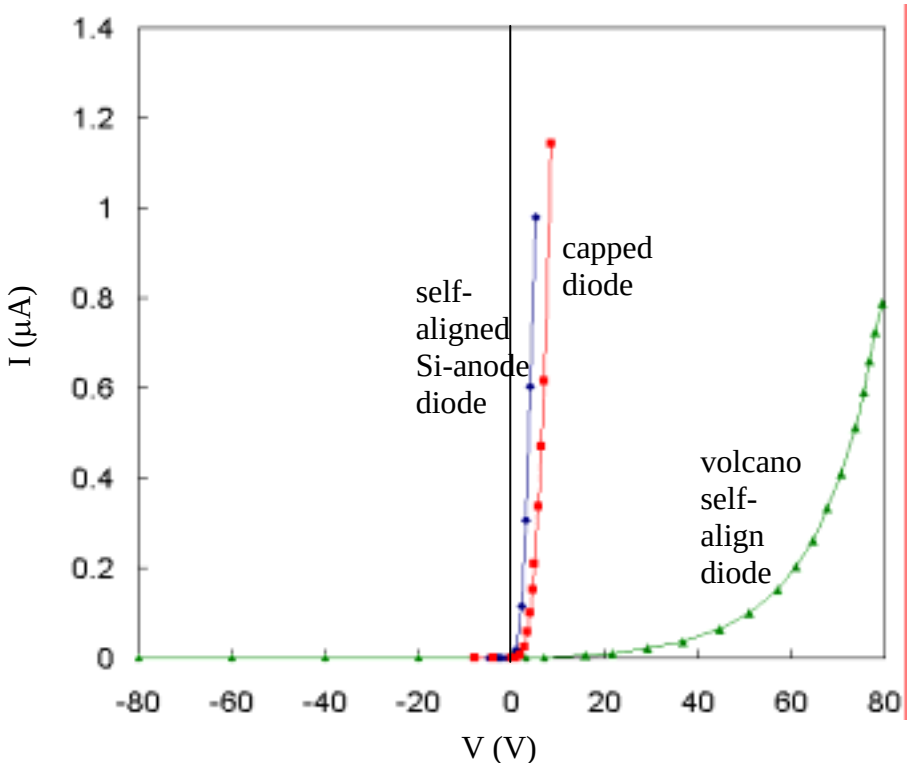


**Figure 6.74.** Typical I-V characteristics of various types of diamond emitter vacuum diode structures.

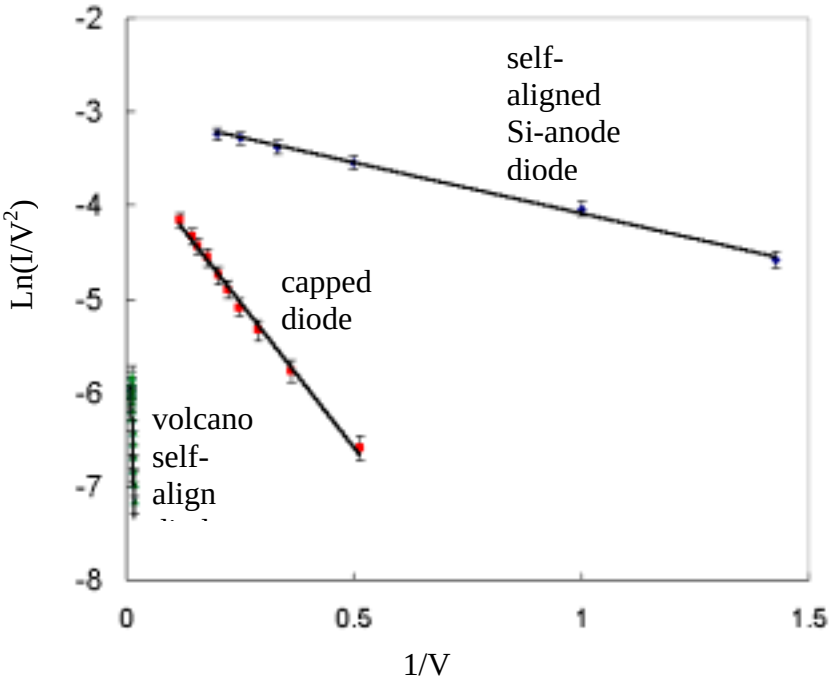


**Figure 6.75.** F-N plots of various types of diamond vacuum diode structures.

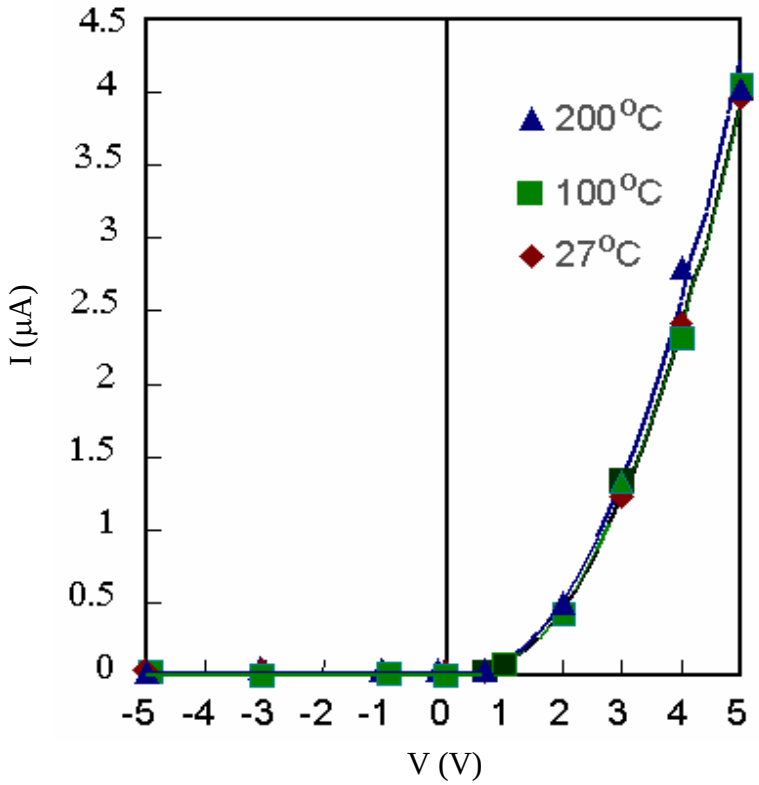


**Figure 6.76.** I-V plots of self-aligned Si-anode diamond vacuum diode for various temperatures.

The volcano self-align diamond diode has higher turn-on voltage than other diodes because $sp^2$ incorporation, boron doping, and tip sharpening were not applied to enhance the emission characteristics. The F-N plots (**Figure 6.75**) demonstrate that volcano self-align diamond diode has steepest F-N slope, which should be due to low field enhancement factor of no $sp^2$, undoped, unsharpened diamond tip. It should be noted that due to complexity in fabrication of volcano self-align diamond diode, we did not pursue to optimize emission characteristic from this structure. The capped diode exhibits better emission characteristics with lower turn-on voltage since $sp^2$ incorporation and boron doping were utilized to enhance emission characteristics. The self-aligned Si-anode diamond diode demonstrates the lowest turn-on voltage and high emission current, which should be attributed to ultra sharp diamond microtip structure, $sp^2$ content, and VTE treatment. It should be noted that boron doping were not applied to the self-aligned Si-anode structure because boron dopants could migrate into $SiO_2$ during PECVD diamond deposition and cause leakage current through $SiO_2$. The F-N plots (**Figure 6.75**) reveal that self-aligned Si-anode diamond diode has shallowest F-N slope, which should be

due to high field enhancement factor contributed by $sp^2$ content, ultra sharp diamond tip structure and VTE treatment.

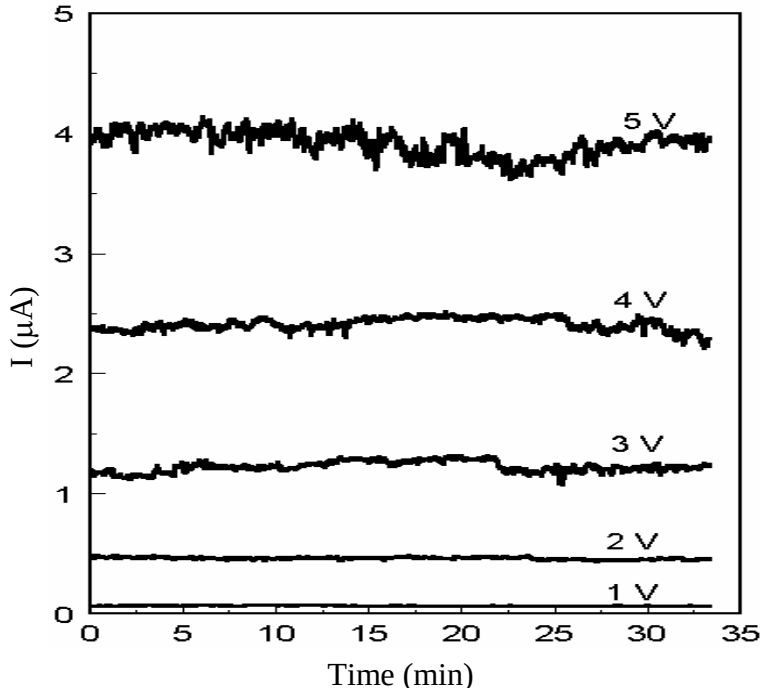


**Figure 6.77.** I-t plot of self-aligned Si-anode diamond vacuum diode.

Furthermore, the self-aligned anode diamond vacuum diode has relatively stable emission current at a given anode voltage. **Figure 6.77** shows a typical current vs. time (I-t) plot of the self-aligned Si-anode diamond vacuum diode for various anode voltages. The fluctuation of emission current was found to be about 2% for low emission current and less than 15% for high emission current. This fluctuation is considerably smaller than that of a typical single silicon tip (50% at the emission current of ~1 μA) [39].

Modeling of monolithic diamond vacuum diode

The I-V characteristics of the monolithic diamond vacuum diodes were modeled by the modified Fowler-Nordhiem equation (in forward bias) as in the analysis of diamond microtip cathode but using slightly different form:

$$I = \begin{cases} CV^2 \exp(-D/V) & V > 0 \\ 0 & -V_B < V \le 0 \end{cases} \qquad (6.8)$$

where $C \equiv A^*K_1^*\beta^2/(d^2\Phi)$ and $D \equiv K_2 d\Phi^{1.5}/\beta$. $V_B$ is the breakdown voltage before reverse field emission. All other variables were previously defined in eq. 6.3. This is a simplified form of F-N equation (eq. 6.3) with anode voltage (V) as the main variable. It should be noted that the reverse emission current from monolithic vacuum diode is hypothetically zero (below noise level). The modeling parameters (C and D) of various monolithic diamond vacuum diodes were found from intercepts and slopes of F-N plots (**Figure 6.77**) and listed along with turn-on voltages ($V_{on}$) and theoretical breakdown voltage ($V_B$) in **Table 6.5**.

**Table 6.5.** Modeling parameters for various diamond vacuum diodes.

| Diamond vacuum diode | C ($\mu A/V^2$) | D (V) | $V_{on}$ (V) | $V_B$ (V) [theoretical] | $V_B/V_{on}$ |
|---|---|---|---|---|---|
| Volcano diode | 0.0012 | 184.74 | 30 | 2700 | 90 |
| Capped diode | 0.030975 | 6.22 | 2 | 5400 | 2700 |
| Self-aligned Si-anode diode | 0.049439 | 1.08 | 0.7 | 1900 | 2700 |

It can be deduced from **Table 6.5** that the turn-on voltage ($V_{on}$) of vacuum diode strongly depends on C and D values. It addition, $V_{on}$ is nearly proportional to D and inversely proportional to C. Thus, small D and large C values are desired to achieve vacuum diode with low turn-on voltage. From the definition, it can be seen that small D and large C values can be achieved by well-designed diamond diode with high field enhancement factor, low work function, large emitting area, and small anode-cathode spacing.

Theoretically, breakdown voltage can be estimated by the assumption that breakdown occurs due to reverse electron field emission from anode to cathode. Thus, the breakdown voltage depends on the work function of anode ($\Phi_A$), anode configuration, and anode-cathode spacing (d), which can be estimated from a simple relationship:

$$V_B = d \times E_b/\beta_A \qquad (6.9)$$

where $E_b$ is the breakdown electric field which is proportional to the work function of anode ($\Phi_A$). $\beta_A$ is the field enhancement factor of anode that depends on anode configuration. $E_b$ can then be approximated based on basic field emission theory of planar cathode [134] by a simple diagram illustrated in **Figure 6.78**.

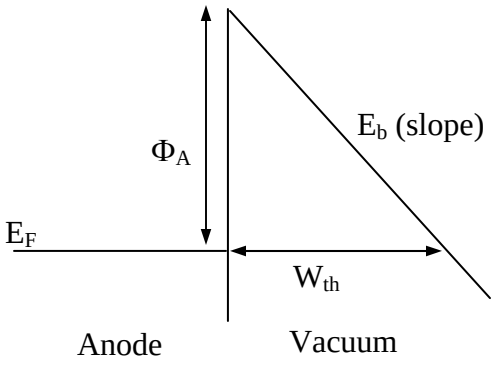


**Figure 6.78.** Diagram for a simple approximation of $E_b$.

From **Figure 6.78**, $E_b$ can be estimated on the condition that the applied electric field $E_b$ thins down the potential barrier width such that the tunneling distance at Fermi level of anode is reduced to a critical value, $W_{th}$, the threshold tunneling distance at which tunneling probability is sufficiently high for electrons to tunnel into vacuum. It can easily be deduced from the diagram that

$$E_b = \Phi_A/W_{th} \tag{6.10}$$

Based on quantum mechanics, $W_{th}$ for tunneling through a triangle barrier is ~1.5 nm. Using $\Phi_A$ = 4.1 eV for an $n^{++}$ silicon anode, $E_b$ is calculated to be ~2700 V/μm.

The geometrical field enhancement factor of anode, $\beta_A$, is normally assumed to be one for anode with planar surface. However, the surface roughness could result in a higher field enhancement. For our first order approximation, $\beta_A$ are all assumed to be one. Thus, breakdown voltages of various diamond vacuum diodes were calculated as shown in **Table 6.5**.

The ratio, $V_B/V_{on}$, is a measure of the rectifying capability of a diode. For rectifying applications, $V_B/ V_{on}$ is desired to be as high as possible. It can be seen from the table that the theoretical rectify capability of diamond vacuum diode can be higher than that of a solid-state diode. However, there are two main factors that may cause breakdown of field emission vacuum diode to occur before the theoretical limit is reached. First is the breakdown of dielectric spacer, which depends on the quality of the dielectric spacer. Second is field ionization or vacuum discharge due to residual gas in the vacuum system, which depends on vacuum conditions [187]. Thus, it is difficult to determine the actual breakdown voltage of a vacuum diode.

Small signal model of diamond vacuum diode

For small signal application, diamond vacuum diode, similar to solid-state diode, can be model as a variable resistor. The dynamic resistance ($r_d$) of diamond vacuum diode (in forward bias) can be derived from the standard definition of the dynamic resistance.

$$\begin{aligned} r_d &= \frac{dV}{dI} \\ &= \frac{\exp(D/V)}{C(2V+D)} \\ &= \frac{V}{I(2+D/V)} \end{aligned} \tag{6.11}$$

**Figure 6.79** shows the calculated dynamic resistance per tip for various diamond vacuum diodes as a function of biasing voltages. Generally, the dynamic resistance per tip for vacuum diodes is relatively high. But the value can be decreased significantly by increasing the number of emitting tips in the diode design. However, the dynamic resistance of diamond vacuum diode may not be lower than that of solid-state diode, of which $r_d = V_T/I$ where $V_T=kT/q$ (k= boltzman's constant, T=temperature (K), and q = electron charge). This is because the dynamic resistance of vacuum diode from Eq. (6.11) is lower than the DC resistance ($R_{dc}=V/I$) by the factor of (2+D/V). It should also be noted that as V increases, $r_d$ of diamond vacuum diode would be approaching the limit of V/(2I). This is a drawback of diamond vacuum diode compared to solid-state diodes.

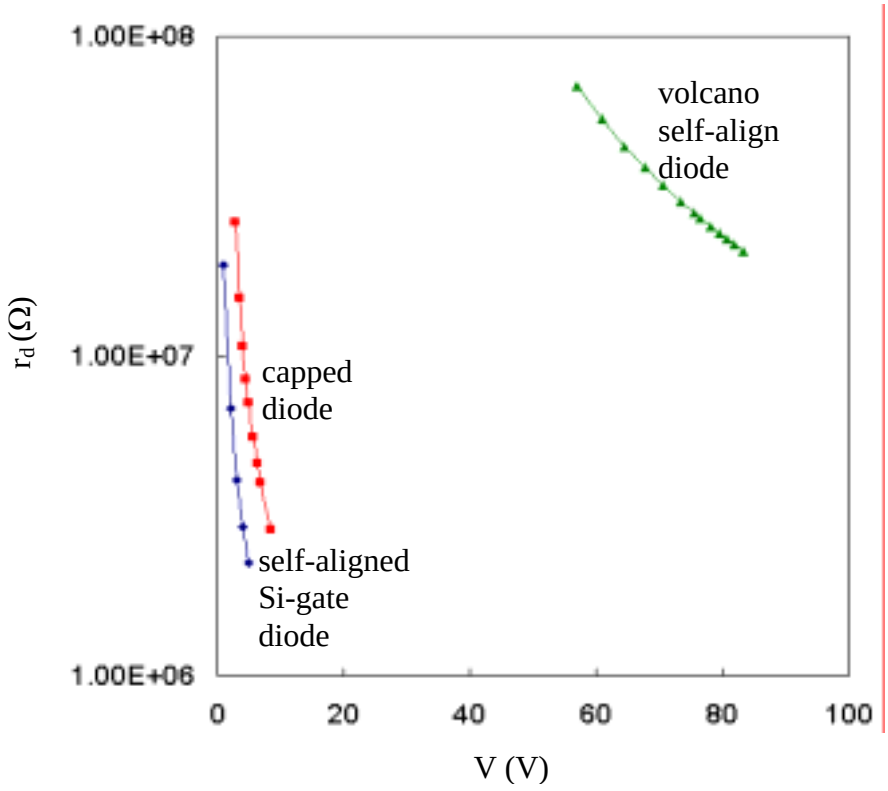


**Figure 6.79.** Calculated dynamic resistances per tip for various diamond vacuum diodes.

Part III: Monolithic diamond vacuum triode

Design and fabrication issues of gated diamond vacuum triode

Fabrication of monolithic diamond vacuum triode is quite complicated. In addition to the requirements needed for gated diamond emitter, there are two main issues involving design and fabrication of monolithic diamond vacuum triode by molding technique: the practicality of the fabrication process for monolithic diamond vacuum triode, and the quality of anode-gate dielectric spacer. To achieve these goals, three fabrication configurations for monolithic diamond vacuum triode structures have been explored and developed.

Discussion of various fabrication processes for monolithic diamond vacuum triode

I. Integrated anode utilizing electrostatic bonding technique

Electrostatic bonding technique as described in chapter V was used to obtain a gated diamond emitter triode with a cap anode. There are two configurations of this type of diamond

emitter triode: gated diamond emitter triode with a cap anode bonded directly on the gate, and a cap anode bonded to a supporting substrate. There are pros and cons between these two techniques. The first configuration is better than the second in term of anode-cathode co-planarity over large area because it is difficult to align a cap anode coplanar to gated cathode arrays. On the other hand, the second configuration is better than the first to maintain the anode-gate dielectric quality after anodic bonding process. The direct anodic boding on the gate would weaken the dielectric spacer quality due to high heat and electric field that must be applied to form a good bond between spacer and silicon gate.

II. Integrated anode utilizing SOI substrate

Integrated anode utilizing SOI bulk layer was investigated to achieve self-align gated diamond emitters with an integrated suspending anode. This fabrication method is practical and efficient because integral parts of triode structure such as gate and anode are inherently embedded in the SOI substrate design. In addition, co-planarity problem is eliminated because anode and cathode are automatically co-planar. Furthermore, anode-cathode dielectric quality may be ensured by the high quality of the embedded silicon dioxide on SOI wafer. However, the anode-gate spacing of triode fabricated by this technique is limited by the thickness (a few microns) of the embedded silicon dioxide layer on commercially available SOI wafer. The small anode-gate spacing of triode may result in low amplification factor for triode, which is not desirable for a number of applications.

Physical structure of monolithic diamond vacuum triode

Physical structures of monolithic diamond vacuum triodes fabricated by various fabrication techniques are shown in **Figures 6.80-6.82**. An SEM micrograph of diamond vacuum triode fabricated by cap-anode electrostatic bonding over gated diamond emitter is shown **Figure 6.80.** It illustrates an array of gated diamond microtips with an integrated silicon anode located ~50 μm above the gated diamond tips. A high-maginification SEM micrograph, **Figure 6.81**, shows gate opening of self-align gated diamond vacuum triodes. It can be seen that diamond tips are approximately at the same level as the gate open with gate opening of ~2 μm in diameter and hence gate-cathode spacing of ~1μm. An SEM micrograph, **Figure 6.82**, shows diamond vacuum triode fabricated by integrated SOI anode approach. It illustrates a self-align Si-gated diamond microtips with gate opening of ~2 μm and an integrated silicon anode located ~3 μm above the diamond tips.

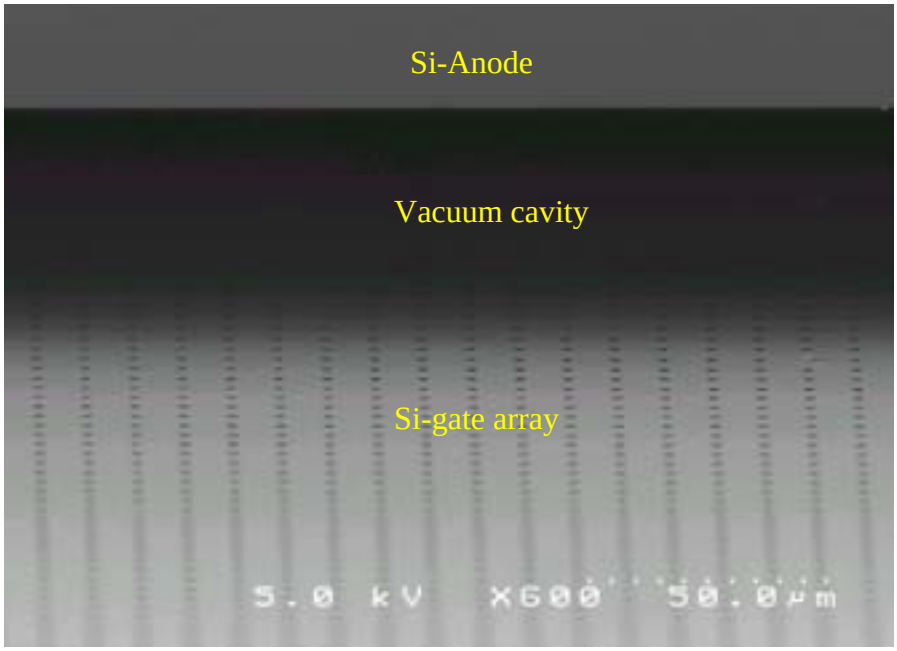


**Figure 6.80.** SEM micrograph of an array of self-align gated diamond vacuum triodes with integrated anode by electrostatic bonding technique.


**Figure 6.81.** SEM micrograph showing gate opening of self-align gated diamond vacuum triodes.

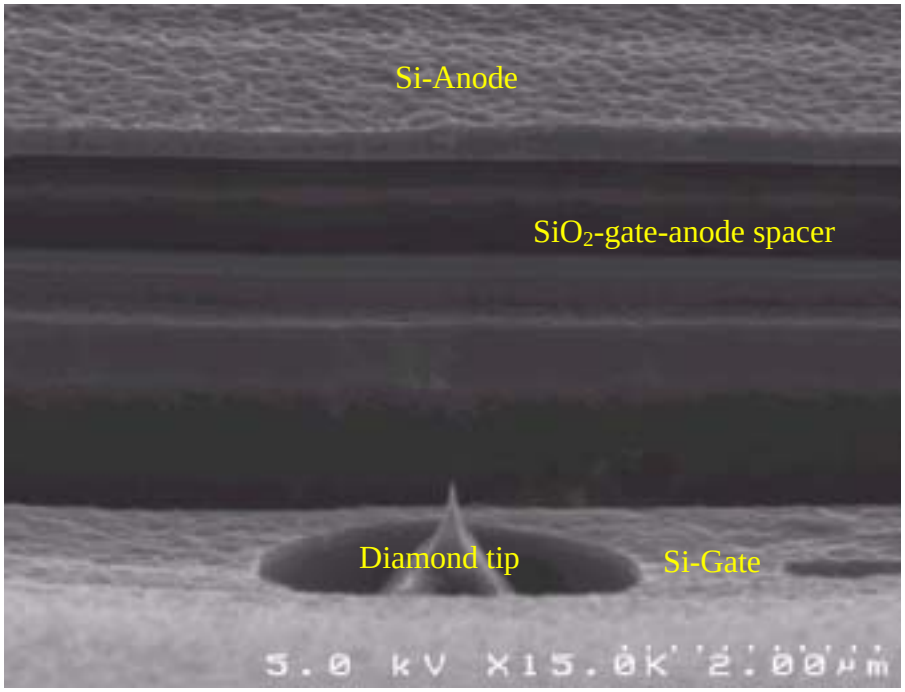


**Figure 6.82.** SEM micrograph of a self-align gated diamond vacuum triode with integrated SOI anode.

Emission characteristics of diamond vacuum triodes

The emission behaviors of diamond vacuum triodes were characterized by anode emission current vs. anode voltage ($I_a$-$V_a$) for various gate voltages ($V_g$). Triode characteristics of four diamond vacuum triodes with different device parameters were studied and evaluated. It should be noted that these triodes were fabricated with the same self-aligned si-gate approach, same $sp^2$ content of diamond cathode (low $sp^2$), same gate opening size (cathode-gate spacing of ~1 μm), and same silicon cap-anode configurations. These triodes, however, have different doping of diamond cathode, array size, and anode-cathode (or gate) spacing (note: gate and cathode are approximately at the same level). The triode labeled "Triode U1" utilized a 4x4 tips array of undoped low $sp^2$ diamond tips and anode-cathode spacing of ~50 μm. The emission characteristics ($I_a$-$V_a$-$V_g$) of Triode U1 are shown in **Figure 6.83**. The triode labeled "Triode U2" used a 64x64 tips array of undoped low $sp^2$ diamond tips and anode-cathode spacing of ~500 μm. The $I_a$-$V_a$-$V_g$ characteristics of Triode U2 are shown in **Figure 6.84**. The triode labeled "Triode B1" utilized a 16x16 tips array of boron-doped low $sp^2$ diamond tips and anode-cathode spacing of ~50 μm. The $I_a$-$V_a$-$V_g$ characteristics of Triode B1 are shown in **Figure 6.85**. The triode labeled "Triode B2" employed a 256x256 tips array of boron-doped low $sp^2$ diamond tips and anode-cathode spacing of ~1 mm. The $I_a$-$V_a$-$V_g$ characteristics of Triode B2 are shown in **Figure 6.86**. It should be noted that Triode B1 and Triode B2 were doped with different doping methods. Triode B1 was doped with high concentration solid boron source whereas Triode B2 was doped with a low concentration of boron gas source. Thus, it is assumed that Triode B2 has lower boron doping concentration than Triode B1. Triode device parameters are summarized in **Table 6.6**.

**Table 6.6.** Device parameters for various diamond vacuum triodes.

| Diamond vacuum triode | U1 | U2 | B1 | B2 |
|---|---|---|---|---|
| Array size | 4x4 | 64x64 | 16x16 | 256x256 |
| Anode-cathode spacing | ~50 μm | ~500 μm | ~50 μm | ~1000 μm |
| doping | undoped | undoped | $p^+$ | p |
| $sp^2$ content | low $sp^2$ | | | |
| Gate-cathode spacing | ~1 μm | | | |
| Structure | Self-aligned Si gate with cap anode | | | |

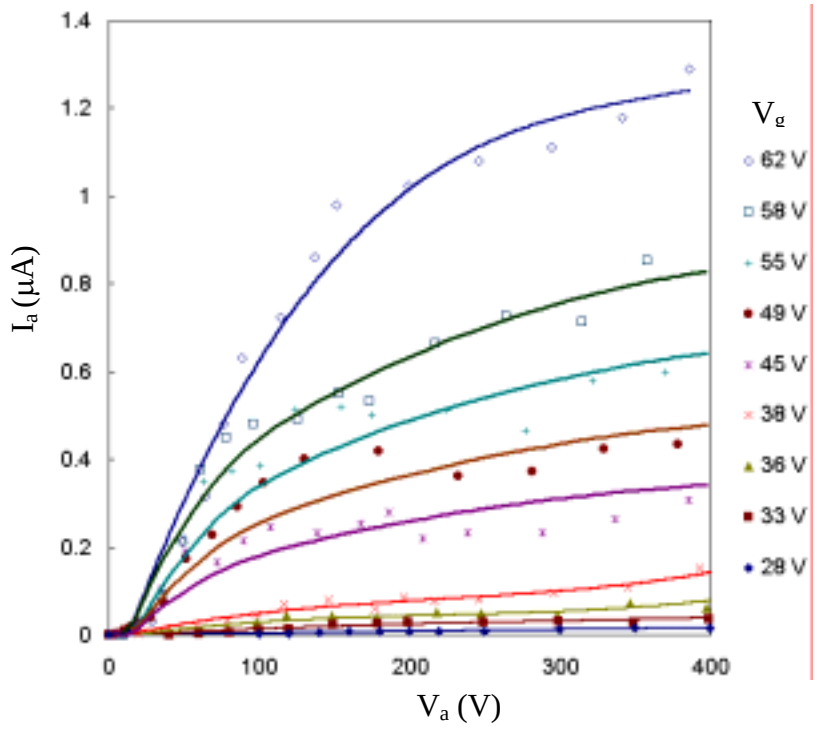


**Figure 6.83.** $I_a$-$V_a$ plots of Triode U1 for various $V_g$.

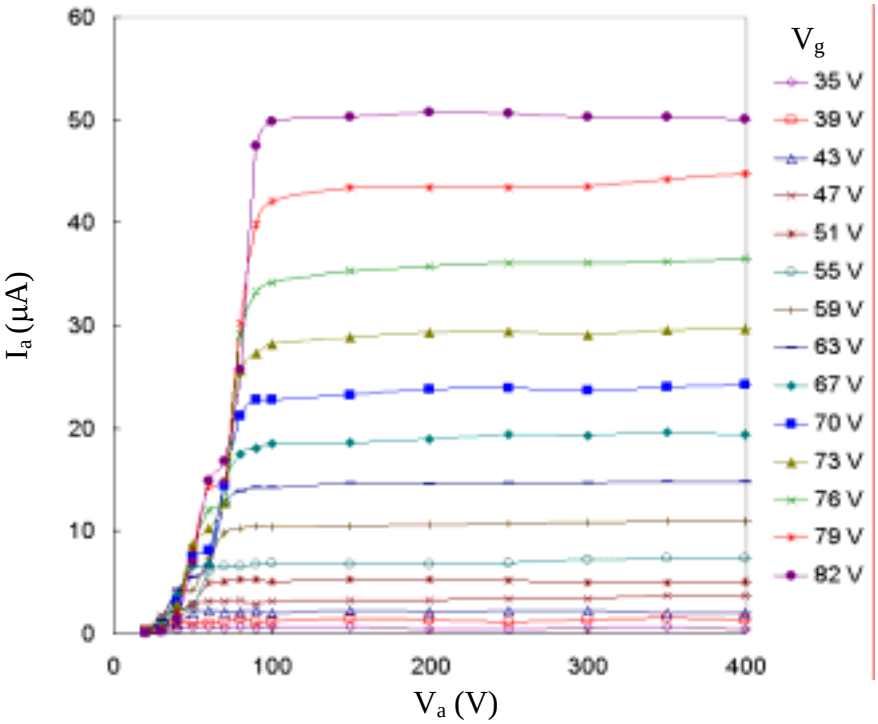


**Figure 6.84.** $I_a$-$V_a$ plots of Triode U2 for various $V_g$.

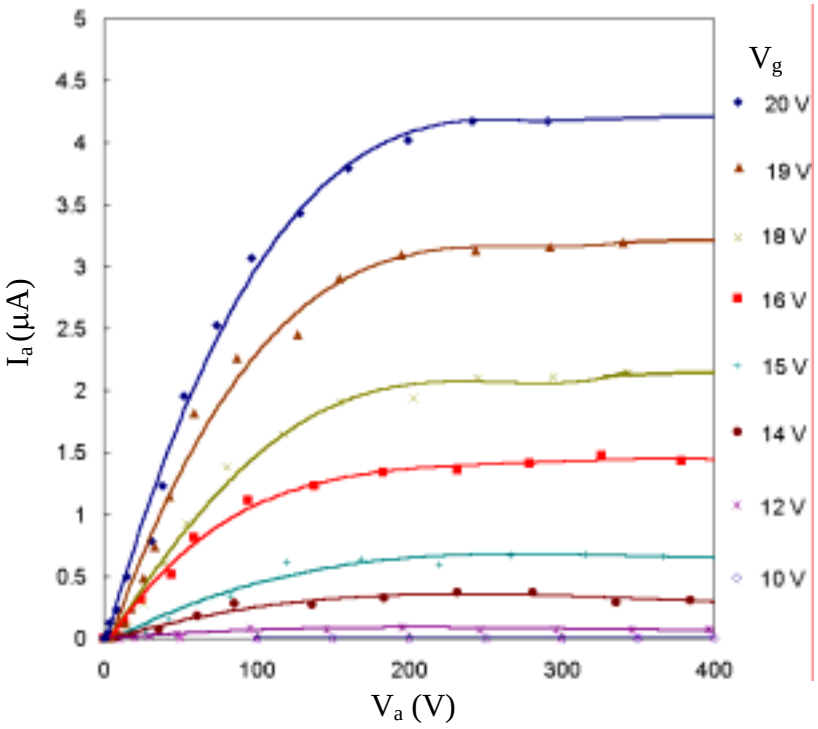


**Figure 6.85.** $I_a$-$V_a$ plots of Triode B1 for various $V_g$.

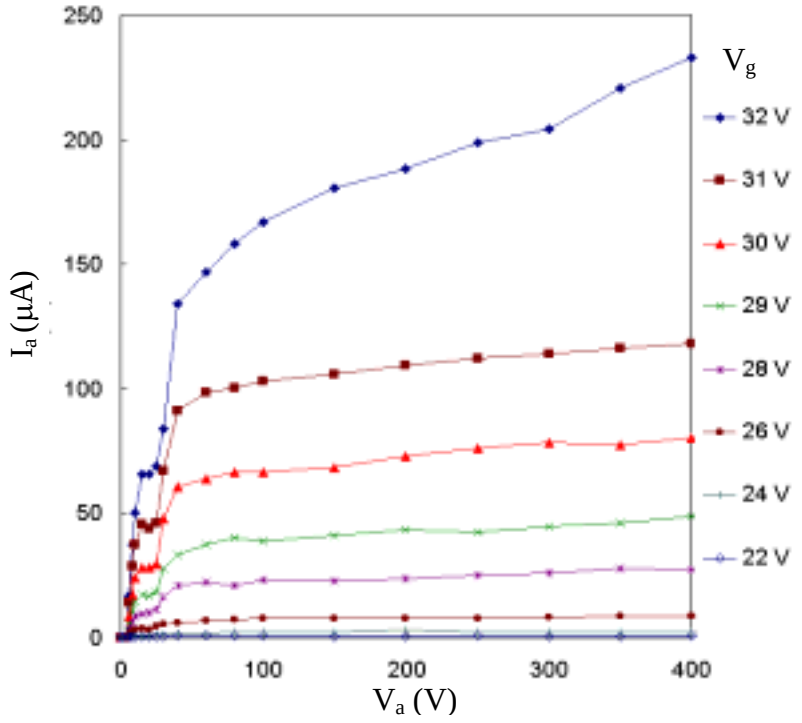


**Figure 6.86.** $I_a$-$V_a$ plots of Triode B2 for various $V_g$.

Discussion of emission results from diamond vacuum triodes

The $I_a$-$V_a$ plots of emission data for various diamond triodes (**Figures 6.83-6.86**) demonstrate that all diamond triodes have the desired saturation behavior of field emission transistors. The saturation regions for various gate voltages are seen at anode voltages above ~200 V, 150 V, 90 V, and 60 V for Triode U1, B1, U2, and B2, respectively. The results imply that the anode saturation voltage ($V_{a,sat}$) tends to decrease as anode-cathode spacing increases (Note that anode-cathode spacing for Triode U1, B1, U2, and B2 are ~50, 50, 500, and 1000 μm, respectively). In addition, the anode saturation voltage for each triode slightly increases as the gate voltage increases. Furthermore, boron-doped diamond triode has a lower anode saturation voltage than undoped diamond triode. This observation will be discussed and explained later.

From $I_a$-$V_g$ plots of emission data for various diamond triodes (**Figures 6.87-6.90**), the gate turn-on voltages for Triode U1, B1, U2, and B2 are ~28, 10, 30, and 22 V, respectively. The result indicates that a boron-doped diamond triode has a lower gate turn-on voltage than an undoped diamond triode, which is expected and in good agreement with the result obtained from diamond field emitter diodes. In addition, Triode B1 has a lower turn-on voltage than Triode B2. This result is also expected because Triode B1 has a higher doping concentration than Triode B2. The gate turn-on voltage of diamond triode is considerably lower than that of comparable silicon field emission triode with the same gate-cathode spacing of 1 μm [18,22-25], whose turn-on voltage is typically >80 V. Furthermore, the anode current at a given gate voltage increases as the array size increases.

The F-N plots of various diamond triodes are shown in **Figure 6.91**. It indicates that the emission characteristics of diamond triodes conform to F-N behaviors. It can be seen that Triode B1 has the shallowest F-N slope, hence the highest field enhancement factor as expected. In addition, Triode U1 and U2 have approximately the same F-N slope as expected because they have the same diamond cathode structure and composition. However, it can be noticed that Triode B2 has the steepest F-N slope. This result is unexpected because boron-doped low $sp^2$ diamond tips should have a higher field enhancement factor than undoped low $sp^2$ diamond tips. This discrepancy may be attributed to the Nickel (Ni) back contact that was used for this particular triode to provide good adhesion for diamond brazing to copper layer on metal substrate (Ni has a high work function of 5.3 eV). These observations will be discussed and explained in the following section.

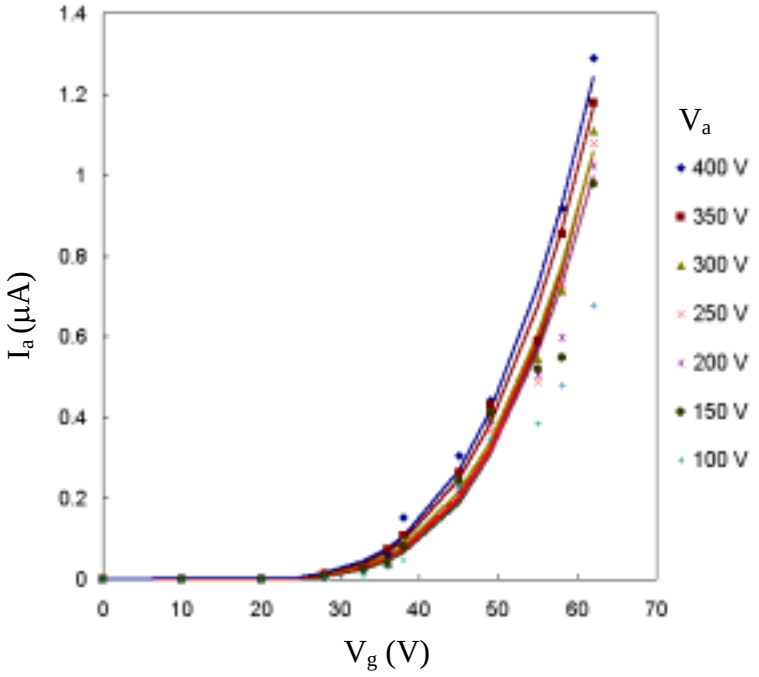


**Figure 6.87.** $I_a$-$V_g$ plots of Triode U1 for various $V_a$.

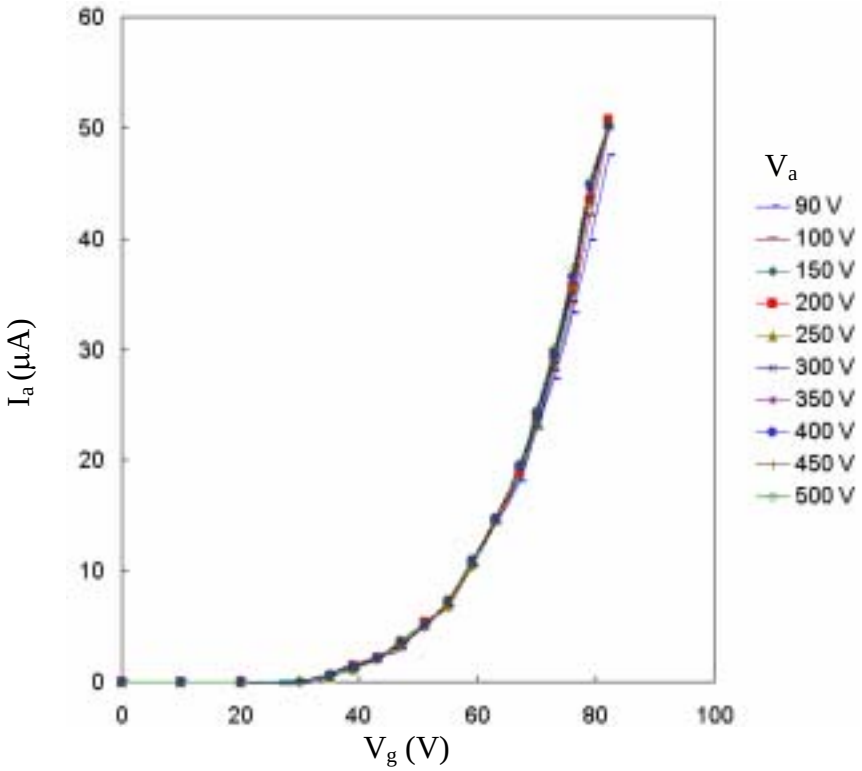


**Figure 6.88.** $I_a$-$V_g$ plots of Triode U2 for various $V_a$.

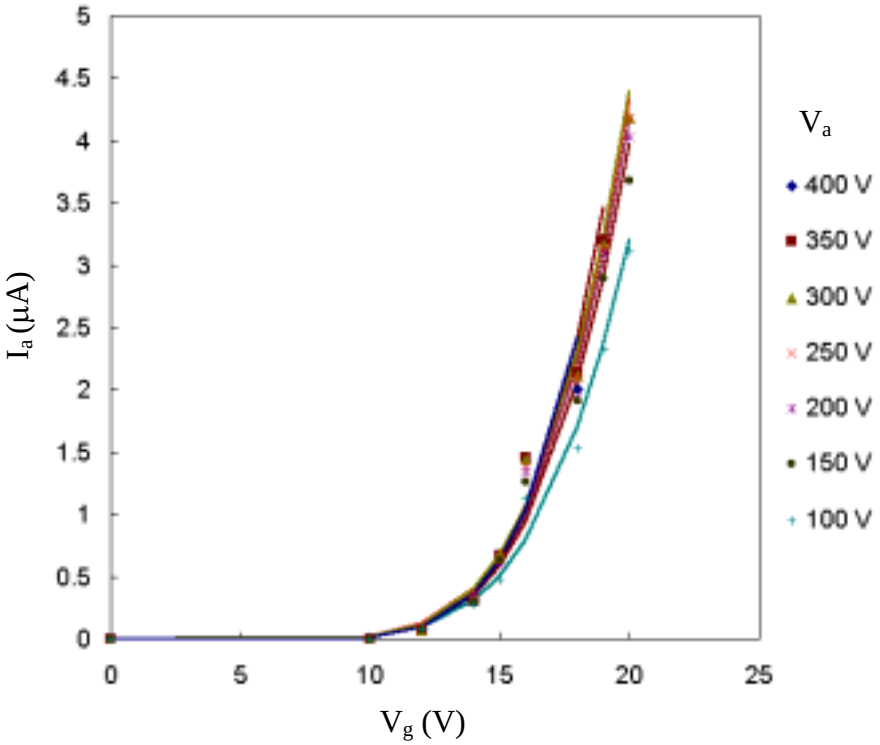


**Figure 6.89.** $I_a$-$V_g$ plots of Triode B1 for various $V_a$.

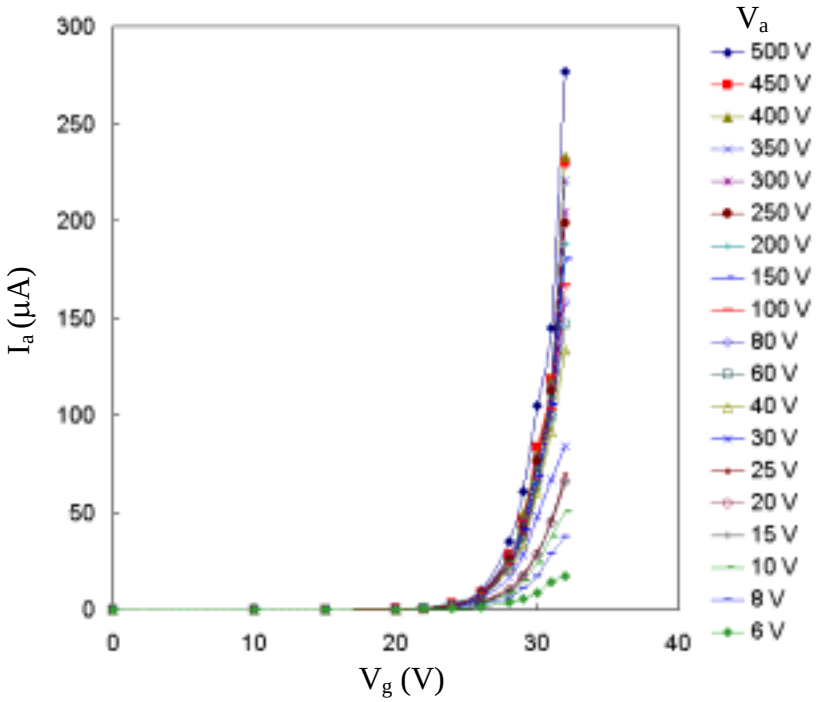


**Figure 6.90.** $I_a$-$V_g$ plots of Triode B2 for various $V_a$.

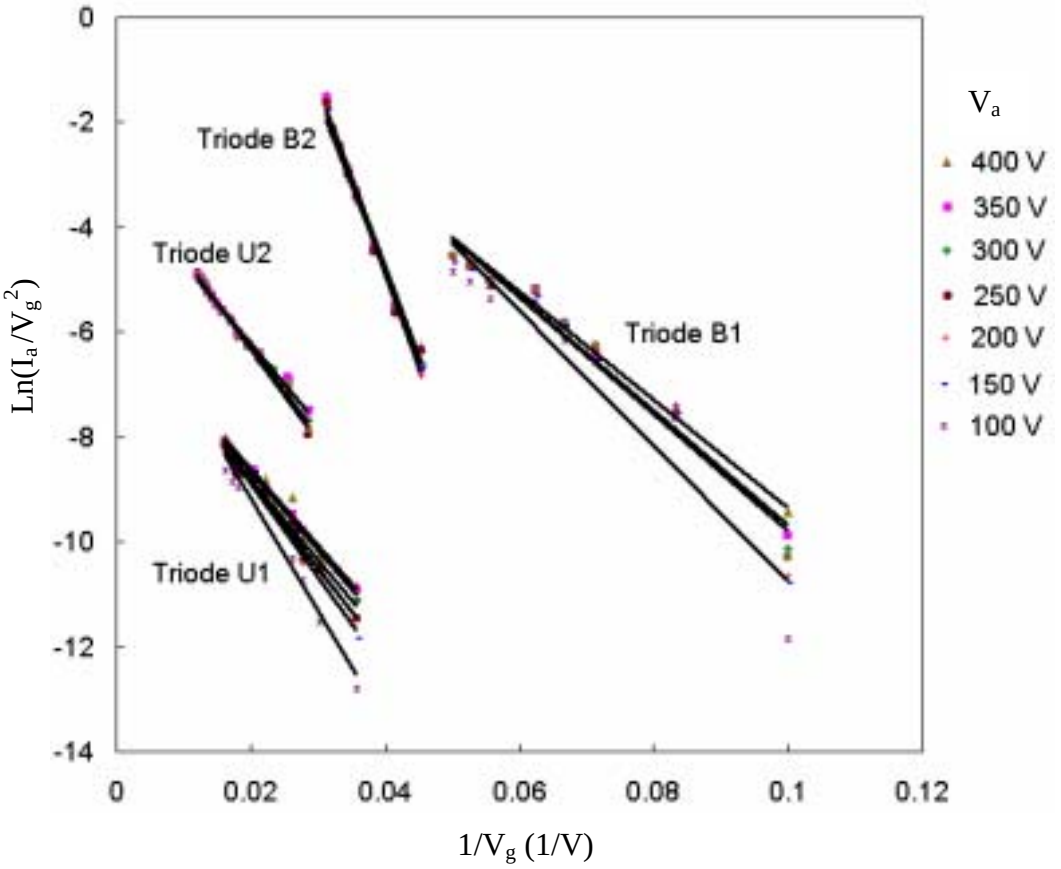


**Figure 6.91.** F-N plots of various diamond emitter triodes for various $V_a$.

Modeling of diamond vacuum triode

The emission characteristics of diamond vacuum triode have been modeled by the modified Fowler-Nordhiem (F-N) equation where the total emission current emitted from the cathode is given by:

$$I_t = XE^2 \exp\left(\frac{-Y}{E}\right) \tag{6.12}$$

where $Y \equiv \frac{K_2 * \Phi^{1.5}}{\beta}$, $X \equiv \frac{A * K_1 * \beta^2}{\Phi}$, $K_1$, $K_2$, $\Phi$, $\beta$, and A are previously defined. X and Y can be obtained from the intercept and slope of F-N plots, respectively. E is the resultant electric field at the cathode due to the applied gate and anode voltages.

$$E = (V_g + V_a/\mu)/d \tag{6.13}$$

where $V_g$, $V_a$, $\mu$, and d are gate voltage, anode voltage, amplification factor, and gate-cathode spacing, respectively. The emission current collected at the anode, $I_a$, is derived from the total emission current as:

$$I_a = \alpha X E^2 \exp\left(\frac{-Y}{E}\right) \tag{6.14}$$

where $\alpha$ is the emission transport factor that is defined as the fraction of emission current collected at the anode to the total emission current emitted from the cathode ($\alpha \equiv I_t/I_a$). It should be noted that $\alpha$ is not a constant, it depends on anode and gate voltages for a given triode structure.

Extracting modeling parameters for diamond vacuum triode

Modeling of diamond vacuum triode is complicated since there are many parameters and unknown functions. We have established a procedure for extracting the related modeling parameters of diamond vacuum triode from the anode emission current:

I. Determine the amplification factor, $\mu$
II. Make corrected F-N plot of emission current
III. Calculate and plot the total emission current ($I_t$) versus the anode current ($I_a$).
IV. Calculate and plot $\alpha$
V. Model $\alpha$
VI. Calculate and verify the modeled anode current with the actual anode current

The following illustrates the detail application of the procedure for all diamond vacuum triodes.

I. Determine the amplification factor, $\mu$

The amplification factor, $\mu$, can be estimated graphically from the basic definition

$$\mu = -\left.\frac{\Delta V_a}{\Delta V_g}\right|_{I_a = cons\tan t} \tag{6.15}$$

Applying to Triode U1, if $V_a$ changes from 350 V to 400 V, $V_g$ is required to change from ~59.85 V to ~59 V at a constant $I_a$ of 1 $\mu$A (see **Figure 6.87**). Thus, $\mu_{U1} \approx 50/0.85 \approx 68$. For Triode U2, if $V_a$ changes from 150 V to 400 V, $V_g$ is required to change from ~67.35 V to ~67.2 V at a constant $I_a$ of 40 $\mu$A (see **Figure 6.88**). Thus, $\mu_{U2} \approx 250/0.43 \approx 580$. For Triode B1, if $V_a$

changes from 350 V to 400 V, $V_g$ is required to change from 19 to 19.2 V at a constant $I_a$ of 3 μA (see **Figure 6.89**). Thus, $\mu_{B1} \approx 50/0.2 \approx 250$. For Triode B2, if $V_a$ changes from 150 V to 400 V, $V_g$ is required to change from 31.7 V to 31.4 Vat a constant $I_a$ of 150 μA (see **Figure 6.90**). Thus, $\mu_{B2} \approx 250/0.3 \approx 800$. Although μ is evaluated for a single operating point in saturation region, it can represent the amplification factors over a wide operating voltage in that region because μ is a very weak function of gate and anode voltages [16]. The high amplification factor value indicates that diamond field emission triode should be good for small signal amplification.

The calculated result shows that $\mu_{U1} < \mu_{B1} < \mu_{U2} < \mu_{B2}$. This result is in accordance with the previous observation and discussion that $V_{a,sat,U1} > V_{a,sat,B1} > V_{a,sat,U2} > V_{a,sat,B2}$ and $D_{U1} \approx D_{B1} < D_{U2} < D_{B2}$ ($V_{a,sat}$ ≡anode saturation voltage and D≡anode-cathode spacing). Two conclusions can be made. First, μ increases and $V_{a,sat}$ decreases as D increases. Second, μ decreases and $V_{a,sat}$ increases with boron doping of diamond cathode. These observed effects can be explained by electrostatic theory.

Analysis on the effect of anode-cathode spacing on the amplification factor

From the definition, μ is a parameter used to evaluate how good gate voltage has control on the anode emission current over anode voltage. For a field emission triode, gate voltage has higher control on emission current than anode voltage by the manner in which they control the electric field at the emitter, and hence μ also corresponds to the factor that dictates how much gate voltage has influence on the cathode electric field over anode voltage. The manner in which gate voltage and anode voltage control the electric field at the emitter can be explained by the electrostatic theory. To explain the effect of D on μ, consider electrostatic problems in field emitter triode structures with different anode-cathode spacing (D) as illustrated in **Figure 6.92**. From electrostatic theory, the potential and electric field in a charge-free space can be found by solving the Laplace's equation:

$$\nabla^2 V(\vec{R}) = 0 \qquad (6.16)$$

where V is a potential at any point and $\vec{R}$ denotes a position vector in the space. The boundary conditions for this problem are the applied potentials from the gate ($V_g$) and anode ($V_a$) with respect to ground at the contact, in triode geometry, as depicted in **Figure 6.92**.

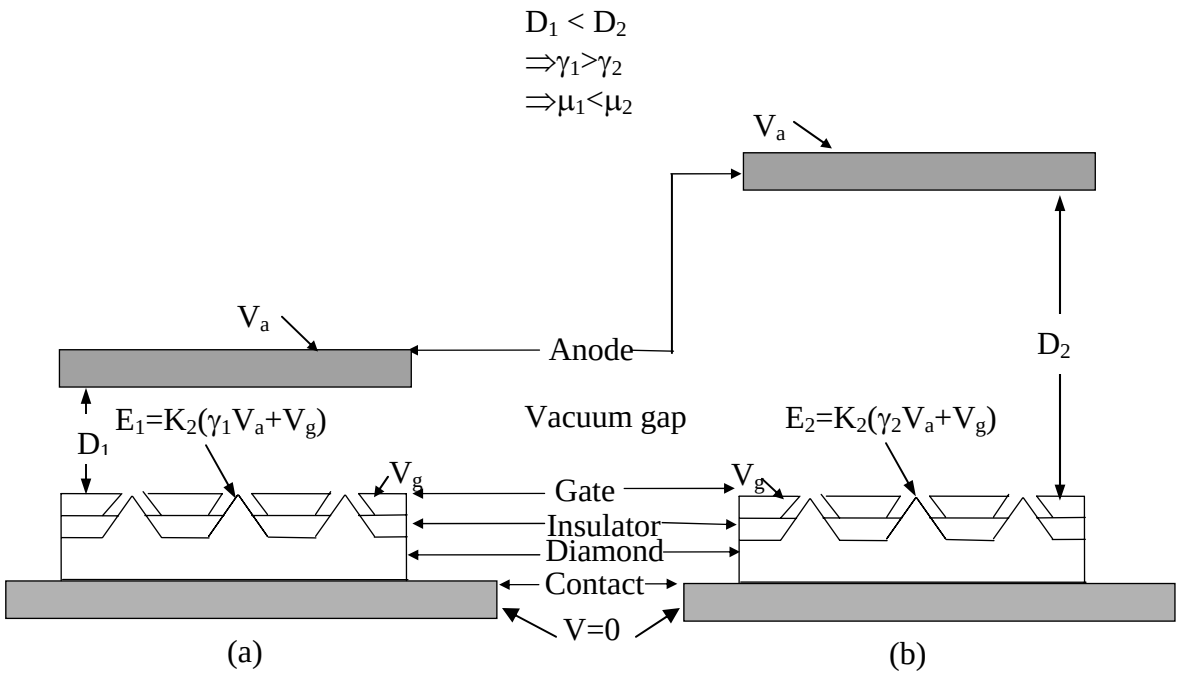


**Figure 6.92.** Diagram illustrating the effect of anode-cathode spacing on amplification factor.

For the given triode geometry, it is difficult to solve the Laplace's equation analytically and hence it is generally done numerically [188]. The numerical simulation for this problem is beyond the scope of this research. However, the magnitude of electric field ($E(\vec{R}) = \left|-\nabla V\right|$) for Eq. (6.16) can generally be expressed in the form:

$$E(\vec{R}) = K_1 V_a + K_2 V_g \equiv K_2(\gamma V_a + V_g) = K_2(V_a/\mu + V_g) \quad (6.17)$$

where $K_1$, $K_2$, $\gamma \equiv K_1/K_2$, and $\mu \equiv 1/\gamma$ are constants. These constants can be obtained from the numerical solution of the Laplace's equation.

The form of $E(\vec{R})$ can also be simply deduced from the superposition theorem of potential fields. Let's consider, the electric field at the tip of the cathode, $E_{tip} = K_2(\gamma V_a + V_g)$. Since the cathode position is farther from $V_a$ than $V_g$, it can be deduced without the explicit solution of Laplace's equation that $K_1 < K_2$ and $\gamma < 1$ (electric field is inversely proportional to a power of distance from a potential source). Physically, it can be explained that the potential source from anode, which is far from cathode, cannot affect the potential and electric field at the cathode position as much as the closer potential source at the gate. For triode in **Figure 6.92(a)**, $E_1 = K_2(\gamma_1 V_a + V_g)$ and triode in **Figure 6.92(b)**, $E_2 = K_2(\gamma_2 V_a + V_g)$. Since anode in **Figure 6.92(a)**

is closer than anode in **Figure 6.92(b)**, one can deduce that $\gamma_1>\gamma_2$ and since $\gamma=1/\mu$, $\mu_1<\mu_2$. Therefore, amplification factor of a field emission triode increases as anode-cathode spacing increases.

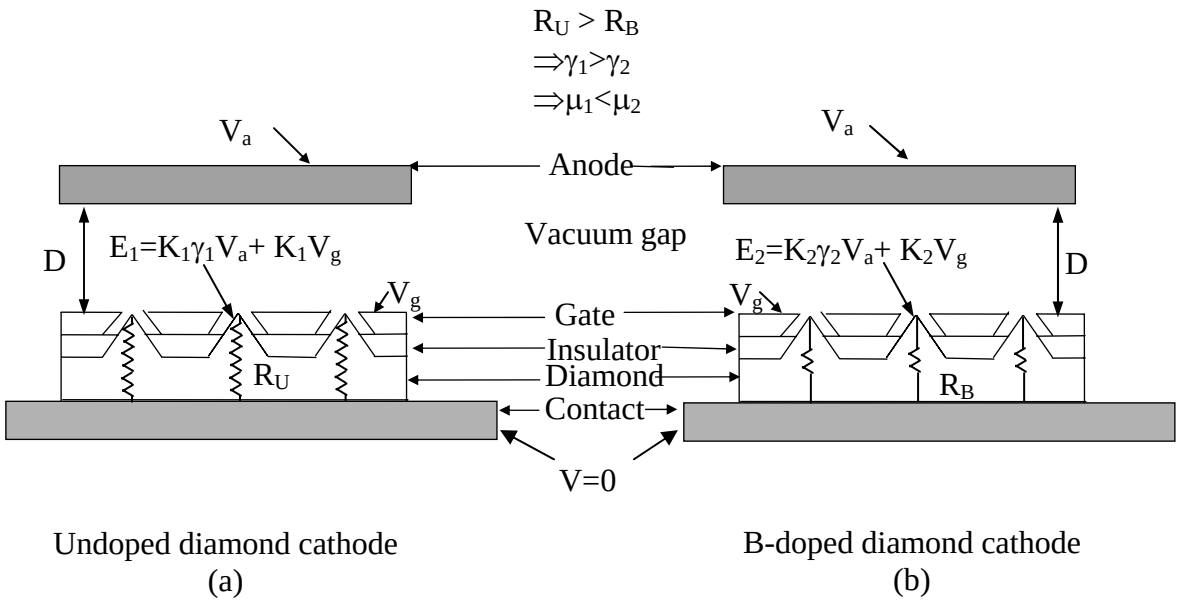


**Figure 6.93.** Diagram illustrating the effect of boron doping of diamond cathode on amplification factor.

Analysis on the effect of boron doping of diamond cathode on the amplification factor

To explain the effect of boron doping of diamond cathode on μ, consider electrostatic problems for undoped and boron-doped field emitter triodes as illustrated in **Figure 6.93**. The effect of boron doping on diamond cathode is modeled by a cathode resistance from the back contact to diamond tips. It is obvious from electrostatic principle that the cathode resistance results in potential drop and electric field reduction at the tip. The potential drop and electric field reduction due to cathode resistance would be more significant for the gate voltage than the anode voltage because the gate is closer to the cathode and potential drop is inversely proportional to a power of distance. For undoped diamond triode with cathode resistance $R_U$, the electric field at a tip is $E_1=K_1\gamma_1V_a+ K_1V_g$. If the diamond cathode is doped with boron, cathode resistance is reduced to $R_B$, then the electric field at a tip becomes $E_2=K_2\gamma_2V_a+ K_2V_g$. It can be implied that

$$K_2/K_1 > (K_2\gamma_2)/(K_1\gamma_1)$$

This inequality states that the change in the field contributed by the gate due to the reduction of cathode resistance is greater than the change in the field contributed by the anode. From the inequality, $\gamma_1 > \gamma_2$ and $\mu_1 < \mu_2$. This should be a reasonable explanation for the effect of boron doping on the amplification factor of diamond triode.

II. Make corrected F-N plot of emission current.

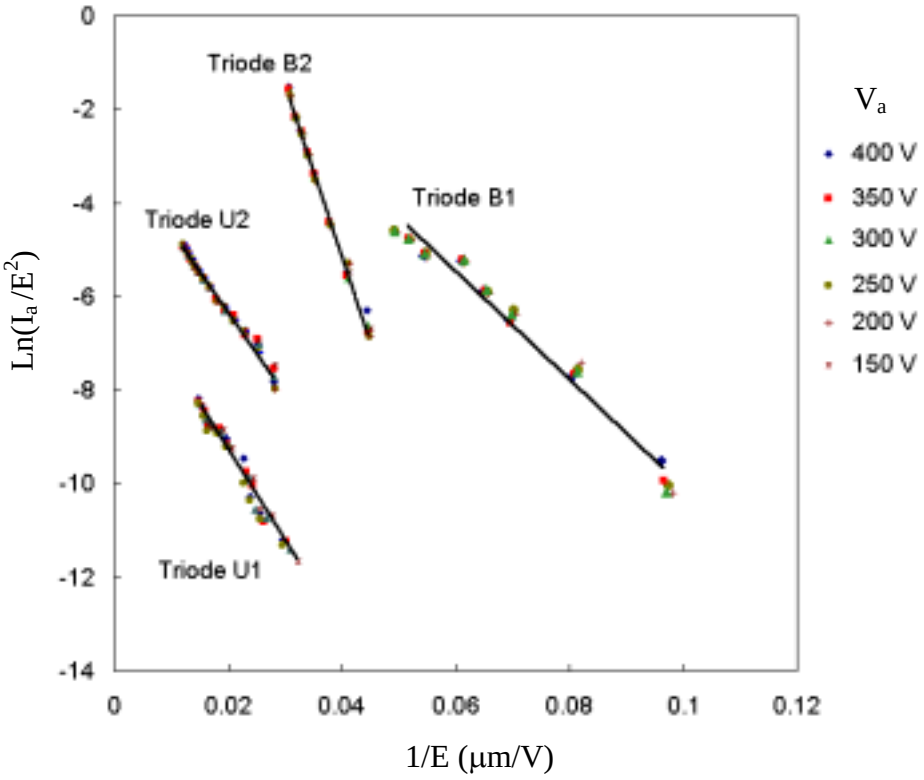


**Figure 6.94.** Corrected F-N plots of various diamond emitter triodes for various $V_a$.

The corrected F-N plots of various diamond emitter triodes are shown in **Figure 6.94**. These corrected F-N plots use actual electric field E (given by equation (6.14)) instead of $V_g$ as was done in **Figure 6.91**. It is important to note that $V_a$ must be chosen such that the triode is in saturation region so that $\alpha = 1$ and hence F-N slope and intercept can be extracted correctly. From **Figure 6.94**, it can be seen that the F-N slope and intercept for various $V_a$ in saturation region of all triode is almost independent of $V_a$. Thus, a single set of F-N parameters can be extracted from emission data. Comparing **Figure 6.94** to **Figure 6.91**, it can be seen that corrected F-N plots of Triode U1 and B1 are significantly different from the simple F-N plots.

This is because Triode U1 and B1 has low μ value this makes $V_g$ not proportional to E and the F-N plots notably depend on $V_a$. For high μ field emission triode, corrected and noncorrected F-N plots are almost the same and thus a simple F-N plot may be used for analysis. From the corrected F-N plots, $Y_{U1}$ = 201.3 V/μm, $X_{U1} = 5.336\times10^{-3}$ μA·(μm/V)$^2$; $Y_{U2}$ = 180.94 V/μm, $X_{U2} = 6.4375\times10^{-2}$ μA·(μm/V)$^2$; $Y_{B1}$ = 81.517 V/μm, $X_{B1}$ = 0.592 μA·(μm/V)$^2$;$Y_{B2}$ = 384.6 V/μm, and $X_{B2}$ = 10.17 μA·(μm/V)$^2$. The subscripts of X and Y denote the associated triode.

III. Calculate and plot the total emission current versus the anode current.

From the known μ, X, and Y for each triode, the total emission current ($I_t$) for all triodes was calculated from Eq. (6.12) and plotted versus actual anode current as shown in **Figures 6.95-6.98**. The purpose of these plots is to illustrate the difference between emission current collected at the anode and the total emission current and to calculate the emission transport factor. The continuous solid lines denote the total emission current and the anode current are the associated markers. It can be seen that in saturation region, $I_t = I_a$, which implies all emitted electrons are collected by the anode. At low anode voltage (non-saturation region), $I_t$ is significantly higher than $I_a$, which implies only a small portion of emitted electrons are collected by the anode.

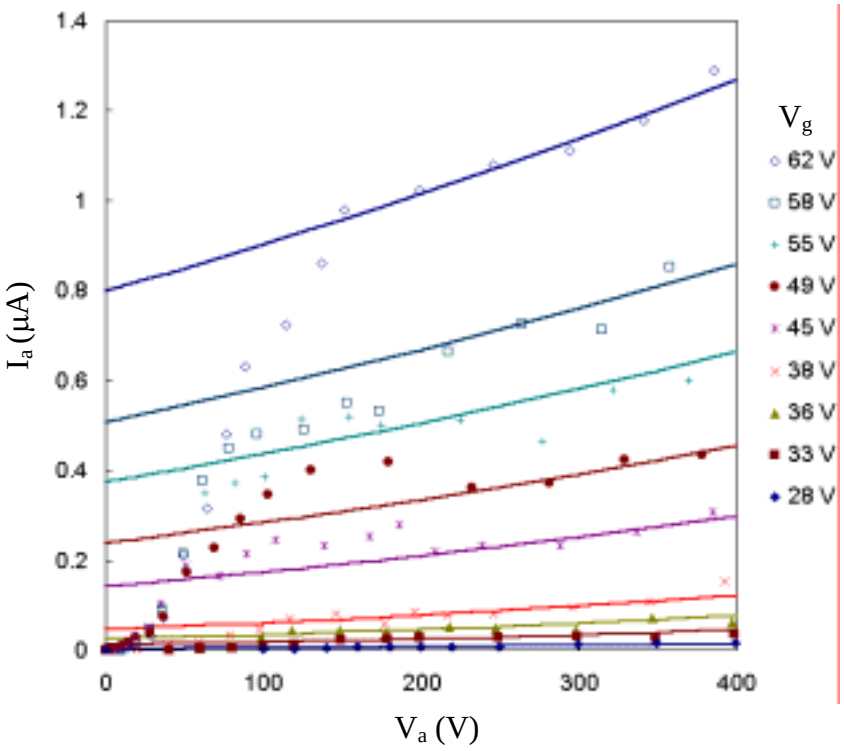


**Figure 6.95.** $I_t$-$I_a$-$V_a$ plots of Triode U1 for various $V_g$.

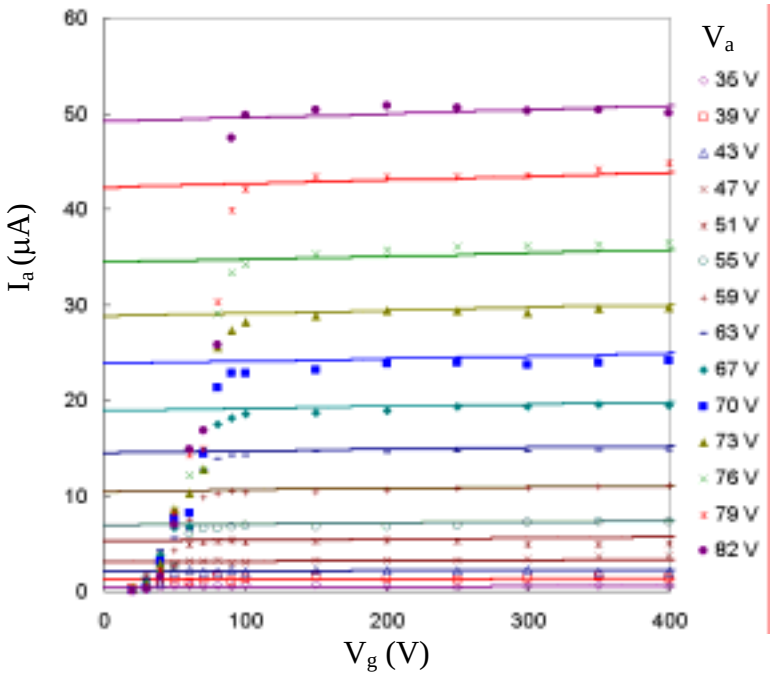


**Figure 6.96.** $I_t$-$I_a$-$V_a$ plots of Triode U2 for various $V_g$.

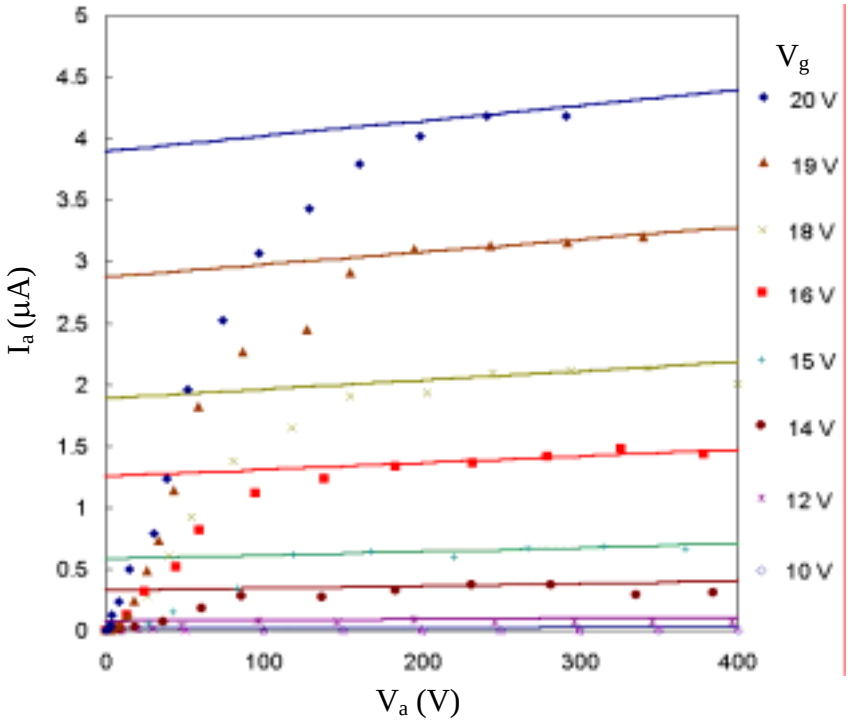


**Figure 6.97.** $I_t$-$I_a$-$V_a$ plots of Triode B1 for various $V_g$.

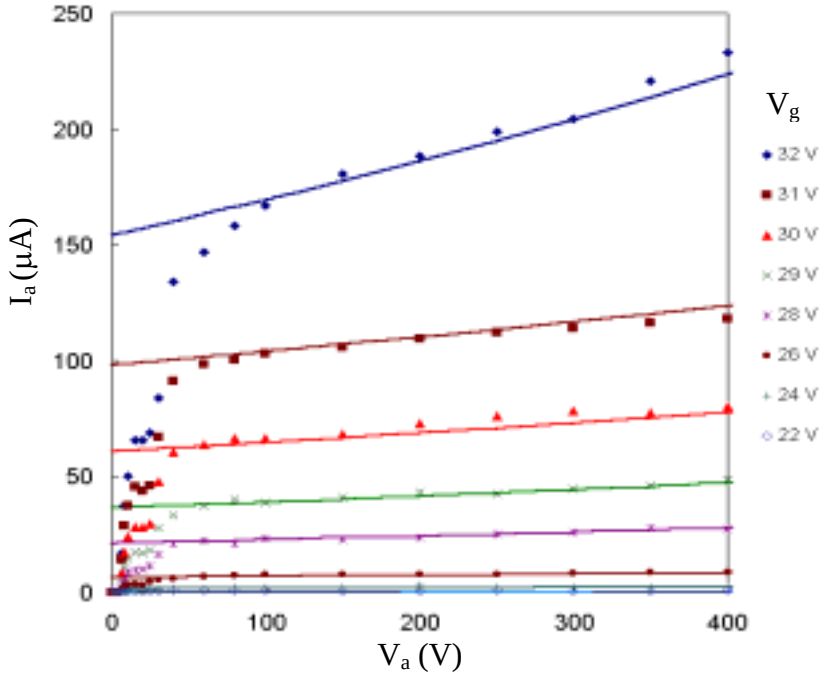


**Figure 6.98.** $I_t$-$I_a$-$V_a$ plots of Triode B2 for various $V_g$.

IV. Calculate and plot $\alpha$

After the total emission current has been computed, the emission transport factor ($\alpha$) can be calculated from its definition $\alpha = I_t/I_a$. The $\alpha$ values calculated for various triodes were plotted as function of gate and anode voltages as shown in **Figures 6.99-6.102**. The result shows that $\alpha$ is a complicated function of anode and gate voltages. In addition, $\alpha$ seems to follow different functions for different triodes. The only common characteristic of $\alpha$ for all triode is that $\alpha$ approaches 1 as anode voltage increases for a given gate voltage.

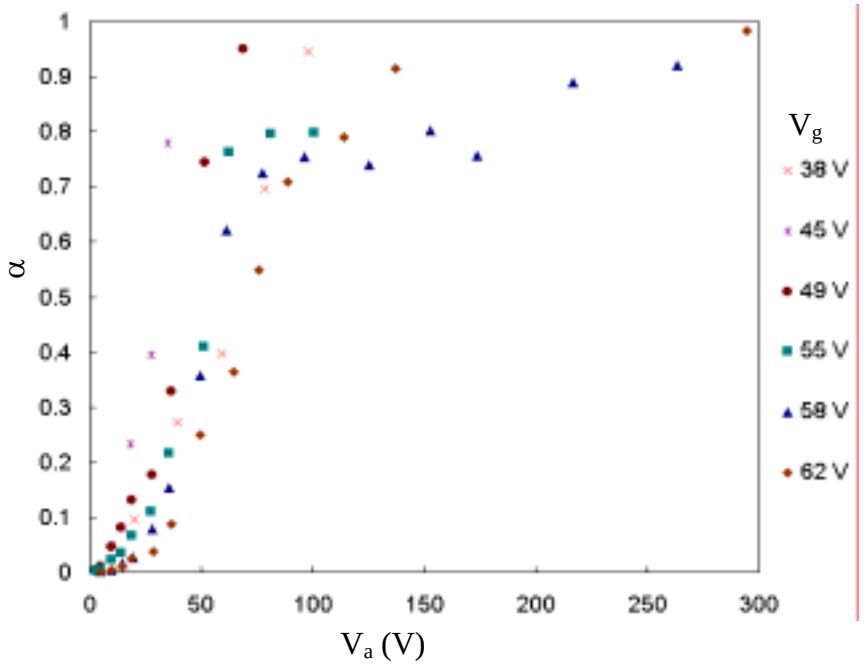


**Figure 6.99.** α-$V_a$ plots of Triode U1 for various $V_g$.

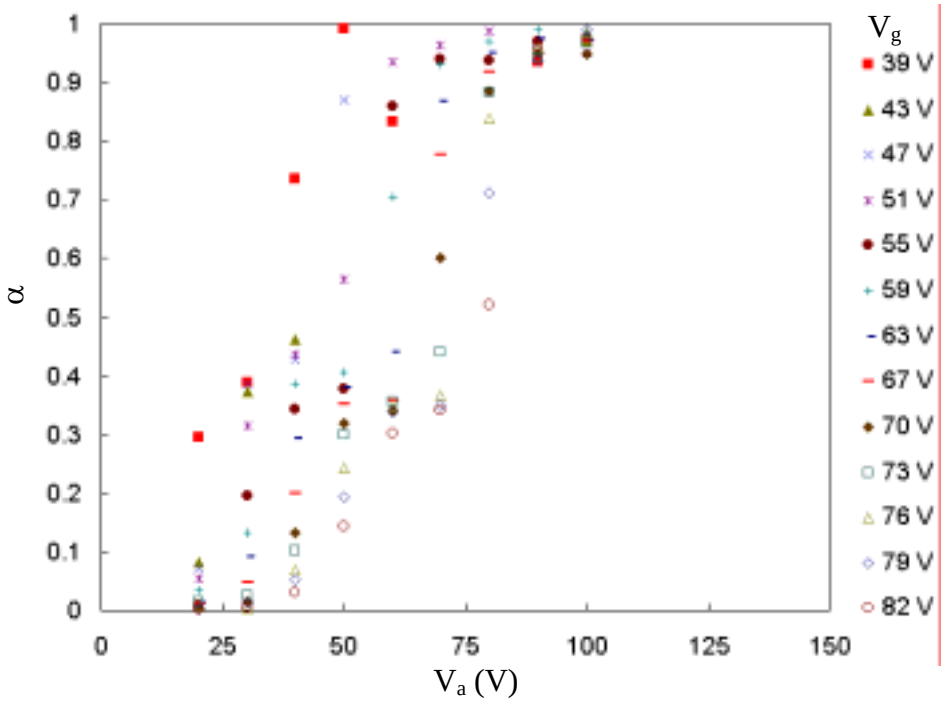


**Figure 6.100.** α-$V_a$ plots of Triode U2 for various $V_g$.

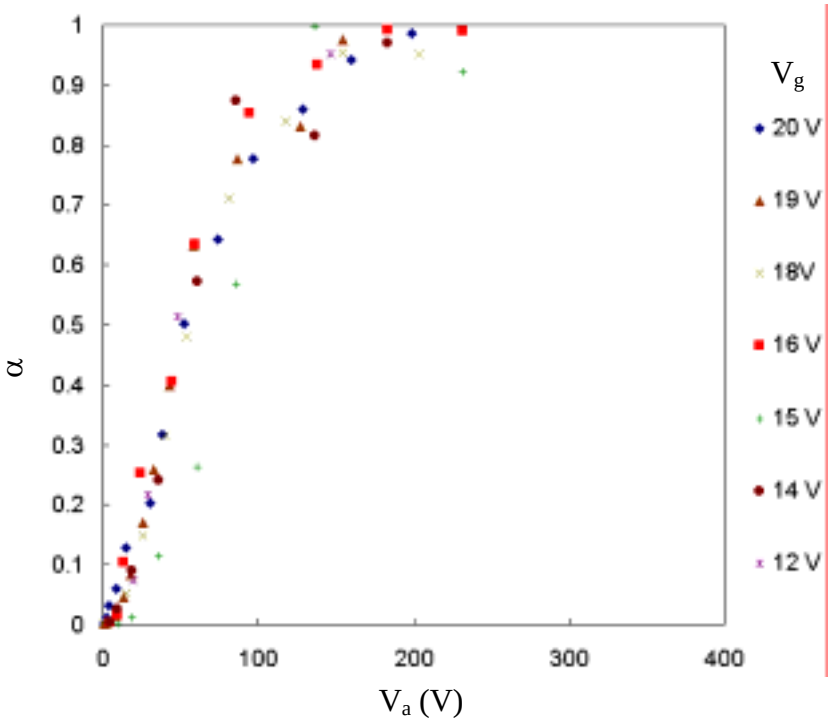


**Figure 6.101.** α-$V_a$ plots of Triode B1 for various $V_g$.

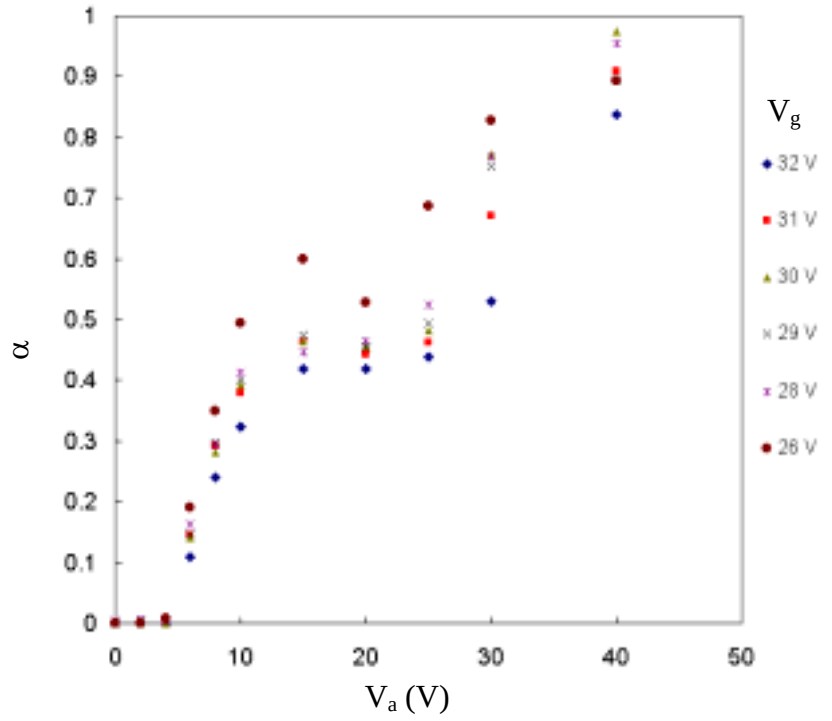


**Figure 6.102.** α-$V_a$ plots of Triode B2 for various $V_g$.

V. Model α.

Conceptually, the fraction of emission current from cathode that is collected by the anode and hence the α function of a field emission triode could be modeled from the basic law of electrostatics and classical mechanics [189]. The first step is to solve Laplace's equation (Eq. 6.16) for the electric field in the triode geometry. Next, classical electron trajectories are solved from the known electric field using the Newton's equation of motion:

$$\frac{d^2\vec{R}}{dt^2} = -\frac{q}{m}\vec{E}(\vec{R}) \tag{6.18}$$

where t = time, q = electron charge, m = electron mass, $\vec{R}$ = position vector, and $\vec{E}$ = electric field vector. The boundary conditions, which include electron initial velocity and position, are determined from the numerical solution of Schrodinger's equation for electron tunneling from the cathode. The last step is to estimate the fraction of electrons arrive at the anode from the known electron trajectory. Since this problem has to be solved by using the Laplace's, Schrodinger's, and Newton's equations simultaneously in three-dimensional triode geometry, it is very difficult to be done analytically but can be done numerically. The numerical simulation for this problem is beyond the scope of this research. To understand the characteristics of α and explain triode operations, it is useful to illustrate qualitative solution of electron trajectory in a field emission triode (based on some numerical simulations [189]) as shown in **Figure 6.103**. For low anode voltage, $V_a << V_g$, most of electric field lines and electron trajectories terminate at the gate as shown **Figure 6.103 (a)**. Hence, few electrons can arrive at the gate and $\alpha \approx 0$. This is an off state in triode operation. For medium anode voltage ($V_a \approx V_g$), some of electric field lines and electron trajectories divert from the gate to terminate at the anode as shown **Figure 6.103 (b)**. Thus, some electrons arrive at the anode and $0<\alpha<1$. This is called the non-saturation (linear) region in triode operation. For high anode voltage ($V_a >> V_g$), most of electric field lines and electron trajectories divert to terminate at the anode as shown **Figure 6.103 (c)**. Therefore, most electrons arrive at the anode and $\alpha \approx 1$. This is called the saturation region in triode operation.

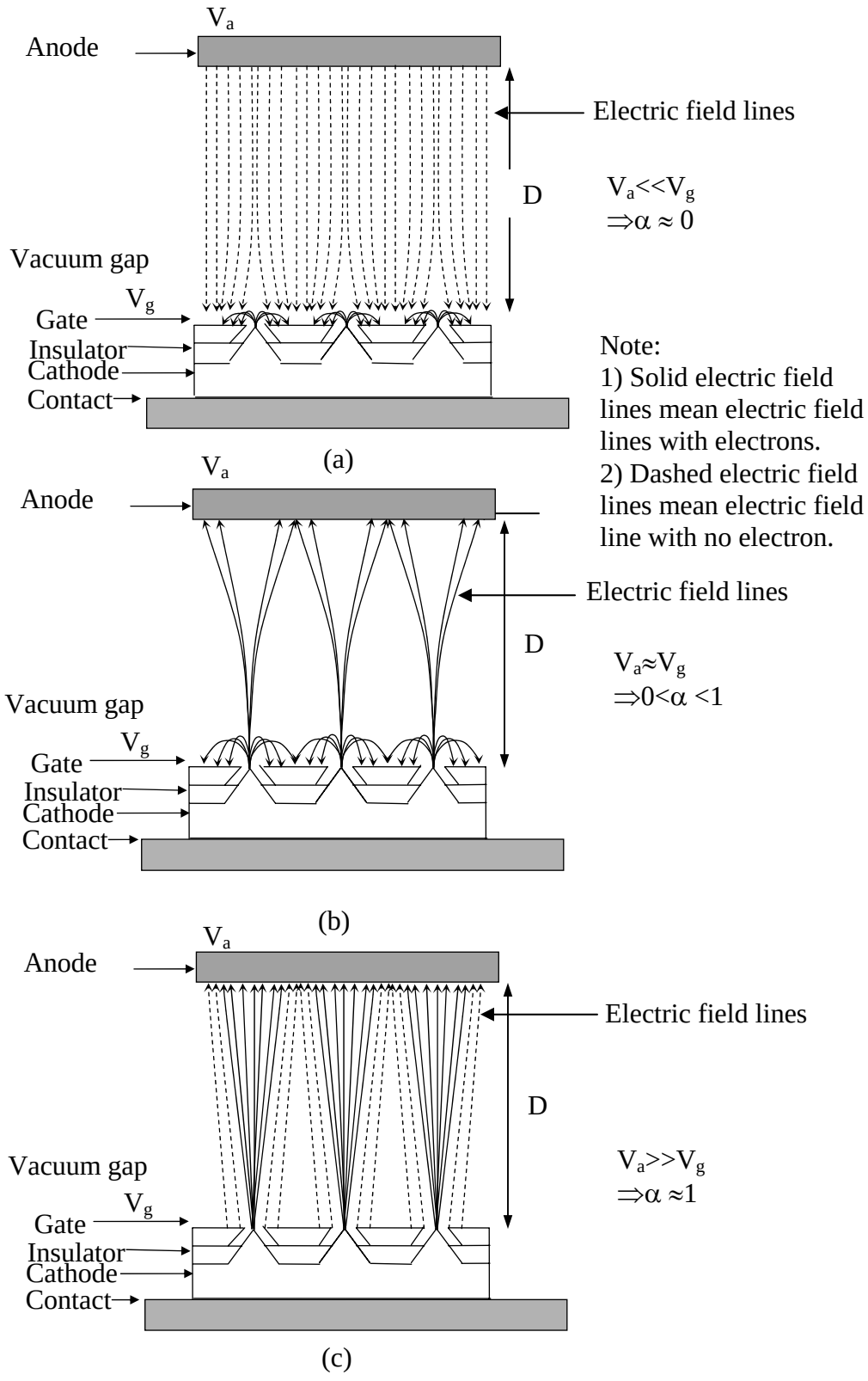


**Figure 6.103.** Electric field lines diagram for a field emission triode demonstrating the effect of gate and anode voltage on $\alpha$.

Since there has been no theoretically derived or general analytical form for α of field emission triode, thus α is modeled empirically. There have been few empirical models for α for a field emitter triode reported [190-191]. For example [190]:

$$\alpha = \tanh\left( a\left[\frac{V_a}{V_g}\right] + b \right) \tag{6.19}$$

where a and b are constants fitting parameters for a given triode. Another example [191]:

$$\alpha = 1 - \exp\left( a_1 V_a + a_2 V_a^2 - \frac{a_3 V_a + a_4 V_a^2}{V_g} + a_5 \right) \tag{6.20}$$

where $a_1$, $a_2$, $a_3$, $a_4$, and $a_5$ are constants fitting parameters for a given triode. However, these proposed empirical models are not sufficiently general and can only be fitted to some specific data. We have attempted to fit these models with our experimental data but found that our data cannot be satisfactorily fitted with these proposed empirical models. Thus, an empirical model for α of our diamond field emission triodes needs to be developed.

Development of the empirical model of α for diamond vacuum triode

To find an unknown empirical model for data of two variables is considerably difficult and complicated and cannot be done by general curve fitting programs. Thus, we begin by finding a simplified assumption that could reduce the complexity. From the previous discussion on theoretical modeling of α, **Figure 6.103**, it can be deduced that α depends on the relative values of $V_a$ and $V_g$, and hence it should depend on $V_a/ V_g$ or $V_g/ V_a$. Let's define $\nu \equiv V_a/ V_g$. To test this hypothesis, the calculated α values (**Figures 6.99-6.102**) were plotted as functions of ν as shown in **Figures 6.104-6.107**. The results indicate that this assumption is mainly valid because α-ν plots tend to follow the same function regardless of $V_g$ for all diamond triodes investigated. Thus, α becomes a function of a single variable, ν. Next, we need to find a general function of ν that assumes a value between 0 and 1 and can fit the plots in **Figures 6.104-6.107**. Based on the shape of the plots, a likely function that should fit the data should be in the form:

$$\alpha = 1 - \exp P(\nu) \tag{6.21}$$

where P(ν) is a fitting polynomial function of ν. P(ν) must assume a negative value to be valid for all ν>0, otherwise α would have an invalid negative value according to Eq. (6.21). From Eq. (6.21), it is obvious that P(ν) can be found by plotting ln(1-α) versus ν and then fitting the plots with the poly-regression method. The plots of ln(1-α) vs. ν for all diamond triodes are

illustrated in **Figures 6.108-6.111**. It should be noted that $R^2$ in the insets are the coefficient of determination for poly-regression. $R^2$ measures the correlation of data to the fitting curve. If $R^2$ is close to 1, it means data is fitted perfectly with the model polynomial. $R^2$ for most data are close to 1,thus the data are well fitted with the polynomial. However, it was found that the best fitted $P(\nu)$ for most of triodes' data (except Triode B1) has some invalid regions ($P(\nu) > 0$ for $\nu > 0$). In addition, some $P(\nu)$ become decreasing function for large or small $\nu$, which will give incorrect prediction for $\alpha$. Thus, the triode data cannot be satisfactorily fitted with the trial function in Eq. (6.21).

Next, $V_g/V_a = 1/\nu \equiv \upsilon$ was tried to be used as the variable for polynomial fitting instead of $\nu$. This means that $P(\nu)$ is replaced with $P'(\upsilon)$. Similar to $P(\nu)$, $P'(\upsilon)$ can be found by plotting $\ln(1-\alpha)$ versus $\upsilon$ and then fitting the plots with the poly-regression method. The plots of $\ln(1-\alpha)$ vs. $\upsilon$ for all diamond triodes are illustrated in **Figures 6.112-6.115**. However, it was found that the best fitted $P'(\upsilon)$ for most of triodes' data result in poor $R^2$ as shown in the insets and $P'(\upsilon)$ have several invalid regions. In addition, $P'(\upsilon)$ are not a desired monotonic function. Thus, replacing $P(\nu)$ with $P'(\upsilon)$ is not the solution for this model. Nevertheless, it can be noticed from $\ln(1-\alpha)$ vs. $\upsilon$ plots for all diamond triodes that the *negative* of $\ln(1-\alpha)$ seem to be exponential function of $\upsilon$., Thus, the original model in Eq. (6.21) can be modified according to this observation to be:

$$-\ln(1-\alpha) = \exp(\Pi(\upsilon)) \qquad (6.22)$$

where $\Pi(\upsilon)$ is a fitting polynomial function. From Eq. (6.22), it is obvious that $\Pi(\upsilon)$ can be found by plotting $\ln(-\ln(1-\alpha))$ versus $\upsilon$ and then fitting the plots with the poly-regression method. The $\ln(-\ln(1-\alpha))$ vs. $\upsilon$ plots for all diamond triodes are illustrated in **Figures 6.116-6.119**. Unlike previous cases, it was found that the best fitted $\Pi(\upsilon)$ for most of triode data is a polynomial function up to the fourth order ($\Pi(\upsilon) \equiv k_4\upsilon^4 + k_3\upsilon^3 + k_2\upsilon^2 + k_1\upsilon + k_0$, where $k_4$, $k_3$, $k_2$, $k_1$, and $k_0$, are polynomial fitting constants), which resulted in good determination coefficients ($R^2 \approx 1$) as shown in the insets and $\Pi(\upsilon)$ has no invalid region because $\Pi(\upsilon)$ can be either positive or negative value for $\upsilon > 0$. This can be clearly seen by rearranging Eq. (6.22) into the final form of $\alpha$:

$$\alpha = 1 - \exp(-\exp(\Pi(\upsilon)) \qquad (6.23)$$

From Eq. (6.23), $\alpha$ always has valid value between 0 and 1 regardless of $\Pi(\upsilon)$ and hence $\Pi(\upsilon)$ can be either positive or negative value. To confirm the validity of this model, $\alpha$ are calculated based on this model using $\Pi(\upsilon)$ in **Figures 6.116-6.119** and plotted versus $V_a$ for various $V_g$ as shown in **Figures 6.120-6.123**. It can be seen that the modeled $\alpha$ can fit over data well except some irregular data points. The error between data and the modeled $\alpha$ for various diamond triodes are acceptable. Thus, overall $\alpha$ data of all diamond triodes can be satisfactorily fitted with this model. Therefore, a new general empirical form for $\alpha$ modeling of diamond triode has successfully been developed. Furthermore, this $\alpha$ model should be applicable for other field emission triodes as well because it is generic and always has valid value between 0 and 1 for all positive $V_a$ and $V_g$.

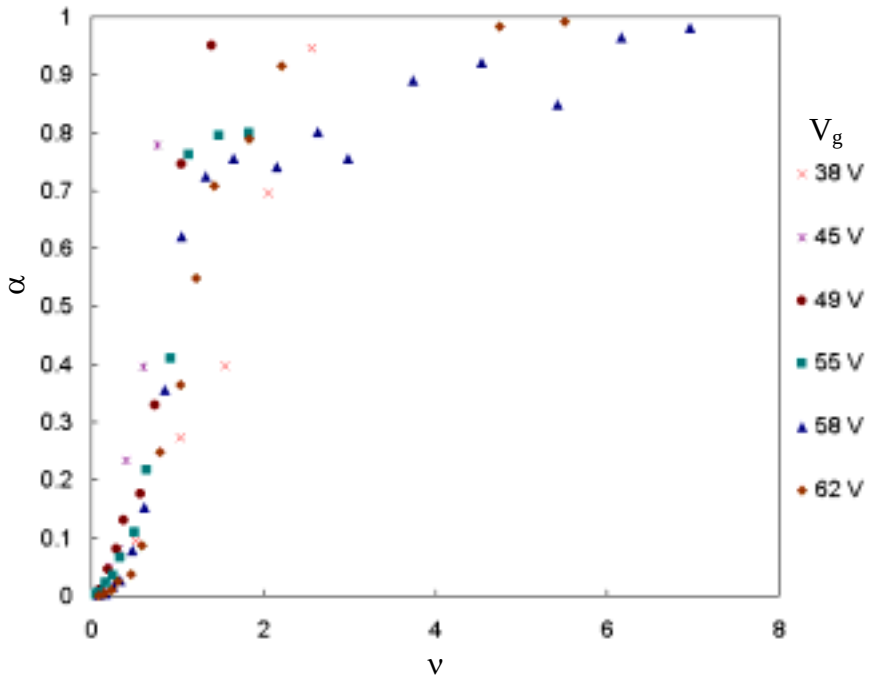


**Figure 6.104.** α-νplots of Triode U1 for various $V_g$.

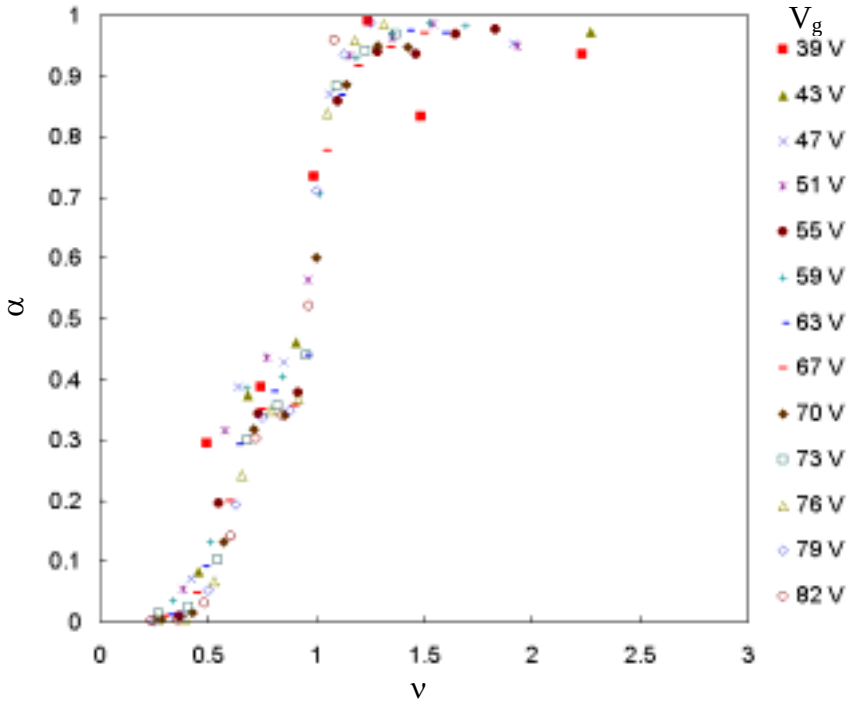


**Figure 6.105.** α-ν plots of Triode U2 for various $V_g$.

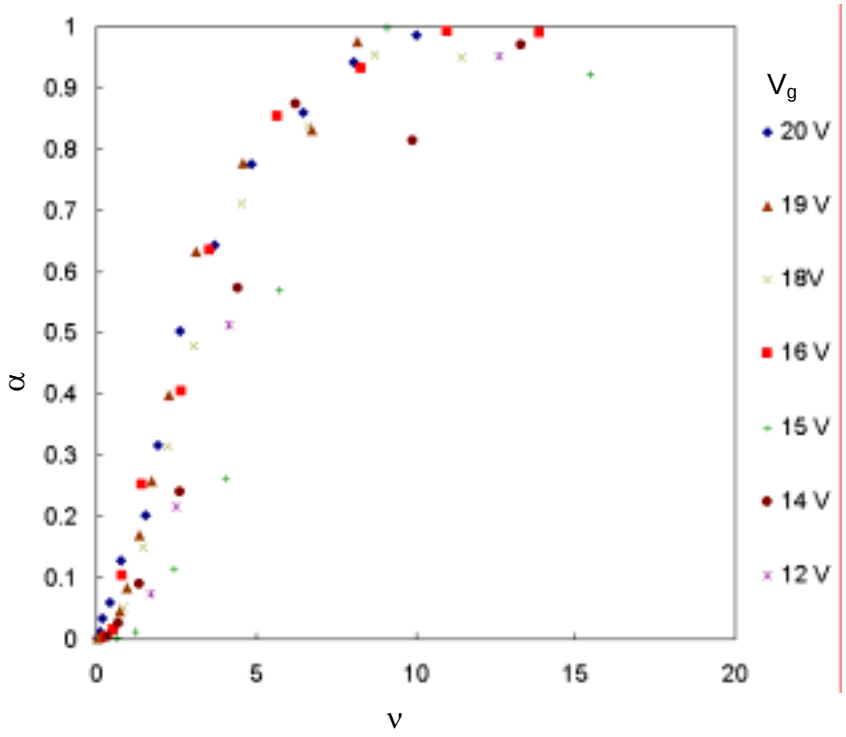


**Figure 6.106.** α-ν plots of Triode B1 for various $V_g$.

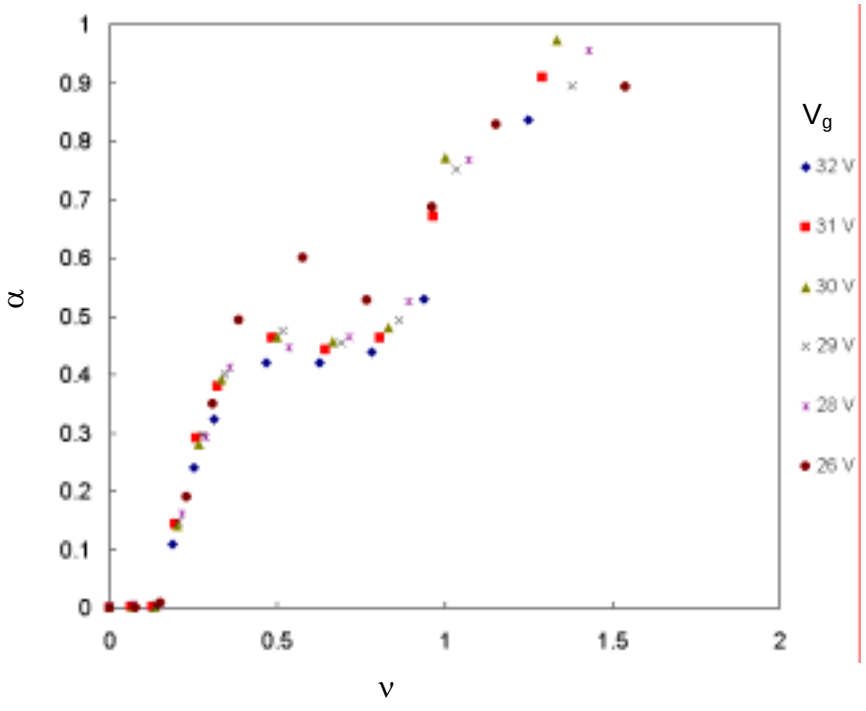


**Figure 6.107.** α-ν plots of Triode B2 for various $V_g$.

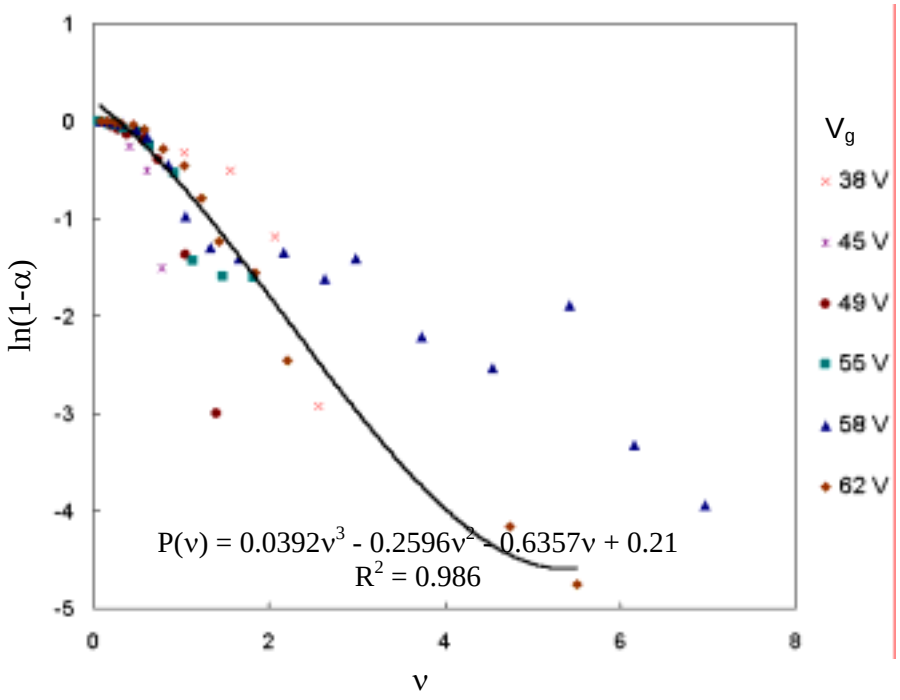


**Figure 6.108.** ln(1-α)-ν plots of Triode U1 for various $V_g$.

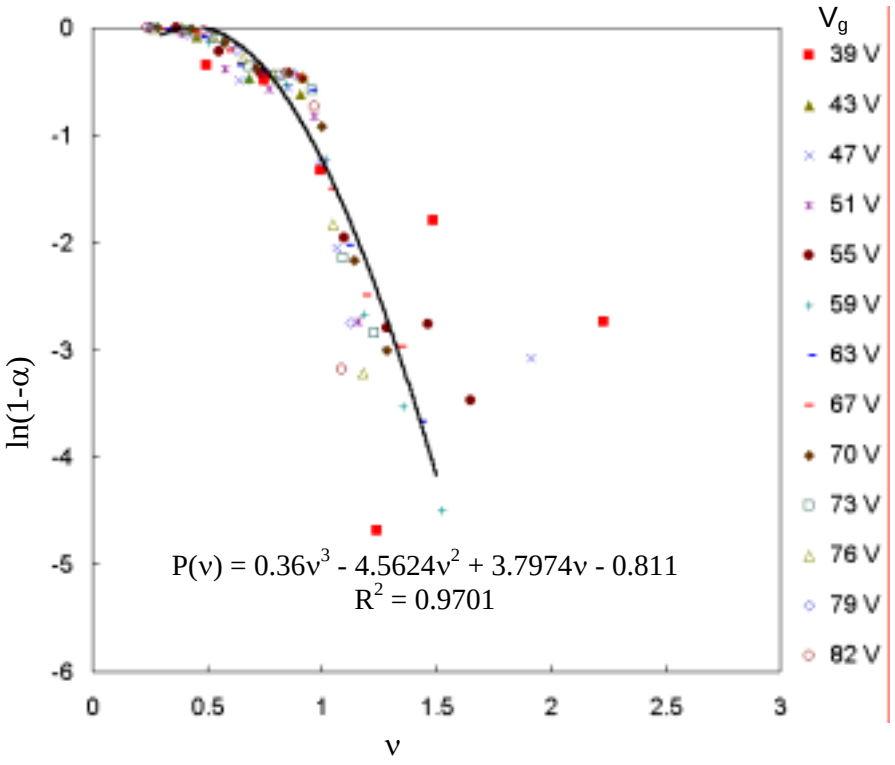


**Figure 6.109.** ln(1-α)-ν plots of Triode U2 for various $V_g$.

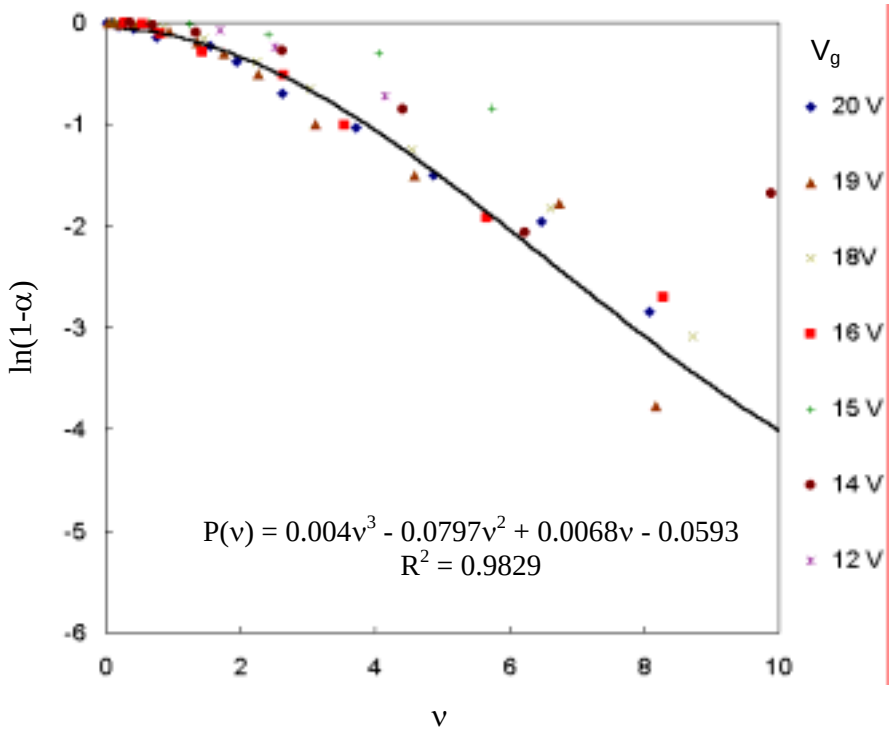


**Figure 6.110.** ln(1-α)-ν plots of Triode B1 for various $V_g$.

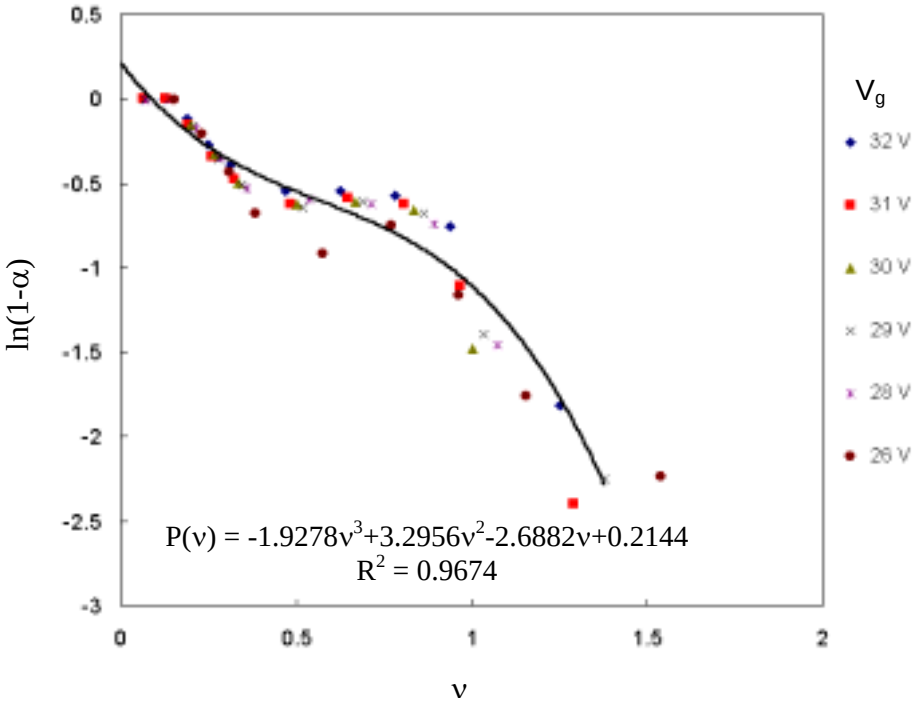


**Figure 6.111.** ln(1-α)-ν plots of Triode B2 for various $V_g$.

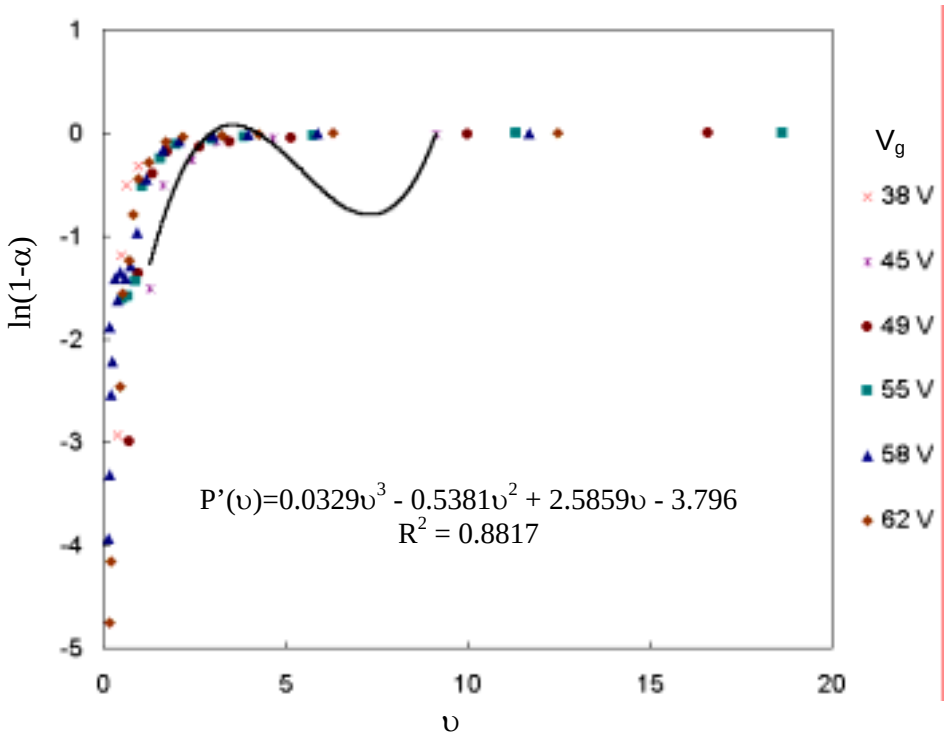


**Figure 6.112.** ln(1-α)-υ plots of Triode U1 for various $V_g$.

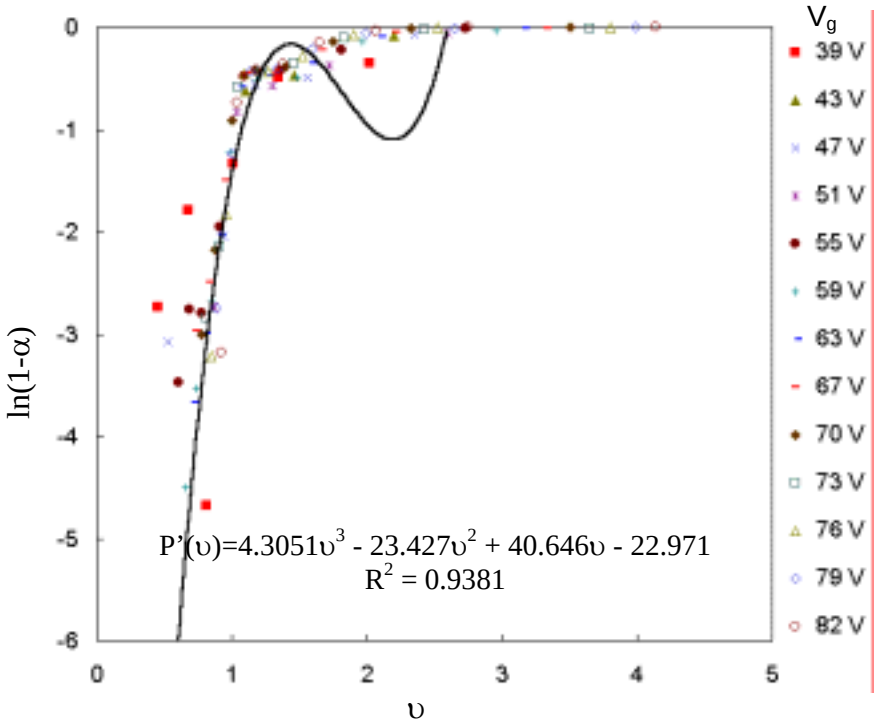


**Figure 6.113.** ln(1-α)-υ plots of Triode U2 for various $V_g$.

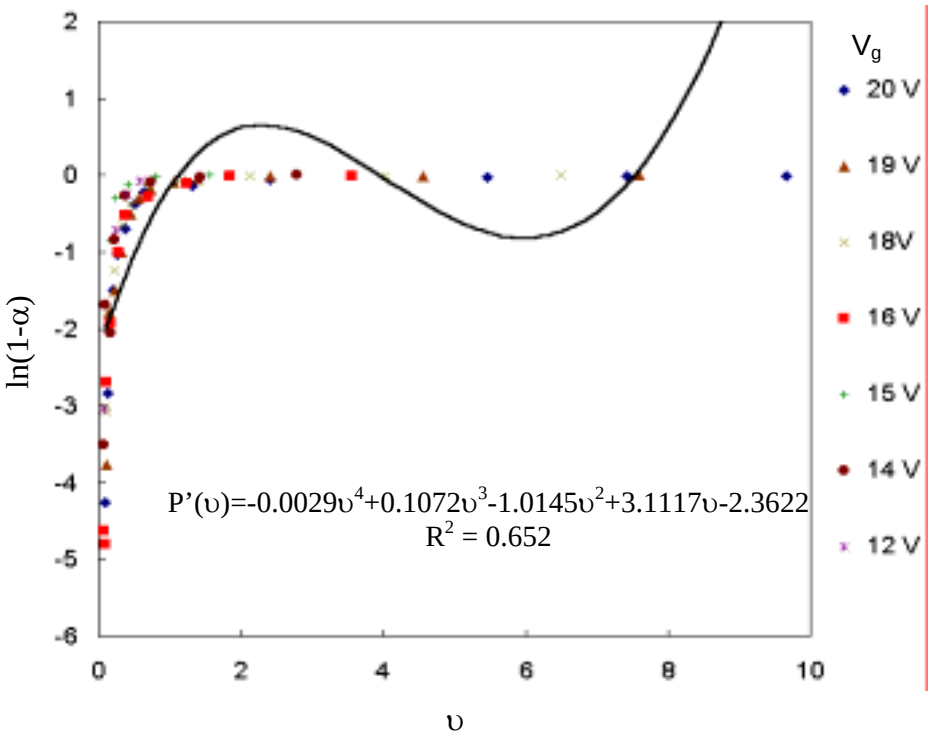


**Figure 6.114.** ln(1-α)-υ plots of Triode B1 for various $V_g$.

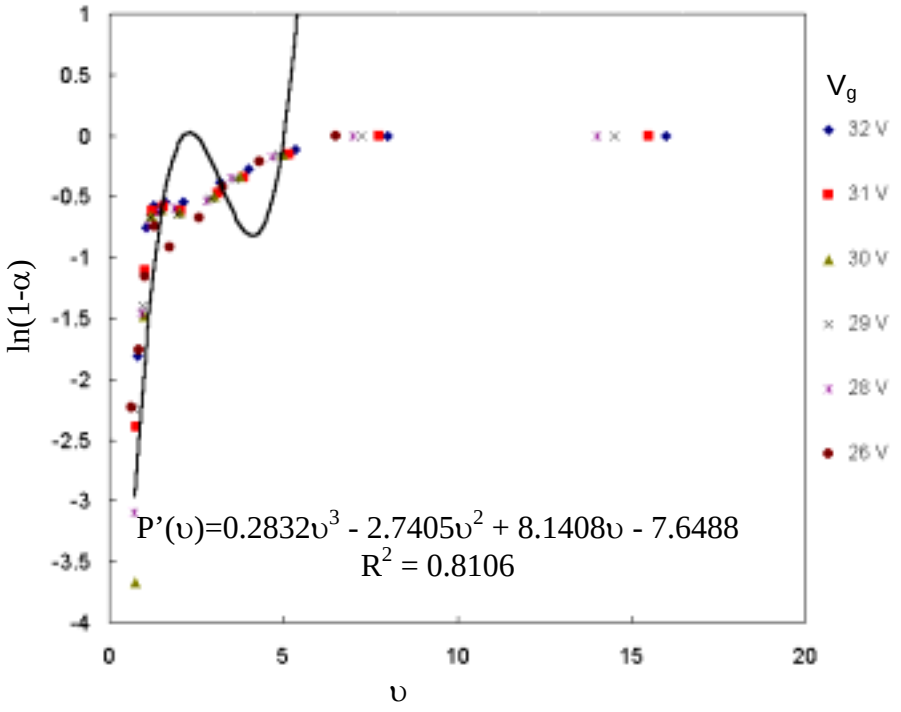


**Figure 6.115.** ln(1-α)-υ plots of Triode B2 for various $V_g$.

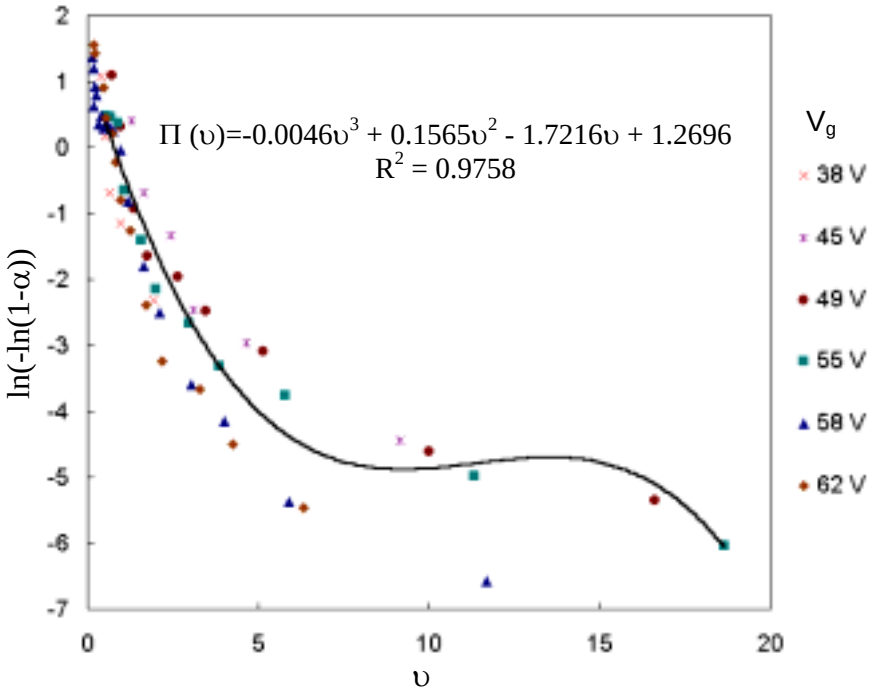


**Figure 6.116.** ln(-ln(1-α))-υ plots of Triode U1 for various $V_g$.

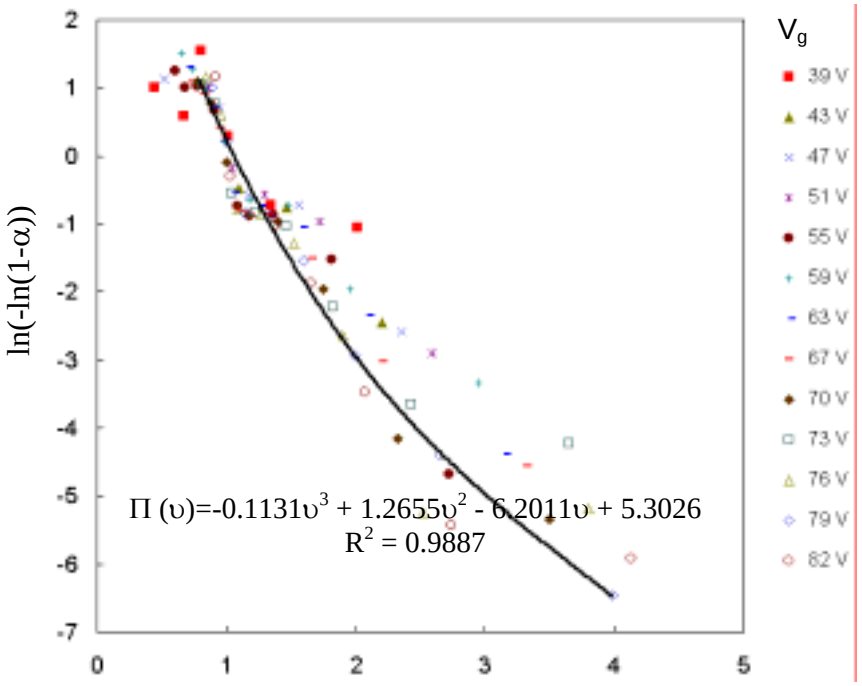


**Figure 6.117.** ln(-ln(1-α))-υ plots of Triode U2 for various $V_g$.

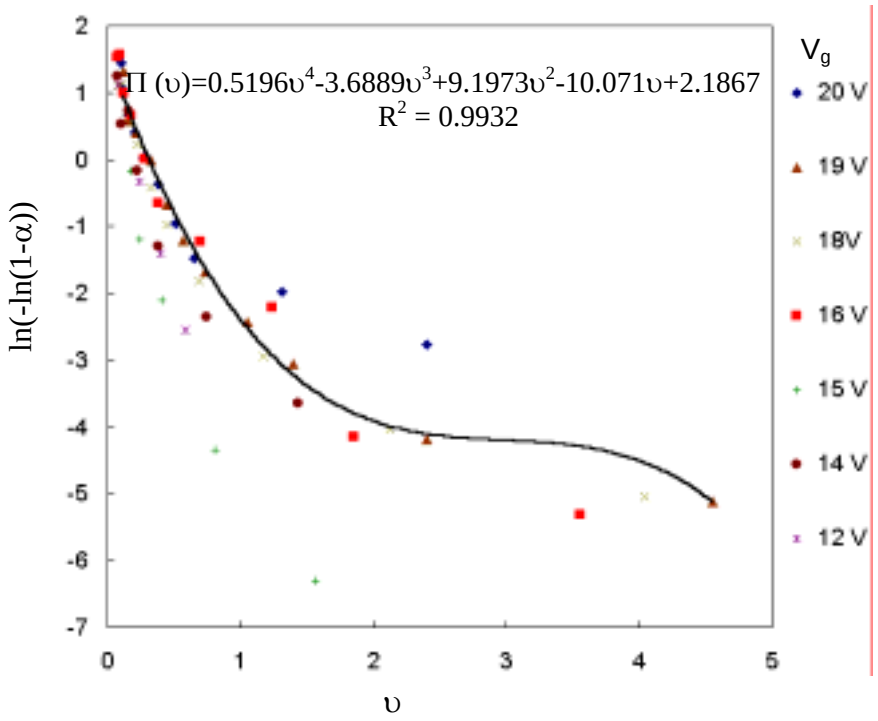


**Figure 6.118.** ln(-ln(1-α))-υ plots of Triode B1 for various $V_g$.

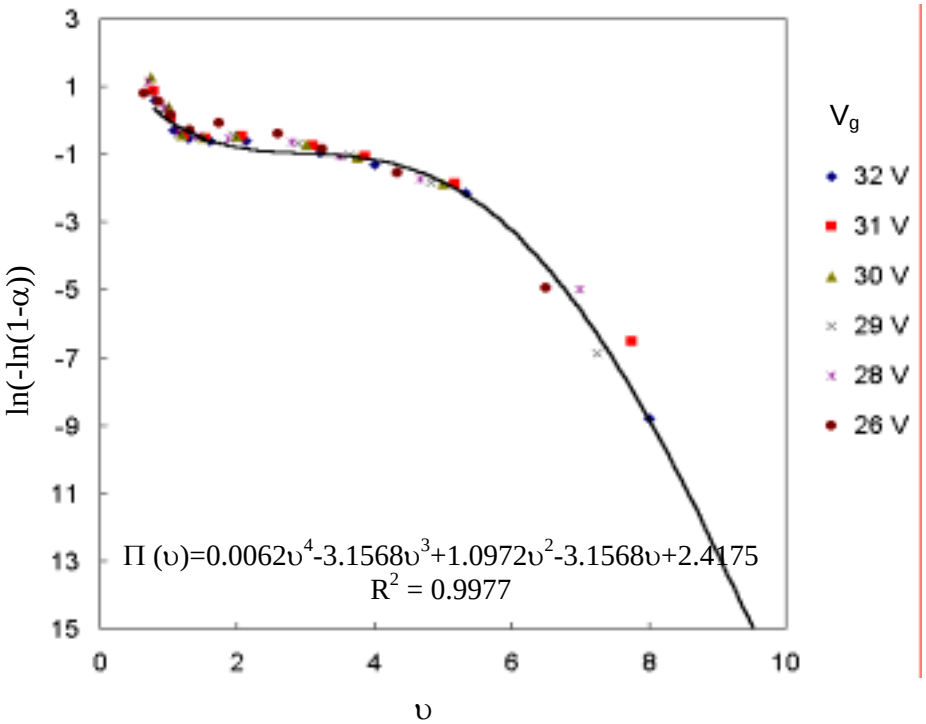


**Figure 6.119.** ln(-ln(1-α))-υ plots of Triode B2 for various $V_g$.

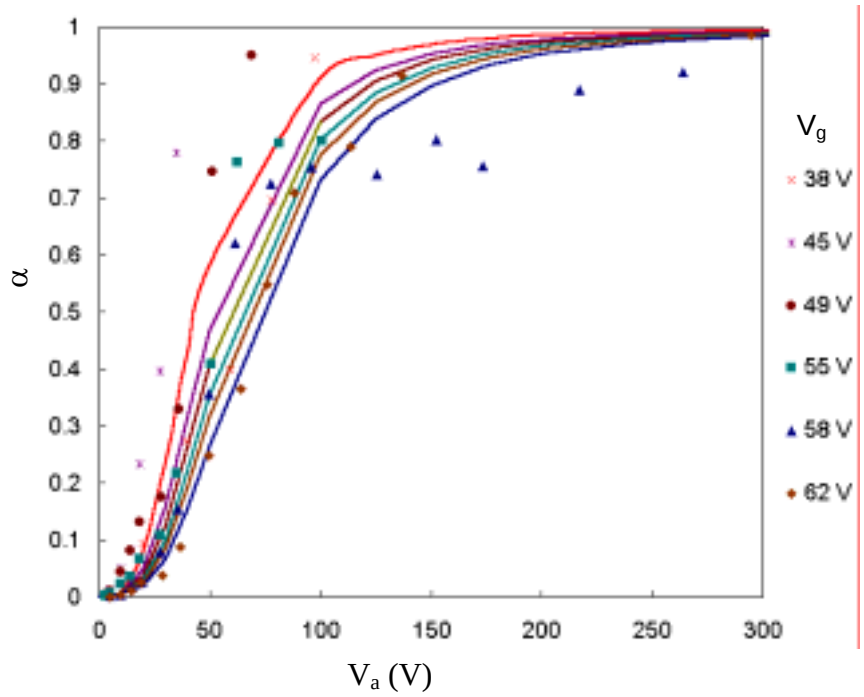


**Figure 6.120.** Modeled and actual $\alpha$-$V_a$ plots of Triode U1 for various $V_g$.

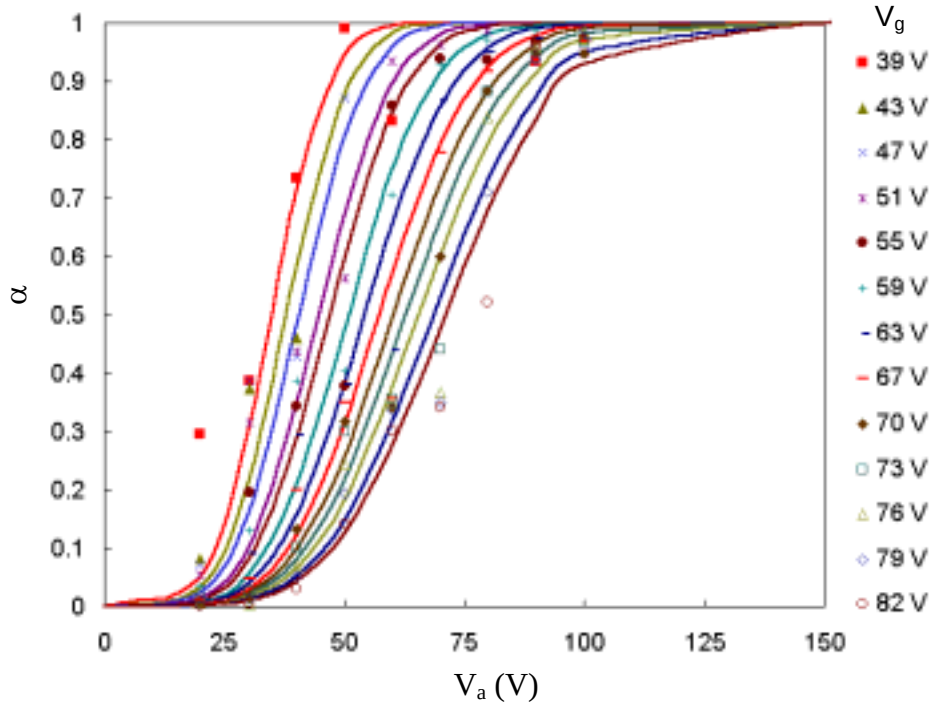


**Figure 6.121.** Modeled and actual $\alpha$-$V_a$ plots of Triode U2 for various $V_g$.

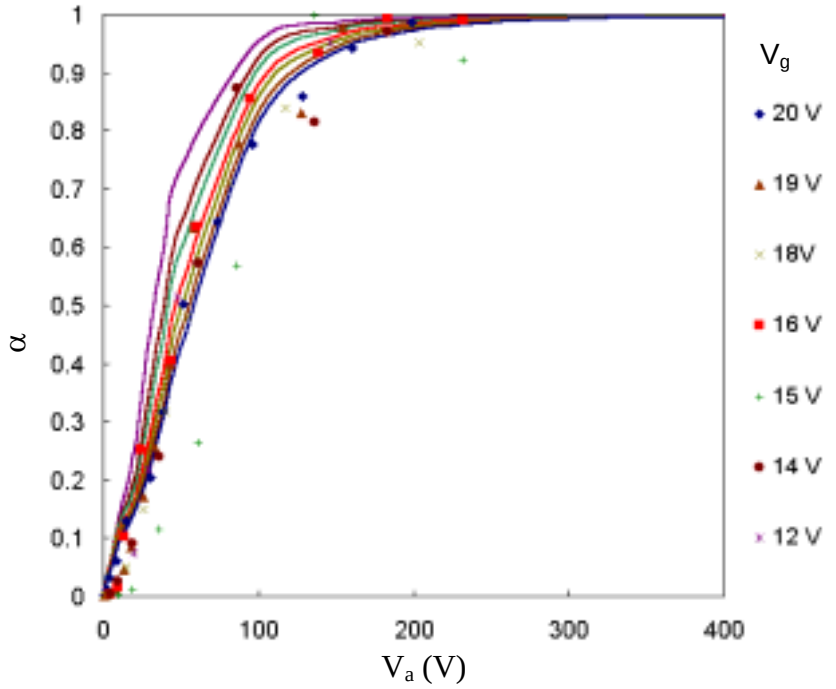


**Figure 6.122.** Modeled and actual $\alpha$-$V_a$ plots of Triode B1 for various $V_g$.

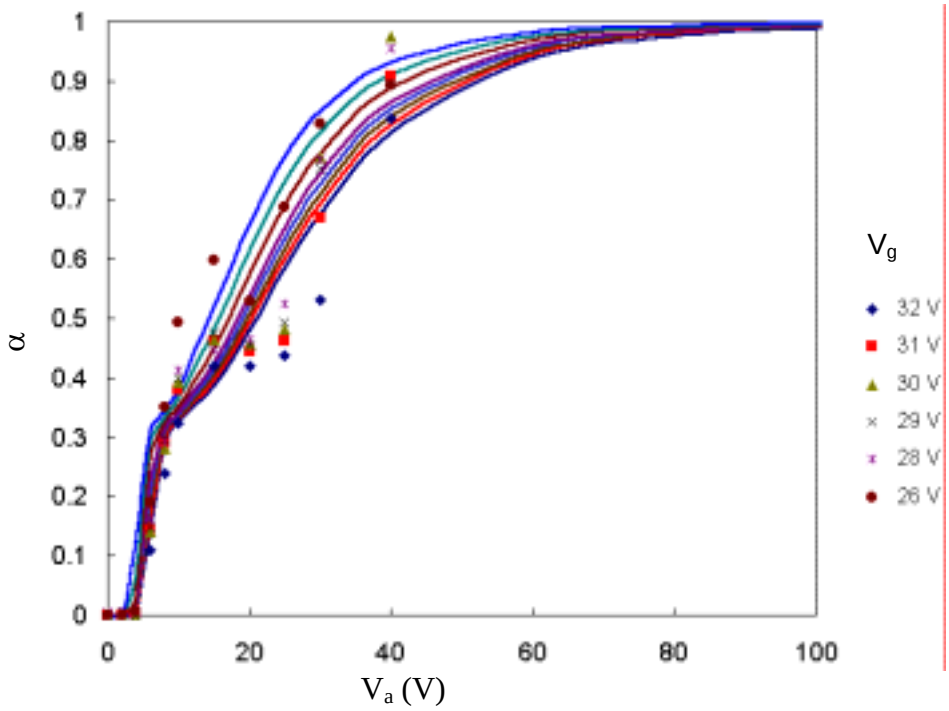


**Figure 6.123.** Modeled and actual $\alpha$-$V_a$ plots of Triode B2 for various $V_g$.

VI. Calculate and verify the modeled anode current with the actual anode current.

All modeling parameters of various diamond triodes are summarized in **Table 6.6** Anode current for various triodes calculated using Eq. (6.13) and the modeling parameters in **Table 6.6** are plotted versus the actual anode current as shown in **Figures 6.124-6.127**. It can be seen that anode emission data of all diamond triodes can be satisfactorily fitted with this model. Thus, all diamond vacuum triodes have been successfully modeled based on the F-N equation for triode and the new general empirical model developed for emission transport factor of diamond triodes.

**Table 6.7.** Modeling parameters for various diamond vacuum triodes.

| Diamond vacuum triode | U1 | U2 | B1 | B2 |
|---|---|---|---|---|
| $\mu$ | 68 | 250 | 580 | 800 |
| X ($\mu A\cdot(\mu m/V)^2$) | $5.336\times10^{-3}$ | $6.4375\times10^{-2}$ | 0.592 | 10.17 |
| Y ($V/\mu m$) | 201.3 | 180.94 | 81.517 | 384.6 |
| $k_0$ | 2.0213 | 5.3026 | 2.1867 | 2.4175 |
| $k_1$ | -3.082 | -6.2011 | -10.071 | -3.1568 |
| $k_2$ | 0.4298 | 1.2655 | 9.1973 | 1.0972 |
| $k_3$ | -0.0195 | -0.1131 | -3.6889 | -3.1568 |
| $k_4$ | 0 | 0 | 0.5196 | 0.0062 |

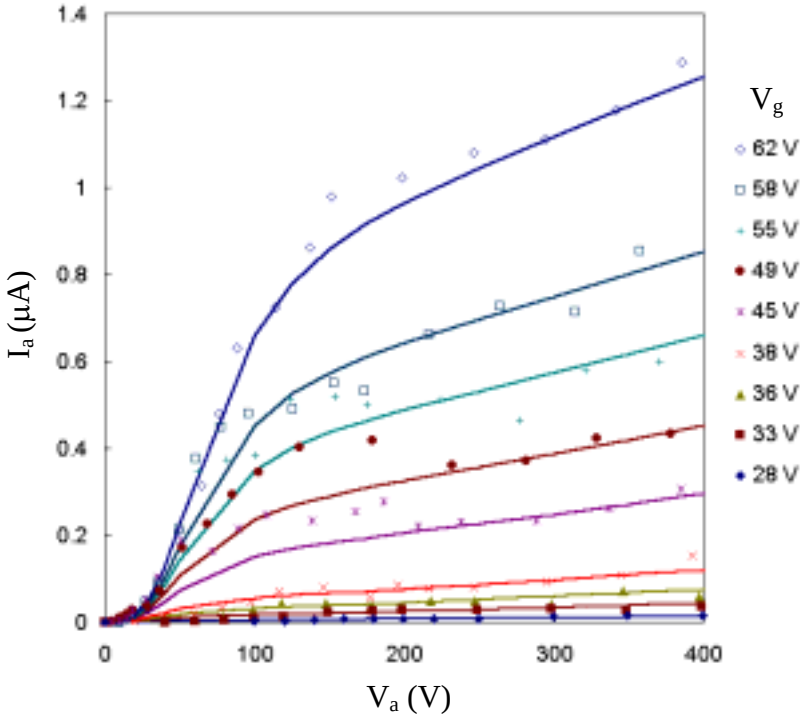


**Figure 6.124.** Modeled and actual $I_a$-$V_a$ plots of Triode U1 for various $V_g$.

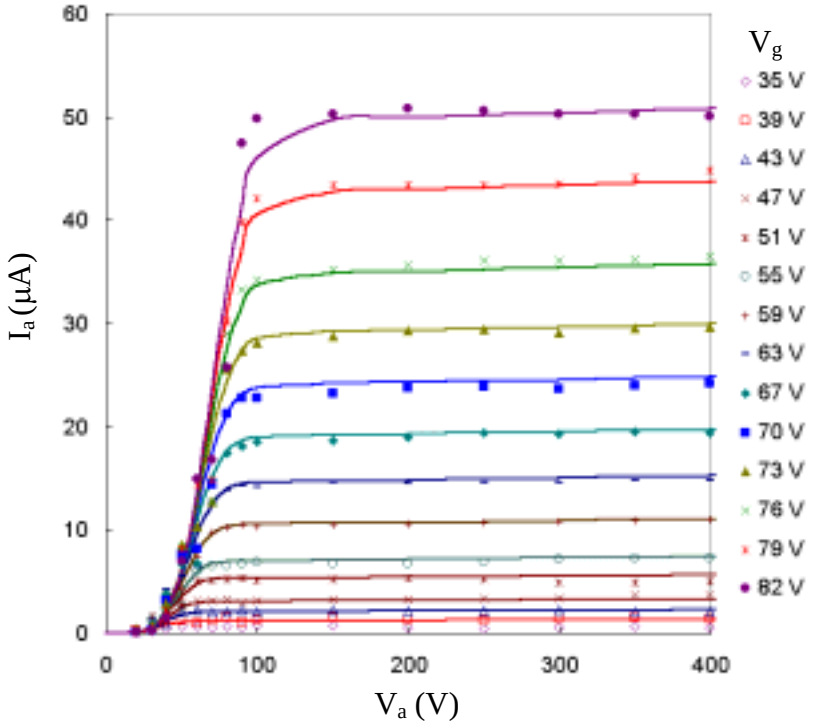


**Figure 6.125.** Modeled and actual $I_a$-$V_a$ plots of Triode U2 for various $V_g$.

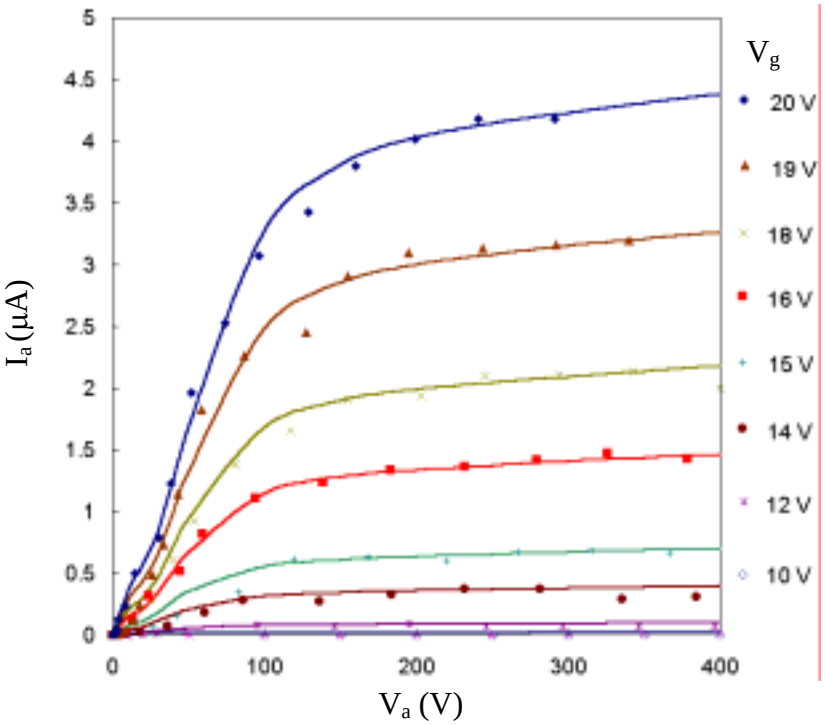


**Figure 6.126.** Modeled and actual $I_a$-$V_a$ plots of Triode B1 for various $V_g$.

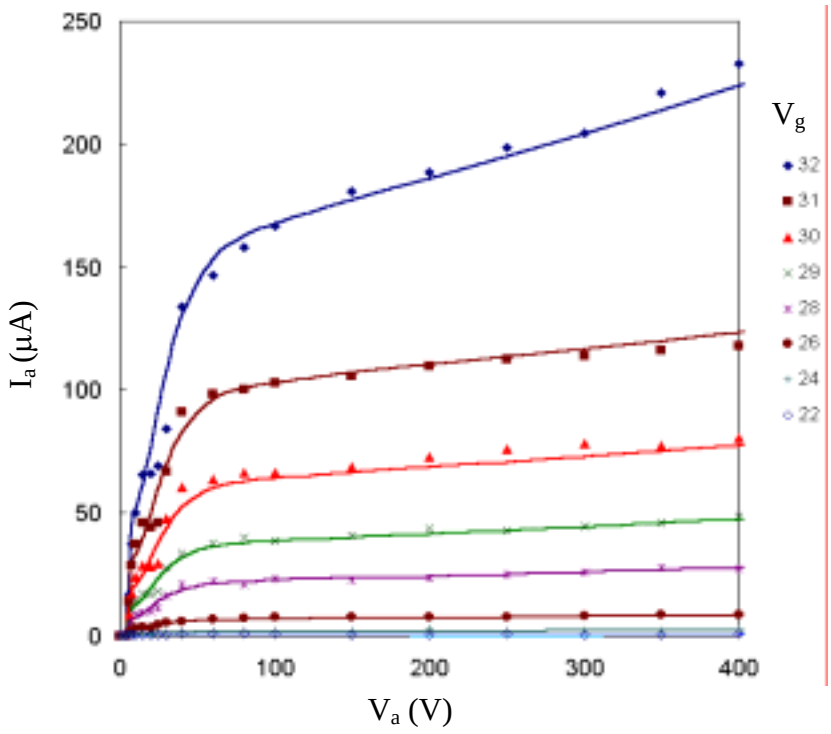


**Figure 6.127.** Modeled and actual $I_a$-$V_a$ plots of Triode B2 for various $V_g$.

Transconductance and anode resistance calculation from the triode model

The transconductance ($g_m$) and anode resistance ($r_a$) are two important triode performance parameters. The transconductance, $g_m$, controls the current driving capability, voltage gain, and high frequency response of a triode when operates as an amplifier. The anode resistance, $r_a$, determines the output resistance and the voltage gain of a triode amplifier. These parameters can be calculated from the complete model of diamond vacuum triodes by differentiating the triode model equation according to the standard definition in Eq. (3.8)-(3.10).

$$\begin{aligned} g_m &= \left.\frac{\partial I_a}{\partial V_g}\right|_{V_a=const} \\ &= X\exp\left(\frac{-Y}{E}\right)\left\{\frac{\partial\alpha}{\partial V_g}E^2+\frac{\alpha}{d}(2E+Y)\right\} \\ &= I_t\left\{\frac{\partial\alpha}{\partial V_g}+\frac{\alpha}{d}\left(\frac{2}{E}+\frac{Y}{E^2}\right)\right\} \end{aligned} \tag{6.24}$$

where $\frac{\partial\alpha}{\partial V_g}$ is given by

$$\frac{\partial\alpha}{\partial V_g}=\frac{1}{V_a}(4k_4\upsilon^3+3k_3\upsilon^2+2k_2\upsilon+k_1)\exp(\Pi(\upsilon))\exp(-\exp(\Pi(\upsilon)) \tag{6.25}$$

All variables were defined previously. In saturation region, the first term of $\frac{\partial\alpha}{\partial V_g}$ in eq. (6.24) is negligible, thus $g_m$ in saturation region ($g_{m,sat}$) is reduced to

$$\begin{aligned} g_{m,sat} &= I_t\frac{\alpha}{d}\left(\frac{2}{E}+\frac{Y}{E^2}\right) \\ &= \frac{I_a}{d}\left(\frac{2}{E}+\frac{Y}{E^2}\right) \end{aligned} \tag{6.26}$$

The calculated transconductance ($g_m$) as a function of $V_g$ for various $V_a$ are shown in **Figures 6.128-131**. For all triodes, it can be seen that $g_m$ increases exponentially as a function of $V_g$ for $V_a$ in saturation region. This is expected because $g_m$ is proportional to $I_a$ in saturation region. In non-saturation region (low $V_a$), $g_m$ increases slowly and finally decreases as $V_g$ increases for Triode U1 and U2. The declining of $g_m$ occurs because $V_g$ become greater than $V_a$ in this region. When $V_g$ is greater than $V_a$, $\alpha$ and $I_a$ decreases because more electrons arrive at the gate instead of the anode. This characteristic is not obviously seen in Triode B1 and B2

because the turn-on and operating gate voltages of boron-doped triodes are lower than the operating anode voltage under operating conditions investigated. It can be seen that undoped diamond triodes yield much less $g_m$ relative to $I_a$ than boron doped diamond triodes. Triode B1 and B2 have much high $g_m$ relative to their anode currents than Triode U1 and U2, respectively, because of their lower turn-on and operating gate voltages. Thus, low turn-on and operating gate voltages are very important for a triode to achieve high transconductance at a given anode current. F-N slope (Y) is another factor that can significantly affect $g_m$. From eq. (6.26), Y is desired to be large for high $g_m$. The effect of Y on $g_m$ can be observed from Triode B2. Triode B2 has the best $g_m$ even though it has higher operating voltage than Triode B1 because it has much higher Y. Thus, F-N slope of cathode is desired to be large for $g_m$ enhancement but F-N slope cannot be too large because turn-on and operating gate voltages will be high and leads to $g_m$ degradation. Therefore, a trading off between F-N slope and operating voltage is an issue to achieve optimum $g_m$. Nevertheless, high $g_m$ (μS range) have been achieved from these diamond triodes.

Anode resistance $r_a$ of a diamond triode is given by

$$r_a = \frac{1}{g_a} \tag{6.27}$$

where $g_a$ is given by

$$\begin{aligned} g_a &= \left.\frac{\partial I_a}{\partial V_a}\right|_{V_g = cons\tan t} \\ &= X \exp\left(\frac{-Y}{E}\right)\left\{\frac{\partial \alpha}{\partial V_g}E^2 + \frac{\alpha}{\mu d}(2E+Y)\right\} \\ &= I_t\left\{\frac{\partial \alpha}{\partial V_a} + \frac{\alpha}{\mu d}\left(\frac{2}{E} + \frac{Y}{E^2}\right)\right\} \end{aligned} \tag{6.28}$$

where $\frac{\partial \alpha}{\partial V_a}$ is given by

$$\frac{\partial \alpha}{\partial V_a} = -\frac{V_g}{V_a^2}(4k_4\upsilon^3 + 3k_3\upsilon^2 + 2k_2\upsilon + k_1)\exp(\Pi(\upsilon))\exp(-\exp(\Pi(\upsilon)) \tag{6.29}$$

In saturation region, the first term of $\frac{\partial \alpha}{\partial V_a}$ in eq. (6.28) is negligible and $r_a$ in saturation region ($r_{a,sat}$) is reduced to

$$r_{a,sat} = \frac{\mu d}{I_a}\left(\frac{E^2}{2E+Y}\right) \tag{6.30}$$

The calculated $r_a$ as a function of $V_a$ for various $V_g$ are shown in **Figures 6.132-135**. For all triodes, it can be seen that in the saturation region $r_a$ remains constant and decreases slightly as anode voltage further increases as implied from Eq. (6.30). In the non-saturation region, as anode voltage decreases below saturation, $r_a$ decreases and then inverts to increase again as anode voltage decreases toward zero. This result can be mathematically explained from Eq. (6.29). The decrease of $r_a$ in non-saturation region (compared to saturation region) is due to strong $\alpha$ dependence on anode voltage. Hence, $\frac{\partial \alpha}{\partial V_a}$ significantly increases, $g_a$ increases, and $r_a$ decreases. From **Figures 6.132-135**, $r_{a,sat}$ of ~700, 230, 700, and 5 MΩ are obtained at $I_a$ of ~700, 230, 700, and 5 MΩ from Triode U1, U2, B1, and B2, respectively. It can be seen that diamond triodes have very high anode resistance. High anode resistance is desirable because it leads to higher anode output load resistance of a triode when operates as an amplifier. Thus, diamond triodes have good anode resistance characteristic. Moreover, it can be seen from Eq. (6.30) that $r_a$ decreases as $I_a$ increases when the number of tip increases for a given gate and anode voltages.

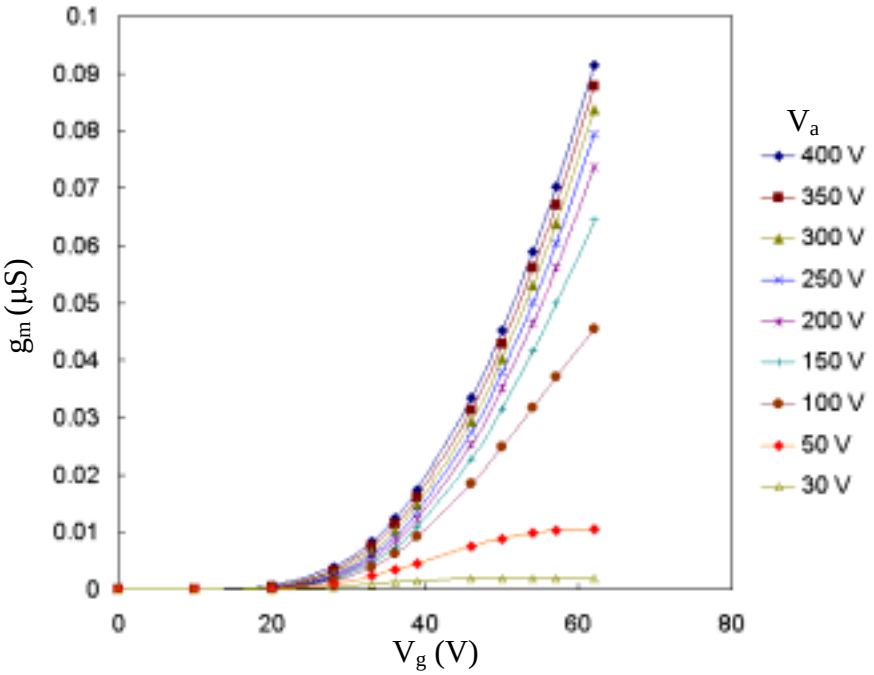


**Figure 6.128.** Modeled $g_m$-$V_g$ plots of Triode U1 for various $V_a$.

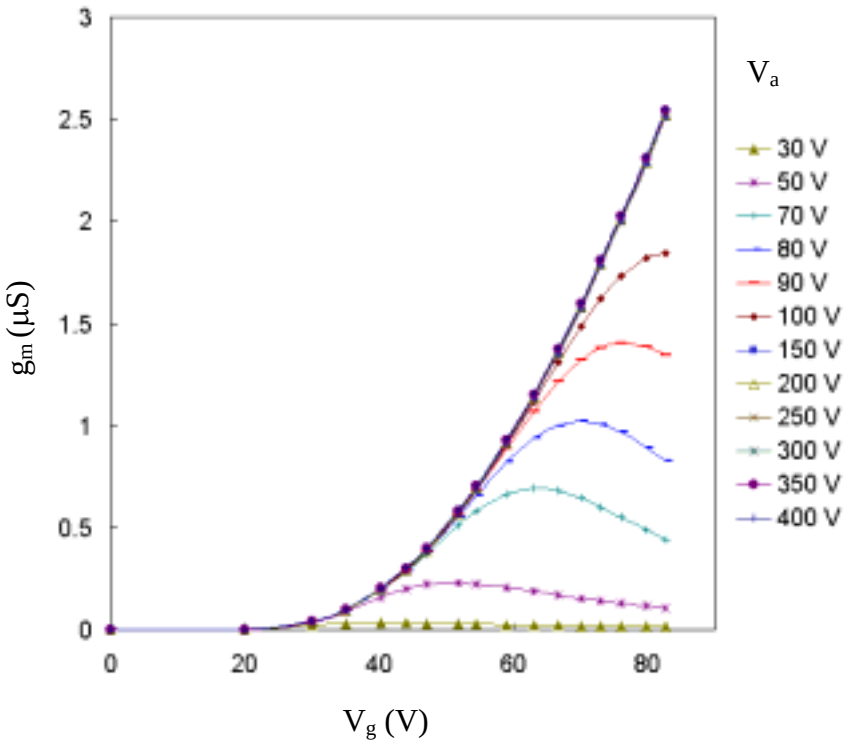


**Figure 6.129.** Modeled $g_m$-$V_g$ plots of Triode U2 for various $V_a$.

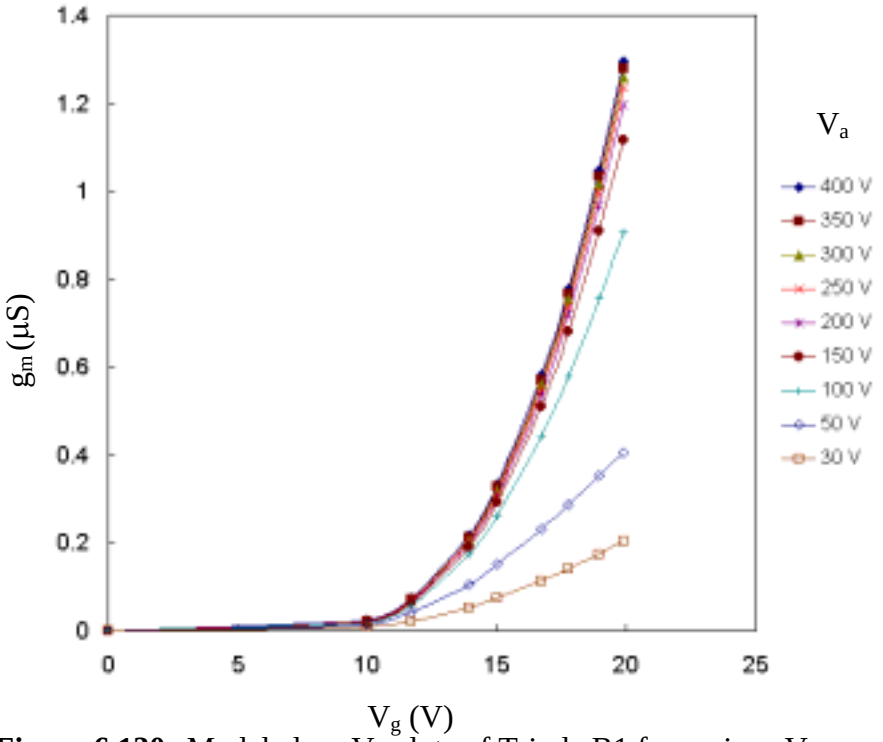


**Figure 6.130.** Modeled $g_m$-$V_g$ plots of Triode B1 for various $V_a$.

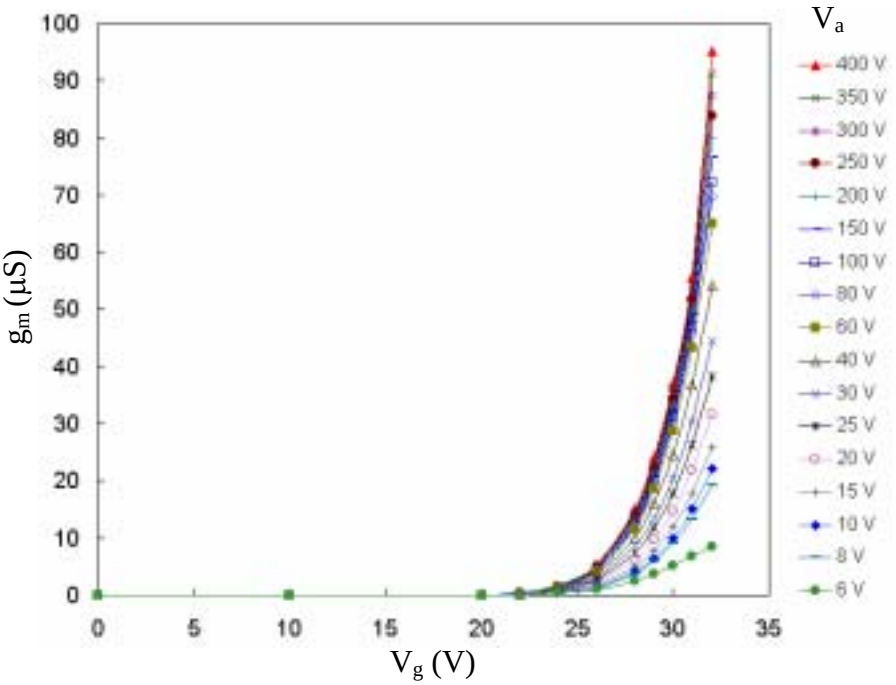


**Figure 6.131.** Modeled $g_m$-$V_g$ plots of Triode B2 for various $V_a$.

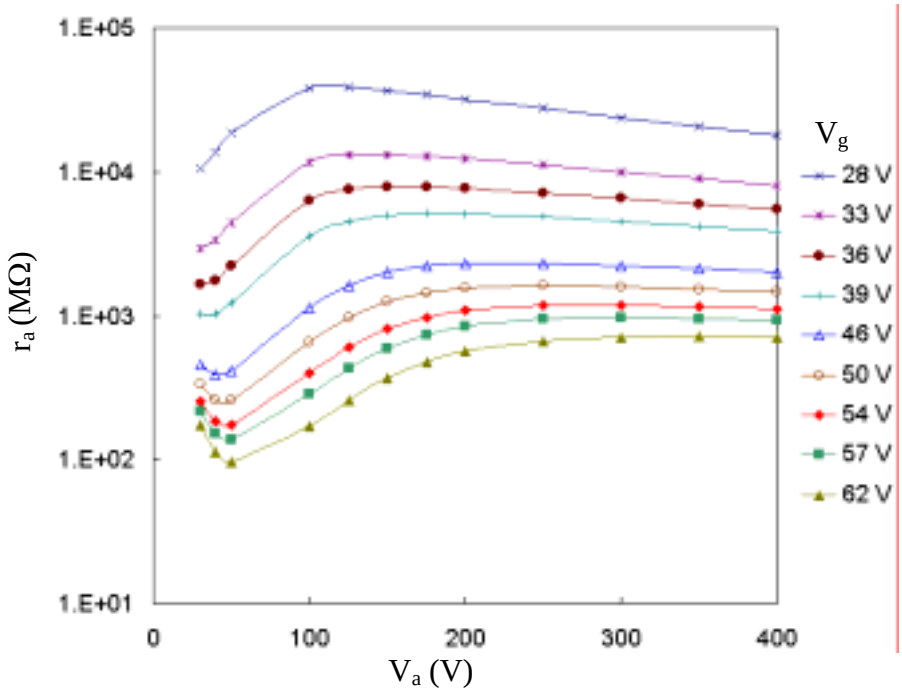


**Figure 6.132.** Modeled $r_a$-$V_g$ plots of Triode U1 for various $V_g$.

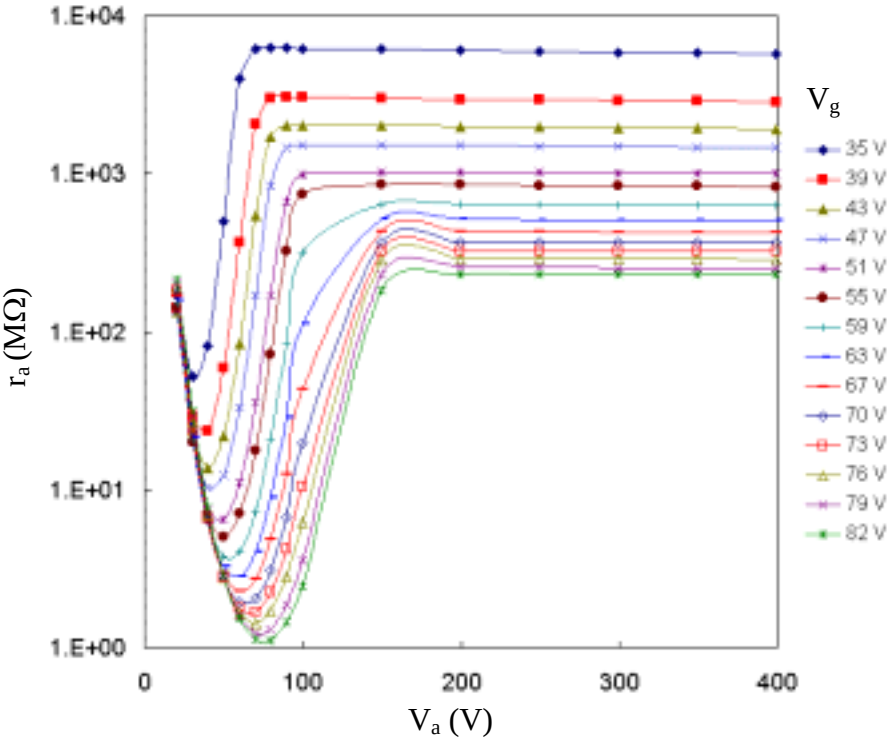


**Figure 6.133.** Modeled $r_a$-$V_a$ plots of Triode U2 for various $V_g$.

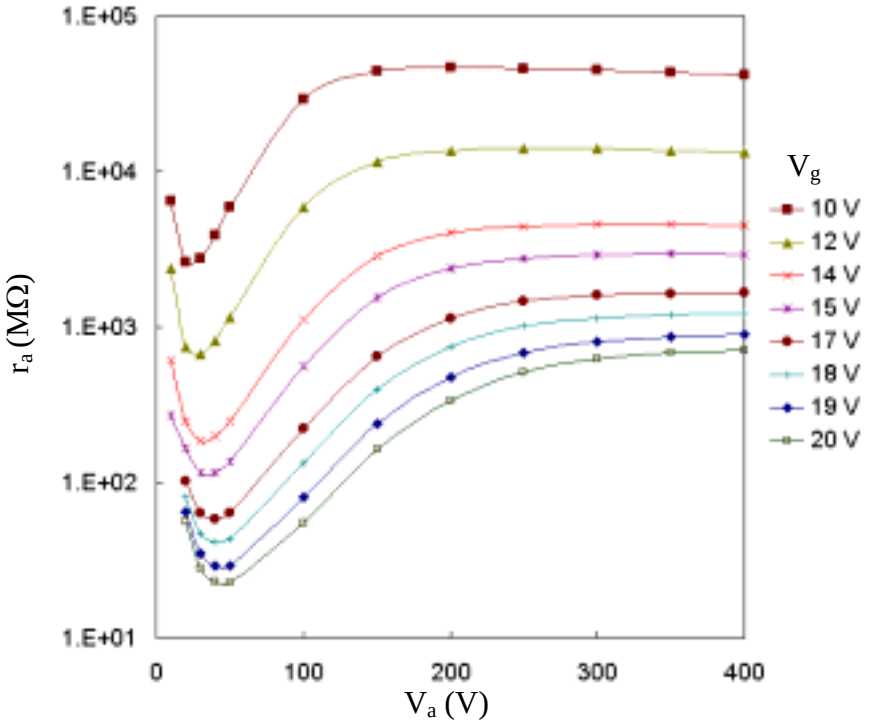


**Figure 6.134.** Modeled $r_a$-$V_a$ plots of Triode B1 for various $V_g$.

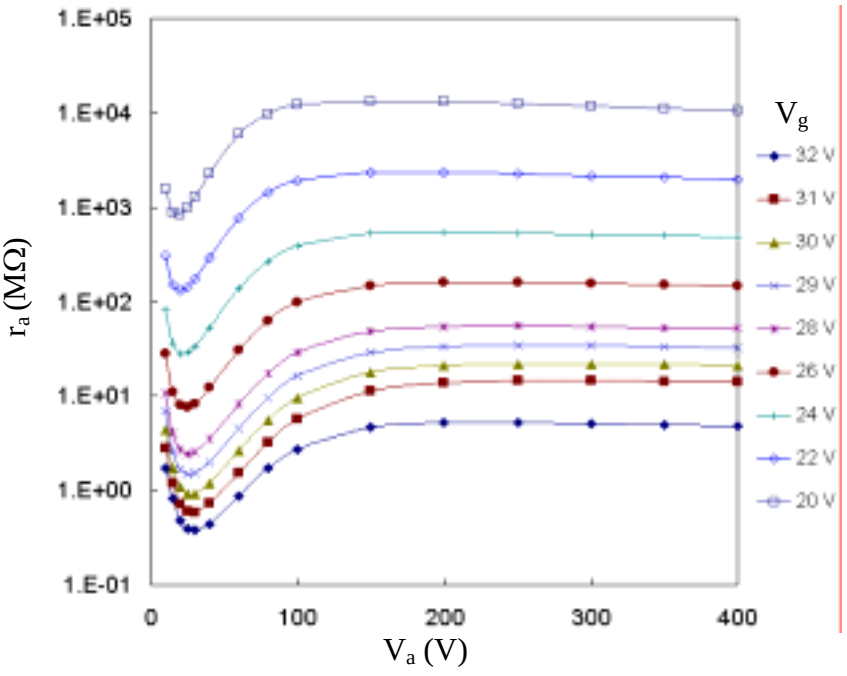


**Figure 6.135.** Modeled $r_a$-$V_a$ plots of Triode B2 for various $V_g$.

AC characteristics of diamond triode amplifier

AC characteristics of a diamond vacuum triode, in common emitter configuration, were characterized by ac input voltage vs. ac output voltage ($v_{in}$-$v_{out}$) plots. The ac characteristics of the diamond triode amplifier operated at frequency 50 Hz and 100 Hz are shown in **Figures 6.136-6.137**. This triode amplifier utilizes Triode B2 (a 256x256 array of boron-doped low $sp^2$ diamond tips with self-aligned Si-gate, gate-cathode-spacing of 1 μm, and anode-cathode spacing of ~1 mm) with a dc load resistor ($R_a$) of 7 MΩ, and ac load resistor ($R_L$) of 1 MΩ. The dc biasing condition are $V_g$ = 31 V, $V_a$ =400 V, and $I_a$ = 120 μA.

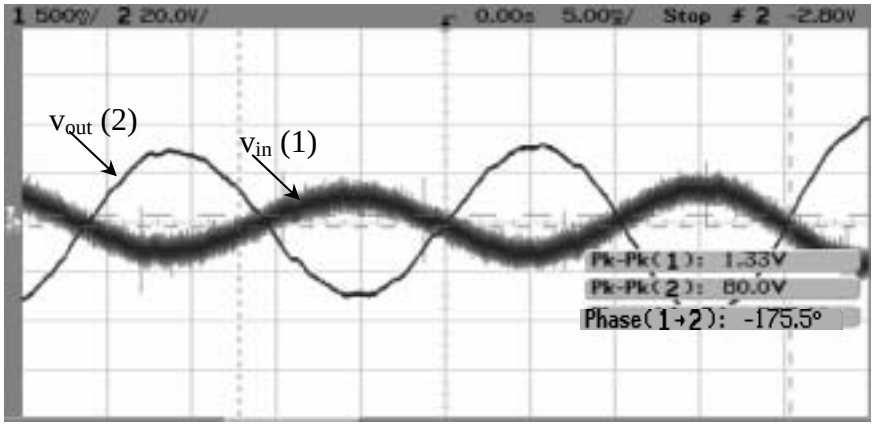


**Figure 6.136.** AC Characteristics for diamond triode amplifier at f=50 Hz.

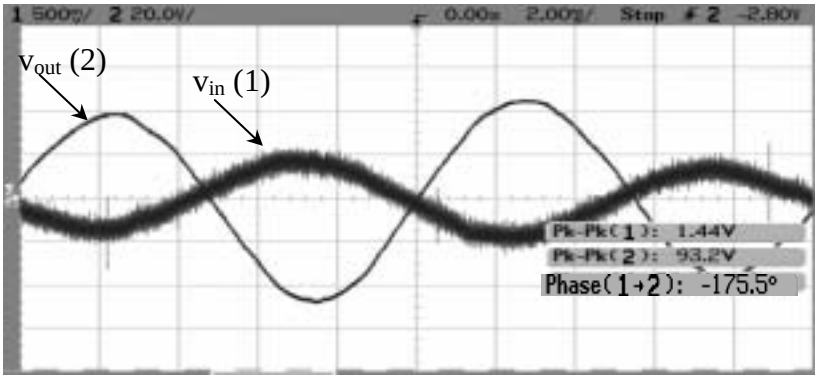


**Figure 6.137.** AC Characteristics for diamond triode amplifier at f=100 Hz.

Modeling of diamond triode amplifier

The magnitude of voltage gain, $A_V = v_{out}/v_{in}$, of the diamond triode amplifier at low frequency is ~65. Moreover, it can be seen from **Figures 6.136-6.137** that diamond vacuum triode is capable of producing large ac output voltage of 90 $V_{peak-peak}$. $A_{v0}$ can also be calculated from the dc characteristics of diamond triode using small signal model of field emission triode as shown in **Figure 6.138**.

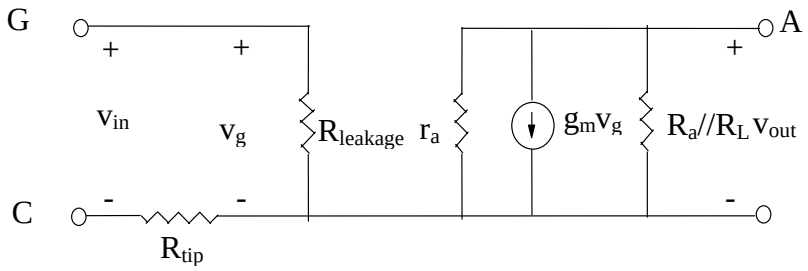


**Figure 6.138.** Small signal model for diamond triode amplifier.

From the small signal model, assuming $R_{tip} << R_{leakgage}$, $A_V$ is given by

$$A_v = -g_m \times (R_L // R_a // r_a) \quad (6.31)$$

where $g_m$ and $r_a$ can be found from the previously calculated values of Triode B2 in **Figures 6.131** and **6.135**, respectively. Using dc biasing condition of $V_g$ = 31 V and $V_a$ =400 V, $g_m \approx 85$ μS and $r_a \approx 9$ MΩ are obtained. Since $R_L$ = 1 MΩ and $R_a$ = 7 MΩ, $R_L // R_a$ = 0.875 MΩ. From the known parameters, $A_{v0}$ = 67.7 is obtained. Thus, $A_{v0}$ calculated from DC characteristics is in good agreement with direct ac measurement. Frequency response of diamond triode amplifier will be further investigated in our future work.

# CHAPTER VII

# CONCLUSION AND RECOMMENDATION

## Conclusion

Part I: Micro-patterned pyramidal diamond field emission cathode

I. A mold transfer technique has been developed to achieve diamond field emission cathodes. This mold transfer technique can produce well controlled micro-patterned diamond emitter with well defined microtip structures and uniformity over a large area.

II. Methods to improve the diamond field emission behavior have been systematically studied. These include the $sp^2$ incorporation into diamond tips, vacuum-thermal-electric (VTE) treatment, p-type doping, and tip sharpening. Some conclusions can be drawn from the study:

A) The effect of $sp^2$ content

$Sp^2$ content in diamond tips enhances the field emission behavior for both undoped and p-type diamond tips. The higher the $sp^2$ content, the lower the turn-on electric field has been observed. Two hypotheses have been proposed to explain how $sp^2$ content improves the electron field emission of diamond tips. The first hypothesis proposes that the defect-induced energy band(s) created by $sp^2$ content is responsible for the field emission enhancement. Defect-induced energy bands can be introduced throughout the energy gap of diamond due to the presence of a wide variety of structural defects created as a consequence of $sp^2$ content particles. The formation of these defect bands raises the Fermi level toward the conduction band, and thus reduces the work function. The second hypothesis proposes that the isolated $sp^2$ particles in the diamond film form cascaded MIM microstructures, which enhance the electric field inside diamond film and thereby increase the field enhancement factor. From the analysis of emission data, the second hypothesis provides a better explanation because the F-N slope ratios are constant independent of VTE treatment.

B) The effect of VTE treatment

VTE treatment on diamond tips without gold coating improves the field emission behavior. A lower turn-on electric field has been observed after VTE treatment. Two

hypotheses have been proposed to explain the effect of VTE treatment for the observed field emission enhancement. The first hypothesis proposes that the VTE treatment results in impurity desorption. As a result of impurity desorption, the surface work function is reduced after VTE treatment. The second hypothesis proposes that VTE treatment results in tip deformation due to field forming process. According to the field forming process, the tip is reformed into a configuration that increases the electric field locally on the tip surface for a given applied field, thereby increases the field enhancement factor β. Analysis of the emission data indicates that the second hypothesis is more likely to occur because F-N slope ratios between before and after VTE treatment are constant independent of $sp^2$ content.

C) The effect of p-type doping

a) For trace $sp^2$ content diamond tips before VTE treatment, the turn-on electric fields and work functions are found to increase with p-type doping. This result is in agreement with the conventional theory based on energy band diagram. The introduction of boron into the diamond crystallite lowers the Fermi-level of the bulk and increases the work function.

b) On the other hand, for low $sp^2$ content diamond tips before VTE treatment, the turn-on electric field decreases with p-type doping. This result can not be explained by the lowering of work function. This contradiction may be explained by the hot electron model. According to the hot electron model, $sp^2$ content particles induce electric field in MIM (metal-diamond-$sp^2$ content particle) microstructures leads to the accumulation of hole at metal-diamond interface. The accumulation of holes reduces the width of tunneling distance. According to this assumption, p-type doping leads to field emission enhancement that depends on $sp^2$ content. For no $sp^2$ content, p-type dopants do not play a role for field emission enhancement, instead they may result in higher work function and degrade field emission enhancement. On the other hand, for low $sp^2$ content, p-type dopants play an important role for field emission enhancement.

c) For the p-type diamond tips after VTE treatment, the turn-on electric field decreases with p-type doping. It is proposed that at room temperature, the

acceptor state of boron is partially ionized because it is in freezing zone. During VTE treatment, the acceptor states become ionized due to thermal energy. According to hot electron model, the presence of holes in combination with $sp^2$ content particles leads to field emission enhancement via the hole accumulation at metal ($sp^2$ content particles)-diamond interface. As a result, the electric field inside the diamond film particularly at the tip region is enhanced. This leads to the accelerated field forming process and hence electron field emission from diamond tip is improved.

D) The effect of tip sharpening

Practical diamond tip sharpening method by the mold sharpening process has been developed. Very sharp diamond tip with the radius of curvature less than 5 nm have been fabricated. Tip sharpening was found to improve diamond field emission significantly by the increasing of geometrical field enhancement factor by the factor of 30.

E) An empirical model for the effect of $sp^2$ content, VTE treatment, p-type doping, and tip sharpening have been developed. We proposed that the total field enhancement factor, $\beta$, in F-N equation consists of four $\beta$ field enhancement components due geometry, ($\beta_g$), $sp^2$ content ($\beta_{sp2}$), VTE treatment ($\beta_t$), and boron doping ($\beta_p$).

$$\beta = \beta_g \beta_{sp2} \beta_t \beta_p$$

F) General conclusion of the field emission of diamond cathode

a) The field emission characteristics of the micro-patterned polycrystalline diamond field emitter can be described by the Fowler-Nordhiem tunneling process.

b) The best emission characteristic is obtained from the p-type sharpened diamond tips with low $sp^2$ content after VTE treatment. The turn-on electric field is as low as 1 V/$\mu$m.

c) In general, the cause of the observed field emission enhancement of diamond tips inclines toward the increasing of the field enhancement factor of the diamond tips. The conclusion of this study is summarized in **Table 7.1**.

**Table 7.1.** Conclusion of the proposed hypothesis.

| Effect of Hypothesis / Control Factor | | Lowering of the surface work function | Increasing of the field enhancement factor | Primary Conclusion |
|---|---|---|---|---|
| $sp^2$ content | | Defect-induced band | Cascaded MIM structure | Cascaded MIM structure is more likely |
| VTE treatment | | Surface cleaning | Field forming Process | Field forming process is more likely |
| Gold coating treatment | | Induced NEA | MIM structure and field forming process | MIM structure and field forming process is more likely |
| P-type doping | Trace $sp^2$ content | Raising of the surface work function due to p-type doping | | At present, this is the only possible hypothesis. |
| | Low $sp^2$ content | | Field enhancement due to hole space charge | At present, this is the only possible hypothesis. |
| Tip sharpening | | | Tip sharpening increase geometrical field enhancement component | This is the only possible hypothesis |

Part II: Monolithic diamond vacuum diode

I. Five fabrication methods: electrostatic bonding, self-align volcano anode, and self-align-anode molding (utilizing standard, epitaxial, and SOI wafers) have been developed for the fabrication of monolithic diamond field emission diode structures. Self-align-molding technique utilizing SOI wafer is the most successful method that we have developed for the fabrication of self-aligned anode diamond vacuum diode. It is a highly efficient method that can produce self-aligned anode diamond vacuum diode over a large area with high fabrication yield.

II. Monolithic diamond vacuum diodes have low turn-on voltage and high emission current characteristics. The lowest turn-on voltage of 0.7 V has been achieved. Excellent diamond diode characteristics are attributed to well-engineered diamond microtip structure, $sp^2$ content, VTE treatment, boron doping, and micron-size anode-cathode spacing.

III. The emission characteristics of monolithic diamond vacuum diodes conform to F-N model. Moreover, the emission current has been confirmed to be temperature insensitive up to 200 °C.

Part III: Monolithic diamond vacuum triode

I. Two fabrication methods: Integrated cap anode by electrostatic bonding technique and integrated anode utilizing SOI substrate have been developed for the fabrication of monolithic diamond field emission triode structures. Each technique has pros and cons and thus they are suitable for different applications.

II. Emission characteristic from diamond vacuum triodes have been studied with three different parameters: anode-cathode spacing, diamond doping, and array sizes. Some conclusion can be drawn from this study.

A) Amplification factor increases and anode saturation voltage decreases as anode-cathode spacing increases. This observation can be explained by electrostatic theory. As the anode-cathode spacing increases, the anode potential will have less affect on electric field at the cathode, and thereby have less influence on anode current. As a result, amplification factor increases and lower saturation anode voltage occurs.

B) Amplification factor increases and anode saturation voltage decreases with boron doping of diamond cathode. We proposed that boron doping on diamond cathode reduces cathode resistance from the back contact to diamond tips, and thereby reduce potential drop and electric field reduction at the cathode. The potential drop and electric field reduction due to cathode resistance would be more significant for the gate voltage than the anode voltage. Consequently, amplification factor increases and saturation anode voltage decrease.

C) Emission current and transconductance increases but anode resistance decrease as the array size increases. This is the direct result of increasing of emitting area.

III. We have developed a semi-empirical model for diamond vacuum triodes. Anode emission current of diamond vacuum triodes have been satisfactorily modeled based on the modified F-N equation for triode and a new general empirical model for emission transport factor.

IV. Diamond vacuum triodes with good emission characteristics have been achieved.

- Low gate turn-on voltage and high emission current. Low gate turn-on voltage of 10 V has been achieved. Good diamond triode characteristics are attributed to well-engineered gated diamond emitter structure, $sp^2$ content, VTE treatment, boron doping.
- High static gain (amplification factor). High amplification factor of 800 have been achieved. High static gain is attributed to well-design gated structure, boron doping of diamond tip, and large anode cathode spacing.
- High transconductance. High transconductance of 100 μS at anode emission current of 200 μA have been achieved. High transconductance is attributed to low turn-on voltage and high emission current characteristics of diamond vacuum triode.

V. Diamond vacuum triode amplifier has been demonstrated. Diamond vacuum triode amplifier exhibits high ac voltage gain of 65 at low frequency and capable of producing large ac output voltage of 90 $V_{peak\text{-}peak}$. Frequency response of diamond vacuum triode amplifier will be further investigated in our future work.

Recommendation for further investigation

It is suggested that the results of this research should be extended and investigated in the following topics.

- The n-type diamond tips should be developed. The n-doped diamond film is an ideal approach to get the best field emission characteristics for the diamond field emitter, because n-type doping provides abundant electrons in conduction band, which is the main contribution of the emitting electron. Therefore, practical techniques to make an effective n-type doping in diamond need to be developed.
- Since the current self-aligned gate diamond field emitters still have leakage current and large gate capacitance problems, the self-aligned gate diamond field emitter should be further improved by utilizing gated diamond tip on a pole structure with thick nitrided-oxide spacer. With this structure, leakage current and large gate capacitance problem should be eliminated, and thus diamond field emitter triodes will be suitable for high frequency applications.
- Physical and theoretical model for diamond field emission devices should be further studied and developed.

- Diamond field emission should be applied in a number of potential applications in vacuum microelectronics. For examples,
  - Integrated circuits utilizing diamond vacuum diode and triode such as differential amplifiers, digital logic circuits
  - High frequency, high power, high current applications
  - High power microwave tubes
  - Neutralizer and electric propulsion
  - Field emission display
  - Vacuum microelectronic sensors

# LIST OF PUBLICATONS

The results of this proposed research have been published in journals and conferences as listed below.

Journal papers


[1] A. Wisitsora-at, W. P. Kang, J. L. Davidson, and D. V. Kerns, "A Study of Diamond Field Emission using Micro-patterned Monolithic Diamond Tips with Different sp2 contents," Appl. Phys. Lett., Vol. 71, No. 23, 1997, pp. 3394-3396.

[2] W. P. Kang, A. Wisitsora-at, J. L. Davidson, D. V. Kerns, Q. Li,, J. F. Xu and C. K. Kim, "The Effect of sp2 Content and Tip Treatment on the Field Emission of Micropatterned Pyramidal Diamond Tips," J. Vac. Sci. Technol. B, Vol. 16, No. 2, 1998, pp.684-688.

[3] W. P. Kang, A. Wisitsora-at, J. L. Davidson, M. Howell, D. V. Kerns, Q. Li, J. F. Xu, and C. K. Kim, "Micropattern Gated Diamond Field Emitter Array," J. Vac. Sci. Technol. B, Vol. 16, No. 2, 1998, pp. 732-735.

[4] W.P. Kang, A. Wisitsora-at, J.L. Davidson, and D.V. Kerns, "Ultra Low Voltage Boron-Doped Diamond Field Emitter Vacuum Diode," IEEE Electron Device Lett., Vol. 19, No. 10, 1998, pp. 379-381.

[5] A. Wisitsora-at, W. P. Kang, J. L. Davidson, Q. Li, J. F. Xu, and D.V. Kerns, "Efficient Electron Emitter Utilizing Boron-Doped High sp2 Diamond Tips," App. Sur. Sci. Vol. 146, 1999, pp. 280-284.

[6] W. P. Kang, A. Wisitsora-at, J. L. Davidson, M. Howell, D. V. Kerns, Q. Li, J. F. Xu, and C. K. Kim, "Sub-V Turn-on Voltage Self-Aligned Gate Diamond Emitter Fabricated by Self-Align-Gate-Sharpened Molding Technique," J. Vac. Sci. Technol. B, Vol. 17, No. 2, 1999, pp. 732-735.

[7] A. Wisitsora-at, W. P. Kang, J. L. Davidson, Y. Gurbuz, Q. Li, J. F. Xu, and D.V. Kerns, "Field emission enhancement of high sp2 boron-doped diamond tips with surface treatment," Diam. Relat. Mater., Vol. 8, pp. 1220-1224, 1999.

[8] J.L. Davidson, W.P. Kang, Y. Gurbuz, K.C. Holmes, L.G. Davis, A. Wisitsora-at, D.V. Kerns, R.L. Edison, and T. Henderson. "Diamond as an active sensor material" Diam. Relat. Mater., Vol. 8, pp.1741-1747, 1999.

[9] A.Wisitsora-at, W.P. Kang, J.L. Davidson, D.V. Kerns, and S. Kerns, "Fabrication of New Self-Align Gated Diamond Emitter Utilizing Silicon on Insulator Based Wafer" J. Vac. Sci. Technol. B, Vol. 19, No. 3, 2001, pp. 971-974.

[10] W. P. Kang, J. L. Davidson, A. Wisitsora-at, D. V. Kerns, and S. Kerns, "Recent Development of Diamond Field Emitter Arrays" J. Vac. Sci. Technol. B, Vol. 19, No. 3, 2001, pp. 936-941.

[11] W.P. Kang, A.Wisitsora-at, J.L. Davidson, O.K. Tan, W.G. Zhu, Q. Li, and, J.F. Xu, "Electron Emission from Silicon Tips Coated by $Ba_{0.67}Sr_{0.33}TiO_3$" J. Vac. Sci. Technol. B, Vol. 19, No. 3, 2001, pp. 1073-1076.

[12] J.L. Davidson, W.P. Kang, K.C. Holmes, A. Wisitsora-at, P. Taylor, V. Pulugurta, R. Venkatasubramanian, and F. Wells, "CVD diamond for components and emitters" Diam. Relat. Mater., Vol. 10, 2001, pp.1736-1742.

Conference papers

[1] A. Wisitsora-at, W.P. Kang, J.L. Davidson, M. Howell, Q. Li, J.F. Xu and D.V. Kerns, "Gated Diamond Field Emitter Array with Ultra Low Operating Voltage and High Emission Current," *The 55th IEEE Annual Device Research Conference*, June 23-25, 1997, Colorado State University, Fort Collins, CO, USA.

[2] W.P. Kang, A. Wisitsora-at, J.L. Davidson, M. Howell, Q. Li, J.F. Xu and D.V. Kerns, "Micropattern Gated Diamond Field Emitter Array," *The 10th International Vacuum Microelectronics Conference*, August 17-21, 1997, K, Korea.

[3] W. P. Kang, A. Wisitsora-at, J. L. Davidson, Q. Li, C. K. Kim, J. F. Xu and D. V. Kerns, "The Effects of $sp^2$ Content and Surface Treatment on the Field Emission of Micropatterned Pyramidal Diamond Tips," *The 10th International Vacuum Microelectronics Conference*, August 17-21, 1997, K, Korea.

[4] A. Wisitsora-at, W. P. Kang, J. L. Davidson, Y. Gurbuz, and D. V. Kerns, "Enhancement of Field Emission Characteristics of Micropatterned Polycrystalline Diamond Tips," *1997 Joint International Meeting - the 192nd Meeting of Electrochemical Society and 48th Annual Meeting of the International Society of Electrochemisty*, August 31-September 5, 1997, Paris, France.

[5] W. P. Kang, A. Wisitsora-at, J. L. Davidson, and D. V. Kerns, "Diamond Field Emitter Array for High Temperature Microelectronics Applications," *International High Temperature Electronics Conference*, June 14-19, 1998, Albuquerque Marriott Hotel, Albuquerque, NM, USA.

[6] A. Wisitsora-at, W.P. Kang, J.L. Davidson, Q. Li, J.F. Xu and D.V. Kerns, "A New Self-Aligned Gated Diamond Field Emitter Array with Sub-V Turn-On Voltage and High Emission Current," *The 56th IEEE Annual Device Research Conference*, June 22-24, 1998, University of Virginia, Charlottesville, VA, USA.

[7] A. Wisitsora-at, W. P. Kang, J. L. Davidson, Q. Li, J. F. Xu, and D.V. Kerns, "Efficient Electron Emitter Utilizing Boron-Doped High $sp^2$ Diamond Tips," *The 2nd*

*International Vacuum Electron Sources Conference*, July 7-10, 1998, Tsukuba Research Center, Tsukuba, Ibaraki, Japan.

[8] W.P. Kang, A. Wisitsora-at, J.L. Davidson, Q. Li, J.F. Xu and D.V. Kerns, "A New Self-Align-Gate-Molding Technique for the Fabrication of Self-Align Gated Sharp Diamond Emitter with Excellent Emission Performance," *The 11th International Vacuum Microelectronics Conference*, July 19-24, 1998, North Carolina State University, Raleigh, NC, USA.

[9] A. Wisitsora-at, W.P. Kang, J.L. Davidson, Q. Li, J.F. Xu, and D.V. Kerns, "Temperature Insensitive Self Align Gated Diamond Field Emitter" *The 11th International Vacuum Microelectronics Conference*, July 19-24, 1998, North Carolina State University, Raleigh, NC, USA.

[10] J.L. Davidson, W.P. Kang, Y. Gurbuz, K.C. Holmes, L.G. Davis, A. Wisitsora-at, D.V. Kerns, R.L. Edison, T. Henderson. "Diamond as an active sensor material" *6th International Conference on New Diamond Science and Technology (ICNDST-6)*, 31 Aug.-4 Sept. 1998, Pretoria, South Africa

[11] W.P. Kang, J.L. Davidson, A. Wisitsora-at, and D.V. Kerns, "Development of Diamond Microtip Field Emitter Devices" 1999 Joint International Meeting - the 196th Meeting of Electrochemical Society, October 17-22, 1999, Hawaii, USA.

[12] K.C. Holmes, A. Wisitsora-at, T.G. Henderson, J.L. Davidson, W.P. Kang, and V. Pulugurta, "Micorstructures in Diamond for "DMEMS" Diamond Micro Electromechanical Systems" 1999 Joint International Meeting - the 196th Meeting of Electrochemical Society, October 17-22, 1999, Hawaii, USA.

[13] A.Wisitsora-at, W.P. Kang, J.L. Davidson, D.V. Kerns, and S.E. Kerns, "Fabrication of New Self-Align Gated Diamond Emitter Utilizing Silicon on Insulator Based Wafer" The 13th International Vacuum Microelectronics Conference, August 14-17, 2000, GuangZhou, China.

[14] W.P. Kang, J.L. Davidson, A.Wisitsora-at, Q. Li, J.F. Xu, and D.V. Kerns, "Recent Development of Diamond Field Emitter Arrays" The 13th International Vacuum Microelectronics Conference, August 14-17, 2000, GuangZhou, China.

[15] W.P. Kang, A.Wisitsora-at, J. Cheng, J.L. Davidson, O.K. Tan, W.G. Zhu, Q. Li, and, J.F. Xu, "Electron Emission from Silicon Tips Coated by $Ba_{0.67}Sr_{0.33}TiO_3$" The 13th International Vacuum Microelectronics Conference, August 14-17, 2000, GuangZhou, China.

[16] W. P. Kang, A. Wisitsora-at, J.L. Davidson, and D.V. Kerns, "Fabrication and Behavior of Diamond Field Emitter Triode utilizing Silicon-on-Insulator Techonology and CVD Diamond" The 6th Applied Diamond Conference/Second Frontier Carbon technology Joint Conference, August 6-10, 2001, Auburn University, Auburn, AL, USA.

[17] A.Wisitsora-at, W.P. Kang, J.L. Davidson, D.V. Kerns, and T. Fisher, "Diamond Field Emission Triode with Low Gate Turn-on Voltage and High Gain" The 14th International Vacuum Microelectronics Conference, August 12-16, 2001, University of California at Davis, Davis, CA, USA.

[18] W.P. Kang, A.Wisitsora-at, J.L. Davidson, D.V. Kerns, and T. Fisher, "Fabrication and Field Emission Characteristics of Later Diamond Field Emitter" The 14th International Vacuum Microelectronics Conference, August 12-16, 2001, University of California at Davis, Davis, CA, USA.

[19] W.P. Kang, A.Wisitsora-at, J.L. Davidson, and D.V. Kerns, "The Effect of Annelaing Temperature on the Electron Emission Characteristic of Silicon Tips Coated with $Ba_{0.67}Sr_{0.33}TiO_3$ Thin Film" The 14th International Vacuum Microelectronics Conference, August 12-16, 2001, University of California at Davis, Davis, CA, USA.

[20] Y.M. Wong, W.P. Kang, J.L. Davidson, A.Wisitsora-at, K. L. Soh, Q. Li, and J.F. Xu, "Field Emitter using Multiwalled Carbon Nanotubes Grown on Silicon Tips by Microwave Plasma Enhanced CVD" The 14th International Vacuum Microelectronics Conference, August 12-16, 2001, University of California at Davis, Davis, CA, USA.

[21] Y.M. Wong, W.P. Kang, J.L. Davidson, A. Wisitsora-at, and K.L. Soh, "Highly Efficient Field Emitter Using Carbon Nanotubes Grown By Microwave Plasma Enhanced CVD" 2001 Joint International Meeting - the 200th Meeting of The Electrochemical Society, Inc. and the 52nd Annual Meeting of the International Society of Electrochemistry, September 2-7, 2001, San Francisco, CA, USA.

[22] J. Davidson, W.P. Kang, T. Fisher, K. Holmes, A. Wisitsora-at, and M. Howell, "Some Practical Examples of Diamond Microelectromechanical Structures (DMEMS)" 2001 Joint International Meeting - the 200th Meeting of The Electrochemical Society, Inc. and the 52nd Annual Meeting of the International Society of Electrochemistry, September 2-7, 2001, San Francisco, CA, USA.

# REFERENCES


[1] C. A. Spindt and K. R. Shoulders, "Research in micron-size field-emission tubes," *IEEE 1966 Eight Conference on Tube Techniques*, p.143, 1966.

[2] C. A. Spindt, C. E. Holland, and R. D. Stowell, "Field emission cathode array development for high current density applications," *Proceedings of the 29th International Field Emission Symposium*, p. 119, 1982.

[3] C. A. Spindt, "A Thin Film Field Emission Cathode," *J. Appl. Phys.*, Vol. 39, p. 3504, 1968.

[4] I. Brodie, "Physical Considerations in Vacuum Micorelectronics Devices," *IEEE Trans. on Electron Devices*, vol. 36, no.11, p. 2641, 1989.

[5] B. C. Djubua and N. N. Chubun, "Emission properties of Spindt-type cold cathodes with different emission cone material," *IEEE Trans. on Electron Devices*, Vol. 38, No. 10, 1991, p. 2314.

[6] C. A. Spindt, C. E. Holland, A. Rosengreen, and I. Brodie, "Field emitter arrays for vacuum microelectronics," *IEEE Trans. on Electron Devices*, vol. 38, no.10, p. 2355, 1991.

[7] E. A. Adler, Z. Bardai, R. Forman, D. M. Goebel, R. T. Longo, and M. Sokolich, "Demonstration of low voltage field emission," *IEEE Trans. on Electron Devices*, vol. 38, no.10, p. 2304, 1991.

[8] C. A. Spindt and I. Brodie, "Molybdenum field emitter array," *IEDM 96 Technical Digest*, S.F., CA, Dec 8-11, 1996.

[9] G. N. Fursey, L. M. Baskin, D. V. Glazanov, A. O. Yevgen'ev, A. V. Kotcheryzhenkov, and S. A. Polezhaev, "Specific features of field emission from submicron cathode surface areas at high current densities," *J. Vac. Sci. Technol. B*, vol. 16, no. 1, p. 232, 1998.

[10] T. Sakai, T. Ono, M. Nakamoto, and N. Sakuma, "Self-align Si gate field emitter arrays using the transfer mold technique," *J. Vac. Sci. Technol. B*, vol. 16, no. 2, p. 770, 1998.

[11] F. Ito, K. Konuma, and A. Okamoto, and A. Yano, "Effects of thermal annealing on emission characteristics and emitter surface properties of a Spindt-type field emission cathode," *J. Vac. Sci. Technol. B*, vol. 16, no. 2, p. 783, 1998.

[12] C. W. Oh, C. G. Lee, B. G. Park, J. D. Lee, and J. H. Lee, "Fabrication of metal field emitter arrays for low voltage and high current operation," *J. Vac. Sci. Technol. B*, vol. 16, no. 2, p. 807, 1998.

[13] H. Adachi, K. Ashihara, Y. Saito, and H. Nakane, "Reduction of work function on W(100) field emitter due to co adsorption of Si and Ti," *J. Vac. Sci. Technol. B*, vol. 16, no. 2, p. 875, 1998.

[14] H. F. Gray, "Silicon field emitter array technology," *Proceedings of the 29th International field emission symposium*, p. 111, 1982.

[15] R. A. Lee, "Electron emission at GEC," *The 1st International Vacuum Microelectronics Conference*, June 13-15, 1988.

[16] W. J. Orvis, C. F. McConaghy, D. R. Ciarlo, J. H. Yee, and E.W. Hee, "Modeling and Fabricating Micro-Cavity Integrated Vacuum Tubes," *IEEE Trans. on Electron Devices*, Vol. 36, No. 11, p. 2615, 1989.

[17] C. E. Hunt, J. T. Trujillo, and W. J. Orvis, "Structure and Electrical Characteristic of Silicon Field Emission Microelectronic Devices," *IEEE Trans. on Electron Devices*, vol. 38, no.10, p. 2309, 1991.

[18] Q. Li, W. P. Kang, M. Y. Yuan, J. F. Xu, D. Zhang, and J. L. Wu, "Fabrication and characterization of silicon field emission diodes and triodes," *J. Vac. Sci. Technol. B*, vol. 12, no. 2, p. 676, 1994.

[19] D. B. King, J. G. Fleming, and R. J. Walko, "The potential of Vacuum microelectronics for space reactor applications," *AIP Conference Proceedings*, Vol. 324, part 1, p. 19, 1995.

[20] S. Kang, J. H. Lee, Y. H. Song, B. G. Yu, K. I. Cho, and H. J. Yoo, "A novel structure of silicon field emission cathode with sputtered TiW for gate electrode and TEOS Oxide for gate dielectric," *IEDM 96 Technical Digest*, S.F., CA, Dec 8-11, 1996.

[21] S. Kang, J. H. Lee, Y. H. Song, B. G. Yu, K. I. Cho, and H. J. Yoo, "A novel lateral field emitter triode with insitu vacuum encapsulation," *IEDM 96 Technical Digest*, S.F., CA, Dec 8-11, 1996.

[22] J. H. Lee, S. Kang, Y. H. Song, K. I. Cho, S. Y. Lee, and H. J. Yoo, "Fabrication and characterization of silicon field emitter arrays by spin-on-glass etch-back process," *J. Vac. Sci. Technol. B*, vol. 16, no. 1, p. 238, 1998.

[23] S. Kang, J. H. Lee, B. G. Yu, K. I. Cho, and H. J. Yoo, "Novel structure of silicon field emission cathode with sputtered TiW for gate electrode," *J. Vac. Sci. Technol. B*, vol. 16, no. 1, p. 242, 1998.

[24] K. Higa, K. Nishii, and T. Asano, “Gated Si field emitter arrays prepared by using anodization,” *J. Vac. Sci. Technol. B*, vol. 16, no. 2, p. 651, 1998.

[25] P. Bruschi, A. Diligenti, F. Iani, A. Nannini, and M. Piotto, “Fabrication of a silicon-vacuum field emission microdiode with a moving anode,” *J. Vac. Sci. Technol. B*, vol. 16, no. 2, p. 665, 1998.

[26] H. Lee, S. Park, D. Park, S. Hahm, J. O. Lee and J. Y. Lee, “Nanometer-scale gap control for low voltage and high current operation of field emission array,” *J. Vac. Sci. Technol. B*, vol. 16, no. 2, p. 762, 1998.

[27] M. R. Rakhshandehroo and S. W. Pang, “Fabrication of self-aligned silicon field emission devices and effects of surface passivation on emission current,” *J. Vac. Sci. Technol. B*, vol. 16, no. 2, p. 765, 1998.

[28] J. H. Lee, Y. Song, S. Kang, K. I Cho, S. Y. Lee, and H. J. Yoo, “Polycrystalline silicon field emitter arrays prepared by silicidation-sharpening technique at low temperature,” *J. Vac. Sci. Technol. B*, vol. 16, no. 2, p. 773, 1998.

[29] J. R. Jessing, H. R. Kim, D. L. Parker, and M. H. Weichold, “Fabrication and characterization of gated porous silicon cathode field emission arrays,” *J. Vac. Sci. Technol. B*, vol. 16, no. 2, p. 777, 1998.

[30] S. E. Huq, M. Huang, P. R. Wilshaw, and P. D. Prewett, “Microfabrication and characterization of gridded polycrystalline silicon field emitter devices,” *J. Vac. Sci. Technol. B*, vol. 16, no. 2, p. 796, 1998.

[31] J. H. Lee, Y. Song, S. Kang, Y. Lee, K. I. Cho, and H. J. Yoo, “Fabrication and characterization of silicon field emitter arrays with focusing electrode by chemical mechanical polishing process,” *J. Vac. Sci. Technol. B*, vol. 16, no. 2, p. 811, 1998.

[32] M. Takai, H. Morimoto, A. Hosono, and S. Kawabuchi, “Effect of gas ambient on improvement in emission behavior of Si field emitter arrays,” *J. Vac. Sci. Technol. B*, vol. 16, no. 2, p. 799, 1998.

[33] Q. Li, J. F. Xu, H. B. Song, X. F. Liu, and W. P. Kang, “Instability and reliability of silicon field emission array,” *J. Vac. Sci. Technol. B*, vol. 14, no. 3, p. 1, 1996.

[34] Y. Song, J. H. Lee, S. Kang, S. G. Kim, K. I. Cho, and H. J. Yoo, “Analysis of electron emission degradation in silicon field emitter arrays,” *J. Vac. Sci. Technol. B*, vol. 16, no. 2, p. 811, 1998.

[35] M. Takai, T. Iriguchi, H. Morimoto, A. Hosono, and S. Kawabuchi, “Electron emission from gated silicide field emitter arrays,” *J. Vac. Sci. Technol. B*, vol. 16, no. 2, p. 790, 1998.

[36] H. S. Uh, B. G. Park, and J. D. Lee, “Surface application of molybdenum silicide on to gated poly-Si emitter for enhanced field emission performance,” *J. Vac. Sci. Technol. B*, vol. 16, no. 2, p. 866, 1998.

[37] S. Kang, J. H. Lee, Y. Song, Y. T. Kim, K. I. Cho, and H. J. Yoo, “Emission characteristics of TiN-coated silicon field emitter arrays,” *J. Vac. Sci. Technol. B*, vol. 16, no. 2, p. 871, 1998.

[38] Q. Li, M. Y. Yuan, W. P. Kang, J. F. Xu, D. Zhang, and J. L. Wu, “Fabrication and characterization of an array of gated avalanche $p^{+}$-$n^{++}$ junction as a micro-vacuum triode,” *J. Vac. Sci. Technol. B*, vol. 12, no. 5, p. 1, 1994.

[39] T. Hirano, S. Kanemaru, and J. Itoh, “A MOSFET-structured Si tip for stable emission current,” *IEDM 96 Technical Digest*, S.F., CA, Dec 8-11, 1996.

[40] Y. Miyamoto, A. Yamaguchi, K. Oshima, W. Saitoh, and M. Asada, “Metal-insulator-semiconductor emitter with an epitaxial $CaF_2$ layer as the insulator,” *J. Vac. Sci. Technol. B*, vol. 16, no. 2, p. 851, 1998.

[41] J. Ishikawa, Y. Gotoh, S. Sadakane, K. Inoue, M. Nagao, and H. Tsuji, “Emission stability analysis of cone-shaped metal-insulator-semiconductor cathode by Monte Carlo simulation,” *J. Vac. Sci. Technol. B*, vol. 16, no. 2, p. 895, 1998.

[42] H. Mimura, Y. Abe, J. Ikeda, K. Tahara, Y. Neo, H. Shimawaki, and K. Yokoo, “Resonant Fowler-Nordheim tunneling emission from metal-oxide-semiconductor cathodes,” *J. Vac. Sci. Technol. B*, vol. 16, no. 2, p. 803, 1998.

[43] J. Ikeda, A. Yamada, K. Okamoto, Y. Abe, K. Tahara, H. Mimura, and K. Yokoo, “Tunneling emission from valence band of Si-metal-oxide-semiconductor electron tunneling cathode,” *J. Vac. Sci. Technol. B*, vol. 16, no. 2, p. 818, 1998.

[44] X. Sheng, H. Koyama, and N. Koshida, “Efficient surface-emitting cold cathodes based on electroluminescent porous silicon diodes,” *J. Vac. Sci. Technol. B*, vol. 16, no. 2, p. 793, 1998.

[45] R. D. Underwood, S. Keller, U. K. Mishra, D. Kapolnek, B. P. Keller, and S. P. Denbaars, “GaN field emitter array diode with integrated anode,” *J. Vac. Sci. Technol. B*, vol. 16, no. 2, p. 822, 1998.

[46] T. Kozawa, M. Suzuki, Y. Taga, Y. Gotoh, and J. Ishikawa, “Fabrication of GaN field emitter arrays by selective area growth technique,” *J. Vac. Sci. Technol. B*, vol. 16, no. 2, p. 833, 1998.

[47] M.S. Chung, B. G. Yoon, J. M. Park, P. H. Cutler, and N. M. Miskovsky, "Calculation of bulk states contributions to field emission from GaN," *J. Vac. Sci. Technol. B*, vol. 16, no. 2, p. 906, 1998.

[48] H. H. Busta, and R. W. Pryor, "Electron emission from a laser ablated and laser annealed BN thin film emitter," *J. Appl. Phys.*, Vol. 82, p5148, 1997.

[49] M. Nagao, Y. Fujimori, Y. Gotoh, H. Tsuji, and J. Ishikawa, "Emission characteristics of ZrN thin film field emitter array fabricated by ion beam assisted deposition technique," *J. Vac. Sci. Technol. B*, vol. 16, no. 2, p. 829, 1998.

[50] F. Ducroquet, P. Kropfeld, O. Yaradou, and A. Vanoverschelde, "Fabrication and emission characteristics of GaAs tip and wedge-shaped field emitter arrays by wet etching," *J. Vac. Sci. Technol. B*, vol. 16, no. 2, p. 787, 1998.

[51] A. Fernandez, H. T. Nguyen, J. A. Britten, R. D. Boyd, M. D. Perry, D. R. Kania, and A. M. Hawryluk, "Use of Interference lithography to pattern arrays of submicron resist structures for field emission flat panel displays," *J. Vac. Sci. Technol. B*, vol. 16, no. 2, p. 729, 1998.

[52] J. van der Weide, Z. Zhang, P. K. Baumann, M.G. Wemnsell, J. Bernholc, and R. J. Nemanich, "Negative-electron affinity effects on the diamond (100) surfaces" *Phys. Rev. B*, Vol. 50, No.19, p. 5803, 1994.

[53] F. J. Himpsel, J. A. Knapp, J. A. Van Vechten, and D. E. Eastman, *Phys. Rev. B*, vol. 20, p.624, 1979.

[54] M. W. Geis, J. A. Gregory, and B.B. Pate, *IEEE Trans. on Electron Devices*, vol. 38, p. 619, 1991.

[55] R. J. Nemanich, P. K. Baumann, and J. Van der Weide, "Diamond negative electron affinity surfaces, structures and devices," *Proceedings of the Applied Diamond Conference*, Vol. 1, p17, 1995.

[56] C. Bandis, and B. B. Pate, "Photoelectric emission form negative-electron-affinity diamond (111) surfaces: exciton breakup versus conduction band," *Phys. Rev. B*, vol. 52, no. 16, p. 12056, 1995.

[57] I. L. Krainsky, V. M. Asnin, G. T. Mearini, and J. A. Dayton, "Negative-electron-affinity effect on the surface of chemical-vapor-deposited diamond polycrystalline films," *Phys. Rev. B*, vol. 53, no. 12, p. 7650, 1996.

[58] C. Bandis and B. B. Pate, "Simultaneous field emission and photoemission from diamond," *Appl. Phys. Lett.*, vol. 69, no. 3, p. 366, 1996.

[59] J. Liu, V. V. Zhirnov, W. B. Choi, G. J. Wojak, A. F. Myers, J. J. Cuomo, and J. J. Hren, "Electron emission from a hydrogenated diamond surface," *Appl. Phys. Lett.*, vol. 69, no. 26, p. 4038, 1996.

[60] T. P. Humphreys, R. E. Thomas, D. P. Malta, J. B. Posthill, M. J. Mantini, R. A. Rudder, G. C. Hudson, R. J. Markunas, and C. Pettenkofer, "The role of atomic hydrogen and its influence on the enhancement of secondary electron emission from C(001) surfaces," *Appl. Phys. Lett.*, vol. 70, no. 10, p. 1257, 1997.

[61] J. E. Yater, A. Shih, and R. Abrams, "Electron transport and emission properties of C(100)," *Phys. Rev. B*, vol. 56, no. 8, p. 56, 1997.

[62] I. L. Krainsky and V. M. Asnin, "Negative electron affinity mechanism for diamond surfaces," *Appl. Phys. Lett.*, vol. 72, no. 20, p. 2574, 1998.

[63] J. Liu, V. V. Zhirnov, A. F. Myers, G. J. Wojak, W. B. Choi, J. J. Hren, S. D. Wolter, M. T. McClure, B. R. Stoner, and J. T. Glass, "Field emission characteristics of diamond coated silicon field emitter," *J. Vac. Sci. Technol. B*, Vol. 13, No. 2, p. 422, 1994.

[64] V. V. Zhirnov, E. I. Givargizov, and P. S. Plekhanov, "Field emission from silicon spike with diamond coatings," *J. Vac. Sci. Technol. B*, vol. 13, no. 2, p. 418, 1994.

[65] E. I. Givargizov, "Silicon tips with diamond particle on them: new field emitters?," *J. Vac. Sci. Technol. B*, vol. 13, no. 2, p. 414, 1994.

[66] J. Liu, V. V. Zhirnov, G. J. Wojak, A. F. Myers, W. B. Choi, J. J. Hren, S. D. Wolter, M. T. McClure, B. R. Stoner, and J. T. Glass, "Electron emission from diamond coated silicon field emitter," *Appl. Phys. Lett.*, vol. 65, no. 22, p. 2842, 1994.

[67] E. I. Givargizov, E. V. Rakova, V. V. Zhirnov, L. L. Aksenova, and D. M. Zverev, "Growth of diamond particles on nanometer-size silicon tips," *Phys. Dokl.*, vol. 39, no. 11, p. 766, 1994.

[68] E. I. Givargizov, V. V. Zhirnov, A. N. Stepanova, E. V. Rakova, A. N. Kiselev, and P. S. Plekhanov, "Microstructure and field emission of diamond particles on silicon tips," *Appl. Surf. Sci.*, Vol. 87-88, p. 24, 1995.

[69] V. V. Zhirnov, E. I. Givargizov, A. V. Kandidov, B. V. Seleznev, and A. N. Alivova, "Emission characterization of diamond-coated Si field emission arrays," *J. Vac. Sci. Technol. B*, vol. 15, no. 2, p. 446, 1997.

[70] E. I. Givargizov, V. V. Zhirnov, N. N. Chubun, and A. B. Voronin, "Diamond cold cathodes for electron guns," *J. Vac. Sci. Technol. B*, vol. 15, no. 2, p. 442, 1997.

[71] E. I. Givargizov, V. V. Zhirnov, N. N. Chubun, and A. B. Voronin, “Fabrication of field emission display prototype based on Si field emission arrays with diamond coating,” *J. Vac. Sci. Technol. B*, vol. 15, no. 2, p. 450, 1997.

[72] S. Albin, J. Zheng, J. B. Cooper, W. Fu, and A. C. Lavarias, “Microwave plasma chemical vapor deposited diamond tips for scanning tunneling microscopy,” *Appl. Phys. Lett.*, vol. 71, no. 19, p. 2848, 1997.

[73] G. Yaun, C. C. Jin, B. L. Zhang, H. Jiang, T. M. Zhou, Y. Q. Ning, Y. Z. Wang, W. B. Wang, Y. X. Jin, H. Ji, and C. Z. Gu, “Influence of silicon tip arrays on effective work function of diamond,” *J. Vac. Sci. Technol. B*, vol. 16, no. 2, p. 710, 1998.

[74] W. B. Choi, J. J. Cuomo, V. V. Zhirnov, A. F. Myers, and J. J. Hren, “Field emission from silicon and molybdenum tips coated with diamond powder by dielectrophoresis,” *Appl. Phys. Lett.*, vol. 68, no. 5, p. 720, 1996.

[75] V. V. Zhirnov, W. B. Choi, J. J. Cuomo, and J. J. Hren, “Diamond coated Si and Mo field emitters diamond thickness effect,” *Appl. Surf. Sci.*, Vol. 94-95, p. 123, 1996.

[76] R. Schlesser, M. T. McClure, W.B. Choi, J. J. Hren, and Z. Sitar, “Electron energy distribution of diamond-coated Mo tip,” *Appl. Phys. Lett.*, vol. 70, no. 12, p. 1596, 1997.

[77] W.B. Choi, R. Schlesser, G. Wojak, J. J. Cuomo, Z. Sitar, and J. J. Hren, “Electron energy distribution of diamond-coated field emitter,” *J. Vac. Sci. Technol. B*, vol. 16, no. 2, p. 716, 1998.

[78] M. T. McClure, R. Schlesser, B. L. McCarson, and Z. Sitar, “Electrical characterization of diamond and graphite coated Mo field emitters,” *J. Vac. Sci. Technol. B*, vol. 15, no. 6, p. 2067, 1997.

[79] M. Q. Ding, A. F. Myers, W. B. Choi, R. D. Vispute, S. M. Camphausen, J. Narayan, J. J. Cuomo, J. J. Hren, and J. Bruley, “Field emission from amorphous diamond-coated Mo tip emitters by pulsed laser deposition,” *J. Vac. Sci. Technol. B*, vol. 15, no. 4, p. 840, 1997.

[80] J. H. Jung, B. K. Jum, Y. H. Lee, M.H. Oh, and J. Jang, “Enhancement of Electron Emission Efficiency and Stability of Molybdenum Field Emitter Array by Diamond-Like Carbon Coating,” *IEDM 96 Technical Digest*, S.F., CA, Dec 8-11, 1996.

[81] S. J. Lee, S. N. Lee, S. W. Lee, D. Jeon, and K. Lee, “Self-aligned silicon tips coated with diamond-like carbon,” *J. Vac. Sci. Technol. B*, vol. 15, no. 2, p. 457, 1997.

[82] J. H. Jung, B. K. Ju, H. Kim, and M. H. Oh, S. J. Chung, and J. Jang, "Effect of N doping on the electron emission properties of diamond-like carbon film on a 2-in. Mo field emitter array panel," *J. Vac. Sci. Technol. B*, vol. 16, no. 2, p. 710, 1998.

[83] F. Y. Chuang, C. Y. Sun, H. F. Cheng, C. M. Huang, and I. N. Lin, "Enhancement of electron emission efficiency of Mo tips by diamond-like carbon coating," *Appl. Phys. Lett.*, vol. 68, no. 12, p. 1666, 1996.

[84] C. Wang, A. Garcia, D. C. Ingram, M. Lake, and M. E. Kordesch, "Cold field emission from CVD diamond films observed in emission electron microscopy," *Electron. Lett.*, Vol 27, No. 16, p. 1459, 1991.

[85] N. S. Xu, Y. Tzeng, and R.V. Latham "Similarities in the 'cold' electron emission characteristics of diamond coated molybdenum electrodes and polished bulk graphite surfaces," *J. Phys. D: Appl. Phys.*, Vol. 26, No. 10, p. 1776, 1993.

[86] N. S. Xu, R.V. Latham, and Y. Tzeng, "Field-dependence of the area density of 'cold' electron emission sites on broad-area CVD diamond films," *Electron. Lett.*, Vol. 29, No. 18, p. 1596, 1993.

[87] N. S. Xu, Y. Tzeng, and R.V. Latham, "A diagnostic study of the field emission characteristics of individual micro-emitters in CVD diamond films," *J. Phys. D: Appl. Phys.*, Vol. 27, No. 9, p. 1988, 1994.

[88] D. Hong and D. M. Aslam, "Field emission from p-type polycrystalline diamond films," *J. Vac. Sci. Technol. B*, Vol. 13, No. 2, p. 427, 1994.

[89] N. Kumar, H. Schmidt, and C. Xie, "Flat panel displays based on nano-crystalline diamond thin films" in IEE Colloquium on 'Diamond in Electronics and Optics', 1993, p 9/1.

[90] N. Kumar, H. Schmidt, and C. Xie, "Diamond-based field emission flat panel displays," *Solid State Technol.*, Vol. 38, No. 5, 1995, p71.

[91] K. Okano and K. K. Gleason, "Electron emission from phosphorus and boron-doped polycrystalline diamond films," *Electron. Lett.*, Vol. 31, No. 1, p. 74, 1995.

[92] M. W. Geis and J. C. Twichell, "Electron field emission from diamond and other carbon materials after $H_2$, $O_2$, and Cs treatment," *Appl. Phys. Lett.*, Vol. 67, No. 9, p. 1328, 1995.

[93] W. Zhu, G. P. Kochanski, S. Jin, and L. Seibles, " Defect-enhanced electron field emission from chemical vapor deposited diamond," *J. Appl. Phys.*, Vol. 78, No. 4, p. 2707, 1995.

[94] W. Zhu, G. P. Kochanski, S. Jin and L. Seibles, “Electron field emission characteristics of chemical vapor deposited diamond,” *Electrochemical Society Proceedings*, Vol. 95-94, p. 531, 1995.

[95] V. L. Humphreys and J. Khachan “Spatial correlation of electron field emission sites with non-diamond carbon content in CVD diamond,” *Electron. Lett.*, Vol. 31, No. 12, p.1018, 1995.

[96] W. Zhu, G. P. Kochanski, S. Jin, L. Seibles, D. C. Jacobson, M. McCormack, and A. E. White, “Electron field emission from ion-implanted diamond,” *Appl. Phys. Lett.*, Vol. 67, No. 8, p. 1157, 1995.

[97] Q. Chen and Z. Lin, “Electron-emission-enhanced diamond nucleation on Si by hot filament chemical vapor deposition,” *Appl. Phys. Lett.*, vol. 68, no. 17, p. 2450, 1996.

[98] W. N. Wang, N. A. Fox, T. J. Davis, D. Richardson, G. M. Lynch, J. W. Steeds, and J. S. Lee, “Growth and field emission properties of multiply twinned diamond films with quintuplet wedges,” *Appl. Phys. Lett.*, Vol. 69, No. 19, p. 2825, 1996.

[99] J. S. Lee, K. S. Lim and I. N. Lin, “Electron field emission characteristics of planar diamond film array synthesized by chemical vapor deposition process,” *Appl. Phys. Lett.*, Vol. 71, No. 4, p. 554, 1997.

[100] N. A. Fox, W. N. Wang, T. J. Davis, J. W. Steeds, and P. W. May, “Field emission properties of diamond films of different qualities,” *Appl. Phys. Lett.*, Vol. 71, No. 16, p. 2337, 1997.

[101] M. Nagao, T. Kondo, Y. Gotoh, H. Tsuji, J. Ishikawa, K. Miyata, and K. Kobashi, “Influence of surface treatment and dopant concentration on field emission characteristics of boron-doped diamond thin films,” *Appl. Phys. Lett.*, Vol. 71, No. 19, p. 2806, 1997.

[102] J. Lee, K. Liu, and I. Lin, “Effect of substrate materials on the electron field emission characteristics of chemical vapor deposited diamond films,” *J. Appl. Phys.*, Vol. 82, p. 3310, 1997.

[103] D. Zhou, A. R. Krauss, L. C. Qin, T. G. McCauley, D. M. Gruen, T. D. Corrigan, R. P. H. Chang, and H. Gnaser, “Synthesis and electron field emission of nanocrystalline diamond thin films grown from $N_2/CH_4$ microwave plasmas,” *J. Appl. Phys.*, Vol. 82, p. 4546, 1997.

[104] T. Habermann, A. Gohl, D. Nau, M. Wedel, G. Muller, M. Crist, M. Schreck, and B. Stritzker, “Modifying chemical vapor deposited diamond films for field emission displays,” *J. Vac. Sci. Technol. B*, vol. 16, no. 2, p. 693, 1998.

[105] S. J. Kwon, Y. H. Shin, D. M. Aslam, and J. D. Lee, "Field emission properties of the polycrystalline diamond film prepared by microwave-assisted plasma chemical vapor deposition," *J. Vac. Sci. Technol. B*, vol. 16, no. 2, p. 712, 1998.

[106] T. Sugion, S. Kawasaki, Y. Yokota, Y. Iwasaki, and J. Shirafuji, "Electron emission characteristics of polycrystalline diamond films," *J. Vac. Sci. Technol. B*, vol. 16, no. 2, p. 720, 1998.

[107] K. H. Park, S. Lee, K. Song, J. I. Park, K. J. Park, S. Han, s. J. Na, N. Lee, and K. H. Koh, "Field emission characteristics of defective diamond films," *J. Vac. Sci. Technol. B*, vol. 16, no. 2, p. 724, 1998.

[108] D. Hong and D. M. Aslam, "Technology and characterization of diamond field emitter structures," *IEEE Trans. on Electron Devices*, Vol. 45, No. 4, p. 977, 1998.

[109] M. W. Geis, J. C. Twichell, and T. M Lyszcazarz, "Diamond Emitters Fabrication and Theory," *J. Vac. Sci. Technol. B*, Vol. 14, No. 2, p. 2060, 1996.

[110] W. N. Wang, N. A. Fox, D. Richardson, G. M. Lynch, and J. W. Steeds, "Field emission properties of diode devices based on amorphic diamond-Si heterojunctions," *J. Appl. Phys.*, Vol. 81, p. 1505, 1997.

[111] Y. W. Ko and S. I. Kim, "Electron emission and structure properties of cesiated carbon films prepared by negative carbon ion beam," *J. Appl. Phys.*, Vol. 82, p. 2631, 1997.

[112] K. C. Walter, H. H. Kung, and C. J. Maggiore, "Improved field emission of electrons from ion irradiated carbon," *Appl. Phys. Lett.*, Vol. 71, No. 10, p. 1320, 1997.

[113] J. Chen, A. X. Wei, S. Z. Deng, Y. Lu, X. G. Zheng, D. H. Chen, D. Mo, S. Q. Peng, and N. S. Xu, "Study of field electron emission phenomenon associated with N-doped amorphous diamond thin films," *J. Vac. Sci. Technol. B*, vol. 16, no. 2, p. 697, 1998.

[114] J. F. Xu, Q. Li, Z. Fan, J. Zhou, Y. Zhu, D. Mao, W. P. Kang, and J. L. Davidson, "Observation and explanation of electron emission from amorphous diamond films," *The 11$^{th}$ International Vacuum Microelectronics Conference*, July 19-24, 1998, North Carolina State University, Raleigh, NC, USA.

[115] L. S. Pan, T. E. Felter, D. A. A. Ohlberg, W. L. Hsu, C. A. Fox, R. Cao, and G. Vergara, "Enhanced field emission of diamond-like carbon films due to cesiation," *J. Appl. Phys.*, Vol. 82, p. 2624, 1997.

[116] S. J. Chung, J. H. Moon, K. C. Park, M. H. Oh, W. I. Milne, J. Jang, "Stability of electron emission current in hydrogen-free diamond-like carbon deposited by

plasma enhanced chemical vapor deposition," *J. Appl. Phys.*, Vol. 82, p. 4707, 1997.

[117] K. C. Park, J. H. Moon, S. J. Chung, M. H. Oh, W. I. Milne, and J. Jang, "Relationship between field emission characteristics and hydrogen content in diamond-like carbon deposited by the layer-by layer technique using plasma enhanced chemical vapor deposition," *J. Vac. Sci. Technol. B*, vol. 15, no. 2, p. 428, 1997.

[118] K. C. Park, J. H. Moon, S. J. Chung, and J. Jang, "Field emission of nitrogen doped diamond-like carbon film deposited by plasma enhanced chemical vapor deposition," *J. Vac. Sci. Technol. B*, vol. 15, no. 2, p. 454, 1997.

[119] B. L. Weiss, A. Badzian, L. Pilione, T. Badzian, and W. Drawl, "Electron emission from disordered tetrahedral carbon," *Appl. Phys. Lett.*, vol. 68, no. 17, p. 2450, 1996.

[120] B. L. Weiss, A. Badzian, L. Pilione, T. Badzian, and W. Drawl, "Fabrication of thin-film cold cathodes by a modified chemical vapor deposition diamond process," *J. Vac. Sci. Technol. B*, vol. 16, no. 2, p. 681, 1998.

[121] T. Ko, B. Chung, J. Y. Lee, and D. Jeon, "Fabrication and simulation of a gated thin film emitter," *J. Vac. Sci. Technol. B*, vol. 16, no. 2, p. 700, 1998.

[122] F. Y. Chuang, C. Y. Sun, T. T. Chen, and I. N. Lin, "Local electron field emission characteristics of pulsed laser deposited diamond-like carbon films," *Appl. Phys. Lett.*, vol. 69, no. 23, p. 3504, 1996.

[123] F. Y. Chuang, W. C. Wang, H. F. Cheng, C. Y. Sun, and I. N. Lin, "Field emission characteristics of diamond-like carbon films synthesized by pulsed laser deposition process using a Au-intermediate layer," *J. Vac. Sci. Technol. B*, vol. 15, no. 2, p. 454, 1997.

[124] Y. K. Hong, J. Kim, C. Park, J. S. Kim, J. K. Kim, "Field electron emission of diamond-like carbon film deposited by a laser ablation method," *J. Vac. Sci. Technol. B*, vol. 16, no. 2, p. 454, 1998.

[125] T. Ko, B. Chung, J. Y. Lee, and D. Jeon, "Preparation of ultrasharp diamond tip emitters by ion-beam etching," *J. Vac. Sci. Technol. B*, vol. 16, no. 2, p. 729, 1998.

[126] T. Asano, Y. Oobuchi, and S. Katsumata, "Field emission from ion-milled diamond films on Si," *J. Vac. Sci. Technol. B*, vol. 13, no. 2, p. 431, 1995.

[127] C. Nutzenadel, O. M. Kuttel, O. Groning, and L Schlapbach, "Electron field emission from diamond tips prepared by ion sputtering," *Appl. Phys. Lett.*, vol. 69, no. 18, p. 2662, 1996.

[128] W. P. Kang, J. L. Davidson, M. Howell, B. Bhuva, D. L Kinser and D. V. Kerns, "Micro-pattern polycrystalline diamond field emitter diode arrays," *J. Vac. Sci. Technol. B*, Vol. 14, No. 3, p. 1, 1996.

[129] W.P. Kang, J.L. Davidson, M.A.George, J. Wittig, I. Milosevlijevic, Q. Li, J.F. Xu, and D.V. Kern, "Physical Characterization of Micro-Patterned Polycrystalline Diamond Field Emitters Arrays," *J. Vac. Sci. Technol. B*, vol. 15, no. 2, p.460 1997.

[130] W. P. Kang, A. Wisitsora-at, J. L. Davidson, D. V. Kerns, Q. Li,, J. F. Xu and C. K. Kim, "The Effect of $sp^2$ Content and Tip Treatment on the Field Emission of Micropatterned Pyramidal Diamond Tips," *J. Vac. Sci. Technol. B*, Vol. 16, No. 2, 1998, pp. 684-688.

[131] W. P. Kang, A. Wisitsora-at, J. L. Davidson, M. Howell, D. V. Kerns, Q. Li, J. F. Xu, and C. K. Kim, "Micropattern Gated Diamond Field Emitter Array," *J. Vac. Sci. Technol. B*, Vol. 16, No. 2, 1998, pp. 732-735.

[132] A. Wisitsora-at, W. P. Kang, J. L. Davidson, Q. Li, J. F. Xu, and D.V. Kerns, "Efficient Electron Emitter Utilizing Boron-Doped High $sp^2$ Diamond Tips," *App. Sur. Sci.* Vol. 14, 1999, pp. 1-2.

[133] A. Wisitsora-at, W. P. Kang, J. L. Davidson, Y. Gurbuz, Q. Li, J. F. Xu, and D.V. Kerns, "Field emission enhancement of high $sp^2$ boron-doped diamond tips with surface treatment," *Diam. Relat. Mater.*, Vol. 8, p989, 1999.

[134] R. H. Fowler, and L. Nordheim, "Electron emission in intense electric fields," *Proc. Royal Soc. London*, Vol. 119, part A, p. 173, 1928.

[135] Rother, *Ann. Der Physik*, Vol. 81, p. 316, 1926.

[136] L. Nordheim, "The effect of the image force on the emission and reflexion of electrons by metals," *Proc. Royal Soc. London*, Vol. 119, part A, p. 173, 1928.

[137] J. M. Houston, "The slope of logarithmic plots of the Fowler-Nordheim equation," *Phys. Rev.*, Vol. 88, No. 2, p. 349, 1952.

[138] R. E. Burgess and H. Kroemer, "Corrected values of Fowler-Nordheim field emission function v(y) and s(y)," *Phys. Rev.*, Vol. 90, No. 4, p. 349, 1953.

[139] N. Garcia, M. I. Marques, A. Asenjo, A. Correia, "Experimental and theoretical characterization of integrated field emission nanotips," *J. Vac. Sci. Technol. B*, vol. 16, no. 2, p. 654, 1998.

[140] G. N. Fursey and D. V. Glazanov, “Deviation from the Folwer-Nordhiem theory and peculiarities of field electron emission from small-scale objects,” *J. Vac. Sci. Technol. B*, vol. 16, no. 2, p. 910, 1998.

[141] J. Jung, B. Lee, and J. D. Lee, “Effective three-demensional simulation of field emitter array and its optimal design methodology using an evolution strategy,” *J. Vac. Sci. Technol. B*, vol. 16, no. 2, p. 920, 1998.

[142] K. Okano, K. Hoshina, M. Lida, S. Koizumi, and T. Inuzuka, “Fabrication of a diamond field emitter array,” *Appl. Phys. Lett.*, Vol. 64, No. 20, p. 2742, 1994.

[143] K. Okano, S. Koizumi, and J. Itoh, “Estimation of The Emission Barrier Height of p-type semiconducting diamond from its field emission property,” *J. J. Appl. Phys.*, Vol. 34, No. 8B, p. L1068, 1995.

[144] K. Okano, T. Yamada, H. Ishihara, S. Koizumi, and J. Itoh, “Electron field emission from nitrogen-doped pyramidal-shape diamond and its battery operation,” *Appl. Phys. Lett.*, vol. 70, no. 16, p. 2201, 1997.

[145] T. Yamada, H. Ishihara, K. Okano, S. Koizumi, and J. Itoh, “Electron emission from the pyramidal-shaped diamond after hydrogen and oxygen surface treatments,” *J. Vac. Sci. Technol. B*, vol. 15, no. 5, p. 1678, 1997.

[146] S. Kim, B. K. Ju, Y. H. Lee, B. S. Park, Y. Baik, S. Lim, and M. H. Oh, “Electron emission of diamond-tip field emitter arrays fabricated by transfer mold technique,” *J. Vac. Sci. Technol. B*, vol. 15, no. 2, p. 499, 1997.

[147] P. K. Baumann and R. J. Nemanich, “Electron affinity and schottky barrier height of metal-diamond (100), (111) and (110) interfaces,” *J. Appl. Phys.*, Vol. 82, p. 5148, 1997.

[148] P. K. Baumann and R. J. Nemanich, “Negative electron affinity effects and Schottky barrier height measurements of Cobalt on diamond (100) surfaces,” *Proceedings of the Applied Diamond Conference*, Vol. 1, p41, 1995.

[149] J. van der Weide and R. J. Nemanich, “Influence of interfacial hydrogen and oxygen on the Schottky barrier height of nickel on (111) and (100) diamond surfaces” in Physical Review B, Vol 49, No19, 1994, p 13629.

[150] C. Bandis, D. Haggerty and B. B. Pate, “Electron emission properties of the negative electron affinity (111)2x1 diamond-TiO interface,” *Proceedings of Material Research Society*, Vol. 339, p. 75, 1994.

[151] W.E. Pickett, “Negative-electron-affinity and low work function surface cesium on oxygenated diamond (100),” *Phys. Rev. Lett.*, Vol. 73, No. 12, p. 1664, 1994.

[152] T. Utsumi, "Keynote address Vacuum Microelectronics: What's new and exciting" *IEEE Trans. on Electron Devices*, Vol. 38, No. 10, 1991, p. 2276.

[153] N. S. Xu and R. V. Latham, "Coherently scattered hot electrons emitted from MIM graphite microstructures deposited on broad-area vacuum-insulated high voltage electrodes," *J. Phys. D: Appl. Phys.*, Vol. 19, p. 477, 1986.

[154] J. G. Simmons, R. R. Verderber, J. Lytollis, and R. Lomax "Coherent scattering of hot electrons in gold film," *Phys. Rev. Lett.*, Vol. 17, No. 13, p. 675, 1966.

[155] J. G. Simmons and R. R. Verderber, "Observations on coherent electron scattering in thin film gold cathodes," *Appl. Phys. Lett.*, Vol. 10, No. 7, p. 197, 1967.

[156] R. V. Latham, "The origin of prebreakdown electron emission from vacuum-insulated high voltage electrodes," *Vacuum*, Vol. 32, No. 3, p. 137, 1982.

[157] Z. H. Huang, P. H. Cutler, N. M. Miskovsky and T. E. Sullivan "Theoretical study of field emission from diamond," *Appl. Phys. Lett.*, Vol. 65, No. 20, p. 2562, 1994.

[158] P. H. Cutler, Z. H. Huang, N. M. Miskovsky and T. E. Sullivan "Calculation of electron field emission from diamond," *J. Vac. Sci. Technol. B*, Vol. 13, No. 2, p. 526, 1995.

[159] P. Lerner, P. H. Cutler, and N. M. Miskovsky, "Theoretical analysis of field emission from a metal diamond cold cathode emitter," *J. Vac. Sci. Technol. B*, Vol. 15, No. 2, p. 337, 1997.

[160] P. Lerner, N. M. Miskovsky, and P. H. Cutler, "Model calculation of internal field emission and J-V characteristics of a composite n-Si and N-diamond cold cathode source," *J. Vac. Sci. Technol. B*, Vol. 16, No. 2, p. 900, 1998.

[161] H. G. Maguire, M. Kamo, H. P. Lang, and H. J. Guntherodt, "Localised structure of homoepitaxial diamond," *Ultramicroscopy*, Vol. 42-44, part A, p 689, 1992.

[162] G. V. Saparin, "Microcharacterization of CVD diamond films by scanning electron microscopy: morphology structure and microdefects," *Diamond and Related Materials*, Vol. 3, p. 1337, 1994.

[163] W. S. Lee, Y. J. Baik, K. Y. Eun, and D. Y. Yoon, "Metallographic etching of polycrystalline diamond films by reaction with metal," *Diam. Relat. Mater.*, Vol. 4, p989, 1995.

[164] W. Zhu, C. A. Randall, A. R. Badzian, and R. Messier, "Graphite formation in diamond film deposition," *J. Vac. Sci. Technol. A*, Vol. 7, No. 3, p. 2315, 1989.

[165] P.H. Cutler, Z. H. Huang, N. M. Miskovsky, P. D. Ambrosio and M. Chung, "Calculation of electronic properties of defects in diamond: Application to electron emission," *The 8th International Vacuum Microelectronics Conference Technical digest*, p. 81, July 30-August 3, 1995.

[166] J. Reistein, W. Stein, and L. Ley, "Defect spectroscopy and determination of the electron diffusion length in single crystal diamond by total photoelectron yield spectroscopy," *Phys. Rev. Lett.*, vol. 78, no. 9, p. 1803, 1997.

[167] R. Schlesser, B. L. McCarson, M. T. McClure, and Z. Sitar, "Field emission energy distribution analysis of wide-band-gap field emitters," *J. Vac. Sci. Technol. B*, Vol. 16, No. 2, p. 689, 1998.

[168] P. H. Cutler, Z. H. Huang, N. M. Miskovsky, P. D Ambrosio, and M. Chung, "Monte Carlo study of hot electron and ballistic transport in diamond: I. Low electric field region," *The 8th International Vacuum Microelectronics Conference Technical digest*, p. 278, July 30-August 3, 1995.

[169] P. Lerner, P. H. Cutler, and N. M. Miskovsky, "Hot electron and quasiballistic transport of nonequilibrium electrons in diamond films," *J. Vac. Sci. Technol. B*, Vol. 16, No. 2, p. 398, 1997.

[170] X. Ma and T. S. Sudarshan, "High field breakdown characteristics of micrometric gaps in vacuum," *J. Vac. Sci. Technol. B*, Vol. 16, No. 2, p. 745, 1998.

[171] W. P. Dyke and W. W. Dolan, "Field emission," *Advances in electronics and electron physics*, Vol. 3, p. 89, 1956.

[172] F. Stern, B. Gossling, and R. H. Fowler, "Further studies in the emission of electrons from cold metals," *Proc. Roy. Soc. A*, Vol. 124, p.699, 1929.

[173] J. P. Barbour, W. W. Dolan, J. K. Trolan, E. E. Martin, and W. P. Dyke, "Space charge effects in field emission," *Phys. Rev.*, Vol. 92, No. 1, 1953.

[174] L. R. Koller, "The physic of electron tubes", McGraw-Hill Book Co. second edition.

[175] A. L. Albert, "Fundamental electronics and vacuum tubes", McGraw-Hill Book Co. second edition.

[176] J. H. Nam, H. S. Uh, J. D. Lee, J. D. Ihm, Y. H. Kim, and K. M. Choi, "Characteristics and circuit model of a field emission triode," *J. Vac. Sci. Technol. B*, Vol. 16, No. 2, p. 689, 1998.

[177] H. Y. Ahn, C. G. Lee, and J. D. Lee, "Numerical analysis on field emission for the effect of the gate oxide," *J. Vac. Sci. Technol. B*, Vol. 13, No. 2, p. 540, 1995.

[178] K. L. Jensen, R. H. Abrams, and R. K. Parker, “Field emitter array development for high frequency applications,” *J. Vac. Sci. Technol. B*, Vol. 16, No. 2, p. 749, 1998.

[179] C. A. Spindt, C. E. Holland, P. R. Schwoebel, and I. Brodie, “Field emitter array development for microwave applications. II,” *J. Vac. Sci. Technol. B*, Vol. 16, No. 2, p. 758, 1998.

[180] C. Schoessler and H. W. P. Koops, “Nanostructured integrated electron source,” *J. Vac. Sci. Technol. B*, Vol. 16, No. 2, p. 862, 1998.

[181] J. Park, J. D. Lera, H. J. Choi, G. H. Buh, C. J. Kang, J. H. Jung, S. S. Choi, D. Jeon, and Y. Kuk, “Characterization of two by two electron-beam microcolumn array with field emission array,” *J. Vac. Sci. Technol. B*, Vol. 16, No. 2, p. 826, 1998.

[182] J. M. Kim, J. P. Hong, J. H. Choi, Y. S. Ryu, and S. S. Hong, “Parameters for improving reliability of full color field emission display devices,” *J. Vac. Sci. Technol. B*, Vol. 16, No. 2, p. 736, 1998.

[183] A. Zoulkarneev, N. S. Park, J. E. Jung, J. W. Kim, J. P. Hong, and J. M. Kim, “Vacuum analysis inside a field emission display panel: Experimental and Monte Carlo simulation results,” *J. Vac. Sci. Technol. B*, Vol. 16, No. 2, p. 741, 1998.

[184] W. P. Kang, J. L. Davidson, and D. V. Kerns, “Mold method for forming vacuum field emitters and method for forming diamond emitters,” US Patent #6,132,278, 2000.

[185] J. D. Shovlin and M. E.Kordesch, “Electron emission from chemical vapor deposited diamond and dielectric breakdown”, *Appl. Phys. Lett.*, Vol. 65, No 7, p. 863, 1994.

[186] R.E. Thomas, R.A. Rudder, and R.J. Markunas, “Thermal desorption from hydrogenated and oxygenated diamond (100) surfaces”, *Journal of Vacuum Science &Technology A*, Vol. 10, No 4, p. 2451, 1992.

[187] R. Gomer, “Field emission and field ionization”, Cambridge, Havard University Press, 1961.

[188] L. Wei, W. Baoping, and Y. Hanchun, “Simulation study on performance of field emitter array,” *J. Vac. Sci. Technol. B*, Vol. 16, No. 5, p. 2881, 1998.

[189] W. Dawson, and C. E. Hunt, “Field emission device modeling for application to flat panel displays,” *J. Vac. Sci. Technol. B*, Vol. 11, No. 2, p. 518, 1993.

[190] C. W. Lu, C. L. Lee; and J. M. Huang, "A SPICE simulation model for field emission triode," *The 9th International Vacuum Microelectronics Conference Technical digest*, p. 62, July 7-12, 1996.

[191] C. Lu, and C. L. Lee, "Direct current circuit simulation model for a field emission triode," *J. Vac. Sci. Technol. B*, Vol. 16, No. 5, p. 2876, 1998.

[192] R. C. Jaeger, "Introduction to microelectronic fabrication", Prentice Hall Co., second edition, 2001.

[193] S. M. Sze, "Modern semiconductor device physics", John Wiley & Sons, Inc., fourth edition, 1998.